Reconstruction of the low-mass dielectron signal in 1.23A GeV Au+Au collisions

Dissertation
zur Erlangung des Doktorgrades
der Naturwissenschaften

vorgelegt beim Fachbereich Physik
der Johann Wolfgang Goethe-Universität
in Frankfurt am Main

von
Patrick Sellheim
aus Hanau

Frankfurt 2017
(D 30)

vom Fachbereich Physik der Johann Wolfgang Goethe - Universität

als Dissertation angenommen.

Dekan:
Prof. Dr. Owe Philipsen

Gutachter:
Prof. Dr. Joachim Stroth
JProf. Dr. Tetyana Galatyuk

Datum der Disputation:
20.07.2017

Abstract

QCD matter is expected to exist in different phases, when heated to high temperatures and getting highly compressed. Each phase could be characterized by distinct properties. A way to access extreme phases of matter in the laboratory are heavy-ion collisions at (ultra-)relativistic energies. During the collision, the temperature and density is evolving and reaches a maximum temperature and density far beyond the ground state of matter. The matter properties depend on the incident collision energy. Typically, a collision is separated into three collisions stages, namely first chance collisions (I), hot and dense stage (II) and freeze-out stage (III). Out of those, the second one is of major interest, since the extreme states of matter are generated within. For this reason, the most prominent change of the hadrons is expected to appear there in. Those changes are caused by i.e. modification of the hadronic spectral function.

However, to retrieve such information is complicated. Hadrons are strongly interacting particles and therefore, carry little information about the hot and dense stage. For that purpose, decays of hadrons (low-mass vector mesons) to e^+e^- pairs via a virtual photon, so-called dielectrons, are an ideal probe. Electrons and positrons do not interact strongly and transport the information about the hot and dense stage nearly undisturbed to the detector. Unfortunately, the production of dielectrons is suppressed by a branching ratio of $\approx 10^{-5}$ and requires a precise lepton identification. Nonetheless, previous experiments have extracted a dilepton signal and observed in the low-mass range an excess over the hadronic cocktail. Latter one is expected to be caused by thermal radiation induced by the medium. Up to now, experiments conducted dilepton measurements with a focus on larger collision energies and large collision systems. Measurements of dielectrons at collision energies of around $1 - 2A$ GeV were only conducted for small and medium size collision systems. HADES continued the systematic studies by a measurement of Au+Au collisions at $1.23A$ GeV.

The detection of dielectrons requires detectors that handle high data rates and specific detectors for a high purity lepton identification. In HADES, the strongest separation of electrons or positrons from the hadronic background is provided by a ring imaging Cherenkov detector (RICH). Its electron identification is based on Cherenkov photons, that are emitted in ring like patterns. In this work a new approach, using the time-of-flight information to preselect electrons and the reconstructed particle trajectory to estimate ring positions, is utilized to improve the lepton identification. The concept of the so-called backtracking algorithm will be explained and applied to e^+e^- identification in Au+Au collisions. The whole analysis chain comprises single lepton identification, pair reconstruction and correction for efficiency and acceptance losses. The final pair spectra will be presented in form of their invariant mass, p_t, m_t and helicity distributions. Subsequently, transport model calculations as well as results from the recently developed coarse-grained transport approach will be compared to the dielectron spectra. Moreover, the centrality dependence of the excess yield and true (not "blue-shifted") temperature of the fireball will be presented. The results will be put in context to measurements of lighter collisions systems and at higher energies.

Zusammenfassung

Es wird erwartet, dass QCD-Materie in verschiedenen Phasen exisitiert, welche durch eine Erhöhung der Temperatur und des Drucks erzeugt werden können. Jede dieser Phasen zeichnet sich dabei durch charakteristische Merkmale aus. Solche Materiezustände können durch Schwerionenkollisionen bei (ultra-)relativistischen Energien erzeugt und auf diese Weise im Labor untersucht werden. Die erzeugten Zustände beschreiben jedoch eine Entwicklung der Temperatur und der Dichte, wobei die Maximalwerte die des Grundzustandes übersteigen und von der Kollisionsenergie abhängig sind. Typischerweise lässt sich eine Kollision in drei verschiedene Phasen unterteilen. Dazu zählen die ersten Kollisionen (I), die heiße und dichte Phase (II) und die Ausfrierphase (III). Davon ist die heiße und dichte Phase von besonderem Interesse, da dort die extremsten Zustände erwartet werden. Daher werden hier auch die größten Veränderungen der Teilchenproduktion erwartet, welche durch eine Veränderung der Spektralfunktion hervorgerufen werden.

Eine Extraktion dieser Informationen ist jedoch kompliziert. Hadronen sind stark wechselwirkende Teilchen und transportieren daher keine Information über die heiße und dichte Kollisionsphase. Deswegen werden Zerfälle von Hadronen (Vektormesonen im niedrigen Massenbereich) mittels eines virtuellen Photons in e^+e^- Paare, sogenannte Dielektronen, gewählt. Elektronen und Positronen wechselwirken nur elektromagnetisch und verlassen das Kollisionsvolumen nahezu unverändert. Die Messung ist jedoch immer noch herausfordernd, da dieser Zerfallskanal mit einem Verzweigungsverhältnis von etwa 10^{-5} unterdrückt ist. Nichtsdestotrotz wurden Dileptonenmessungen von Experimenten durchgeführt. Verglichen mit den erwarteten Beiträgen des hadronischen Cocktails wurde dabei ein Teilchenüberschuss beobachtet. Dieser Überschuss wird den Beiträgen der heißen und dichten Phase zugeordnet. Bisherige Messungen fokussierten sich auf große Kollisionssysteme und hohe Kollisionsenergien. Dielektronenmessungen im Energiebereich von etwa $1 - 2A$ GeV wurden jedoch nur für leichte und mittelschwere Kollisionssysteme durchgeführt. Daher erweitert HADES die systematischen Untersuchungen mittels der Messung von Au+Au Kollisionen bei einer Energie von $1.23A$ GeV.

Bei niedrigen Energien ist die Messung von Dielektronen nochmals erschwert, da sie unterhalb der elementaren Produktionsschwelle produziert werden. Die Dielektronenmessung setzt die Aufzeichnung hoher Datenraten und spezifische Detektoren zur Elektronenidentifikation voraus. Die stärksten Identifikationsmöglichkeiten werden durch den Ring Imaging Cherenkov (RICH) Detektor bereitgestellt. Die Elektronenidentifikation basiert auf den von der e^+/e^- Spur emittierten Tscherenkow Photonen, die in Ringmustern detektiert werden. Zur Effizienzsteigerung wurde ein neues Backtrackingverfahren implementiert. Die Implementierung des Backtrackingverfahrens wird präsentiert und zur Identifikation von e^+/e^- angewandt. Die komplette Dielektronenanalyse umfasst die Identifikation einzelner Leptonen, Paarrekonstruktion und die Korrektur der Verluste aufgrund von Effizienz- und Akzeptanzeinschränkungen. Die rekonstruierten Paarspektren der invarianten Masse, p_T, m_T und Helizität wird präsentiert. Danach werden die Ergebnisse mit Rechnungen von Transportmodellen, aber auch von dem neu ent-

wickelten "coarse-grained" Transportmodell Ansatz verglichen. Des Weiteren wird eine zentralitätsabhängige Extraktion des Teilchenüberschusses und die Bestimmung einer echten (ohne "Blauverschiebung") Temperatur des Feuerballs präsentiert. Die Ergebnisse werden zusammen mit den Ergebnissen leichterer Systeme oder höherer Energie verglichen.

Contents

Chapter 1

Introduction

In the last century, a lot of effort has been made to understand the fundamental structure of matter. This is very challenging due to the small extension of its building blocks (e.g., atom size $\approx 10^{-10}m$, proton size $\approx 10^{-15}m$, quark size $< 10^{-16}m$). In order to gain insights, scatterings or collisions of elementary particles with each other are necessary. Such experiments were conducted by Rutherford at the beginning of the 20th century and demonstrated that the atom has a structure, namely a heavy and positively charged core (*nucleus*) surrounded by electrons. Further experiments using particle accelerators, revealed protons and neutrons (*nucleons*) as constituents of a nucleus. In the year 1964, substructures, so-called *quarks*, were postulated by Murray Gell-Mann [1]. After the first experimental evidences of the quark existence [2], the standard model containing six different types of quarks and six different types of leptons was proposed in the mid-70s. In addition, five force carriers, so-called bosons, are included in the standard model.

Advances in technology, made the acceleration of heavy ions possible and opened a new research field, in which extreme states of strongly interacting matter at high temperatures and densities could be created and investigated. The first experiments were conducted at the Bevatron in Berkeley with beam energies of 1-2A GeV. Higher acceleration energies were achieved with the AGS[1] at BNL[2] and SPS[3] at CERN[4]. Even higher beam energies are reached with RHIC[5] at BNL and with the LHC[6] at CERN. At the LHC, beam energies reach 5.76 TeV for heavy-ion collisions and thus the highest collision energies achieved so far. Due to the increase in energy, matter at higher temperatures is generated, similar to the temperature during the early stages of the universe. At such high temperatures, hadrons do not exist anymore, quarks and gluons are liberated and result in a state of matter called QGP[7] [3]. Besides the trend towards

[1] Alternating Gradient Synchrotron
[2] Brookhaven National Laboratory
[3] Super Proton Synchrotron
[4] European Organization for Nuclear Research
[5] Relativistic Heavy Ion Collider
[6] Large Hadron Collider
[7] Quark gluon plasma

higher beam energies to explore the QGP, experiments at smaller energies are operated as well. In this energy regime, the interest is on investigation of the physics of baryon-rich matter. One of such experiments is the High Acceptance DiElectron Spectrometer (HADES) located at the SIS18[8] which provides collision energies of up to 1.25A GeV for heavy ions (Au). According to transport model calculations, densities up to three times of the normal nuclear density are generated during those collisions [4]. Matter under such high densities is predicted to exist in the core of neutron stars or neutron star mergers [5].

One of the observables to directly access the information of the extreme states of matter is electromagnetic probes, i.e. real and virtual photons (*dileptons*, *dielectrons*). As motivation to study heavy-ion collisions, an introduction to the fundamental forces and building blocks of matter is presented in section 1.1. Subsequently, the advantages of accessing matter properties with dileptons will be discussed in section 1.2. In addition, a historical overview of dilepton results in heavy-ion collisions will be shown (see section 1.3). An emphasis of matter characteristics at high densities, that is created in case of heavy-ion collisions at low beam energies, will be presented and discussed as the main part of this thesis based on HADES results.

1.1 Fundamental structure of QCD matter

1.1.1 Characteristics of the strong interaction

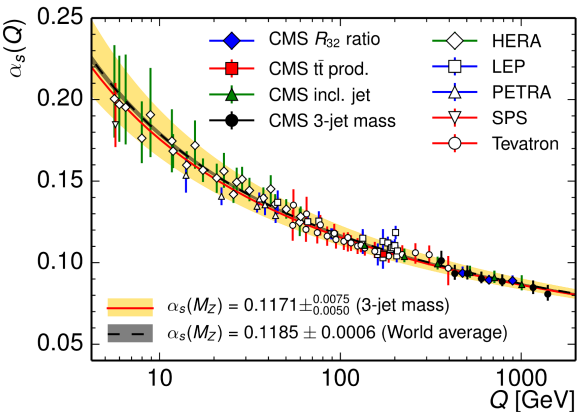

Figure 1.1: Measurements of the QCD coupling constant $\alpha_S(Q)$ compared to the world average. [6]

The strong interaction [7] has the largest strength of the four fundamental forces. This force is responsible for binding of quarks to nucleons and nuclei. Its corresponding quantum field theory is QCD[9] [8]. A major difference of the strong force to the characteristics of the well understood electromagnetic interaction is its color charge [9]. In QCD, gluons are the force carrier of the strong interaction. In contrast to the photon, the gluon also carries the color charge and can interact with each other. The QCD Lagrangian [10] density is used to describe the quark and gluon interaction:

$$\mathcal{L} = \sum_f \overline{\psi}_k (i\gamma_\mu \partial^\mu - \alpha_s \gamma_\mu A_a^\mu G_a - m_f)\psi_k - \frac{1}{4} F_a^{\mu\nu} F_{\mu\nu}^a, \tag{1.1}$$

[8] Schwerionensynchrotron
[9] Quantum Cromo Dynamics

where ψ_k are quark-field spinors, γ^μ the Dirac γ-matrices, G_a matrices that are generators of the SU(3) group, A_a^μ the gluon fields, α_s the QCD coupling constant, $F_{\mu\nu}^A$ the field tensor and m_f the mass of quarks for a given quark flavor f.

The coupling constant is a fundamental property of each theory. As shown in Fig. 1.1, the QCD coupling constant (α_s) is not constant. This fact determines the special characteristics of the strong interaction. One of them is the *confinement* [11] of the strong charge. In that case, the required color neutrality forbids the appearance of a single quark. This results in an increasing force strength for larger interaction distances (see Fig. 1.1). A second phenomenon is the weaker interaction strength for short distances, wherefore the particle moves freely. This phenomenon is called *asymptotic freedom* [12].

Due to the attractive force, bound states are created. Baryons consist of three quarks carrying different colors that add up to a color neutral object. Another typical state is a meson consisting of a quark and anti-quark pair with color and anti-color respectively. A comparison of the masses of bound states to the sum of constituent masses shows a factor of ≈100 difference, e.g. m_{proton} =938 MeV/c^2 (uud) $\neq$ 2 $\times$ 2 MeV/c^2 (u) + 5 MeV/c^2 (d). As a consequence, additional sources have to contribute to the mass generation of hadrons. It has been discovered, that in addition to the valence quarks hadrons also consist of so-called *sea quarks*. These are pairs of a quark and an anti-quark that are created for short time scales. Also the QCD vacuum is not empty, but filled with quark and anti-quark pairs, so-called *condensates*. The expectation value of $< \bar{q}q >$ is unequal to zero. An inclusion of the additional quark pairs and their dynamics for description of the hadron and mesons masses improves model calculation results that fit to the observed hadron masses [13]. The description and also prediction of bounds states proofs QCD as a successful theory for description of the interaction strength. However, many body interactions are more complex and therefore difficult to describe analytically with QCD. A way to overcome these limitations, is lattice QCD [14]. It is a theoretical approach that approximates QCD by division in small space time cells and solves the QCD equations for each point separately, which is computationally expensive. Those calculations are applied to estimate bound hadronic states and explore changes of matter properties as a function of temperature and density [13; 15; 16].

1.1.2 Chiral symmetry of QCD

Symmetries, in particular, chiral symmetry has an important role in description of QCD. Chiral symmetry is an approximate symmetry of the QCD Lagrangian for $m_q = 0$. In that case, chiral partners, (e.g, π-σ, $\rho - a_1$ or $p - N(1535)$), are expected to have the same mass. In the vacuum, chiral symmetry is spontaneously broken [17; 18], by that, one means that while the Hamiltonian possesses the symmetry its ground state does not. This state is known as Nambu Goldstone mode [19; 20]. As a consequence of chiral symmetry breaking, the masses of chiral partners are split (see Fig. 1.2). Moreover, the Goldstone theorem [20] states that three massless Nambu Goldstone bosons exist in case a symmetry is spontaneously broken. This is approxi-

mately fulfilled by the π, K and η mesons which are significantly lighter than all other mesons. The symmetry breaking itself is induced by non zero two-quark condensate $< \bar{q}q >$ in the QCD vacuum state. A connection between the pion decay constant and/or the pion mass and the quark condensate is given by the Gell-Mann-Oakes-Renner relation [21]:

$$m_\pi^2 f_\pi^2 = -m_q < \bar{q}q >, \tag{1.2}$$

where m_π^2 is the mass of the pion, f_π^2 the pion decay constant and m_q the quark masses for different flavors q. The relation between f_π^2 and the difference between vector and axial vector spectral functions is given by the Weinberg sum rules [22]:

$$f_\pi^2 = -\int \frac{ds}{\pi s}(Im\Pi_V - Im\Pi_A), \tag{1.3}$$

where $Im\Pi$ is the imaginary part of the current-current correlator of a vector (V) or a axial-vector (A), the so-called *spectral functions*. In conclusion, the strength of symmetry breaking depends on the strength of the quark condensate. The condensate, which is the order parameter for chiral symmetry breaking, can not be directly measured. However, measurements of the spectral functions provide information of the chiral symmetry breaking or its restoration at high temperatures and/or densities.

For example, a measurement of the vacuum ρ and a_1 spectral function (see Fig. 1.2) shows a clear splitting of the two chiral partners due to chiral symmetry breaking.

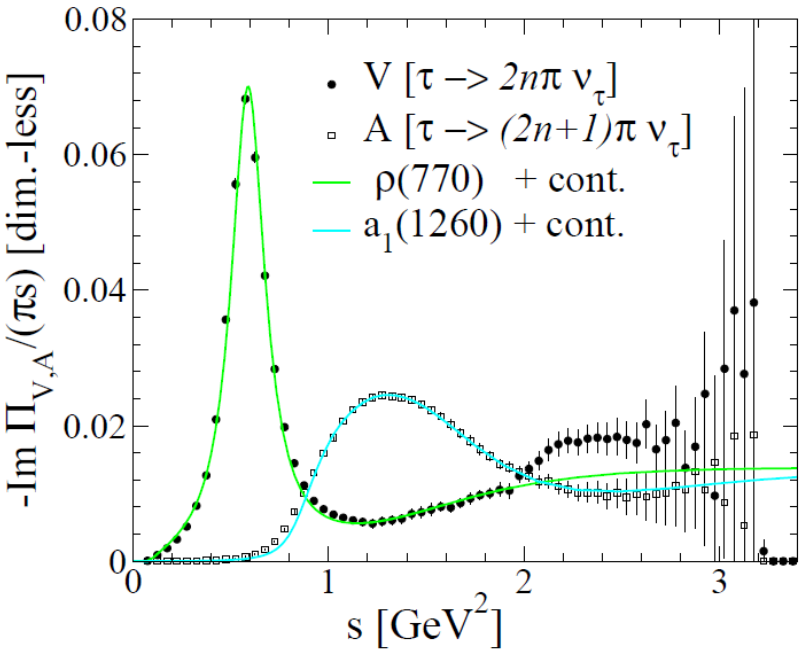

Figure 1.2: Measurement of the vector and axial vector spectral functions from τ decays [23] fitted by ρ and a_1 spectral functions. The perturbative continua are included in the fit [24].

1.1.3 Exploration of the QCD matter at extreme conditions

In the previous chapter, the concept of chiral symmetry breaking, induced by the two-quark condensate, was introduced. A search for chiral symmetry restoration requires the investigation of the quark condensate strength with varying matter properties. Those properties are the temperature (T) and *baryon chemical potential* (μ_B, that is a measure for the symmetry between matter and antimatter). Due to the interplay of QCD features, new states of matter, where chiral symmetry is expected to be partially of fully restored, are predicted for a variation of temperature and density.

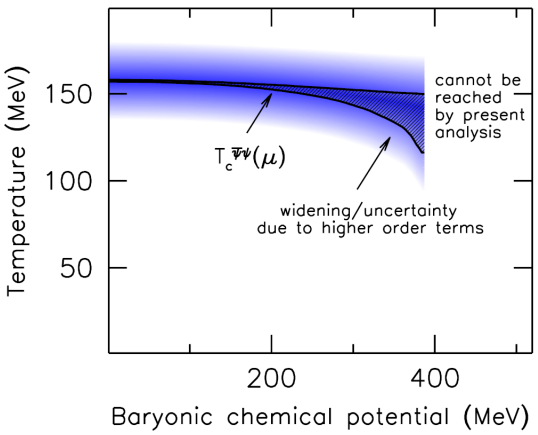

Figure 1.3: Phase transition at low μ_B estimated with lattice QCD by analytical continuation of the imaginary chemical potential [25]. The phase transition is indicated by the black line and obtained by the chiral condensate. Its width is indicated by the blue band.

An expectation of matter properties could be set by lattice QCD calculations. It forecasts a phase transition between two different phases [16] (see Fig. 1.3) with a rapid crossover at a temperature of $T \approx 154 - 156$ MeV [26; 27]. Fig. 1.4 indicates, that at T_c hadrons do still exist, while the condensate has nearly vanished. This allows to use hadrons in order to investigate the two-quark condensate. Furthermore, when increasing the baryon chemical potential, a critical point connecting the crossover with a phase transition, is expected by lattice QCD [28; 29]. However, lattice QCD is not able to predict a precise position of the critical endpoint, since the calculations are limited to vanishing baryon chemical potential. Nevertheless, it is stated that the critical endpoint is assumed to be characterized by increased fluctuations of conserved quantum numbers (e.g., baryon, strangeness, charge) [30]. Measuring these fluctuations is an experimental approach to search for the critical endpoint.

A picture of the phase diagram of matter is shown in Fig. 1.5. At temperatures above the critical point, large momentum transfers during the interaction are dominant [31]. Consequently, asymptotic freedom is the dominant QCD characteristic and leads to a deconfined state of matter, in which the chiral symmetry is assumed to be restored [18]. When decreasing the temperature and increasing the baryon chemical potential, another phase transition, between confined and quarkyonic matter [32], is expected. An increase of the density leads, similar to an increase of temperature, to asymptotic freedom. Based on theoretical calculations, this phase is still confined with a much larger number of degrees of freedom than in hadronic matter [33]. The chiral symmetry is yet fully or partially restored [34]. A possible realization of this phase are hadronic states squeezed together, that could merge to larger bound objects.

The ground state of matter is located at $T = 0$ and the normal nuclear density $\mu_B = 938$ MeV [18]. As a consequence of the large interaction distances, confinement is dominant in the low

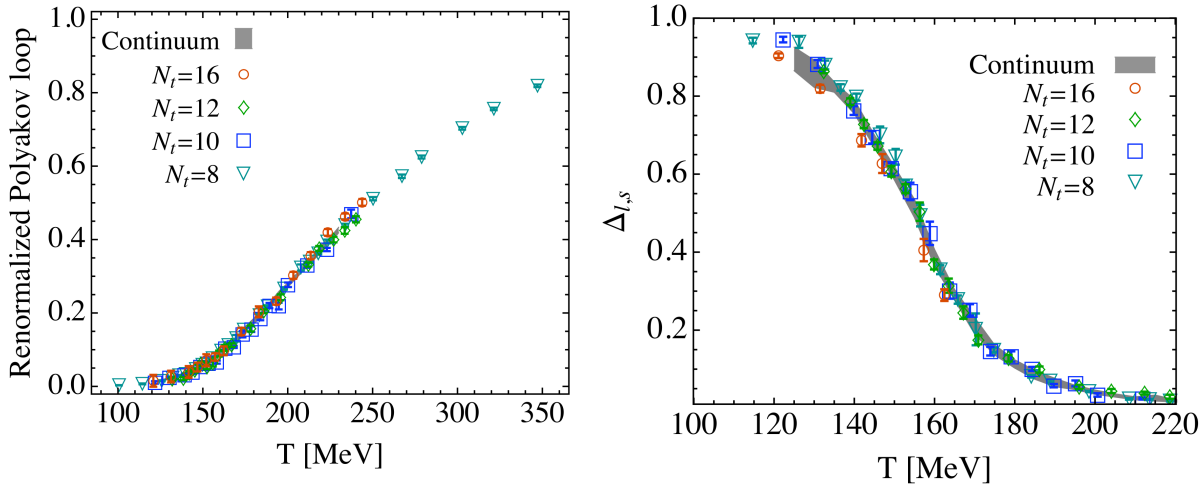

Figure 1.4: Renormalized Polyakov loop (**left**) and subtracted chiral condensate (**right**) as a function of T estimated with lattice QCD [26].

temperature regime, for which reason color-neutral hadrons are formed [18]. At higher densities but still small temperatures, additional exotic states of matter are predicted [18].

The above described phases in the QCD phase diagram are accessible in the laboratory in heavy-ion collisions (HIC) at (ultra-)relativistic energies. Colliding nuclei generate transient hot and dense phases. The collision is dynamically evolving, resulting in a variation of density and temperature (see Fig. 1.6). According to microscopic model calculations one could reach up to 8 times of normal nuclear matter density (ρ_0) when going to beam energies $\geq 20A$ GeV, and up to $3\rho_0$ at energies of $\approx 1A$ GeV with substantial duration of the dense phase. A process of a heavy-ion collision at energies of a few GeV per nucleon in general could be separated into three collisions stages:

- **First chance collisions:** The first interaction of nucleons is representing this stage. Hard processes of nucleon nucleon interactions with a high energy transfer are characteristic for this stage.

- **Hot and dense stage:** The highest temperatures and densities are reached at this collision stage. In case new phases of matter are created, they are expected to be originated within this stage often called hot and dense fireball. Due to expansion, the temperature and density of the system decrease with time.

- **Freeze-out stage:** This stage begins when inelastic scatterings stop, hadrons are formed and furthermore any interactions among them stop. In more detail, this stage can be separated in a chemical freeze-out, where inelastic scatterings stop, and a kinetic one at the point when elastic collisions terminate.

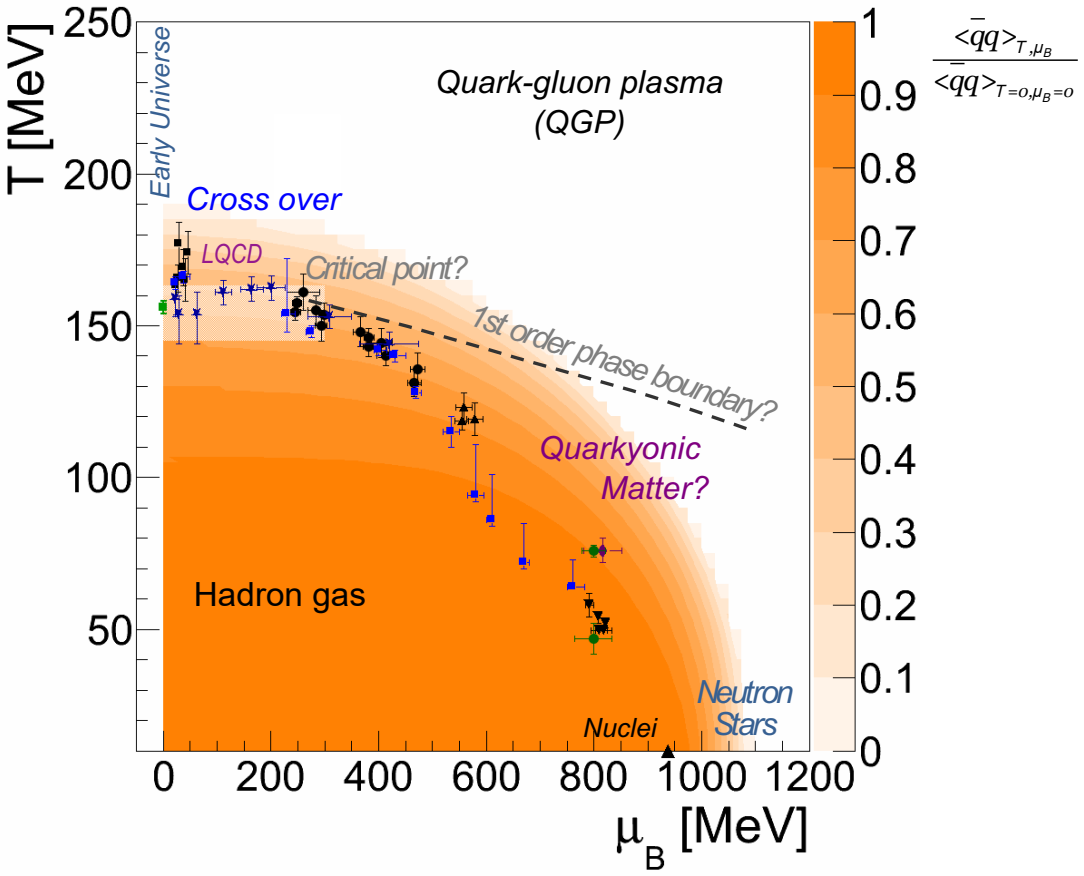

Figure 1.5: Strength of the two-quark condensate $< \bar{q}q >$ as a function of baryon chemical potential and temperature. Towards higher densities or temperatures matter becomes deconfined. Lattice QCD also predicts a critical point, but is due to limitations not able to predict a precise position. Every data point is estimated with the thermal model. The data points fit on an universal freeze-out curve from SIS energies in the energy range of $1A$ GeV up to LHC energies in the low TeV/u range. (LQCD: [35], Condensate: [36], data: [33; 37; 38; 39])

A specific particle species is mostly produced at a specific collision stage and can be used to probe the latter. In general, the high temperature region at low net-baryon densities is accessible in high collision energies around 1 TeV. The high momenta of beam particles result in a large fireball temperature and similar production rates of matter and anti-matter particles. Consequently, the baryon chemical potential is small. By decreasing the collision energy (ranging from, 200 GeV down to 2 GeV), the temperature is reduced while the baryon chemical potential increases due to the reduced production of anti-particles.

The properties of matter can be obtained by measurements of particles and utilization of the thermal model [33; 38; 40]. This simple model is based on the expectation of statistical particle production. Therefore, a partition function of a grand canonical ensemble is applied. In addition, the modification of the number of produced particles due to decays has to be considered. A fit of the model to the measured particle yields returns a temperature, baryon chemical potential and volume at the freeze-out stage [33; 38]. Instead of particle yields, ratios are used to cancel

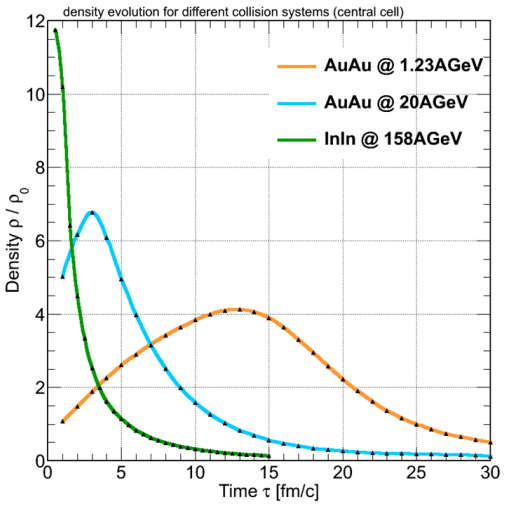

Figure 1.6: Density evolution in a heavy-ion collision for different collision systems and beam energies. Towards smaller energies, the system needs more time to build up the pressure [41].

out volume effects. In Fig. 1.5 temperatures and μ_B extracted from various experiments are shown as colorful points. However, it is important to remind that these points are extracted at the moment of chemical freeze-out. Due to its evolution, the hot and dense state of the heavy-ion collision might have reached phases with higher temperatures and higher baryon chemical potentials (see Fig. 1.5). All data points follow a trend, namely the universal freeze-out curve. The thermal model fits well to the entire range of collision energies. This indicates that the system, before it was frozen out, has been in the thermal equilibrium. The mechanism of thermal equilibrium, in particular, at small collision energies has to be understood.

1.2 Medium modifications of hadrons and the role of electromagnetic probes

It has been shown, that chiral symmetry is spontaneously broken in the vacuum due to presence of the quark condensate. It might be restored when the temperature and density are high enough. A proof of chiral symmetry restoration requires the reconstruction of vector and axial-vector behavior in hot and dense matter. A probe to search for chiral symmetry restoration has to fulfill the following properties:

- Created inside the hot and dense collision stage.
- The probe is not modified by further evolution of the collision system and strong interactions.
- The measured particles can be distinguished from background sources of different phases.

In the beginning of this section, the expected modifications of particle production mechanisms in matter are presented. Afterwards, the advantages of electromagnetic probes are discussed. Subsequently, the challenges of their reconstruction are explained. Finally, models to describe the dilepton production in heavy-ions collisions are discussed.

1.2.1 Medium modifications of hadrons in QCD matter

Besides the confined phase of matter, new deconfined phases are expected at high temperatures or high densities (see section 1.1.3) when the quark condensate is reduced. Since latter one is an order parameter for chiral symmetry [18], the symmetry is expected to be restored when the condensate vanishes. The symmetry restoration will be revealed in modifications of the spectral functions. Expectations on the relation between the medium modifications and the condensate are provided by theoretical models [42].

The theoretical approach which relates the order parameters of the chiral symmetry to the vector and axial-vector spectral functions of mesons is the Weinberg Sum Rules and predicts degeneracy of chiral partners [18]. Figure 1.7 compares the spectral functions of ρ and a_1 for different temperatures, that are expected to degenerate when the temperature is high enough. However, the sum rules only constrain specific integrals over the difference of spectral functions, but not physical observables (e.g. mass distributions). Latter constraints, can only be extracted from hadronic models [43]. Different hadronic models use various approximations of the hadronic model Lagrangian and require constraints on input parameters in vacuum for different energies (e.g. decay widths) [43]. Two different scenarios, namely a broadening or dropping of the spectral function, are predicted by models. The broadening of the spectral function has been proven by experimental results [44] by investigating the ρ mass distribution in hot and dense matter [44].

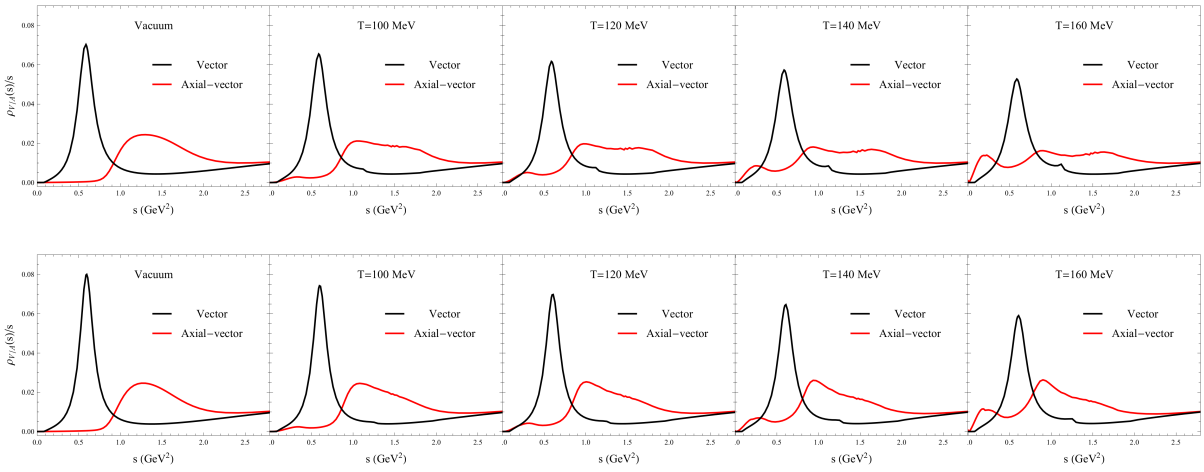

Figure 1.7: Modification of vector and axial-vector spectral function for different temperatures. The shapes are presented for non-linear realization (upper) and linear realization (lower). [42]

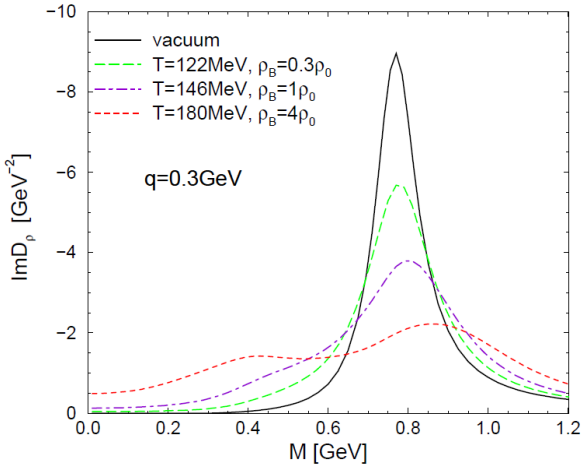

Figure 1.8: Modification of the ρ meson spectral function in hot and dense hadronic matter. The spectral functions are plotted for a constant 3-momentum (q= 0.3 GeV) and averaged over the spin. All functions are presented for a constant baryon chemical potential of $\mu_B = 0.408\ GeV$ and show a melting of the spectral function for increased temperatures and densities. [43]

The broadening is explained by interactions ρ with the hadrons (mesons and baryons)in the medium that are investigated in [43; 45; 46]. Couplings of the ρ meson to resonance-hole excitations modify its spectral function (see Fig. 1.9). Moreover, it is additionally modified due to the direct coupling of ρ to the baryons and mesons (see Fig. 1.9) [47]. The additional interactions result in a modification of the ρ mass distribution by increasing the yield towards lower masses (see Fig. 1.8). This effect is accompanied by a slight up-shift of the pole mass [48; 49]. A comparison of both effects has shown, that the modification due to hot pion gas is smaller than due to interactions with resonances [47; 50].

Even more information of chiral system restoration, can be obtained by measurements of both chiral partners. The search for degeneration of e.g. the ρ and a_1 spectral function could directly proof chiral symmetry restoration.

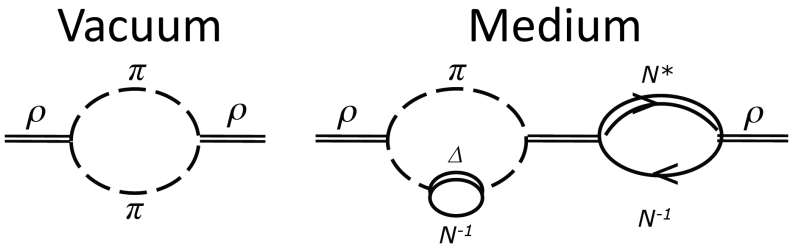

Figure 1.9: Typical interactions of the ρ meson in vacuum and inside the medium are shown. Additional resonance hole excitations of baryonic resonances modify the ρ meson in the medium.

1.2.2 Dileptons as a tool to study medium modifications of hadrons

Dileptons and photons are electromagnetic probes. They only couple to other particles via electromagnetic interaction which is described by QED. Due to the small coupling, the mean free path of a lepton inside heavy-ion collisions, is larger than the typical system size of the collision itself. Therefore, they are an ideal probe to the study the medium modifications of hadrons in QCD matter, which were discussed in the previous section.

In general, one distinguishes real and virtual photons. Real photons do not have a mass and therefore can't decay. Virtual photons can decay, but their existence is restricted by the Heisenberg uncertainty relation, which limits their appearance to short times ($\approx 10^{-23}\ s$). A unique

feature of virtual photons is their direct decay to a lepton pair, since the process is not forbidden by momentum conservation. Such photons decaying into two leptons are called *dileptons* (*dielectrons*).

In more detail, the virtual photons themselves are categorized in so-called *space-like* and *time-like* photons. While space-like photons mostly transfer momentum, time-like photons mostly transfer energy during the interaction. This allows to probe the interaction in two different regions of momentum transfer. The momentum transferred by the virtual photon (q) is given by [51]:

$$q^2 = (\Delta E_l)^2 - (\Delta p_l)^2, \tag{1.4}$$

where ΔE is the energy and Δp the momentum change of a lepton. The emission of dileptons is described by:

$$\frac{dN_{ll}}{d^4x d^4q} = -\frac{\alpha_{EM}^2}{\pi^3}\frac{L(M)}{M^2} f^B(q.u;T) Im\Pi_{EM}(M,q;\mu_B,T), \tag{1.5}$$

where α is the electromagnetic coupling constant, $L(M)$ a phase space factor of dilepton production that includes the lepton masses, f^B the Jüttner function and Π_{EM} is the EM current-current correlator. The imaginary part of Π_{EM} is the photon self-energy and called spectral function. It describes the dielectron emission rates which result from QED interactions.

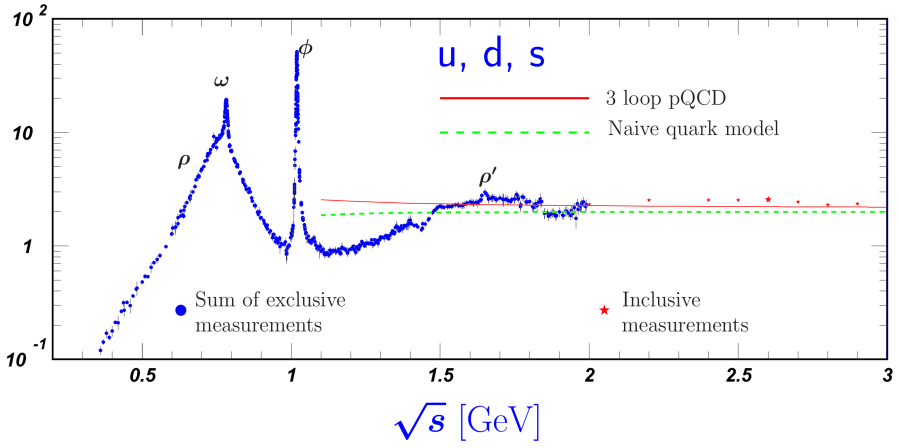

Figure 1.10: Measurement of e^+ e^- annihilation, where a ratio (R) of decay particles is estimated as R=$\frac{\pi^+\pi^-}{\mu^+\mu^-}$. Especially the low-mass region deviates from the hadronic continuum and displays peak structures belonging to the vector mesons.[52]

Particle	Mass $[MeV/c^2]$	Branching ratio: e^+e^-	Lifetime [fm/c]	Model prediction [%]
ρ	775	$4.72 \cdot 10^-5$	1.32	75
ω	783	$7.28 \cdot 10^-5$	23.4	8
ϕ	1019	$2.95 \cdot 10^-4$	46.2	17

Table 1.1: Summary of vector meson properties [53] that indicate differences between the lifetimes of them. The model prediction value is the fraction of the specific vector meson compared to all vector mesons and is predicted by the quark model.

The simplest QED interactions, which are suppressed by $1/\alpha$, are called point-like interactions. Deviations from point-like interactions are described by a form factor. Latter one can be directly measured by e^+e^- annihilation for the vacuum case (see Fig. 1.10). In the low-mass region the photon self-energy is saturated by vector mesons:

$$Im\Pi_{EM} \sim [ImD_\rho + \frac{1}{2}ImD_\omega + \frac{2}{9}ImD_\phi] \tag{1.6}$$

giving rise to the vector meson dominance. Out of the light vector mesons, ρ is, according to the Gell-Mann and Zweig quark model [1], the most frequent vector meson (see table 1.1). A description of vector meson contribution in the low-mass region[10] is given by the *vector meson dominance* model (VDM) model [7]. It states that virtual photons can acquire a hadronic character. Vector mesons are the only suited hadron candidates, since only their quantum numbers ($J^P = 1^-$) are equal to the ones of a photon. As a result, in the low-mass region the spectral function in the vacuum is dominated by vector mesons.
The yield in the low-mass region is expected to be strongly modified for different medium properties, since additional processes contribute to the photon self-energy (see Fig. 1.9):

$$D_\rho(M, q, \mu_B, T) = \frac{1}{M^2 - m_\rho^2 - \Sigma_{\rho\pi\pi} - \Sigma_{\rho B} - \Sigma_{\rho M}}. \tag{1.7}$$

In this way, medium properties of matter can be directly probed with dileptons. Since ρ has the shortest life-time of all light vector mesons, it decays most likely inside the fireball. As a consequence, it is the best probe to investigate medium modifications present in the hot and dense collision phase of heavy-ion collisions.

1.2.3 Challenges and strategies of dilepton measurements at SIS18 energies

Medium modifications of mesons in matter can be accessed via their electromagnetic decays. The Feynman diagram in Fig. 1.11 sketches main vector meson production processes at SIS18 energies. A significant feature of dileptons is their small production and decay probability, which makes their measurement very challenging. The branching ratio is caused by their pro-

[10] $M_{ee} < 1.1\ GeV/c^2$

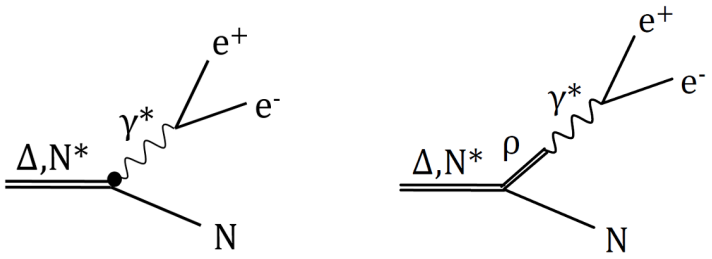

Figure 1.11: Left: Feynman diagram showing the simple resonance decays that are dominating at low collision energies. **Right:** Modification of the resonance decays based on the vector meson dominance model.

duction mechanism, where two electromagnetic reaction vertices contribute. Hence, as already mentioned dilepton production is suppressed by a factor of $1/\alpha^2$, which corresponds to a branching ratio of BR$\approx 10^{-5}$. In case of small collision energies (e.g. SIS18), dilepton production is suppressed further due to their production below the free nucleon-nucleon (NN) production threshold. The particle production threshold energy E_{th} is evaluated by

$$E_{th} \geq 2m_p + m_x, \tag{1.8}$$

where m_p is the proton mass of the colliding nucleons and m_x the mass of the created particle. All the energy, not required for fulfilling the momentum conservation, is available for particle production.

The produced particles are measured in the detector. Since the lifetime of the vector mesons is too short, only their decay products, namely e^+ and e^- are measured. For the reconstruction of their mother particle properties, the invariant mass of a e^+e^- is evaluated by the sum of 4-momentum vectors:

$$M^2 \equiv (p_{l+} + p_{l-})^2 = (E_{l+} + E_{l-})^2 - (\vec{p_{l+}} + \vec{p_{l-}})^2, \tag{1.9}$$

$$M^2 = E_{l+}^2 + E_{l-}^2 + 2E_{l+}E_{l-} - \vec{p_{l+}}^{\,2} - \vec{p_{l-}}^{\,2} - 2\vec{p_{l+}} \cdot \vec{p_{l-}}, \tag{1.10}$$

where $\vec{p}$ are the three momentum vectors of the leptons in natural units and E the energy of each lepton. In case momenta are large compared to the particle mass, the energy $E_l = (p)^2 + (m_0)^2$ is only determined by its momentum. Therefore, the energy term simplifies to $E_l = (pc)^2$ and the invariant mass is simplified to the following expression:

$$M^2 = 2E_{l+}E_{l-} - 2\vec{p_{l+}} \cdot \vec{p_{l-}}, \tag{1.11}$$

$$M = 2sin\frac{\Theta}{2}\sqrt{p_{l+}p_{l-}}, \tag{1.12}$$

where the invariant mass only depends on the input momentum of the decay particles p_l and their opening angle θ. Further characterization of the mother particle is given by the isolation of the transverse momentum p_T :

$$p_T = \sqrt{(p_{l+x} + p_{l-x})^2 + (p_{l+y} + p_{l+y})^2}, \tag{1.13}$$

which is defined by the lepton momenta p_l in the plane perpendicular to the beam direction z. The longitudinal direction is described by the rapidity y, which is defined by the momentum p and momentum in beam direction p_z:

$$y = \frac{1}{2} ln \frac{(p_{l+} + p_{l-}) + (p_{l+z} + p_{l-z})}{(p_{l+} + p_{l-}) - (p_{l+z} + p_{l-z})}. \tag{1.14}$$

All three observables allow the differential analysis of medium effects that could appear more pronounced in specific regions. However, the most important observable is the invariant mass spectrum since it provides a separation of the different lepton pair sources. A simulated dilepton spectrum is presented for Au+Au collisions at a beam energy of 25A GeV (see Fig. 1.12) . This spectrum consists of overlapping contributions from different sources. Their intensity varies with beam energy, due to the variation of available energy for particle production. Typically, the mass spectrum is grouped into three different mass regions that are governed by peak structures of ϕ and J/ψ:

- **Low-mass region** (LMR): $M_{ee} < 1.1$ GeV/c^2
- **Intermediate-mass region** (IMR): 1.1 GeV/c^2 $< M_{ee} < 2.7$ GeV/c^2
- **High-mass region**: $M_{ee} > 2.7$ GeV/c^2.

Each specific mass region is populated by various particle sources which appear as continuous distributions or peak structures. For example, the high mass region contains continuous sources (e.g., Drell-Yan) as well as peaks (e.g., J/ψ). In the intermediate mass region, correlated pairs from semi-leptonic decays of D mesons ($c\overline{c}$) are dominant. A smaller fraction is expected to be resulting from thermal radiation of the QGP. Its yield determination requires a precise knowledge of the dominant e^+e^- background from correlated D meson decays. Once the physical background is estimated and subtracted, the slope of the continuous distribution can be utilized to also determine a temperature of the radiation source [54].

Vector mesons contribute to the low-mass region of the spectrum and are related to chiral symmetry restoration. Additionally, e^+e^- from decays of π^0, η and ω, i.e. freeze-out sources, need to be considered. Unfortunately, Dalitz decays (e.g., mostly π^0 and η) form a background that complicates the determination the ρ yield. A way to estimate their yield is the measurement of these particle yields in other production channels. Once the ρ yield is isolated in the low-mass region, one could use it to estimate the lifetime of the radiating source.

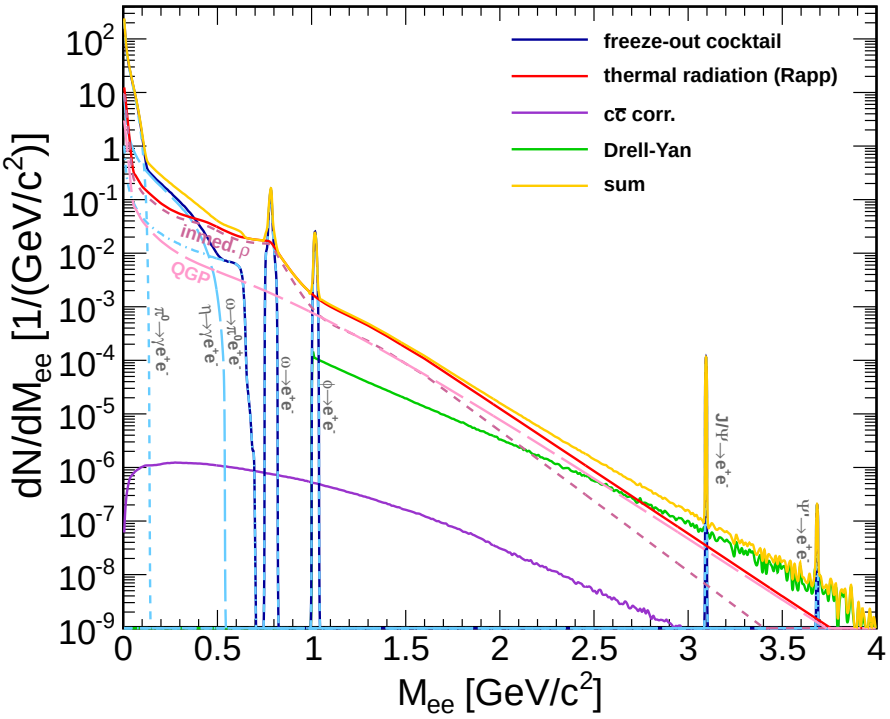

Figure 1.12: Results from theoretical model calculations [4] of a dilepton spectrum of Au+Au collisions at a beam energy of 25A GeV. Various sources contribute to the final spectrum yield. This includes continuum sources (i.e. open charm), Dalitz decays of π^0 or peak structures from dileptonic decays of vector mesons. The sum of medium radiation comprises QGP radiation ($q\overline{q} \rightarrow l^+l^-$), in-medium radiation ($\rho, \omega \rightarrow l^+l^-$) and 4π annihilation ($\pi a_1 \rightarrow l^+l^-$).

1.2.4 Models of heavy-ion collisions

It has be shown that the dilepton spectrum contains many overlapping sources. Those can be disentangled experimentally but also with models of heavy-ion collisions. Moreover, different medium effects can also be modeled. In general, the models help to connect measured observables to the properties of matter, which can not be accessed directly. A simple approach, using a statistical model, was already presented in section 1.1.3. It is applicable to determine the temperature and density μ_B over a large range of collision energies. However, it only describes the final state, requires thermal equilibrium and does not include any system evolution dynamics. Since a heavy-ion collision evolves rapidly, changes in the temperature and density are drastic. Therefore, a precise collision model requires a dynamical description. Several approaches for description of heavy-ion collisions and their dynamics, including their advantages and limitations, are presented with a focus on the SIS18 energy regime.

The most common approach is a *microscopic transport model*, that is based on the motion of microscopic particles. In general, transport models are based on the Boltzmann equation. Specific models use simplified versions of it. In addition, quantum mechanical effects are introduced by replacing the particles with a Gaussian wave package. Transport models have the advantage, that they cover the full space-time evolution of a collision.

As process for particle production, the model contains inelastic scattering, resonance decays and string fragmentation. At lower collision energies only resonance decays are applied for particle production, while the string fragmentation is only applied at higher collision energies. This process is included by additional models like PYTHIA [55]. Moreover, the particle production requires cross sections as input, that are varying as a function of temperature and density. This is challenging, since some of those measurements are missing or have large uncertainties.

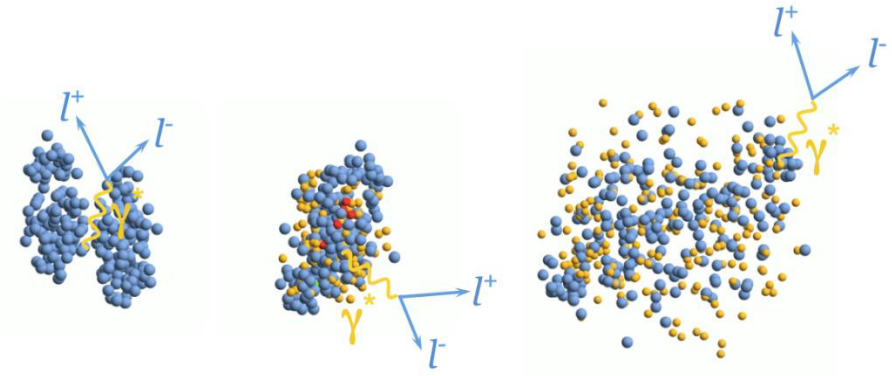

Figure 1.13: Schematic evolution of a heavy-ion collision [56]. Transport models are able to describe the full evolution besides the initial state conditions.

Several transport models for heavy-ion collisions are Ultra relativistic Quantum Molecular Dynamics (UrQMD) [57; 58], Relativistic Quantum Molecular Dynamics (RQMD) [59], Giessen Boltzmann-Uehling-Uhlenbeck (GiBUU) [60] and Hadron-String-Dynamics (HSD) [56]. Furthermore, a new model, Simulating Many Accelerated Strongly-interacting Hadrons (SMASH), with focus on SIS100 energies is being developed [61]. The generation of dileptons is treated with special approaches, that vary within the different models. In GiBUU, baryonic resonances are of major importance for description of the particle yields. The sum of all included Δ and N^* resonances contribute to the dielectron spectrum via their $R \rightarrow e^+e^-N$ decay. This approach is based on the assumption, that a lot of nulceons are excited to higher lying baryonic resonances. Those decay and regenerate in the course of a heavy-ion collisions. They add the extra yield to the dilepton spectrum. In SMASH, the Boltzmann equation for a hadron resonance gas is solved [62]. Its main sources for dilepton production are decays of excited hadronic states. Moreover, the decay-widths parametrization of Manley et al. [63] are applied. A similar approach, relying on a strong dilepton contribution from baryonic resonances, is used in HSD. However, only $\Delta(1232)$ is implemented, since it is assumed as the major contribution at SIS18 beam energies. Additionally, collisional broadening[11] and a mass shift are implemented to simulate in-medium effects. UrQMD uses a different approach, assuming that a particle is able to emit virtual photons over their whole lifetime. Finally, the dilepton yield is estimated by integration of the emission rate over time. Only the vacuum spectral functions are considered.

[11] This effect has been observed for spectral lines as well. In the analysis difference in the emission pattern was observed due to the collision of atoms during the emission process [64].

More detailed results are presented with the help of the *coarse-grained* approach [4; 65]. It is motivated by the problem, that an application of the thermal dilepton rates in the medium [54] requires equilibrium. However, due to smaller collision energies, an equilibrium is not guaranteed over a major part of the collision volume. Therefore, the evolution of UrQMD collisions is divided in small space cells ($\approx 1 \times 1 \times 1$ fm^3) and time steps. A large number of collisions is averaged and used to estimate the temperature and density of each cell. Furthermore, it is checked whether a specific cell is in thermal equilibrium. In case an equilibrium is fulfilled, the thermal rates, are applied accordingly to the temperature and density of the specific cell.

1.3 Experimental results on dilepton production

Dilepton measurements are proposed to probe the hot and dense phase of a heavy-ion collision directly. An experimental challenge is the small decay branching ratio of vector mesons to dileptons. It requires high rate detectors to collect a sufficient number of events. Moreover, the identification of a specific medium modification scenario requires a good mass resolution in the vector meson region. More detailed results can be provided, if a major fraction of the produced particles in the relevant momentum region is detected. As a consequence, a detector has to have a large geometrical coverage to reduce the uncertainties due to acceptance corrections and extrapolation to the full phase space. The measurements of heavy-ion collisions are compared to elementary (pp, np, pA) collision systems as reference. For this reason, various collision systems are measured:

- Elementary collisions: p+p, d+p, π+p,
- "Cold" nuclear matter experiments: p+A, d+A, π+A, γ+A,
- Heavy-ion collisions: A+A.

The simplest, with respect to event reconstruction, are collisions of π and nucleon, since only a small number of particles is created. Consequently, they are easy to measure. Proton/pion-nucleus collisions include additional effects due to many body interactions inside the nucleus. The temperature is larger than for normal nuclear matter, while the density is at ρ_0. Hot and dense matter is created in heavy-ion collisions. A large temperature and density is created within the collision volume leading to creation of new phases of matter.

Besides the variation of the system size, medium modifications are expected to vary as a function of collision energy. At higher collisions energies, a medium with much higher temperature is created. The center of mass energy $\sqrt{s}$ (see section 1.2.2), describing the available energy for particle production, depends on the accelerator type. The available energy for a fixed target experiment, where an accelerated beam collides with a stationary target is described by:

$$Fixed\,target: \ \sqrt{s} = \sqrt{{m_1}^2 + {m_2}^2 + 2E_1^{lab} m_2} \approx \sqrt{2E_1^{lab} m_2}, \tag{1.15}$$

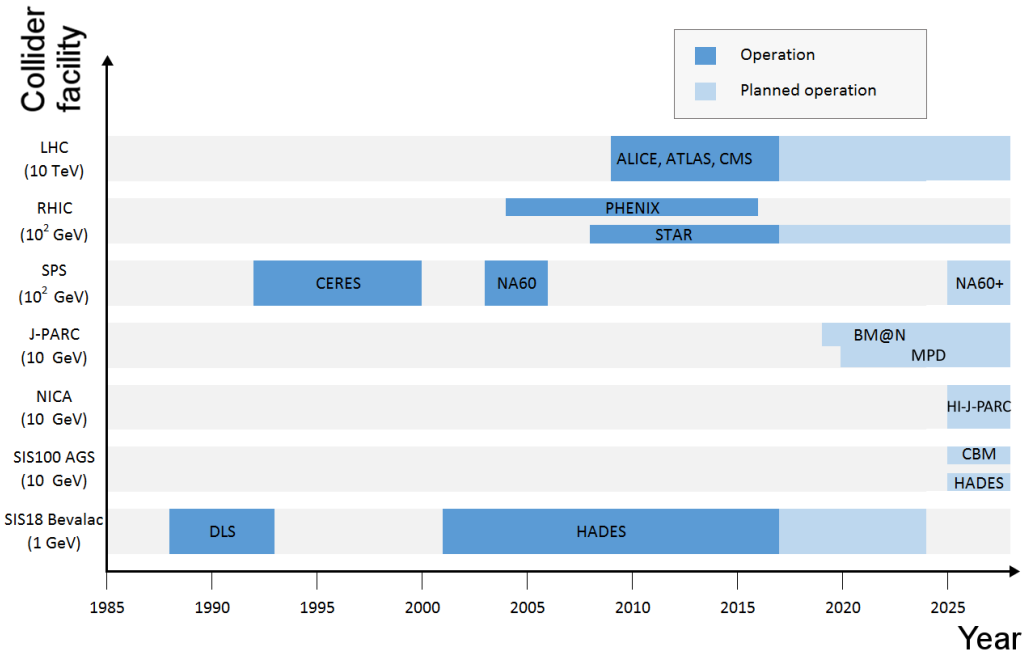

Figure 1.14: Experiments that focus on measurements of dilepton production. They are sorted by time of operation and energy regime depending on the accelerator. The energy regime is indicated by the values in brackets.

where m_1 and m_2 are the masses of the particles at rest and E_{lab} the energy in the lab frame of the incident particle. It is simplified for high energies ($E_1^{lab} >> m_1 m_2$). The expression for the center-of-mass energy differs for particle colliders, in which case two accelerated beams are collided:

$$Collider: \ \sqrt{s} = \sqrt{{m_1}^2 + m_2^2 + 2(E_1^{lab} E_2^{lab} + \vec{p_1}^{lab} \vec{p_2}^{lab})} \approx 2E_1^{lab}, \tag{1.16}$$

where p is the 3-momentum of a particle from the corresponding beam. The expression simplifies if the masses are small and the energies are identical. A comparison of both $\sqrt{s}$ formulas indicates that the collider achieves higher energies than the fixed target experiment at the same incident beam energies. In case of fixed target experiments, a part of the energy goes to momentum conservation. An advantage of fixed target experiments is that the target has a higher density than a particle beam. Therefore, these experiments are superior in terms of reaction rates.

Due to an increase of the energy of particle accelerators, experiments focus on measurements at the highest available energies (see Fig. 1.14). In this energy regime, higher energy densities are produced. Moreover, also more energetic particles are produced and require efficient detectors to detect particles over a broad momentum range. A history of dilepton measurements towards larger center of mass energies is given in section 1.3.1.

Another emphasis is put on the exploration of the high baryon chemical potential region of the phase diagram by investigation of lower collision energies. As discussed previously, dilepton production is expected to be modified in baryon rich but low temperature systems and therefore

also of interest. Advances in the accelerator and detector technology improve with time. As a result, the data collection rate improves and allows a multi-differential analysis to characterize measured effects more precisely. The emphasis in baryon rich matter measurements will be discussed in 1.3.2 which is the focus of HADES.

1.3.1 The history of dilepton measurements in heavy-ion collisions

First dielectron observations at DLS

First measurements of dielectrons in heavy-ion collisions were obtained by the DLS collaboration at the BEVALAC accelerator in the energy regime of around $1A$ GeV. Two different campaigns were conducted, whereof the second one has been done after detector upgrades. After realization of the detector upgrades, p+p and p+d reactions were measured at different energies [66]. Furthermore, Ca+Ca, C+C, He+Ca and d+Ca collisions were measured with DLS [67]. The measurements reveal a significant feature in Ca+Ca collisions. While the mass region below 0.15 GeV/c^2 is in agreement with theoretical predictions, the one above 0.15 GeV/c^2 indicates an enhancement compared to the hadronic cocktail (see Fig. 1.15). This enhancement could not be described by theoretical models [68; 69; 70][12].

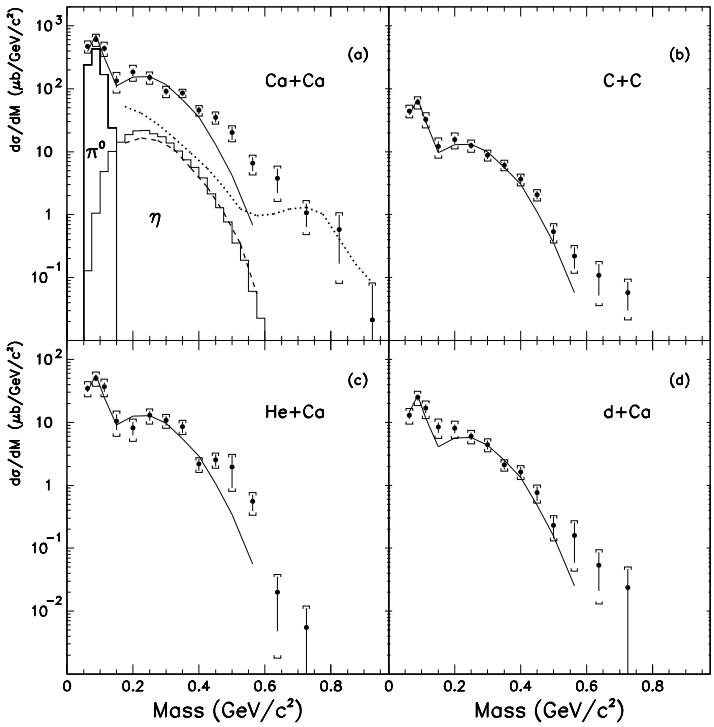

Figure 1.15: DLS measurements compared to simulated yield estimated by the BUU model (dotted lines) and to the π^0 and η contributions as estimated from the TAPS measurement and isotropic model (histograms). The shapes of π^0 and η are used to fit with data and the estimated the yield is shown by the solid line, which is in agreement up to 0.4 GeV$/$c^2 in all measured systems [67].

[12] See section 1.3.2 for further discussion.

Extension of measurements at high densities

HADES conducts measurements at the same energy as DLS. Advances in technology allow data taking at much higher interaction rates, which reduces statistical and systematic errors. In the heaviest collision system Au+Au, reaction rates of about 8 kHz were measured in 2012. The maximum rate is even higher for smaller system sizes. The high acceptance allows to access leptons over a wide range in rapidity and transverse momentum. Various systems and energies were measured in addition and will be discussed in more detail in section 1.3.2.

Measurements at SPS energies with CERES

Dielectron measurements in heavy-ion collisions at the SPS energy regime were performed by the CERES[13] collaboration. For the electron identification in CERES, two RICH detectors were installed. Later, a new TPC[14] was added to the experimental setup and extended the particle identification capability by inclusion of the specific energy loss of particles as additional selection criterion. CERES measured p+Be and p+Au collisions at 450 GeV [71] and S+Au collisions at 200A GeV [72]. As a result, e^+e^- spectra in proton induced reactions were reconstructed and are well reproduced by a simulated cocktail. But the measurement of S+Au collisions showed an enhancement by a factor of 5. In Pb+Au collisions measured at 158A GeV, the data showed an enhancement of a factor 2.45 [73]. At an even lower collision energy of 40A GeV the largest enhancement factor was observed [74].

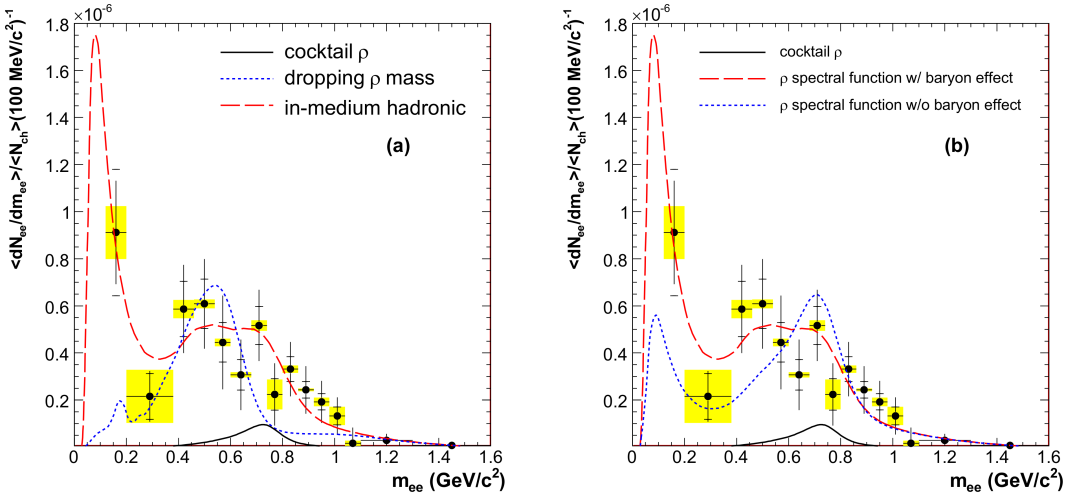

Figure 1.16: Both figures show the dielectron yield after subtraction of the hadronic cocktail. In **(a)** the cocktail ρ is compared to model predictions for a dropping mass and a mass broadening scenario. The mass region above the pole mass favors a broadening scenario. In **(b)** the effect of baryonic interactions is studied. While the high mass region is not conclusive, the yield below a mass $m = 0.6$ GeV/c^2 demonstrates the necessity of baryonic interactions in order to describe the measured yields.

[13] ChErenkov Ring Electron Spectrometer
[14] Time Projection Chamber

In order to develop an understanding of the enhancement and its origin, the data were compared with predictions of a ρ broadening and dropping mass scenario (see Fig. 1.16 (left)). Below the ω pole mass, the data yield is very similar to both model calculations and does not favor a specific model due to the large errors. But the region above the ρ pole mass fits well to the spectrum including the mass broadening of the ρ. In addition, a χ^2 test was applied to check the exclusion probability of a certain model. The test favors the broadening scenario and excludes the dropping mass scenario by $\sigma = 1.6$. Additionally, the influence of the ρ-baryon interactions to the modifications was investigated (see Fig. 1.16 (right)). For this reason, a model with and without baryonic effects was compared to the excess yield. Latter one was estimated by subtraction of theoretically estimated dilepton contributions from the full spectrum. While the region above the ρ pole mass predicts similar results for both modification scenarios, the region below the pole mass is better described by the model including baryonic effects. Consequently, CERES results favor the mass broadening scenario and proves that baryonic effects are essential to describe the measured data. However, a definite exclusion of the dropping mass scenario is not possible due to large errors.

Dimuon measurements with NA60 at SPS

The first results on dimuon measurements in the low-mass region were presented by the NA60 [44] experiment. It is based on the NA50 [75] experiment with addition of a silicon vertex detector. Latter one is positioned before the hadron absorber and determines a more precise vertex position, which is utilized to remove background from off-vertex decays of open charm. The tracks are reconstructed by matching a track segment in front of to a second one behind the absorber. Its matching quality is dependent on momentum and angular position resolution.

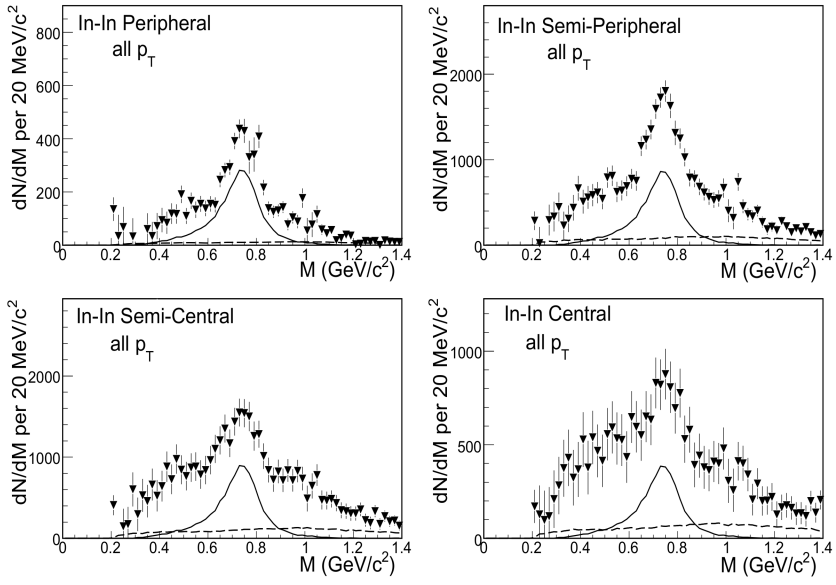

Figure 1.17: Excess mass after hadronic cocktail subtraction for different centrality classes. The vacuum ρ (solid) and open charm (dashed) contributions are shown as comparison. The excess grows towards more central collisions.

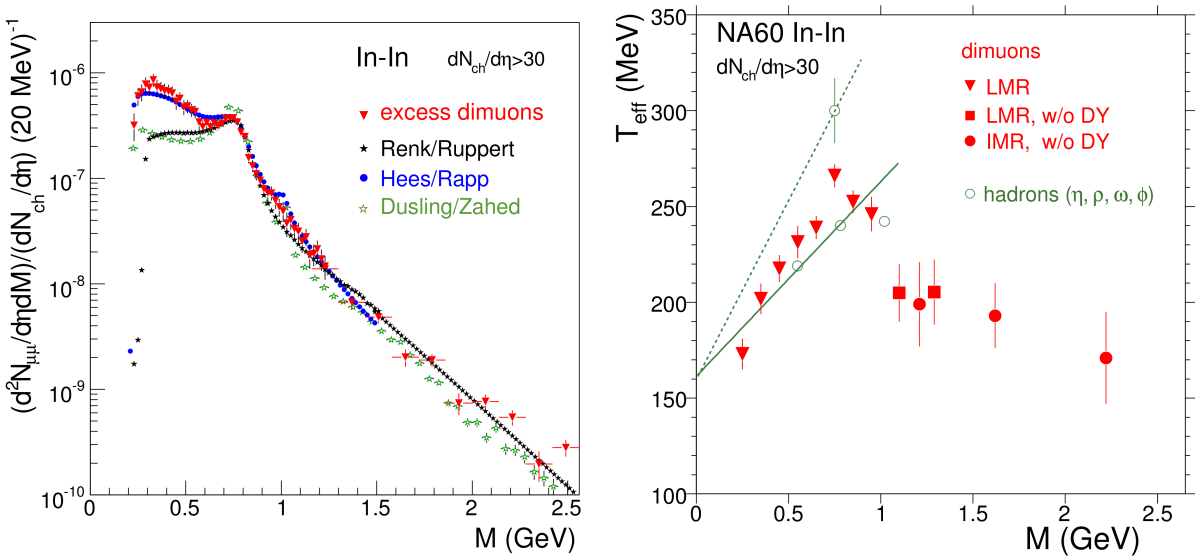

Figure 1.18: Acceptance corrected invariant mass (**left**) and T_{eff} (**right**) distribution measured by NA60.

Measurements of In+In at 158A GeV were performed in 2003 and 230 million events were recorded. Due to the large number of events, the measurements allow for a multi-differential analysis. In Fig. 1.17, ρ is shown as isolated contribution for four centrality classes. For the shown distributions, yields of ω and ϕ resonance and η, η' and ω-Dalitz decays were subtracted from the measured spectrum. As a result, the data indicates an increasing yield with increasing centrality, whereof a comparison of data to the so-called cocktail ρ reveals a larger enhancement for more central collisions. A comparison of semi-central collisions to model calculations [76] agrees to an in-medium broadening scenario (see Fig. 1.18 (left)). Consequently, the mass dropping scenario was disproved [44].

Further results were obtained by fitting the m_T distributions for different mass ranges with a Boltzmann function. An effective temperature (T_{eff}) was obtained and plotted as a function of mass. T_{eff} shows a rise up to $M \approx 0.7$ GeV/c^2 (hadronic phase dominated mass region) and then a drop to ≈190 MeV and stays constant, indicating early QGP emission where flow is not yet developed [77] (see Fig. 1.18 (right)). Additionally, an exponential "Planck" fit to the dielectron mass range 1.1 < M < 2.0 GeV/c^2 delivers the source temperature, which is found to be 205±12 MeV [78].

In addition, the high statistics allow for an analysis of mass dependent angular distributions [79]. This analysis is focused on a more precise characterization of the excess by identification of its polarization. As a result, no polarization is found, which is said to be consistent with thermal radiation [79]. Due to the precision of the NA60 measurements, the knowledge of in-medium effects has improved significantly. Furthermore, it was the first observation of a completely resolved η, ϕ and ω in the dilepton channel, which was possible due to the good resolution around the ω mass of around 20 MeV/c^2.

Dilepton observations at RHIC energies

Dilepton measurements at RHIC energies were conducted by two experiments, that measured Au+Au collisions at $\sqrt{s} = 200$ GeV. In the PHENIX[15]experiment, electrons are identified via RICH[16], EmCal[17], and TOF[18] detectors. For the beamtime in 2010, an HBD[19] was installed for further hadron suppression. The results for the separate centrality classes reveal an enhancement over the cocktail in the low-mass region, which increases with centrality. An enhancement factor of $2.3 \pm 0.4(stat) \pm 0.4(syst) \pm 0.2(model)$ is extracted in case of open charm estimation with PYTHIA (see Fig. 1.19 (left)). Moreover, it is claimed that the excess is distributed over the whole p_T range up to 5 GeV/c [80]. The measured mass and p_T distributions are consistent with the model of Rapp and Wambach [43]. The latest measurements [80] show an lower excess than previous results from 2010 [81]. Due to the detector upgrade and improvements in the analysis, latest data is more reliable and agrees with the following results presented by the STAR[20] experiment [82].

Also, this experiment was upgraded by a new time-of-flight barrel detector. The electron identification in STAR is based on velocity measured in TOF, energy loss measured in the TPC in combination with the momentum. In the low-mass region, an excess of $1.76 \pm 0.06(stat) \pm 0.26(syst) \pm 0.29(cocktail)$ is measured (see Fig. 1.19 (right)) in case of subtraction of the correlated charm cross section from PYTHIA. Those results agree within errors with PHENIX. In addition, ω and ϕ were also tested for in-medium modifications. But the extracted width and mass position are consistent with a scenario of no modification, which is reasonable due to their longer life-time.

Besides the measurement at the highest RHIC energies, STAR began an energy scan program (BES I) consisting of five different measurements down to beam energies of $\sqrt{s}$ = 19.6 GeV [83]. Its main purpose is a study of collision characteristics to search for indications of the critical endpoint in the phase diagram. Also the dielectron yield is studied to analyze the evolution of the excess yield in the low-mass range [84]. Therefore, mass and p_T distributions are extracted and compared to the cocktail yield. Since the cocktail does not contain a contribution of in-medium radiation, the measured yield exceeds the sum of the cocktail yield. However, the precision of the spectrum is limited by statistical errors and requires the integration of the yield in the low-mass region for a quantitative comparison. The results of the integration in the mass region 0.30 GeV/c^2 $< M_{ee} <$0.70 GeV/c^2 are presented in Fig. 1.20 and reveal no variation as a function of beam energy. The yield is influenced by differences and lifetime of the temperature and density in the hot and dense phase. But the result is limited by the statistical errors. The large errors arise due the reduced beam intensity of the accelerator and the reduced dielec-

[15]Pioneering High Energy Nuclear Interactions eXperiment
[16]Ring Imaging Cherenkov
[17]Electromagnetic Calorimeter
[18]Time Of Flight
[19]Hadron Blind Detector
[20]Solenoidal Tracker at RHIC

tron rates at lower collision energies. As a consequence, measurements below the lowest beam energy would be even worse in terms of their statistical error. However, this energy regime is highly interesting since a strong rise of the excess yield is predicted by some model calculations (see Fig. 1.20). Further improvements are expected in the energy scan BES II which profits from improvements of the accelerator performance and detector setup that will decrease the statistical uncertainties [85]. This will be helpful to disentangle differences between data and the two model results from a thermal dilepton emission source [54] and PHSD [86], since up to now both models are able to describe the dilepton yield from SPS up to RHIC energies.

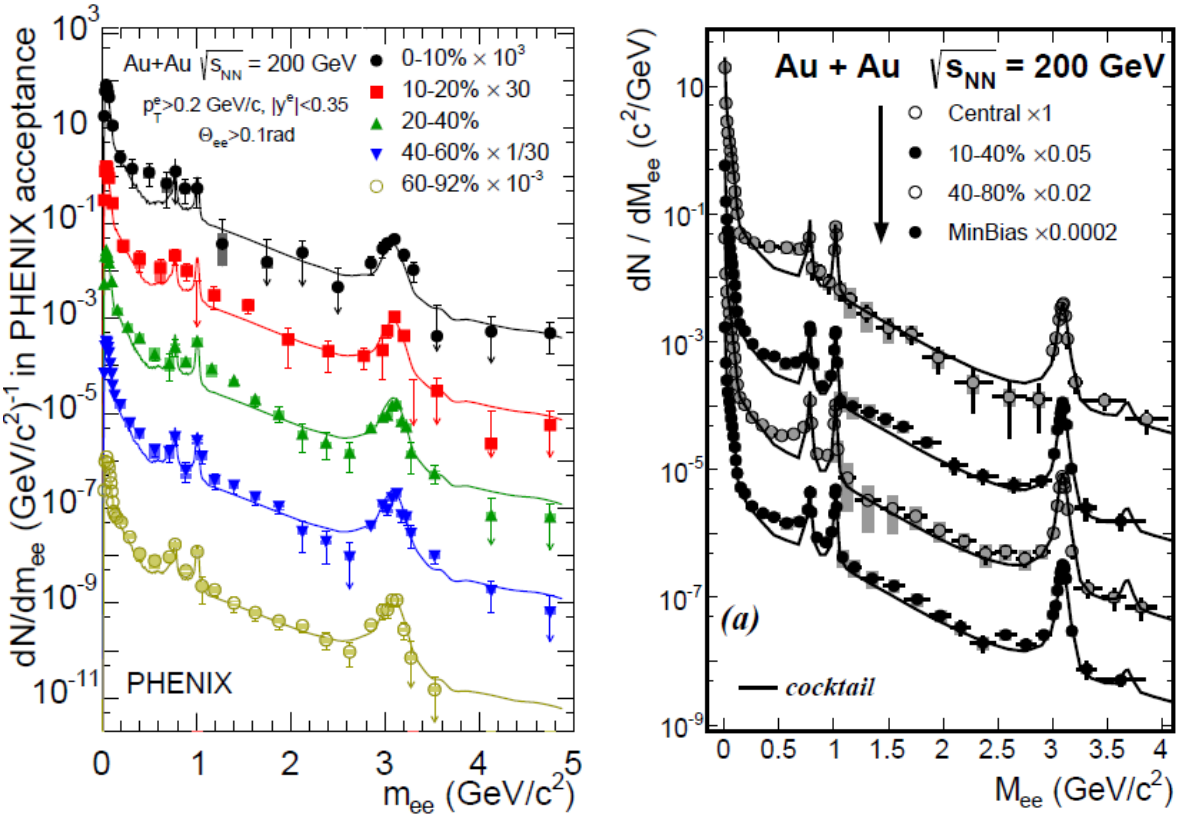

Figure 1.19: Centrality dependent measurements by the PHENIX (**left**) and the STAR (**right**) collaborations. Measurements of both experiments show an excess in the low-mass region in all centrality classes that rises slightly towards higher centrality. The strength of the excess is in agreement for both measurements.

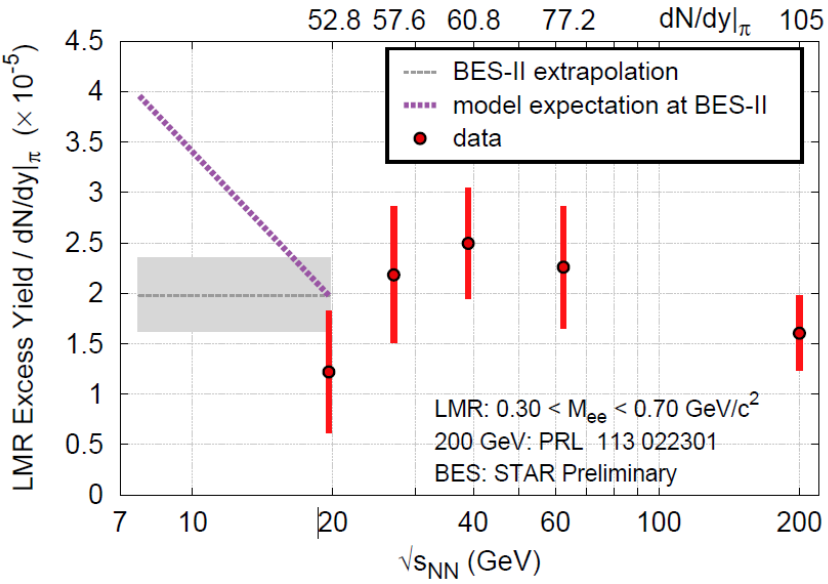

Figure 1.20: Measured excess yield in the low- mass region is normalized to dN/dy_π. The box indicates the average excess obtained in BES-I. The model expectations at lower energies are estimated with PHSD calculations.

Accessing highest collision energies at LHC

ALICE [21] conducts measurements using beams provided by the LHC accelerator, the highest collision energies ever reached on earth so far. The experiment is optimized for heavy-ion collisions but also measures p+p collisions as reference and p-Pb collisions to study "cold" nuclear matter effects. In the first run, p+p collisions were measured at $\sqrt{s} = 7$ TeV, p+Pb at $\sqrt{s} = 5.02$ TeV while Pb+Pb collisions were measured at $\sqrt{s} = 2.76$ TeV. In ALICE, electrons are identified via their specific energy loss in the ITS[22] and TPC[23], which is combined with time-of-flight information. Results from p+Pb data are shown in Fig. 1.21 (left) [87]. Within errors, the data agrees to the hadronic cocktail, for what reason an additional excess yield is not told to be necessary for description. In Pb+Pb collisions, the signal-to-background ratio is reduced compared to p+Pb data and complicates the analysis. Fig. 1.21 (right) displays the results [88] in the low-mass region. Within errors, the mass region below the ρ pole mass does not indicate an enhanced yield compared to the cocktail contributions. More detailed conclusions can only be drawn, if the errors due to subtraction of combinatorial background are decreased. Improvements of the data quality are expected by an upgrade of the ITS and TPC for LHC run 3 [87]. ATLAS [89], CMS [90] and LHCb [91] are also able to measure the dimuon spectrum in heavy-ion collisions. However, these experiments are optimized for particle physics and have a different acceptance coverage which does not allow low p_T measurements like in ALICE.

[21] A Large Ion Collider Experiment
[22] Inner Tracking System
[23] Time Projection Chamber

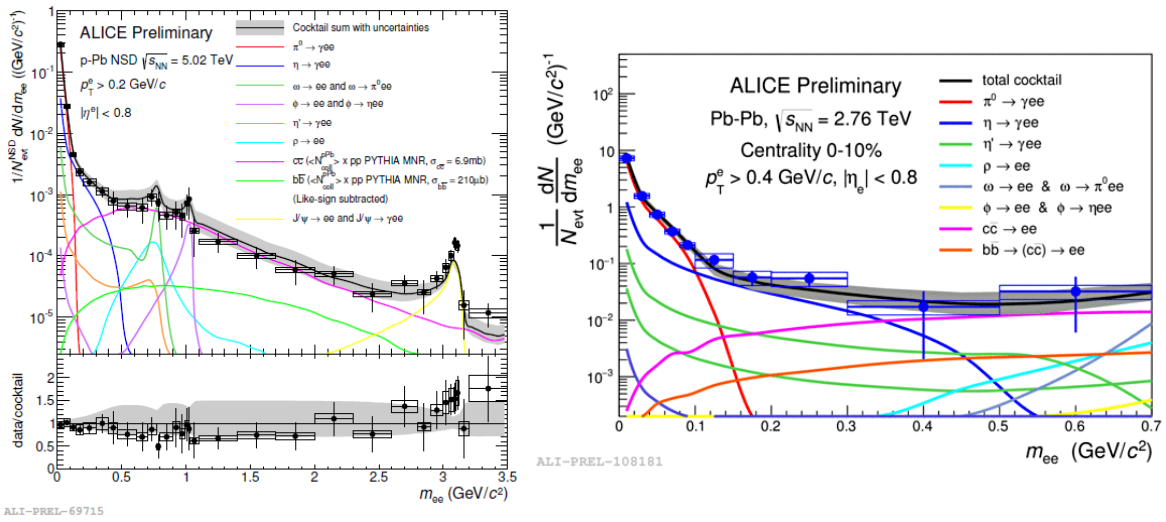

Figure 1.21: Left: Dilepton spectrum in p+Pb collisions including the hadronic cocktail. Within error, data is described well by the hadronic cocktail. **Right:** Measured dilepton spectrum in Pb+Pb is compared to the cocktail contributions and does not show any deviation from it within errors.

Future experiments

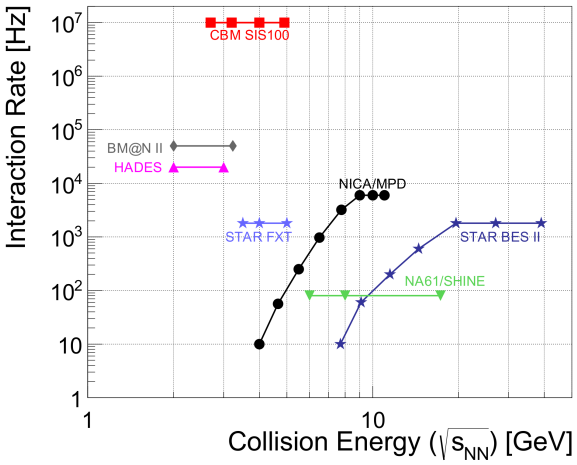

Figure 1.22: Interaction rates of experiments for heavy-ion collisions.

Measurements over the whole energy range are still ongoing (see Fig. 1.14). While the collision energy at the LHC is the highest, at RHIC lower collision energies are investigated in the beam energy scan program [92; 93]. At low collision energies, HADES measures and will also conduct the physics program at slightly higher energies at SIS100 at FAIR[24]. The CBM[25] experiment will then take over at higher collision energies at SIS100[26] to investigate the QCD matter in, up to now, a barely know regime of the phase diagram with the highest interaction rates (see Fig. 1.22) [18]. In parallel the collider experiment at NICA[27] [94] is planned at the JINR [28] and shall cover a similar energy range. The combination of measurements will help to systematically improve the understanding of the in medium modifications in more detail and search for a consistent description of the mechanism over a broad range of collision energies.

[24]Facility for Antiproton and Ion Research
[25]Compressed Baryonic Matter
[26]Schwerionensynchrotron 100
[27]Nuclotron-based Ion Collider fAcility
[28]Joint Institute for Nuclear Research

Collision system	Energy [A GeV]	Year	$N_{events} \cdot 10^6$
C+C	2	2002	265
p+p	2.2	2004	534
C+C	1	2004	660
Ar+KCl	1.765	2005	955
p+p	1.25	2006	900
p+p	3.5	2007	1801
d+p	1.25	2007	1328
p+Nb	3.5	2008	4385
Au+Au	1.23	2012	7359
$\pi^- + A$	Various	2014	425
$\pi^- + p$	Various	2014	1234

Table 1.2: Statistics of HADES data taking with various collision systems. Number of events summarizes all recorded events stored in the database, which were recorded by the trigger condition of the respective beamtime.

1.3.2 Dielectron measurements at low collision energies with HADES

The experimental observations and theory predictions point to in-medium modifications not only at high temperatures but also at high densities. Matter with such properties could be produced at SIS18. Those measurements are challenging since vector mesons are produced slightly above or even below their free NN production threshold. HADES started measurements in this specific region in 2002 (see table 1.2). Compared to previous experiments (DLS), improvements arise due to higher data rates and improved mass resolution. Moreover, it is important to search for an e^+e^- excess in collision systems heavier than C+C and Ca+Ca. In order to cope with the large number of produced particles and to identify them with the highest efficiency, high precision detectors are required. Furthermore, HADES is designed to have a high acceptance [29] which helps to cover a wide phase space range for most of the particles. This allows to access the phase space regions where strong medium modifications are expected. A variation of the collision systems, covering elementary, i.e. p and π induced reactions, and nucleus nucleus collisions, offers the possibility to disentangle medium effects from e^+e^-production processes in elementary collisions.

Solving the DLS puzzle

As already presented in section 1.3.1, the DLS experiment measured dielectron yields in small and medium sized collision systems (i.e. C+C, Ca+Ca). A comparison with the available theoretical predictions revealed an enhancement of the data over the yield from model calculations. A theoretical description of the data is based on the soft photon approximation and the one boson exchange (OBE) model, but could not fully describe the data [95], leaving the origin of the e^+e^-mass excess unresolved. The measurements at DLS have shown that the interpretation

[29] See chapter 2 for a detailed overview.

of their data requires more precise measurements and understanding of e^+e^- production in p+p and n+p collisions.

The first HADES measurements were conducted with C+C at $2A$ GeV [95] and $1A$ GeV [96]. At low-masses $M_{ee} < 0.15$ GeV/c^2 the data agrees among each other due to normalization to the number of π^0 measured correspondingly in each experiment (see Fig. 1.23 (left)). In the higher mass region up to $M_{ee} < 0.5$ GeV/c^2, an excess of the data over the cocktail, which is mainly represented by η in this mass range, is seen in both measurements. An estimation of the enhancement factor results in $2.07 \pm 0.21(stat) \pm 0.38(syst)$ for collisions at $2A$ GeV and $6.8 \pm 0.6(stat) \pm 1.3(syst)$ at $1A$ GeV. The excitation function of the excess is investigated by comparing it to long living sources, namely i.e. π^0, η (see Fig. 1.23 (right)). As a result, the measured yield of the η rises much more stronger with collision energy than the yield of π^0.

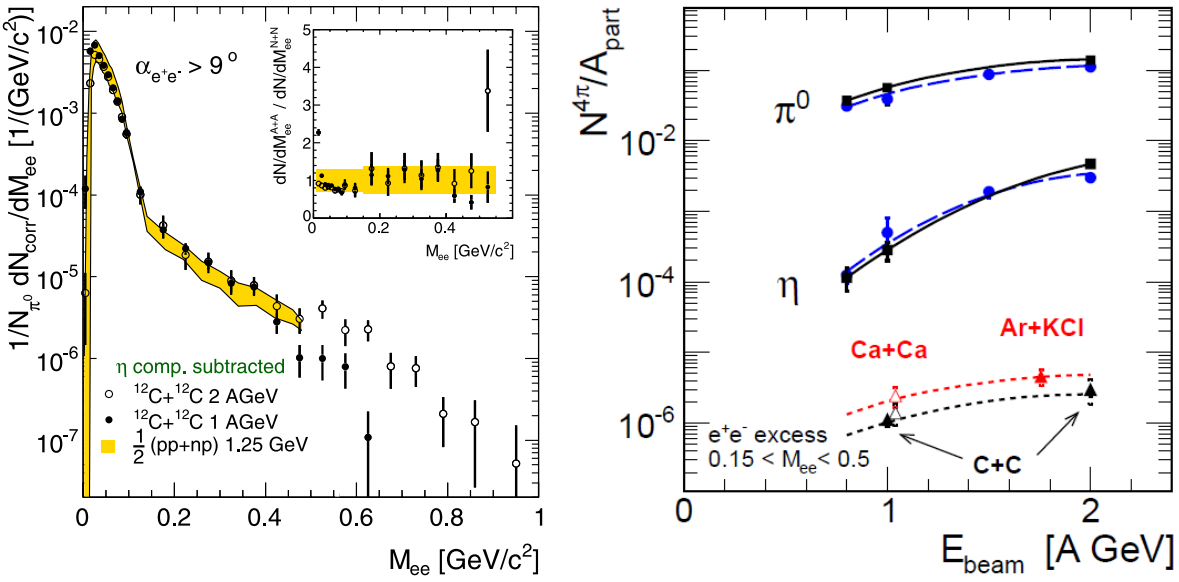

Figure 1.23: Left: Overlap of the reference spectrum, built as average of elementary p+p and n+p collisions, and the C+C data at $1A$ GeV and $2A$ GeV. The η yield is subtracted. In the available mass range, C+C data overlaps with the reference spectrum, which is also proven by the ratio plot in the upper right. **Right:** Inclusive multiplicity per participant of π^0, η and e^+e^-excess in the mass region $0.15 < M_{ee} < 0.5$ GeV/c^2. HADES (full triangles+full circles) data are complemented by DLS data points (open triangles). Furthermore, the blue (long dashed, circles) results belong to Ca+Ca and the black (solid, squares) belong to C+C measurements from TAPS. All results are extrapolated to 4π and the π^0 as well as η measurements are downscaled for better visualization. [97]

On the other hand, the measured e^+e^- excess yield scales, as a function of beam energy, very similar to the π^0 yield and slowly increases with collision energy (see Fig. 1.23 (right)). An inclusion of the DLS measurements results in a consistent picture of the "excess" over η yield. It became apparent that understanding of e^+e^- production in elementary collisions is important in order to constrain the so-called *reference spectrum*. Therefore, p+p and d+p collision at 1.25 GeV [98] were recorded by HADES. The detection of fast spectator protons in the forward forward scintillator wall from a deuterium break-up made the measurement of quasi-free

n+p collisions doable. Therefore, an investigation of isospin effects of the e^+e^- production in n+p and p+p collisions and construction of a reference spectrum were possible. Since the beam energy is below the η production threshold, the e^+e^- spectrum contains only following sources: π^0-Dalitz decays ($\pi^0 \rightarrow \gamma e^+e^-$), Δ-Dalitz decays $\Delta \rightarrow Ne^+e^-$, quasi elastic scattering-bremsstrahlung ($NN \rightarrow NNe^+e^-$).

The reconstructed invariant mass distributions for p+p and n+p collisions are presented in Fig. 1.24 and reveal different shapes in the mass region above π^0. The increased π^0 yield, of the order of two, is due to an isopin effect. However, in the higher mass region the hadronic cocktail is only consistent with the p+p data but disagrees with n+p data. A comparison between the spectra shows a strong isospin effect, that results in an enhancement of the n+p data over the theoretical cocktail at higher masses. The reference spectrum, estimated as average of p+p and n+p collisions is compared to C+C data at $1A$ GeV and $2A$ GeV. The η contribution of the C+C as well as from the n+p spectra has been subtracted for a proper comparison of the data samples. Figure 1.23 (left) shows a good agreement between the data and its elementary reference. A ratio of light nucleus nucleus collisions to elementary data also proves the agreement of both samples. With this, the DLS puzzle has been experimentally solved [98]. Since the the C+C data is described by elementary collisions, medium modifications are not the origin of differences to model calculations. Consequently, the theoretical explanation is lacking a good description of p+p and in particular n+p data. Further, explanations based on a di-baryon approach [99] and the one-boson exchange model including virtual photon radiation from the internal line [100] improve the description of the data.

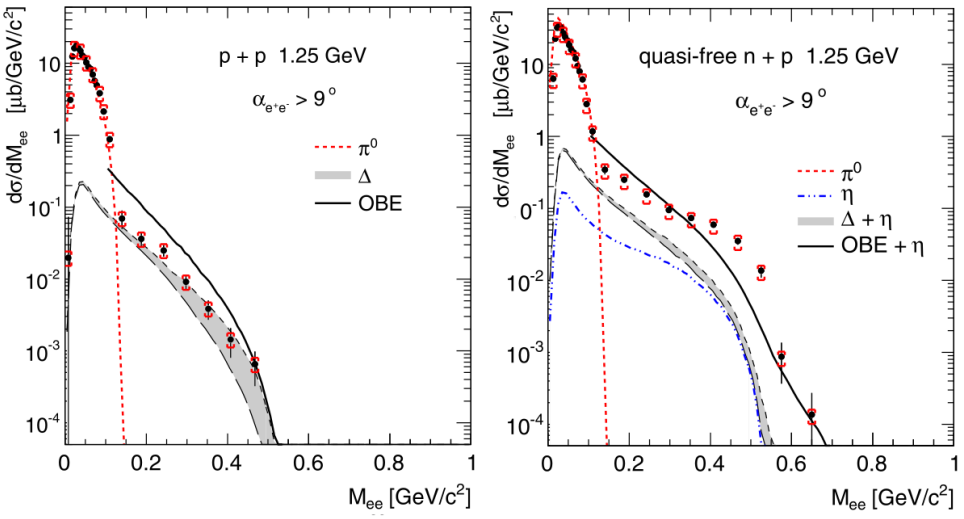

Figure 1.24: Results of elementary collisions from p+p (**left**) and n+p (**right**) reactions. Due to the production threshold only π^0 and baryonic resonances contribute to the spectrum. The p+p data is in agreement with this theoretical assumption. In contrast, n+p data does not agree with the prediction and shows a cutoff at a higher mass. The included results from OBE calculations fail to describe the data above the π^0 mass.

Proton induced reactions measured with HADES

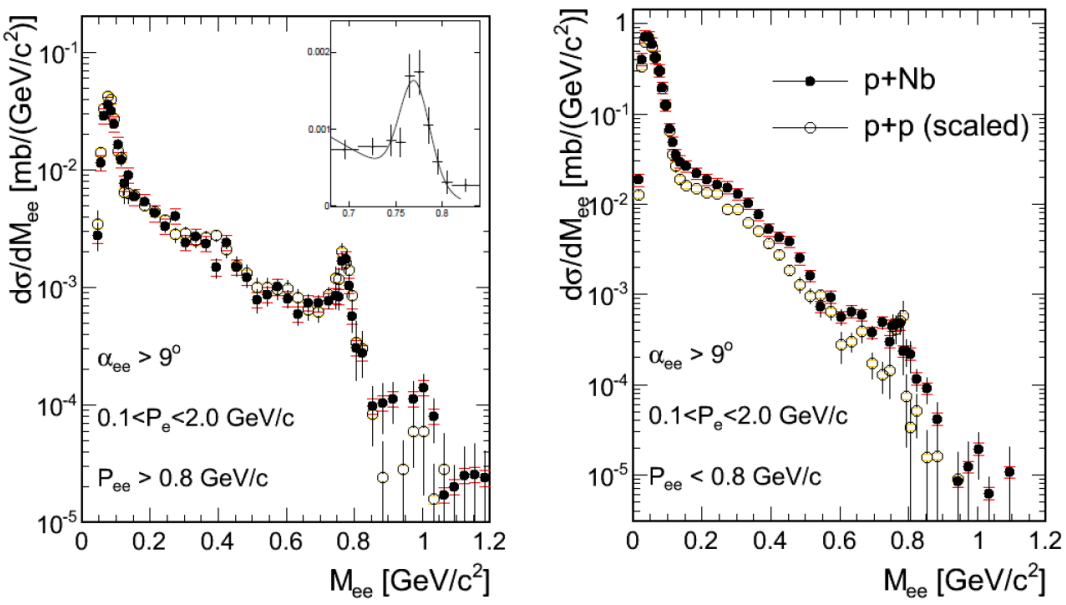

Figure 1.25: The invariant mass yield in p+Nb collisions. The pair momenta are limited to $P_{ee} > 0.8\ GeV/c$ (**left**) and $P_{ee} < 0.8\ GeV/c$ (**right**). Since low momentum pairs are moving more slowly, a higher medium modifications is expected. Indeed the enhancement over elementary collisions is only measured for the low momentum spectrum.

In 2008, p+Nb collisions were measured at a beam energy of 3.5 GeV [101]. Furthermore, p+p collisions were also recorded at the same energy to provide a consistent reference. Due to slightly enhanced temperatures and normal nuclear density, in-medium modifications are expected to change the vector meson distributions. Therefore, an excess in the low-mass region is expected. To investigate the excess, the data is split in samples based on their pair momenta $p_{ee} < 0.8$ GeV/c and $p_{ee} > 0.8$ GeV/c.

A comparison of the p+Nb spectra to the elementary reference for the pair momenta larger than 0.8 GeV/c (see Fig. 1.25 (left)) indicates no significant difference. However, a clear difference emerges for pair momenta smaller than 0.8 GeV/c (see Fig.1.25 (right)). As can be seen, the yield of p+Nb invariant mass spectrum is reduced around the ω pole mass and enhanced at lower masses. This is interpreted as additional ρ production due to multi-particle collisions. Those are observed due to baryonic resonances that enter in the ρ meson production mechanism and modify the ρ propagating in the medium. Additionally, the collisional broadening may explain the reduction of the ω yield.

Hot and dense matter at SIS18

As continuation of systematic studies of e^+e^-, the first medium size collision, namely Ar+KCl at $1.76A$ GeV, was conducted with HADES in the year 2005 [97]. The measured Ar+KCl spectrum and isospin-averaged (pp+np) data at $1.25A$ GeV were scaled by the respective number of

π^0. The e^+e^-spectrum of 1/2(pp+np) is compared to the Ar+KCl spectrum and clearly underestimates it (see Fig. 1.26 (left)). An excess over the reference spectrum up to a factor of three (see Fig. 1.26 (right)) has been reached. Moreover, the scaling of the excess yield is summarized for different collision systems at different energies in Fig. 1.23 (right). As a result, the figure demonstrates that the excess increases for larger system sizes.

Ar+KCl data provides the first observation of an ω peak at such low collision energies. The extraction of the ω peak properties does not reveal a medium modification, since most of the ω are expected to decay outside the fireball due to their large decay length. For this reason, the modifications are shadowed by strong interactions with numerous hadrons inside the fireball and the modification in the final spectrum is reduced.

Further studies to extract medium properties, are performed by reconstruction of the e^+e^- transverse mass distribution. Splitting the spectrum in different invariant mass bins allows access to specific dilepton sources. This feature is used to extract the effective temperature of specific sources to gather more insights about their production mechanism. The so-called effective temperature T_{eff} is the slope retrieved by a fit of an exponential function to the transverse mass spectra. It is a measurement of temperature in convolution with flow contributions. As a result, a rise of T_{eff} as a function of invariant mass is observed and $T_{eff} = 131 \pm 26$ is estimated for the vector meson mass range [97]. Additionally, the polarization of the excess yield was extracted. The combination of both features suggest baryon induced medium effects as source of the excess [97].

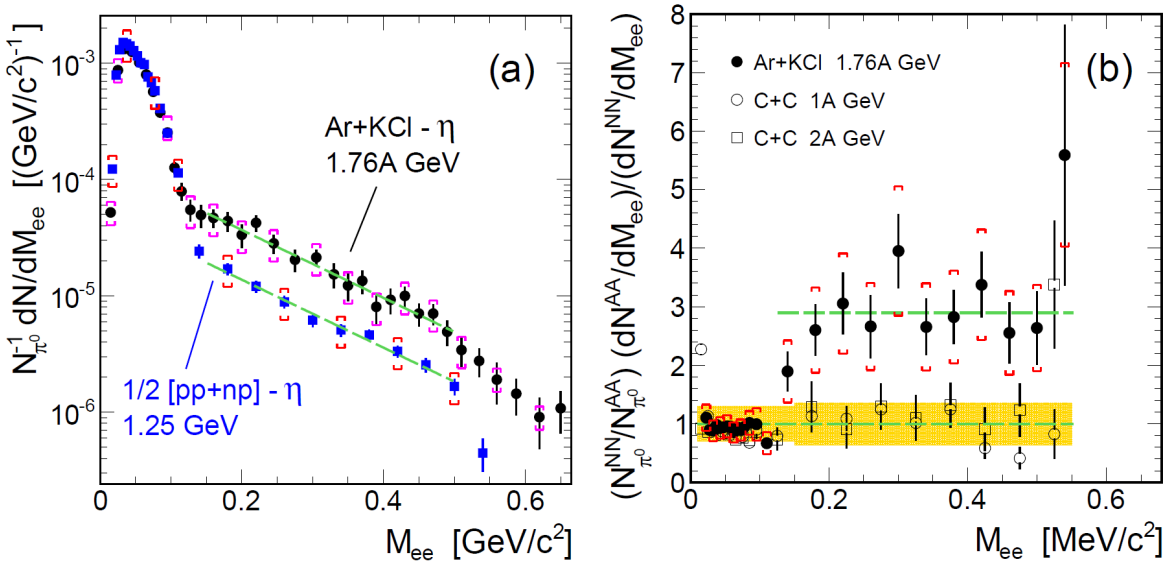

Figure 1.26: Left: Comparison of the Ar+KCl dilepton spectrum to the reference spectrum with subtracted η contribution. An enhancement in the mass range above the π^0 mass is present. **Right:** Ratio of the Ar+KCl data to the reference spectrum. While C+C collisions are at unity. Ar+KCl data shows some significant enhancement, which is within errors constant as a function of mass.

1.3.3 Dielectron production obtained by transport models

HADES has measured various collision systems at various energies. Most of the light collision systems are described by elementary processes. First medium effects have been seen in medium-size collisions of Ar+KCl. In this chapter, results of e^+e^- production in heavy-ion collision will be compared to transport models (see section 1.2.4). Calculations from UrQMD, GiBUU and HSD will be presented. They are based on the same underlying concept, but vary in the details of dilepton production mechanisms (see section 1.2.4). In all models, dielectron sources are treated incoherently. GiBUU and UrQMD do not include a medium spectral function of vector mesons. The outcomes of model calculations are compared to existing data and used to predict results for heavier collision systems. As presented before, the light collisions system are described by elementary collisions. Since the interest is focused on medium effects induced by heavy-ion collions, only Ar+KCl data will be discussed here.
The results of GiBUU calculations [102] (see Fig. 1.27) are in agreement with the data points in the π^0 mass range. In the range above, dileptons from various baryonic resonances contribute to the dilepton yield. Up to a mass of 0.5 GeV/c^2, the data points are underestimated by a factor of approximately two. The high mass region is well described due to the large contribution of resonances (ρ, ω and ϕ). Similar to GiBUU, the dilepton cocktail obtained by UrQMD does not describe the data (see Fig. 1.28) [103]. Since, both models do not include in-medium effects, the excess of data over model is expected to originate from a medium source.

Ar+KCl data is further compared to model calculations provided by HSD [104] (see Fig. 1.29). HSD overestimates the mass range just below the ω pole mass. The lower mass range is described well since the model incorporates some type of medium effects. However, this approach is different to GiBUU and UrQMD, since not a variety of baryonic resonances contributes the the dielectron yield. Instead, the yield is dominantly described by the $\Delta(1232)$ and NN Bremsstrahlung. Furthermore, the regeneration of Δ-Resonances is a key to describe the data. Models which use the vacuum spectral function fail to describe the data in the mass range above π^0 and call for an alternative approach with in-medium effects included.

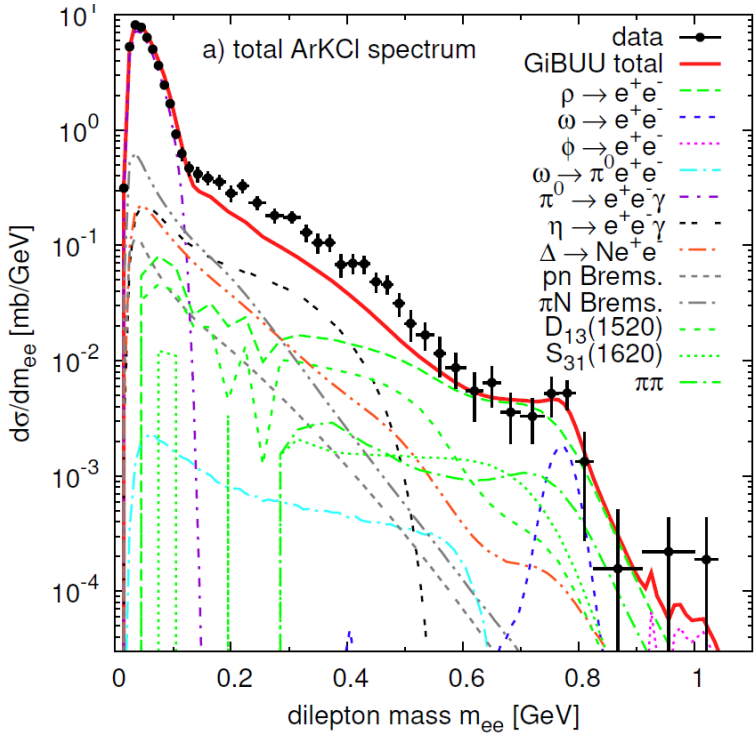

Figure 1.27: Comparison of HADES Ar+KCl data to a model calculations from GiBUU. The sum of cocktail contributions is indicated by the red solid line in order to compare the cocktail to data.

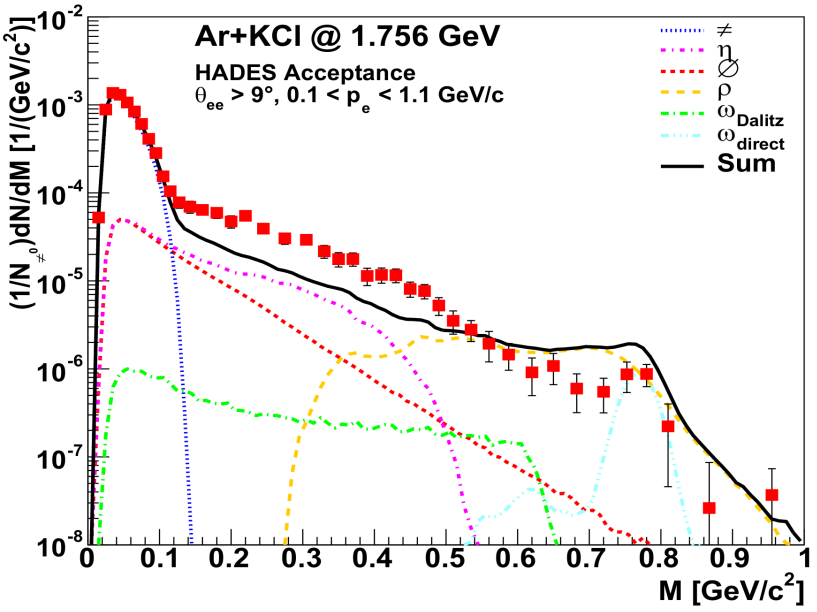

Figure 1.28: Comparison of HADES Ar+KCl data to model calculations from UrQMD. The sum of cocktail contributions is indicated by the black solid line in order to compare the cocktail to data.

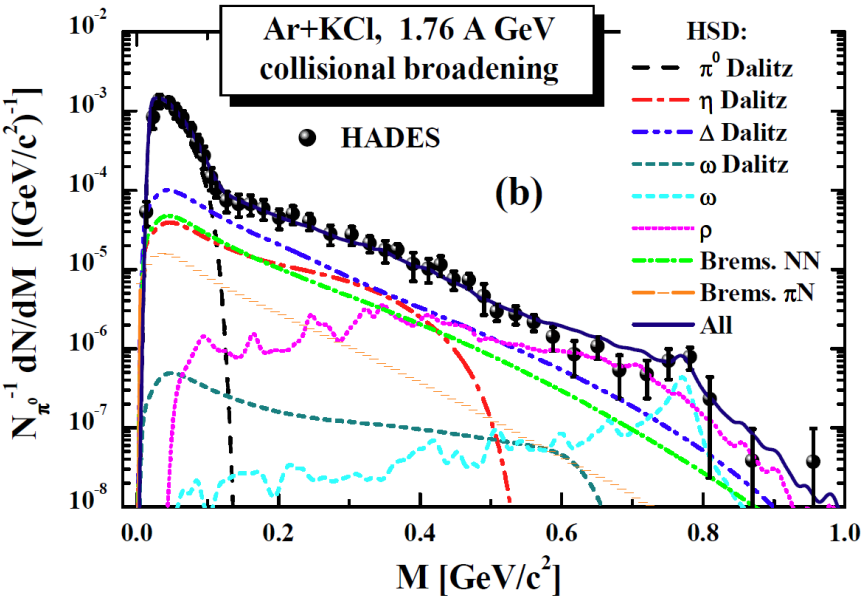

Figure 1.29: Comparison of HADES Ar+KCl data to model calculations from UrQMD (**upper**) and HSD (**lower**). The sum of cocktail contributions is indicated by the black solid line in order to compare the cocktail to data.

1.3.4 A coarse-grained transport approach

Another approach is a coarse-grained transport model convoluted with thermal rates (see section 1.2.4). The thermal rates are the same that are used for SPS and RHIC collision energies [54]. The rates are applied according to the T and ρ_{eff} of each cell that is estimated with averaging many UrQMD collisions. By summation of the dileptons radiated in each cell, the resulting invariant mass spectrum is calculated.

The averaging over collisions provides the opportunity to access the information of the evolution of collision dynamics. A temperature evolution is presented in Fig. 1.30 (left) [65]. Each curve represents the number of cells above the respective temperature. The model demonstrates a similar maximum temperature for both collision systems, but predicts a longer lifetime for Au+Au collisions. At maximum, both collision systems reach a density of approximately three times normal nuclear density together with a maximum temperature of around $T < 100$ MeV. In contrast to the maximum value, the time period of the high density and high temperature phases increases in Au+Au collisions significantly. A second approach [4] provides an averaged temperature and density evolution (see Fig. 1.30 (right)). Both properties reach a maximum at around 10 fm. Additionally, the pion chemical potential, related to the number of produced pions, is shown. Since pions are not a part of the nucleon, they have to be produced within the collision. Their occurrence is a measure of particle production within the collision and is steadily rising till the freeze-out stage.

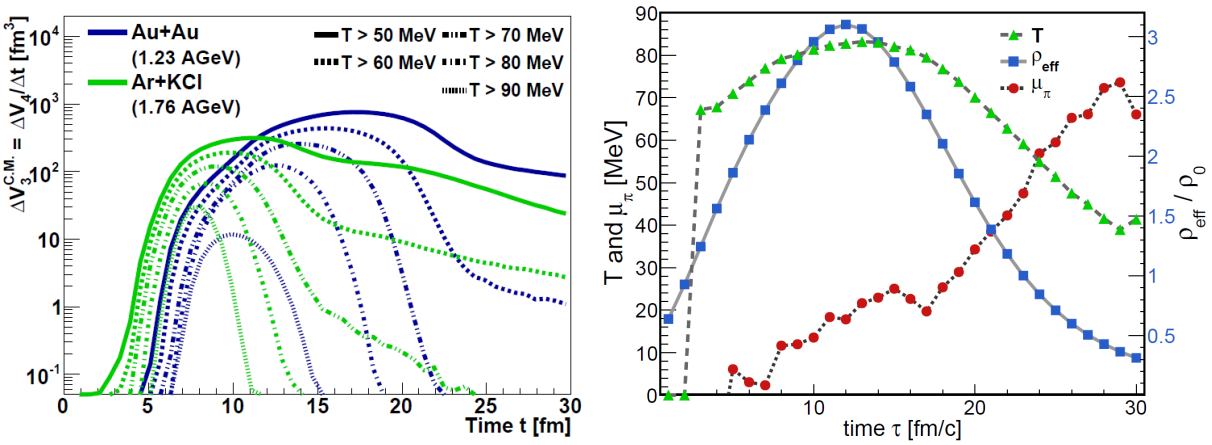

Figure 1.30: Matter properties estimated by coarse-graining approaches. **Left:** Time evolution of an Ar+KCl and Au+Au collision in the center of momentum frame. The evolution of the thermal volume is presented and predicts longer existence of a large hot volume for the heavier collision system. [65] **Right:** Temperature (T), effective baryon density (ρ_{eff}) and pion chemical potential (μ_π) for Au+Au collisions at 1.23A GeV. The values are averaged of the the inner cube of 7^3 cells with a size of 1x1x1 fm^3. [4]

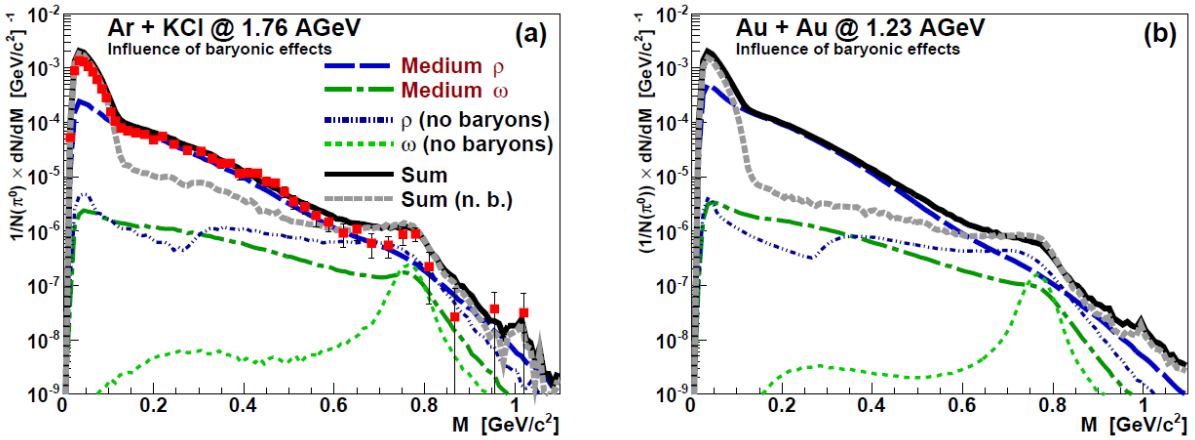

Figure 1.31: Dilepton invariant mass spectra in HADES acceptance for Ar+KCl (**left**) and Au+Au (**right**) data. A comparison of the prediction of Ar+KCl data shows good agreement if baryon interaction is included. It will be interesting to compare the Au+Au spectrum with data to confirm this observation.

Both models used to estimate the dilepton spectra. Up to now, a full cocktail description is only provided by one model [65]. The results for Ar+KCl data are presented in Fig. 1.31 (left). Besides the region around the ω pole mass, that shows deviations from data, the spectrum is well described by the model. The plot includes a scenario with and without baryonic effects. Inclusion the ρ-baryon coupling modifies the shape strongly and is essential for data description in the mass range above π^0. The effect is even stronger in Au+Au collisions and coincides with the expectation of more excess due to longer lifetime of the fireball.

1.4 Goal of this thesis

Theoretical predictions of in-medium modifications of hadrons under extreme conditions motivated the measurements of heavy-ion collisions at (ultra-) relativistic energies. The modification of the ρ and a_1 spectral functions could be related to chiral symmetry restoration. Measurements were conducted by a number of experiments and lead to an observation of an excess yield in the mass region below the ρ meson pole mass. This excess in heavy-ion collisions is proven for a wide collision energy range up to 200 GeV. Moreover, it is estimated as a function of system size and by binning the data samples in different centrality classes.

Measurements at lowest energies were provided by DLS only. They were limited in precision and did not cover a heavy collision system. In order to understand e^+e^- production in the SIS18/BEVALAC energy range, HADES has measured e^+e^- production in elementary and light collisions systems. In Ar+KCl collisions an excess above the experimentally defined cocktail has been observed, and has been attributed to medium effects.

For systematic studies, a heavier collision system was measured in 2012, namely Au+Au at 1.23A GeV, corresponding to the maximum energy for Au ions at SIS18. This analysis aims at reconstruction of dielectron spectra to estimate the system size and energy dependence of e^+e^- production. Furthermore, data will be confronted with model calculations to develop a deeper understanding of the dielectron production mechanism. In addition, the measurement of this collisions system extends the range of the beam energy program (BES) started by STAR [84]. Also a mass dependent effective temperature and angular distribution as well as centrality dependence of the source temperature will be estimated.

Compared to the previous HADES measurements, Au+Au collisions are challenging due to the higher detector occupancy. Previous measurements have shown that high efficiency and high purity electron identification are essential for a high e^+e^- signal quality. Therefore, a new method for electron and positron signal extraction with the RICH detector is proposed. It is expected that the so-called backtracking algorithm will enhance the lepton reconstruction efficiency and improve the reconstruction of lepton pairs which are characterized by small opening angles. This is supposed to reduce the combinatorial background due to fake identifications and exclude conversion pairs characterized by small opening angles.

In chapter 2 the HADES detector will be introduced. The framework for data analysis will be discussed in details in chapter 3. The event reconstruction in Au+Au collisions will be presented in chapter 4. Subsequently, the backtracking algorithm (see chapter 5) will be introduced. After a data quality study, discussed in chapter 6, the identification of single electrons using a multivariate analysis will be presented in chapter 7. It is followed by the pair reconstruction (see chapter 8), the estimation of combinatorial background, efficiency and acceptance correction factors as well as spectra normalization (see chapter 9). Finally, the results are discussed in chapter 10.

Chapter 2

The HADES

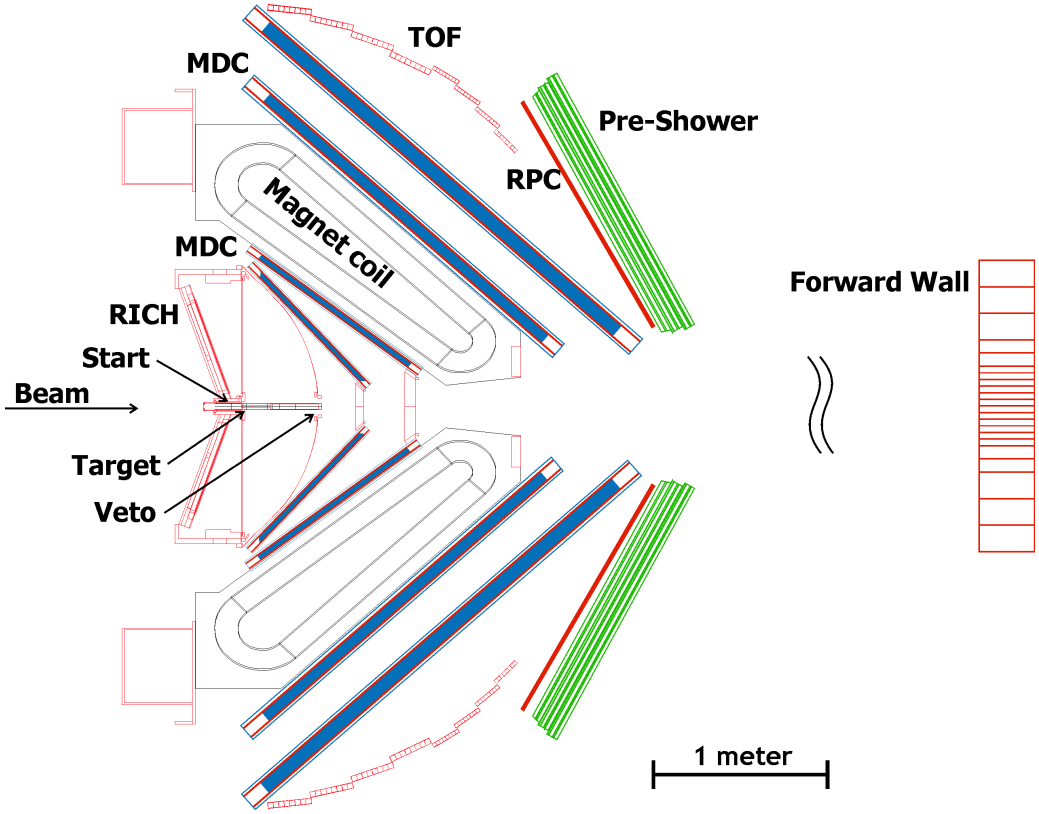

Figure 2.1: Schematic side view of the HADES detector showing its compact design. The detectors are symmetrically arranged in the azimuthal angle around the beam axis.

HADES [105] is a fixed target experiment located at the GSI Helmholtzzentrum für Schwerionenforschung in Darmstadt [106]. An ion beam is provided by the SIS18 accelerator [107] which offers a large variety of possible ions with beam energies up to 1.25A GeV for heavy ions (Au) as well as pion and proton beams with incident beam energies of up to 3.5 GeV for protons. The detector design of HADES is driven by the detection of rare leptonic decay products (e^+e^-) of vector mesons [108]. Due to the small branching ratio (BR $\approx 10^{-5}$) of vector mesons to dileptons and the sub-threshold production of vector mesons at SIS18 energies, measurements of dileptons are very challenging because of the large hadronic background. Therefore,

the whole detector design of HADES is optimized for measurements of rare electron positron pairs:

- High rate capability,
- Large geometrical acceptance,
- Light weight and compact construction to minimize multiple scattering,
- Good invariant mass resolution in the vector meson region.

Most of the spectrometer components are constructed with a sixfold construction symmetry around the beam axis. The spectrometer covers a polar angle region from 18–85° and an azimuthal angle region of nearly 360°. The sub detectors (see Fig. 2.1) are grouped in four categories with different purposes. The track reconstruction detectors for particle trajectory and momentum reconstruction together with the magnet. Time-of-flight detectors to determine the particle velocity together with the track path length. Furthermore, additional detectors for lepton identification, supported by energy loss information from different detectors, are installed. Furthermore, detectors in front of and behind the target as well as detector positioned close to the beam line and behind the spectrometer are used for event characterization. In this chapter, all sub detectors will be presented briefly. A more detailed description can be found in [105].

2.1 Track and momentum reconstruction

The reconstruction of the particle momentum is obtained by the measurement of its deflection by a magnetic field. Therefore, a magnetic field is generated by a superconducting magnet and the particle positions are measured in front of and behind it by four planes of multiwire drift chambers.

2.1.1 Superconducting Magnet

An important measurement for particle identification with HADES is a precise momentum determination for particles in the range between p = 0.1 GeV/c and p = 2.0 GeV/c. The measurement is based on a momentum kick by the magnetic field. Besides the required momentum range, a compact design is required to reduce multiple scattering and losses of particles in the acceptance area due to reactions with the magnet material. Furthermore, the desired momentum resolution for electrons is $\frac{\sigma_p}{p} = 1.5 - 2.0\%$. A better precision in momentum could be achieved by a stronger deflection. However, the momentum kick is limited by the polar detector acceptance, since too large deflections will bend the track out of the acceptance.

The installed superconducting magnet [109] has a toroidal field geometry with six narrow coils around the beam axis (see Fig. 2.2). The superconductivity is necessary to provide the required field strength together with a compact design of the coils. In order to minimize the

acceptance losses, the magnet coils are placed behind the broader frames of the tracking detectors. The cooling is performed by liquid nitrogen and helium which cools down the magnet to a temperature of 4.7 K.

With this setup, a weak field around target and inside the RICH detector is achieved. The maximum field strength is 3.6 T, which was reduced to 72% of the maximum value in the Au+Au beam time. However, the field strength is varying strongly along the coil. As a consequence, the magnetic field is rather inhomogeneous inside the geometrical acceptance as a function of the polar and azimuthal position. Therefore, an exact measurement of the field was performed to produce field maps with precision better than 1% [105]. Those field maps are included in simulation and are used for tracking.

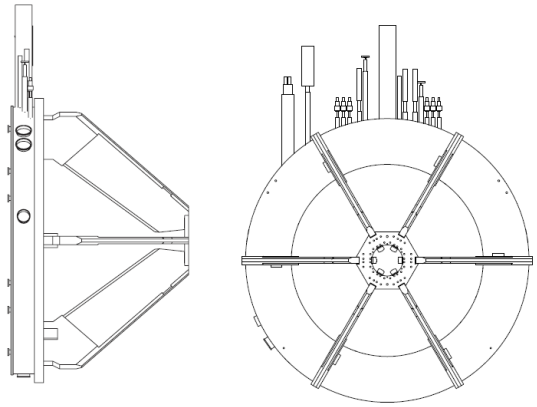

Figure 2.2: Technical drawing of the superconducting magnet whose symmetry is defined by the beam axis. The magnet coils are stabilized by the two support ring structures and beam is passing through the hole in the center.

2.1.2 Mini-Drift chambers

Like the detector system described in the previous section, also the mini-drift chambers (MDC) [110], as tracking detectors, are governed by the aim of a low material budget. Furthermore, the desired invariant mass resolution for dielectrons of $\sigma_{M_{ee}}/M_{ee} \approx 2.5\%$ [105] requires a precision in the momentum measurement of $\frac{\sigma_p}{p} = 1.5 - 2\%$. The detector granularity is also governed by the expected particle multiplicity, for which reason a maximum cell occupancy of 30% in central Au+Au collisions at $1A$ GeV is aspired.

The drift chamber geometry follows the global detector geometry consisting out of six trapezoidal sectors. Four planes of drift chambers are part of the tracking system (see Fig. 2.3 (left)). Two planes are positioned in front and two are positioned behind the magnet. Their size rises towards the backmost chambers in order to assure a constant polar angle coverage of 18–85° [111]. Each chamber is built out of 13 wire planes which form six drift cell layers (see Fig. 2.3 (right)) and a frame which is hidden behind the magnet coils. The layers of drift cells are oriented in different angles of $\pm 0°$, $\pm 20°$, $\pm 40°$. The chambers of plane I are filled with Ar/CO_2 (70/30) while all other chambers are filled with Ar/C_4H_{10} (84/16) and are enclosed by a thin aluminized Mylar foil at front and back side.

The traversing particles are detected via gas ionization inside the chambers. The electrons and positively charged gas ions drift to the sense and field wires, respectively. Only the electrons are subject to gas amplification and generate the signal together with the back-drifting ions (see section 6.1.1). This construction with thin materials results in a radiation length of 0.2% per chamber while the radiation length of the air between the drift chambers is at 0.3%. The

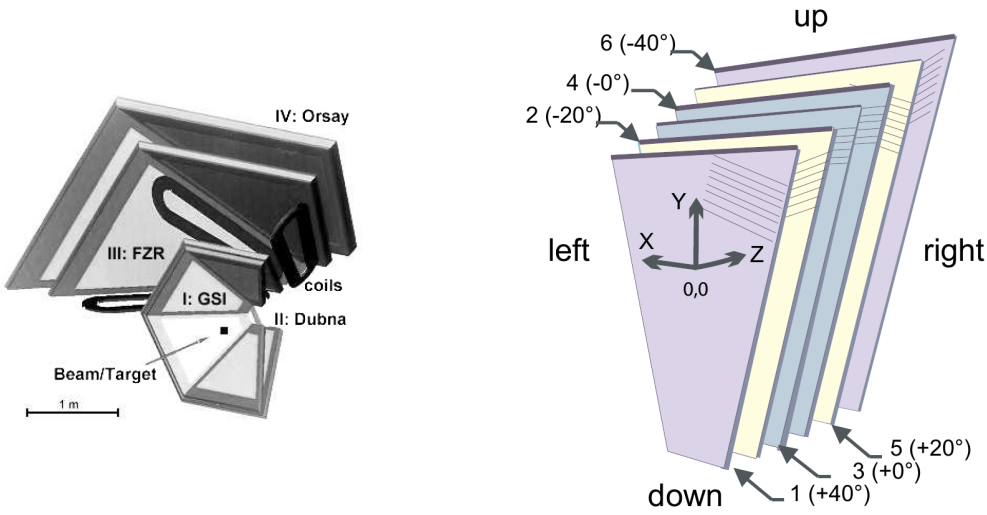

Figure 2.3: Left: Arrangement of the drift chambers in four different planes where the frames of the chambers match with the coil positions of the magnet. **Right:** Wire layer structure of the drift chambers.

spatial resolution is about 60-100 μm in polar angle direction and 120-200 μm in azimuthal angle direction [105]. The combination of the measurements in each layer to a full track and reconstruction of its momentum will be discussed in section 3.2 and 3.3)

2.2 Time-of-flight estimation

The velocity of a particle is calculated by the path length and its time-of-flight (ToF). A reconstruction of the time-of-flight requires a measurement of the start time and stop time. Therefore, the START detector is positioned in front of the target and two stop time detectors are positioned behind at the back of the spectrometer. A detailed description of the time-of-flight reconstruction is presented in section 3.5.

2.2.1 Start time measurement

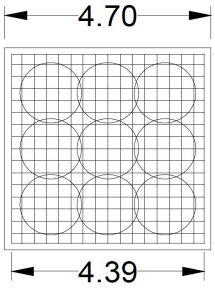

Figure 2.4: Active area of the START detector and the circles indicate 9 possible areas for measurement (scale in mm) [112].

The START [113] detector is positioned in front of the target and measures the absolute arrival time of incoming beam particles. Besides the time measurements, a position measurement is also performed in parallel and is used to monitor the beam position. A good radiation hardness and a fast measurement process is required due to the heavy load of the high intensity beam. The detector itself is built out of two planes of diamonds [113],

which are selected due to their good charge collection efficiency resulting in a good energy resolution and high drift velocity. Each detector plane consists of 16 stripes with a width of 200 μm which are separated by 90 μm gaps [114]. The total size of the START detector is $4.6\,\mathrm{mm} \times 4.6\,\mathrm{mm}$ which is much larger than the cross sectional area of the beam. This allows to move the detector during the beam time to reduce the integral dose per area of the detector (see Fig. 2.4) to avoid large efficiency drops due to radiation damage. This setup reaches a time resolution $t \approx 50\,\mathrm{ps}$ for the start time estimation.

2.2.2 Resistive Plate Chamber

The Au+Au collisions at $1.23A$ GeV impose the highest particle multiplicities measured with HADES so far. For this reason, the new resistive plate chamber (RPC) detector [115] replaced the low-granularity TOFINO detector [105]. Its task is the determination of the stop time of particles for which reason a good time resolution is essential. Moreover, a good position resolution for track matching of the tracks reconstructed in the drift chambers is needed as well.

The detector is covering the forward polar angle region between 18–45° of the HADES detector. Each of the six sectors consists of partially overlapping elements arranged in 31 rows and 3 columns (see Fig. 2.5 (left)). Each element consists of three aluminum electrodes and glass electrodes that are installed between two aluminum electrodes (see Fig. 2.5 (right)). All the electrodes are separated by a small gap that is filled with $C_2H_2F_4$ and SF_6 (90/10) gas mixtures [116].

The detector is operated at a nominal voltage of 5600 V. Charged particles crossing a cell ionize the gas. Due to the high electrical fields, ionized electrons are accelerated towards the anode where an electron avalanche is triggered. The advantage of RPC is that by construction it is possible to generate a very high electrical field, which results in a large, but localized amplification of primary electrons produced by the ionizing particle traversing the detector. Furthermore, the signal is locally restricted by high-resistance electrodes. This setup results in a good time resolution of $\sigma_t \approx 70$ ps and good position resolution of 8 mm in longitudinal direction [117]. The detector system is able to measure particle rates up to $1\ \frac{\mathrm{kHz}}{\mathrm{cm}^2}$. In the Au+Au collisions at $1.23A$ GeV, an average double hit probability of below 10% and a detection efficiency of 95% is reached [115].

2.2.3 TOF time-of-flight wall

The time-of-flight measurement in the polar angle region between 44–88° is performed by the time-of-flight detector (TOF) [118]. Besides the time measurement, a fast multiplicity determination is also required to determine the particle multiplicity in case a reaction with the target took place. The detector is constructed in six sectors, whereof all sectors consist of eight modules that contain eight rods each. Every rod comprises of a plastic scintillator and a photo multiplier tube and light guide [118].

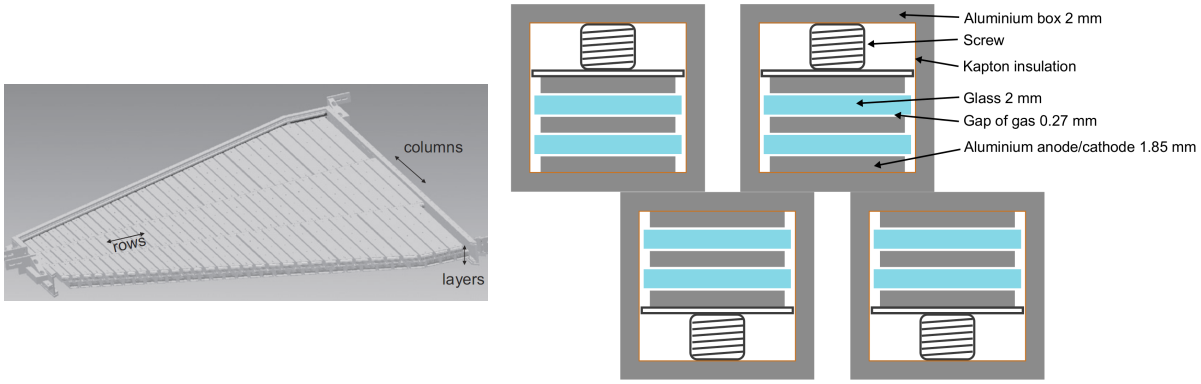

Figure 2.5: Schematic structure of one RPC chamber. **Left:** Arrangement of cells inside one chamber. **Right:** Alignment of overlapping cells and inner construction of single cells. [115]

The particle identification is based on scintillator material. Particles that transverse the material lose energy which is afterwards partially emitted as photons. The photons travel towards the photo multiplier tubes at the left and right side of each scintillator. Finally, the photon signal is amplified and its width and height is extracted. The stop time, x-position and energy loss of a track is estimated by the left and right measurement (see section 3.5 for a more detailed explanation).

This setup allows to measure the time of flight with a resolution σ_t = 100–150 ps as well as the position with a resolution of σ_x = 25 mm and σ_y = 27 mm. The resolution was obtained by measurements without magnetic field. Furthermore, the deposited energy is also extracted and available as energy loss information for particle identification. With this setup, a double hit probability below 20% in Au+Au collisions is reached [105].

2.3 Lepton identification detectors

The reconstruction of lepton pairs requires a high purity lepton sample. Therefore, additional lepton identification detectors are installed. A Cherenkov detector covers the full acceptance and the small polar angular region (Θ <45°) is additionally covered by the Pre-Shower detector to discriminate the enhanced hadronic background (see Fig. 2.6 (left)) in this detector part.

2.3.1 RICH detector

The purpose of the ring imaging Cherenkov (RICH) detector is the identification of relativistic $e^{\pm}$ tracks in the momentum range from 0.1 to 1.5 GeV/c [119]. The detection is based on the Cherenkov effect. Latter one appears if particles travel faster than the speed of light in the corresponding medium. In that case, Cherenkov photons are emitted in a fixed polar angle

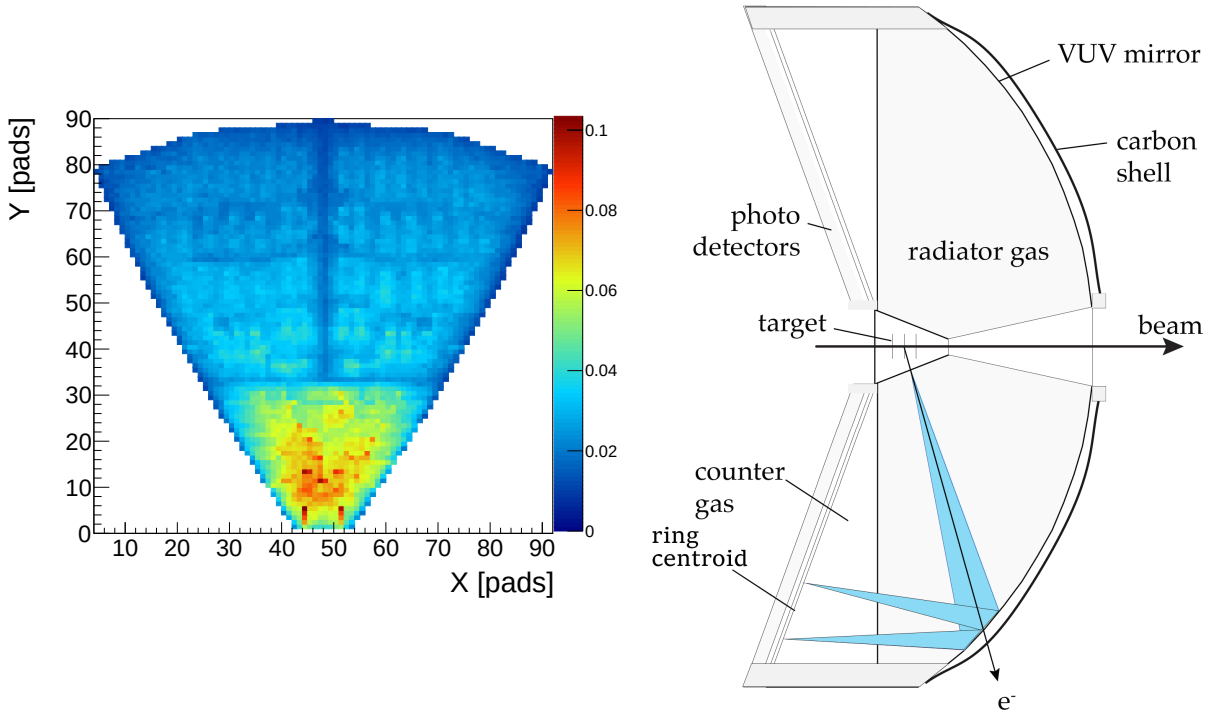

Figure 2.6: Left: Fired RICH pads distribution per event extracted from Au+Au data. The y pad number is correlated to the polar angle. **Right:** Schematic side view of the RICH detector. An emitted lepton and its Cherenkov cone is indicated.

relative to the particle's velocity vector. They are emitted in the Cherenkov angle Θ_C relative to the particle direction and the number of emitted photons is estimated by [120]:

$$N_{det}^{\gamma} \approx N_0 Z^2 D sin^2 \Theta_C(\lambda) \tag{2.1}$$

where N_0 = Detector property, Z = Atomic number, D = Flight distance and λ = Wavelength. Since in the given momentum range, only leptons are faster than the speed of light in the RICH radiator gas, this effect is perfectly applicable to isolate leptons from heavier particles.

The detector itself is shown in Fig. 2.6 (right). Its construction is constrained by the aim of a low material budget and compact setup in conjunction with a sufficient number of emitted Cherenkov photons. The low material budget is essential to reduce multiple scattering and photon conversion. The RICH consists out of a radiator volume, four carbon and two glass mirrors, a photon detector and is optimized to identify photons in the vacuum ultraviolet (VUV) region. The radiator is filled with a C_4F_{10} gas mixture and surrounds the target region in order to have leptons emitted in the focal point of the mirror. The mirror needs a high reflectivity while the window separating the radiator gas from the photon detector counter gas volume needs a high VUV transmission capability [119].

The photon detector plane is placed upstream to reduce the detection of particles emitted from the vertex. It consists of six modules of trapezoidal shape that contain a multi-wire proportional chamber (MWPC). Each chamber has 4712 pads that have a width of 6.6 mm while

their length rises from 4.5 mm to 7.0 mm. The variable size corrects partially for elliptical rings due the photon plane approximation which will be discussed in more detail in section 5.2.3. Due to the requirement of a small material budget, the mirror has a thickness smaller than 1% of the radiation length. By inserting materials and the distance from the target to the mirror in formula 2.1, N_0 = 109 is estimated as the mean number of produced photons per lepton emitted from the target. This value rises slightly from smaller towards larger polar angles since the distance, which electrons or positrons travel inside the radiator gas, grows for larger polar angles [105].

2.3.2 Pre-Shower detector

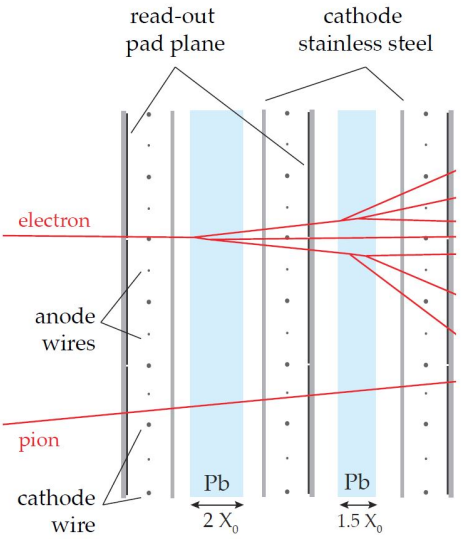

Figure 2.7: Structure of the Pre-Shower detector. Electromagnetic showers triggered by a crossing particle are indicated by red lines. The figure shows the three positions of charge measurements: Q_{pre} (pre-conv), Q_{post1} (post1) und Q_{post2} (post2) [105].

The Pre-Shower detector [121] is installed in the polar angle region 18–45° to improve lepton identification power which is required due to higher particle track densities in the smaller polar angle region (see Fig. 2.6 (left)). Another reason is the reduced path length in the inner part of the RICH detector (see Fig. 2.6 (right)). For that reason less photons are emitted per ring. Consequently, the lepton identification efficiency is lower towards smaller polar angles. The Pre-Shower detector is build out of two lead converters and three drift chambers that are installed alternately (see Fig. 2.7). The drift chambers are built out of one cathode plane, one anode plane and are filled with $Ar/C_4H_{10}/C_7H_{16}$ (33/65/2). The cell size increases for larger polar angles to maintain a constant granularity.

For the identification of particles, the charge produced in electromagnetic showers is measured by all three chambers. While passing the lead converters, particles produce Bremsstrahlung electrons and electrons due to electron pair production. This triggers an electromagnetic shower, which is measured in the second and third chambers. The charges are measured at the corresponding chamber position demonstrated in Fig. 2.7. For particle identification, the difference between charge measurements of the first and the two following chambers is calculated:

$$Q_{sig} = Q_{post1} + Q_{post2} - Q_{pre} \tag{2.2}$$

Since the charge difference is expected to be larger for electrons and positrons, it is used to separate them from the heavy hadrons (e.g $\pi^{\pm}, p$). This results in an additional method for electron identification for momenta $p >$ 300 MeV/c. In Au+Au collisions, the detector has a low double hit probability of around 5% [105].

2.4 Event recording and characterization

Collisions are created by an interaction of the beam ions with a target, which is required to have a low conversion probability to reduce the background contribution from electrons and positrons of photon conversion. In order to select and characterize collisions a VETO and Forward Wall detector are installed, respectively.

2.4.1 Target and reaction trigger

The target is installed in the focal point of the RICH detector. It needs to have a small interaction length since the large lepton pair background from gamma conversion shall be minimized. For this reason, the target is segmented in 15 thin circular gold disks (see Fig. 2.8), which reduces the conversion since photons have the chance to pass the upcoming foils in front of them without interaction. In the setup, each foil has diameter of 2.2 mm and a thickness of 25 μm [122]. The foils are fixed by a kapton strip that has a hole a the central position of the gold foil. All kapton strips are held by a carbon fiber tube with a length of 54.5 mm. The usage of materials with a small atomic number reduces the interaction length of the target and its holder to 1.35%.

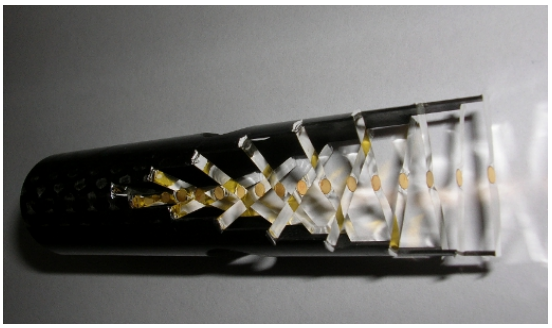

Figure 2.8: Gold target segmented into 15 target foils with a distance of 3.6 mm between each foil in order to decrease the conversion probability of photons [112].

Since more central events are of physical interest, the collision centrality is estimated by the number of hits in the outer time-of-flight detector TOF. Furthermore, a coincidence in time between a measurement in START and the stop time measurements from RPC and TOF is used to reduce the number of events that overlap in time, so-called *pile-up* events. An additional event quality estimation is provided by the VETO [114] detector that is positioned downstream of the target. It is a diamond based detector [113] that is used to identify signals correlated in space and time between START and VETO. Incoming beam particles without a reaction in the target or a very peripheral target collision are therefore rejected.

2.4.2 Forward wall

The forward wall (FW) detector [123] is installed to extend the acceptance in the low polar angle region in order to measure the spectators of the collision. It is situated seven meters downstream of the target and placed behind a helium balloon to reduce the multiple scattering of the spectators. The detector consists of scintillators together with photomultiplier tubes and covers an area of $1.8\,\mathrm{m} \times 1.8\,\mathrm{m}$ which corresponds to a polar angle coverage of $0.3 < \Theta < 7.3°$. In total, 288 elements are installed and vary in size due to the increased spectator multiplicity

in the more central region. The cell size decreases from 16 cm × 16 cm to 8 cm × 8 cm cells and 4 cm × 4 cm towards smaller polar angles. A hole of 8 cm × 8 cm is in the center (see Fig. 2.9).

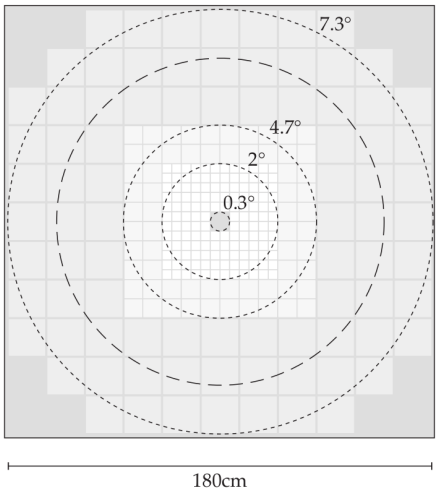

Figure 2.9: Arrangement of the Forward Wall detector modules showing the pad sizes. The angular coverage is indicated by the the circles.

The measurements provide information on the position, charge and time-of-flight of charged particles. The spectators are identified via their time-of-flight and energy loss in the modules. In the elementary d+p collisions, the spectator measurement was used to identify forward going protons to select quasi-free n+p reactions [124]. The information of the spectator position is important since it is used to reconstruct the reaction plane and estimate the centrality in Au+Au collisions. In addition, the spectator measurement is used for centrality determination (see section 4.3). In the Au+Au beamtime a time resolution of σ_{ToF} = 400–500 ps in combination with START is reached and a momentum resolution for protons is estimated to be 11%.

2.4.3 Data acquisition and trigger

Due to the new challenges, of the high particle multiplicities and reaction rates in Au+Au collisions, the data acquisition (DAQ) system was upgraded [125]. The aim of the upgrade is to achieve data rates of up to 400 MByte/s which correspond to a rate of up to 100 kHz in light collision systems and up to 20 kHz in Au+Au collisions. Therefore, a trigger and readout board (TRB) [126], that handles the read out and data transfer, is used. In addition, a trigger signal and slow control access is provided.

The recorded data is transported in a common network which is based on the TrbNet protocol. It manages the data transport from the digital signals that were obtained by converting the analog information from the front ends. The central trigger system (CTS) controls the data acquisition and selects good events based on a pre-defined trigger criterion. All the data is transported via a Gigabit Ethernet connection to the server farm. Four servers, with two event-builders each, analyze the data event-wise and reconstructed events are written to files which are saved to the local storage as HADES list-mode data (HLD). Afterwards, the files are written to the file system (e.g. HERA [127]). The detector hardware is controlled by a slow control system that is based on EPICS [128]. Besides the controlling of the hardware, the data recording and the detector parameters are monitored as well.

The Au+Au beam was delivered in 10-second spills separated by a 2-second break. Based on measurements with the START detector, up to 22 Million ions per spill were reached as maximum and resulted in approximately 70000 reconstructed events per spill (see Fig. 2.10). In case of the Au+Au beam time, the physics trigger 3 (PT3) was selected and requires a minimum number of 20 hits in the outer time-of-flight detector TOF. With this setup 140 TB of data were recorded in 557 hours of beam. This results in $7.3 \cdot 10^9$ events that were recorded with a data rate of around 4 kHz sustained rate within four weeks. Since this rate is reduced due to parasitic users, downtime and the spill structure, the real rate within a spill is about 8 kHz. The data rate is reduced compared to the design value, but this is caused due to limitations of the detector load and not by the data acquisition itself [129].

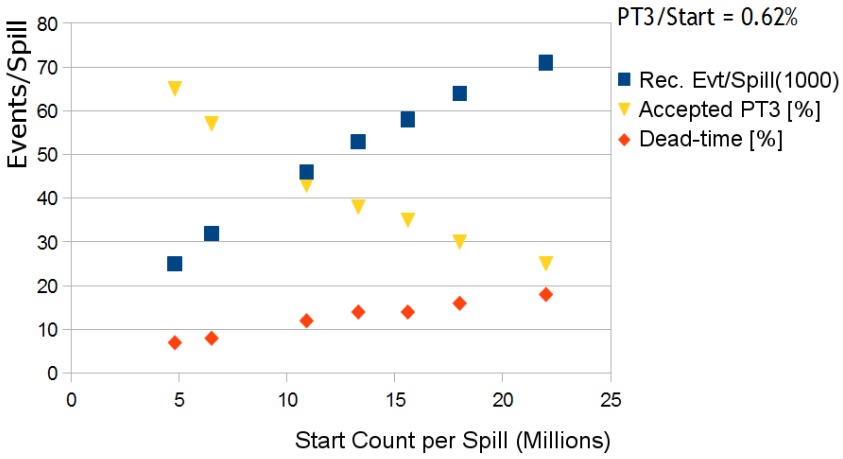

Figure 2.10: Performance of the data acquisition during the Au+Au beamtime. The increasing number of events reduces the efficiency of the data recording.

Chapter 3

Data processing and track reconstruction

HADES is capable to record data with high event rates. For this reason, an analysis framework (HYDRA) [130] suited for reconstruction and analysis of many events and tracks per event was developed. It is based on ROOT [130], an object-oriented framework that is written in the programming language C++. ROOT is optimized to handle and analyze large amounts of data and is commonly used in the field of high energy and nuclear physics. Mathematical functions and operations as well as visualization in multi-dimensional histograms are provided for analysis. Furthermore, the functionality is extended by packages for specific tasks (e.g. TMVA for multivariate analysis methods). HYDRA extends the ROOT functionality with detector specific tasks, functions for track reconstruction and functions for data analysis. An overview of the analysis chain from raw data to reconstructed track candidates is provided in this chapter.

3.1 Data processing of detector measurements

The data acquisition and storage has been described in section 2.4.3. The recorded data is stored as uncalibrated data in the HLD files. In order to retrieve fully reconstructed particle candidates, a track reconstruction needs to be executed (see section 3.2). Simulated data is handled by an identical reconstruction chain as experimental data, to assure a high comparability. A realistic simulation of the detector response is necessary to understand how the detector characteristics affect the particle reconstruction.

In simulation, the heavy-ion collisions are generated using model calculations (see Fig. 3.1). The transport model UrQMD [131] (see section 1.2.4) is used to generate the global event activity. In case rare particle species need to be investigated, an embedding technique is applied. The particles of interest are generated using the Monte Carlo event generator Pluto [132] and merged with UrQMD or real events. Typically, such an event contains one embedded particle per event or sector. In a subsequent step, the simulated particles are transported through the detector material using GEANT [133], which simulates secondary particle production, as well as energy loss and multiple scattering of the energetic particles. The detector signals of the generated particles are reproduced in the digitizers. The digitizer is tuned to match with the resolution

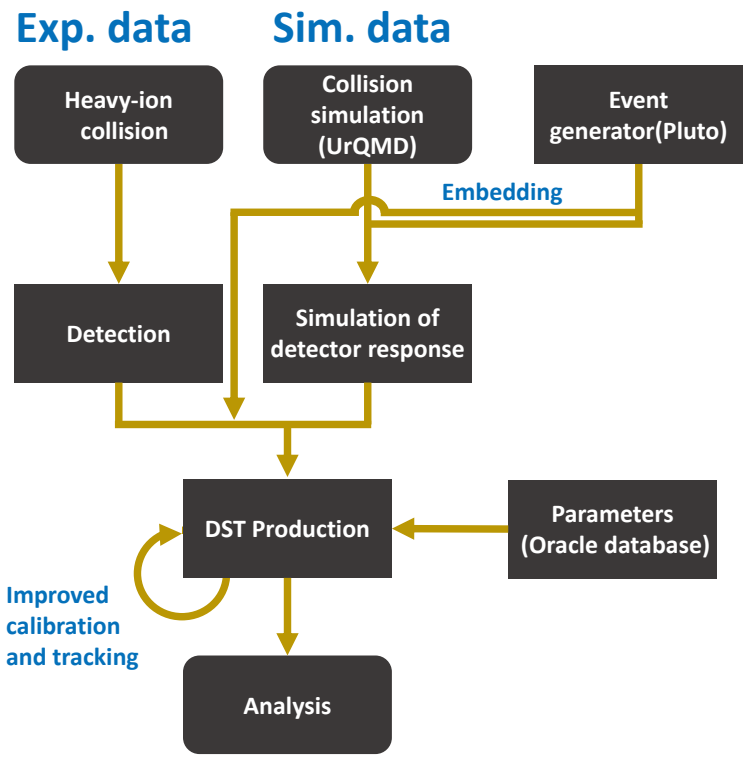

Figure 3.1: Schematic process of the DST production for experimental and simulated data.

of real detector measurements and thus smears the signals in simulation. Afterwards, the data format for real and simulated data are the same. They only differ in the additional information of the input particle, that is provided in simulation. The detector measurements serve as input for track reconstruction, that includes trajectory, momentum and time-of-flight reconstruction. Moreover, tracking algorithms combine particle tracks from different sub detectors to track candidates. All parameters, necessary for the reconstruction procedure, are stored in a database. All detectors require a calibration to convert the measurements properly to the physical observables. The calibration is based on the observables provided by already reconstructed measurements. It is improved iteratively with each generation of data since the newly calibrated data allows a more precise analysis due to the enhanced data quality. Finally, the reconstructed real and simulated events and particles are stored as data summary tapes (DST) and used as input for the event reconstruction. The detailed reproduction of the measurement and reconstruction process results in a realistic simulation output. The simulated data can be used to test various analysis techniques and interpret the results, since every simulated track is monitored. Moreover, the reproduction of experimental data allows the usage of the simulation to correct for reconstruction inefficiencies in real data.

3.2 Track reconstruction with MDC

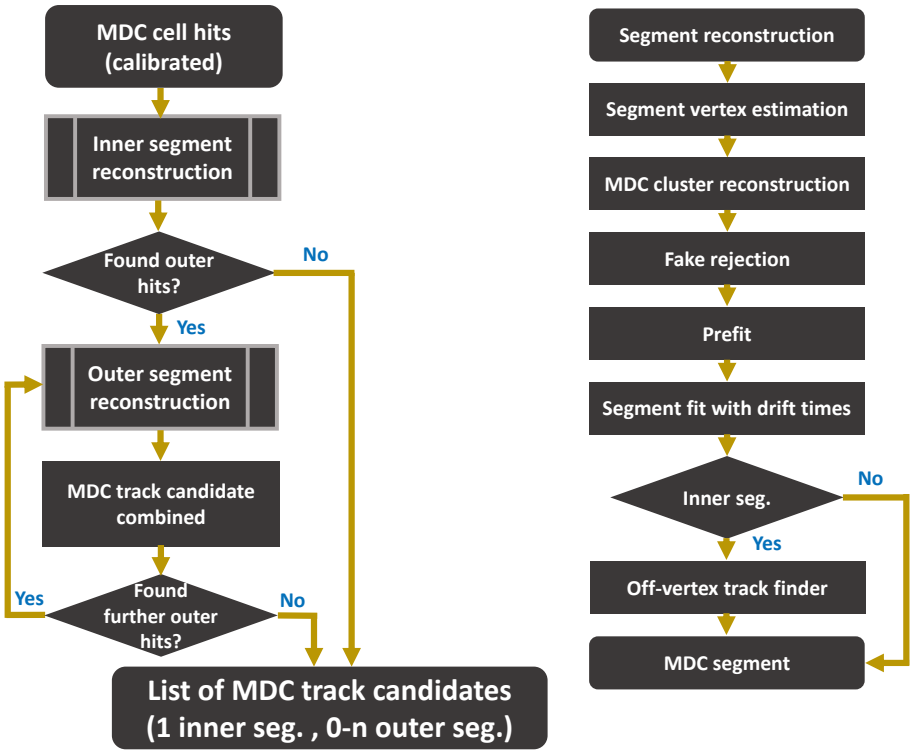

Figure 3.2: Summary of track reconstruction procedure steps. Besides the segment vertex estimation, the segment fitter works similar for inner and outer MDC segment reconstruction. Only an additional search for off-vertex tracks is included in the inner segment fitter. As a result, only an inner segment, a MDC track candidate, comprising an inner and outer MDC segment, or multiple of MDC track candidates are reconstructed.

The measured and stored raw data contains only single detector signals that are not yet combined to full tracks. One specific track finding task is the track reconstruction in MDC. The main challenge of a proper track reconstruction stems from the high particle multiplicity in Au+Au collisions. Due to the various MDC layers, many possible track combinations, including fake combinations, are possible. Therefore, an elaborated selection method for a pure track reconstruction is applied (see Fig. 3.2). The track reconstruction searches for an inner MDC segment and for one or multiple suited outer MDC segments. A reconstructed inner MDC segment is combined with all suited outer MDC segments. This results in one or multiple MDC track candidates. The reconstruction will be explained in more detail in the following.

The starting point of the track reconstruction are the hits in the inner MDC segment. They are used to determine the reaction vertex position by projection of the MDC clusters on a plane with a reference point within the vertex range. Only the z-vertex position of the so-called *cluster vertex* is determined. Once this position is determined, the clusters of the inner drift chambers are reconstructed. Wires from each layer are summed up and show maxima in case of correlated

wire positions (see Fig. 3.3 (left)). At this stage, fake contributions of close clusters are already removed by investigation of the MDC layer hit patterns.

Subsequently, the wires are combined by the prefit procedure. In this reconstruction step, all cluster hits are compared to a track segment assumption using a straight line. The straight line with the smallest deviation from the signals is selected within the prefit procedure. A vertex position is neglected for this reconstruction step. A more precise segment is estimated by the segment fitter, using the values estimated with the prefit procedure as starting point. This reduces the probability for misidentification of a local as a global fit minimum. The final segment fitter is more precise than the prefit because of the inclusion of drift times and errors in the fitting procedure. By inclusion of the drift time, the distance of the possible hit to the wire is restricted. The signal position reduces from the whole area of the cell to a tube-like area around the wire (see Fig. 3.3 (right)). Due to the reduced area and the already determined start parameters for the segment fit, a more precise position of the segment is obtained. Finally, a segment is further used in the track reconstruction procedure if at least nine layers contributed to the segment.

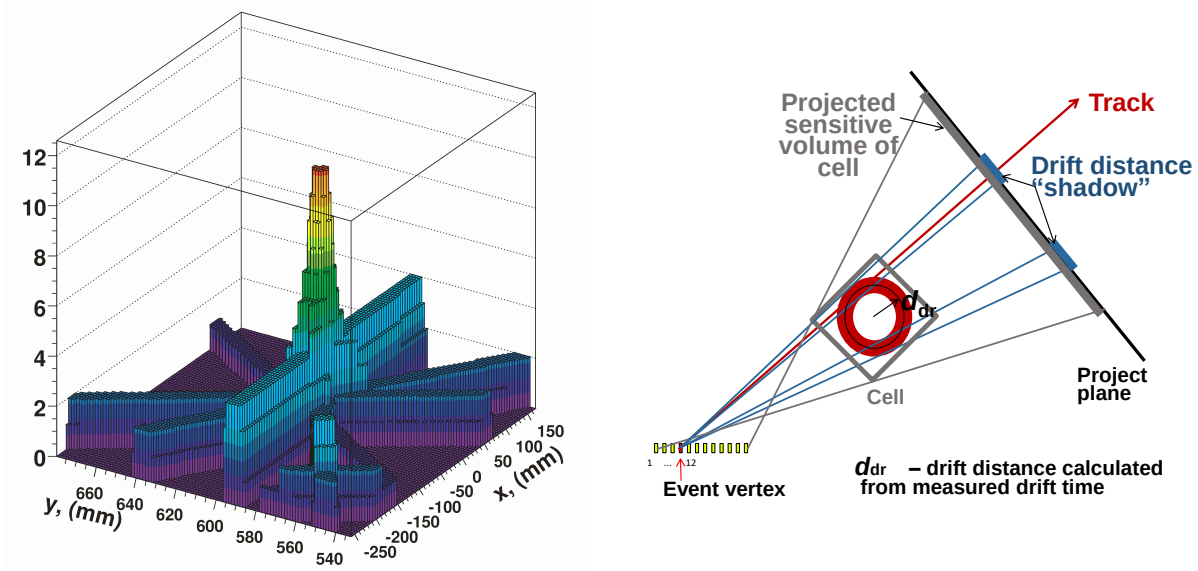

Figure 3.3: Left: Hit finding procedure in the MDC chambers. Fired drift cell volumes are projected onto a plane, that is perpendicular direction of the particle track, and result in a peak structure in case of a particle hit. Only a high number of correlated signals in wire planes returns a signal that is perfectly separated from background. **Right:** Application of calculated drift time to reduce the possible track position inside a cell. The allowed area for a track is reduced from the cell size (grey) to two bands left and right to the sense wire (red).

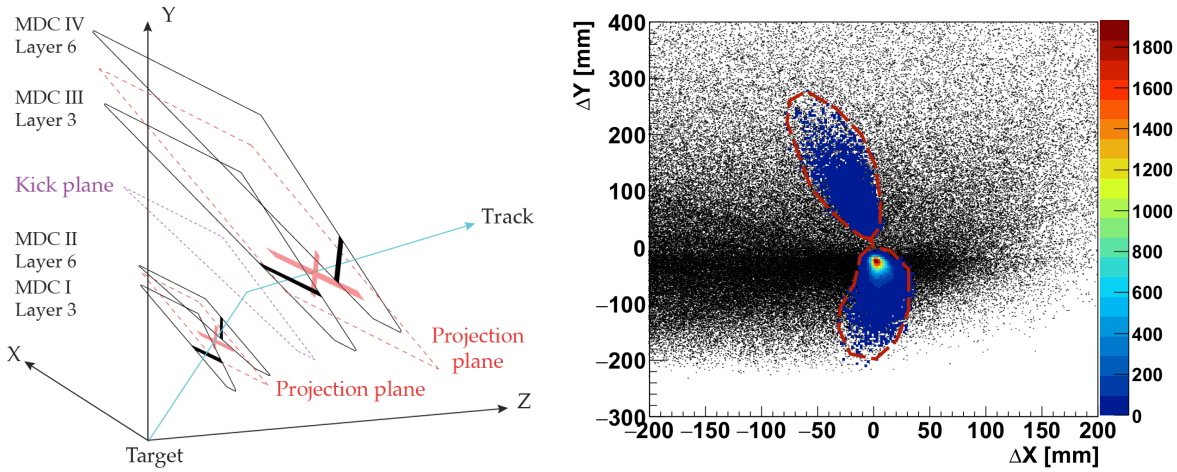

Figure 3.4: Left: Application of the kick plane track finding procedure. The influence of the magnetic field on the particle track (blue) is approximated by a local momentum kick. An inner segment that matches with an outer segment in a physically possible region is considered as track candidate. **Right:** Possible Track candidates and their deflection (ΔX = Inner segment, ΔY = Inner segment). The angular selection region varies with the azimuthal and polar angle of the inner track segment. Good tracks are shown as colored distribution while fake tracks are marked by black points. The selection area is indicated by the red line.

For the search of suited outer segments for the reconstructed inner segment, a so-called *kick plane* method is used. It is a simple approximation of the particle deflection by assuming a momentum kick due to the magnetic field (see Fig. 3.4 (left)). Once the hit point on the kick plane is estimated, it is used as vertex for cluster finding in the outer MDC chambers. The search area is restricted to the physical region of particle deflections (see Fig. 3.4 (right)). Similar to the inner segments, also fakes in the outer segments are removed to achieve a clean MDC cluster sample. The outer MDC segment is estimated with a straight line in the prefit procedure. Analogously to the reconstruction of the inner segment, the final estimation of the outer segment is obtained by a fit including the drift times.

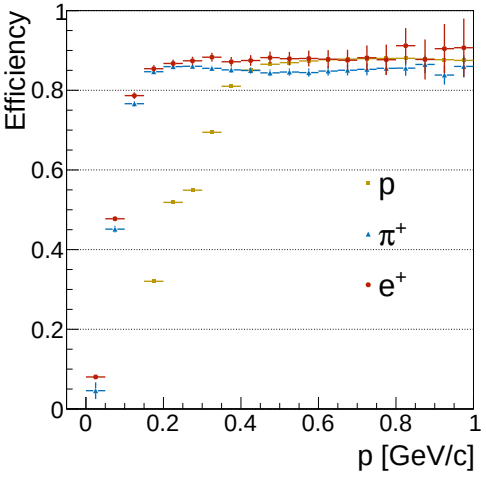

Figure 3.5: Tracking efficiency for three particle species obtained from simulation.

Finally, a combination of all matched inner and outer MDC segments is obtained as MDC track candidates. As a result, Fig. 3.5 shows a tracking efficiency of around 90% for leptons over a broad momentum range. Only for momenta smaller than $p < 0.18$ GeV/c an efficiency drop due to the larger track curvature is present. Heavier particles have similar maximum tracking efficiency value.

3.3 Momentum reconstruction of charged particles

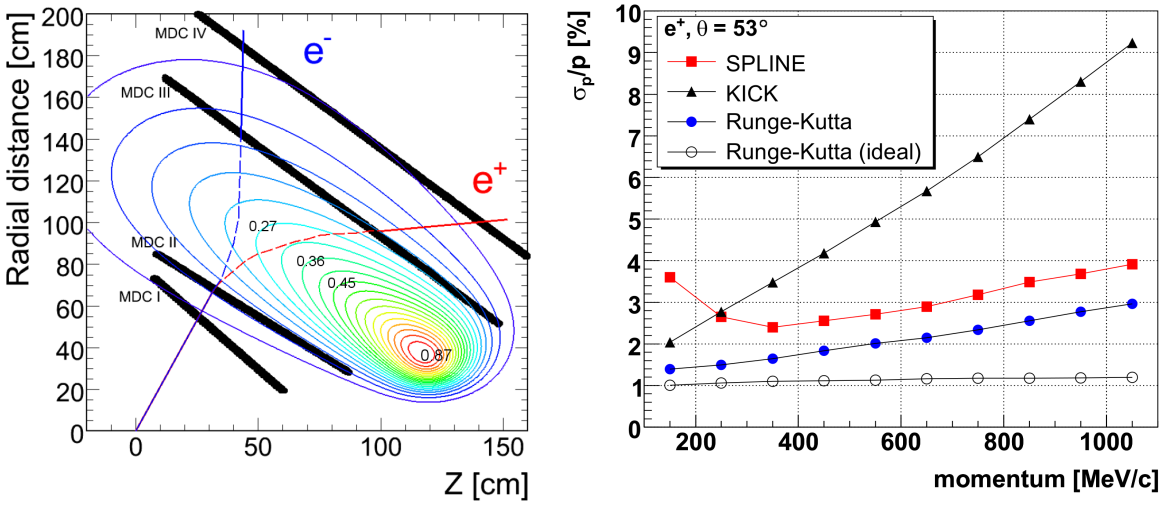

Figure 3.6: Left: Sketch demonstrating the interplay of MDC and magnet for momentum reconstruction. The relative field strength is indicated by the colored lines and the numbers represent the magnetic field strength in tesla at the corresponding position. Reconstructed segments (solid lines) and connected by a reconstructed particle trajectory (dashed) between the drift chamber segments. [105] **Right**: Comparison of the momentum resolution for three momentum reconstruction methods revealing the Runge-Kutta method as the best one. A decreased resolution at higher momenta is caused by the smaller deflection angle for particles while having the same spatial resolution for the position measurement.

The particle trajectory was estimated by the MDC track candidate reconstruction in the previous section. Using this trajectory allows to determine the momentum by the deflection of the particle due to the magnetic field (see Fig. 3.6 (left)). The particle deflection $\Delta\vec{p}$ is caused by the Lorentz force $\vec{F} = q(\vec{v} \times \vec{B})$, where $\vec{B}$ is the magnetic field and $\vec{v}$ the particle velocity. The total deflection of a particle is given by the difference of the incoming (p_{in}) and outgoing (p_{out}) momentum vectors:

$$\Delta\vec{p} = \vec{p_{out}} - \vec{p_{in}} = \int \vec{F} dt = -q \int \vec{B} \times d\vec{s} \tag{3.1}$$

As given by the formula of the Lorentz force, the particle deflection is oriented perpendicular to the magnetic field. Due to the magnet construction, particles are dominantly deflected in polar angle direction and the angular difference is given by:

$$sin(\frac{\Delta\theta}{2}) = \frac{|\Delta\vec{p}|}{2\,|\vec{p}|} \tag{3.2}$$

In order to improve the momentum resolution, the wire planes are oriented perpendicular to the direction of deflection. This results in a higher spatial measurement precision in the polar angle direction which improves the momentum resolution. The *kick-plane*, *spline* and *Runge-Kutta* methods are available for momentum determination [105]. Their differences are a trade-off between computation time and momentum resolution.

The method with the lowest requirements is the *kick plane method*, using the kick plane approximation that was already applied for track reconstruction in section 3.2. In this approach, the deflection in the space between the inner and outer drift chambers is substituted by a single momentum change at the kick plane position. The momentum value is obtained by a look up table which was computed in advance. In Au+Au data, this method is only used for track reconstruction[1], since the following methods provide more accurate results. The first approach for momentum reconstruction in Au+Au is the *cubic spline method*. A cubic spline function is taken as assumption of the particle trajectory. A minimization of a cubic function, that describes the particle trajectory, is applied and used to estimate the momentum of the particle track. In this procedure, the MDC hit positions are not modified to improve the results. At the end, systematic corrections have to be applied since the trajectory of a charged particle is not modeled exactly.

A more precise momentum value is determined by the *Runge-Kutta method* of the fourth order [134], which is used for particle trajectory reconstruction (see Fig. 3.6 (left)). It solves the equations of motion of a particle propagating through a magnetic field. The momentum, polarity, vertex and direction of the track are needed as input and provided by the spline method and the segment fitter. For the preparation of the fit, the Runge-Kutta propagation is used to calculate errors for the χ^2 fit. Therefore, the input values for the propagation are varied in each direction separately and propagated by the Runge-Kutta method. The resulting propagation is used to evaluate the errors at the layer positions. Finally, a least-square minimization procedure optimizes the particle trajectory for the given layer hits in order to determine the momentum. Also, a modification of the MDC hit positions is allowed to improve the fit quality.

Besides the momentum and the initial direction of the track, a specific track quality χ^2_{RK} is provided as output value. A comparison between the different reconstruction procedures is presented in Fig. 3.6 (right). As a result, the spline and Runge-Kutta approach achieve a much better momentum resolution than the kick plane method over a broad momentum range. Furthermore, the Runge-Kutta precision is always better than the spline method. The improvement is the largest for low momentum particles.

3.4 Spatial MDC-META matching

In order to enrich the information of a reconstructed particle track, the MDC track information can be combined with the time-of-flight measurement. Therefore, the position of a track in the Multiplicity Electron Trigger Array (META), which includes the RPC, TOF and Pre-Shower detectors, is estimated. Thereof, only RPC and TOF are of interest since the Pre-Shower detector does not provide a precise stop time measurement. Subsequently, the measured signals in the META detectors are reconstructed and matched to the MDC track candidates (see Fig. 3.7 (left)).

[1] See section 3.2

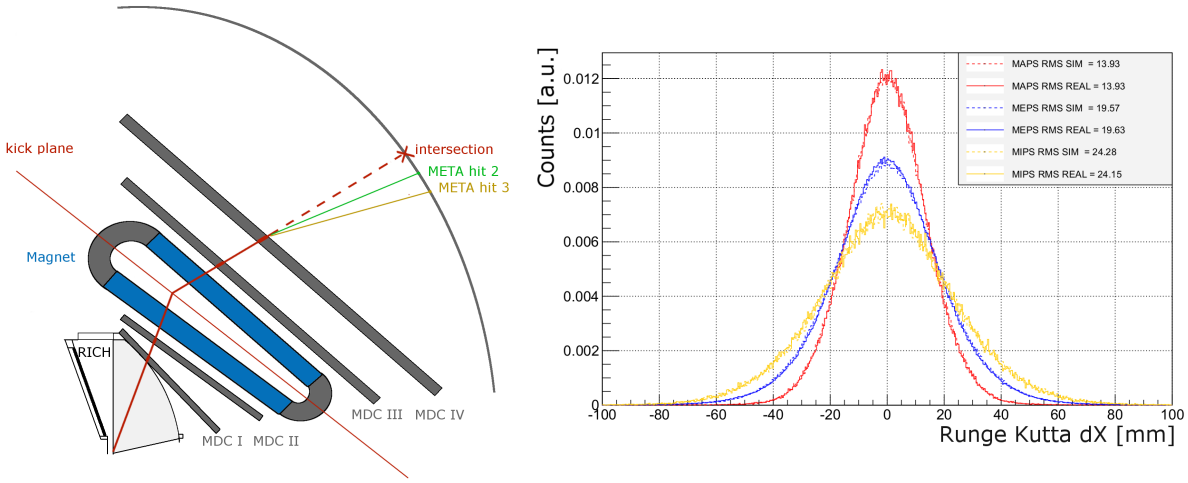

Figure 3.7: Left: Sketch of the META matching procedure. **Right**: Position resolution for three different energy loss classes (MIPS = minimum ionizing, MEPS = medium ionizing, MAPS = maximum ionizing). It is estimated by distance to the reconstructed Runge-Kutta tracks to the corresponding META hits. A comparison between simulated and experimental data shows a good agreement between both.

The signal in RPC and TOF is reconstructed by a measurement of the left and right signal. Attenuation due to the detector modifies both signals differently, for which reason the resolution depends on the signal attenuation. The RPC has a negligible attenuation, that only the resolution in TOF has to be adjusted. Finally, a quality estimator for the position resolution in x direction (`METAQa`) is provided by:

$$\texttt{METAQa} = \frac{\Delta \mathrm{x}}{\sigma_{\mathrm{x}}(\mathrm{E})}. \tag{3.3}$$

To search for possible matching META signals, the particle's Runge-Kutta trajectory is extended to the them. The Runge-Kutta hit is required to point within the active volume exactly, besides a deviation[2] factor to account for pointing uncertainties of the Runge-Kutta track due to multiple scattering. For every track, up to three reconstructed META signals in the detectors can be combined. The best candidate is chosen by the matching quality, which allows to determine the track direction with excellent precision. The resolution depends on the energy loss (see Fig. 3.7 (right)) of particles traversing within the rod and is described in units of the standard deviation σ.

3.5 Time-of-flight reconstruction

HADES' main particle identification technique is based on the velocity-momentum correlation. The momentum is obtained from the bending of the trajectory in the magnetic field, and the

[2]The deviation factor is set to 4 mm for a straight line and rises for tracks with smaller momenta since they are more strongly distorted by multiple scattering.

velocity from the particle's time-of-fight. Its reconstruction requires the measurement of a start t_{start} and stop t_{stop} time and the length of the particle trajectory l. The start time is measured by the START detector and the stop time by the TOF or RPC detector.

The start time is given by the measurement of the absolute time in the START detector, that is produced by the Au ion while crossing START before a collision with the target. Compared to the start time measurement, the ones in the stop detectors are more complicated since their rod length is much larger than the travel distance of a signal in the START detector. A particle crossing one of the stop detectors creates a signal that travels to both ends of the detector with a group velocity v_g. On the right and left end of a rod the times t_l and t_r are measured. The time of flight is estimated by:

$$ToF = \frac{1}{2}(t_l + t_r - \frac{L}{v_g} - t_{Start} + t_{Corr}) \tag{3.4}$$

where L is the rod length and v_g is the group velocity of the propagation in the scintillator or the electrode of the RPC, the t_{Start} is the time measured by the START detector and t_{Corr} comprises the different correction terms of the time measurement, mainly a constant offset and the walk correction needed for both detectors. The nature of the walk effect is the correlation of the measured charge and the time the signal crosses the threshold. The smaller the charge, the the larger the time to cross the signal threshold. The measured time-of-flight is then combined with the track length, given by the RK method and the particles velocity is obtained.

After matching of the MDC track with one of the META detectors, for every track its momentum, polarity, specific energy loss in the tracking detectors and the velocity is known. With that information a particle identification hypothesis can be done. As last step of the time-of-flight technique, a procedure to improve the start time is performed to enhance the separation power of the particles with velocities close to that of light. This technique is called T_0 reconstruction. For such a purpose, all the reconstructed tracks are pre-identified and their four momentum is calculated. After that, an expected time-of-flight is computed, considering the different detector response, energy loss and the multiple scattering previously studied in monte carlo simulation. With that value, the difference to the real measurement is obtained, as well as its uncertainty. Then, for each track, the weighted sum of that differences is calculated for all the other pre-identified particles in the event. Finally, the obtained correction is subtracted and the velocity is afterwards re-evaluated again. As shown in Fig. 3.8 (left), this procedure is multiplicity dependent. The more identified tracks in the event, the better is the determination of the collision time. This improves the START time resolution from a constant value of 57 ps to 54 ps in case of peripheral and to 31 ps in case of most central events. This reduction allows to achieve a resolution of 81 ps for electron tracks in the RPC detector, extending the separation power of electrons and positrons from charged pions by the ToF technique to momenta around 500 MeV/c of (see Fig. 3.8 (right)) [135].

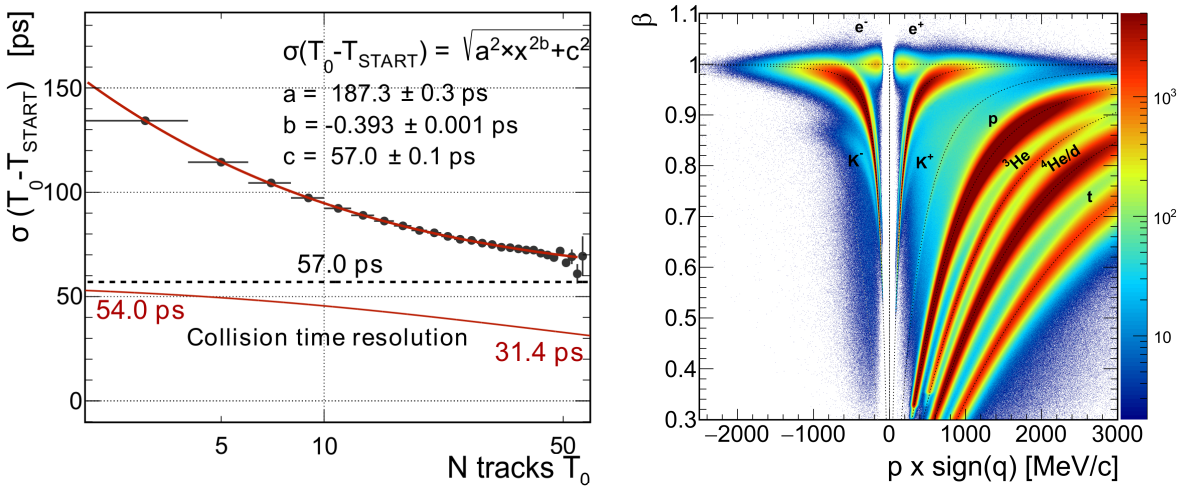

Figure 3.8: Left: Collision time determination in HADES as a function of identified track multiplicity used in the T0 algorithm. For central events a time resolution of about 31 ps is achieved, for the smallest multiplicities the accuracy is about 54 ps. The diamond START detector has a resolution of 57 ps (dashed line). **Right:** The velocity distribution as a function of momentum demonstrates the separation power of the velocity to determine a specific particle species.

3.6 Ring reconstruction in the RICH detector

The aim is to search for ring shaped photon distributions in the RICH detector. Found ring signatures will later on be matched to tracks reconstructed with MDC. In case of a spatial matching between ring and track position, this track is assumed to be an electron candidate. For the ring signal search in the RICH, all single photon hits on the pad plane are used. At first, a cleaning and labeling procedure is executed. It is followed by the execution of two different ring finding procedures [136].

The cleaning procedure before the ring reconstruction is helpful since background contributions (e.g. like electronic noise or correlated background hits) disturb the ring finding methods. A detailed discussion of the influence of noise is given in section 6.2.2. Groups of pads that contain at least one pad with a very high charge are claimed to result from a direct impact, of particles originating from the target region. Those hits on the RICH pad plane are removed. Additionally, single pads with a small charge that are isolated by seven empty pads are also removed. Due to the small occupancy of the RICH detector, a labeling procedure is performed in the next step. In this step, only regions containing groups of pads are marked as possible search areas for rings. This reduces the time needed for the ring search and thus the computation time.

One algorithm for the ring search is the *pattern matrix* method. An 11×11 matrix describing a ring pattern is compared to the hit distributions on the pad plane in order to estimate the ring quality. The pattern matrix ring mask was estimated by collecting hit distributions from real measured rings. As an output the matrix is filled with positive and negative weights, symmetrized and normalized to zero (see Fig. 3.9 (left)). The actual search is performed for each pad position of the already defined search areas. For fired pads inside the matrix, each weight

is added to produce a quality observable as output. A good ring will return a high quality since most of the pads match with the ring shape. Hits not matching with the ring shape, that are caused by background hits, decrease the ring quality due to the negative weights. The position with the best pattern matrix quality is chosen as the ring position.

A second approach for ring finding is the *Hough transform*. It uses a specific geometrical pattern and parametrization as input. Hence, a circle with a radius of four pads is given as input. The procedure combines three randomly fired pads belonging to the same search region. A ring is fitted to every combination of pads. This step is repeated for all combinations and is only restricted by the minimum position of half the radius between two pixels. As a final result, a two dimensional distribution of the x and y position of the ring center is received (see Fig. 3.9 (right)). The maximum of this position distribution marks the center position of the ring. The number of positions in the same bin mark the quality of the Hough transformation. This method is less influenced by noisy pads but might misidentify large particle clusters as rings. Both algorithms have different advantages and disadvantages. The pattern matrix algorithm is fast but has a worse accuracy in case of influence of noise to overlapping rings. In contrast to the pattern matrix, the Hough transformation is more flexible and does not strictly depend on the ring radius. But large clusters may be also identified as a ring. In conclusion, a good ring requires an agreement of both ring finding procedures. This helps to reduce the number of fake rings.

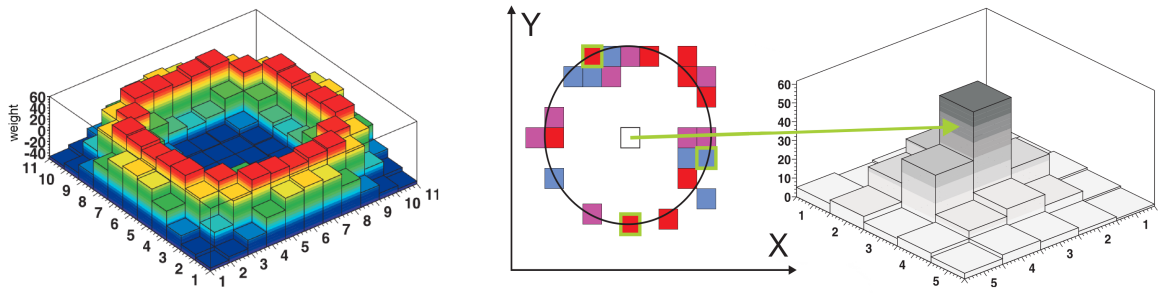

Figure 3.9: Left: Weight distribution of the pattern matrix mask. It contains positive values on the ring shape and negative values outside and inside the ring shape. **Right:** Schematic application of the Hough transformation, that selects three single pads and searches the best ring solution. The resulting pad position is plotted and the most probable position is chosen as ring center.

Chapter 4

Event reconstruction

In the previous chapter, the reconstruction of particle detector signals from their raw measurements was presented. All track candidates, that were reconstructed are stored in DST files events-wise. However, a quality and characterization of tracks and events was not performed yet. To improve the data quality, single events are removed by applying event quality observables. The resulting data sample can be used to estimate the detector performance as a function of time to exclude measurements from periods with unstable detector performance. In addition, the reconstructed tracks are used to estimate the collision centrality. Finally, tracks are selected from the list of track candidates of reconstructed events.

4.1 Event selection

One of the requirements to obtain a high purity electron sample are clean events. However, the sample of all events is contaminated by bad events which need to be excluded from the analysis. The measured event properties are restricted to remove bad quality events. Overlapping events, so-called *pile-up events* events, contribute as main source for event distortion. Also, a wrongly estimated start time will lead to shifts in the time-of-flight of particles and modify the particle velocity distribution. A large temporary noise contribution can produce multiple detector hits, making a precise event reconstruction impossible and needs to be removed as well. Moreover, measurements need to be constrained by their event properties (see section 4.3) since it is of interest to extract trends depending on the event characteristics. The event selection is based on the following standard selection criteria:

- **Good trigger (PT3)**: Peripheral events are excluded by requiring the PT3 condition (i.e. at least 20 hits in TOF).
- **Good cluster vertex (Good vertex)**: The cluster vertex is determined by projections of the MDC hits to the target region and has a good resolution in z direction. It is used to reject reactions of beam ions with material around the target (e.g. target holder, START detector) by requirement of vertex position $z > -65$ mm.

- **Good candidate vertex (Good vertex)**: Conditions applied to the candidate vertex are stricter, since at least two fully reconstructed candidates are required. This improves the reliability of the estimated vertex position. Moreover, the candidate vertex has also a good resolution perpendicular to the beam axis
- **Good START**: A well defined event requires a measurement in the START detector to estimate the time-of-flight of particles.
- **No pile up START**: The event is removed in case a second cluster is measured by START. This criterion rejects pile-up events.
- **No VETO**: The VETO is used to measure whether a collision with the target took place. Without a collision in the target, a hit in the VETO is expected within the time range of $\pm$ 10 ns around the START hit.
- **Good VETO START**: Requires a time range of 15 ns < τ < 350 ns without an additional START signal correlated to a VETO signal within a time window of $\pm$ 2 ns.
- **Good META START**: The event is removed in case of an additional START hit in a time window 80 ns < τ < 350 ns which is also correlated to META hits.
- **Good sector (Event characteristics)**: The definition of good sectors is based on the lepton file list explained in section 4.2.
- **Centrality selection (Event characteristics)**: Only events between $0 - 40\%$ centrality are chosen for the analysis (see section 4.3 for centrality estimation).
- **Reconstructed reaction plane (Event characteristics)** : Events without a reconstructed reaction plane are rejected, since this information is needed to estimate the combinatorial background in the pair analysis properly.

All conditions listed above are applied as event selection criteria. All of those were tested systematically by application to data analysis. Their impact was evaluated by quality differences of the dielectron signal [1]. A smooth invariant mass distribution is expected and indicates a good quality of the event sample. Several combinations of removal criteraia were tested. This analysis has shown, that `GoodSTARTVETO` and `GoodSTARTMETA` offer the smallest improvements in the signal quality of the invariant mass spectrum. Anyhow, latter ones do only reject a few events in total and are therefore included in the event selection. For the characterization of the event, its multiplicity class is estimated and only events within multiplicity range from $0 - 40\%$ are used. This range is chosen as to be unaffected by uncertainties of centrality estimation close to the trigger edge ($\approx 45\%$). Furthermore, each collision is characterized by the orientation of its event plane, which is reconstructed by the forward wall. In case no event plane is reconstructed,

[1] See chapter 8 for reconstruction of the invariant mass spectrum.

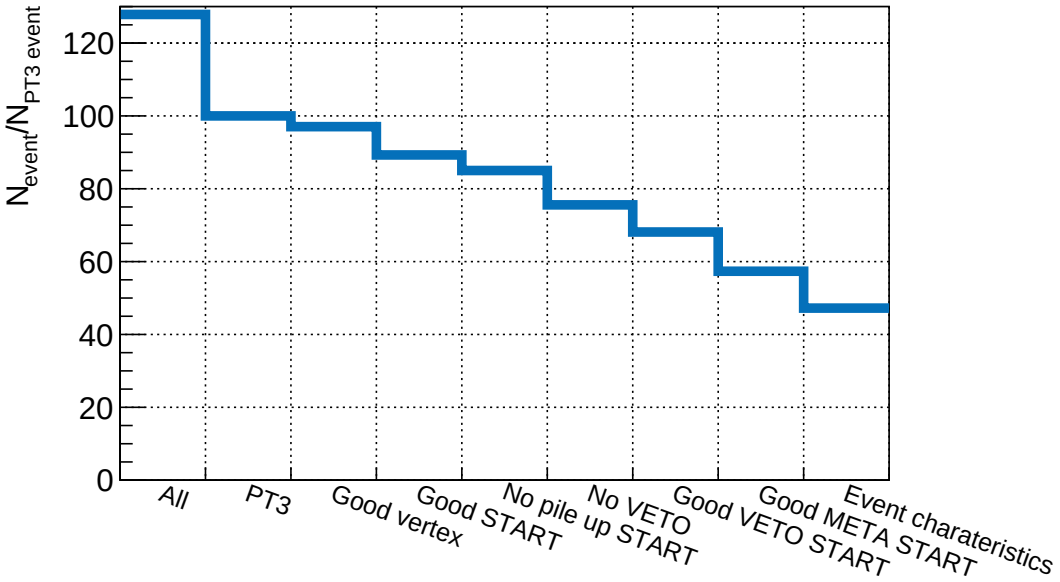

Figure 4.1: Reduction of events at each step of the selection procedure. The number is normalized to the number of PT3 events.

the event is rejected. Events taken in periods when single detector systems were not fully operational, e.g., trips or FEE failures, are rejected based on the file list estimated in the next chapter. At least four sectors have to operate normally, otherwise the event will be rejected. Figure 4.1 shows the reduction of the number of events when applying the event selection criteria step-by-step. After application of all event selection criteria, the data sample used for dielectron analysis contains $2.6 \cdot 10^9$ events.

4.2 Sector quality estimation

In order to obtain a most realistic detector performance in simulation, detectors including their efficiencies are modeled within digitizers [105]. A temporary reduced performance of single sectors is not considered by the mean efficiency in simulation. In order to identify low performance events, an analysis of the stability of single sectors is analyzed in experimental data. The aim is to remove only low performance sectors from analysis instead of neglecting the whole event. Since the electron and hadron identification is based on different detectors, the evaluation of the sector performance should be done separately for the hadron and electron analysis. The hadron track identification is mainly based on the MDC operation but also influenced by the time-of-flight measurement. Hence, the track stability is estimated by the number of reconstructed charged pions, that are identified using particle velocity and momentum constraints in a 3σ region around the mean values. The lepton efficiency depends additionally on the signifi-

cance of the RICH response. Therefore, the RICH performance is monitored by the number of reconstructed rings.

As an example, the number of reconstructed pions and rings for a single day of Au+Au beam time is presented in Fig. 4.2. Besides sector 2, all sectors show a stable number of reconstructed pions over the whole time period. Only very small and smooth or very short but stronger changes in the number of pions appear. Simultaneous changes of all sectors are an indication of an external (e.g. change in beam intensity) source that affects the efficiency. In case of the number of pions, sector 2 shows a strongly reduced performance which is also fluctuating and sometimes below 0.2 pions per event. A more detailed explanation for the reduced number of pions is given in chapter 6.1 by estimation of the layer efficiencies in each chamber.

The measurements of reconstructed rings are independent from the tracking detectors. As a result, the efficiency of sector 2 is as good as for sector 1. In comparison to the number of pions, the number of reconstructed rings in the RICH fluctuates more and sector 3 shows losses of efficiency multiple times. The losses in this sector are reduced in the following days due to execution of a high voltage ramping procedure to prevent streamers. This procedure reduced the detector performance losses to less than five minutes once per hour.

This analysis provides two separate lists of all files, storing the detector performance sector-wise for electrons and hadrons. A good hadron identification performance requires the number of reconstructed pions to be within a range of $\pm 5\%$ around the truncated mean of charged pions which estimated for each day separately. However, sectors that are continuously operating with reduced performance (e.g. MDC sector 2), that are indicated by a small number of reconstructed pions, are marked bad as well. In case of leptons, the fit ranges for the mean number of rings are $\pm 15\%$ (sector 0,4,5) or $\pm 20\%$ (sector 1,2,3) around the truncated mean value since the number of rings is more unstable. A well performing electron identification requires a sufficient number of reconstructed pions and rings as well.

By investigating the mean number of rings per day, a continuous decrease during the beam time is observed for all sectors. Sector 5 shows 0.5 rings per event at the beginning while only 0.4 rings per event are measured 22 days later. The RICH digitizer is tuned to the mean value of the simulation whereas an analysis of the full data set does not require an additional correction factor for the continuous performance decrease.

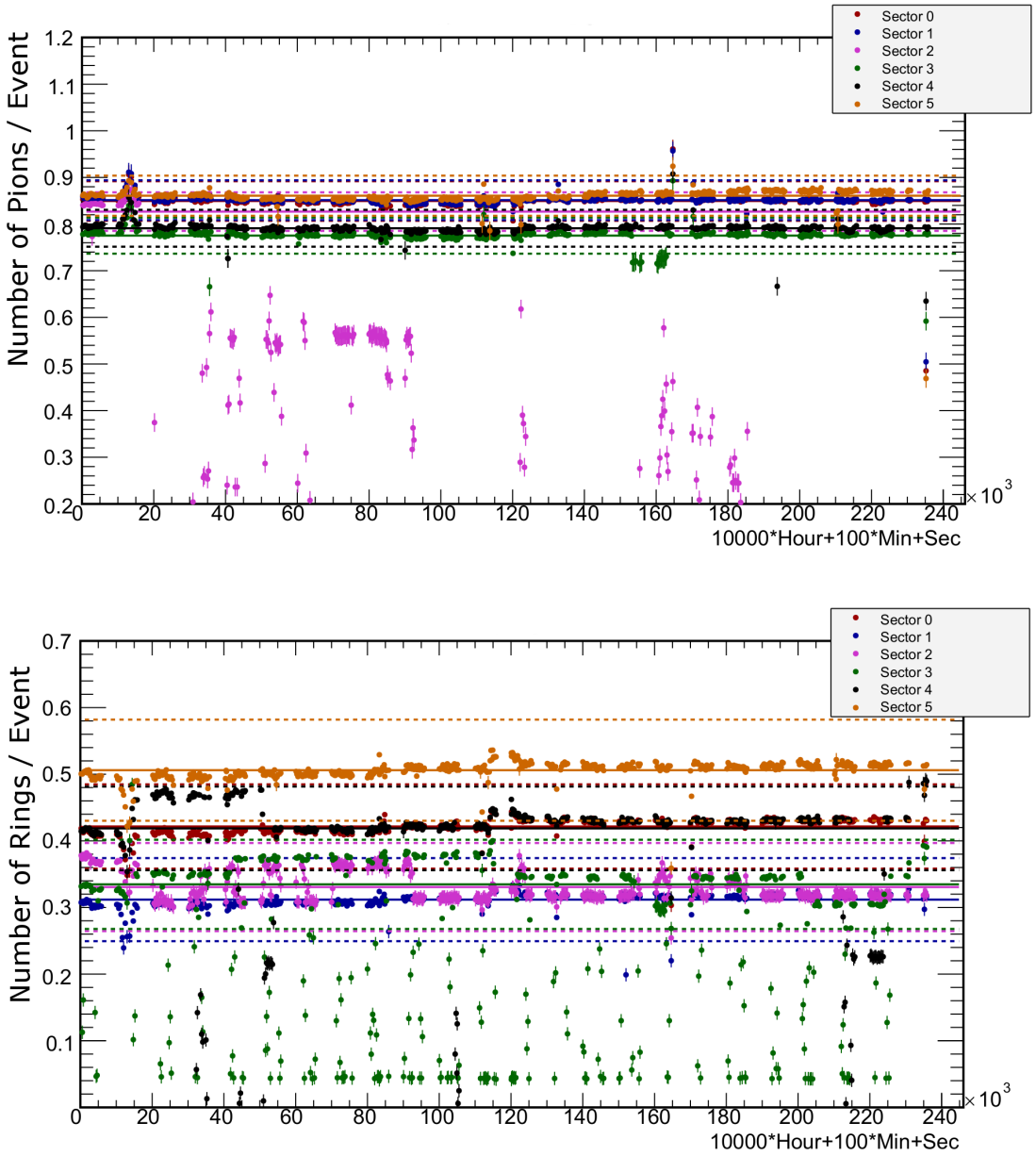

Figure 4.2: Mean number of pions (**Upper**) and rings (**Lower**) per event together with the mean value (solid line) for a single day. All tracks within the given range, which is indicated by the dotted line, are considered as good sector for particle identification. Good lepton files require a good number of pions and RICH rings. Each point covers the time period of the recorded file. The rejected files are marked with small error bars.

4.3 Event centrality determination

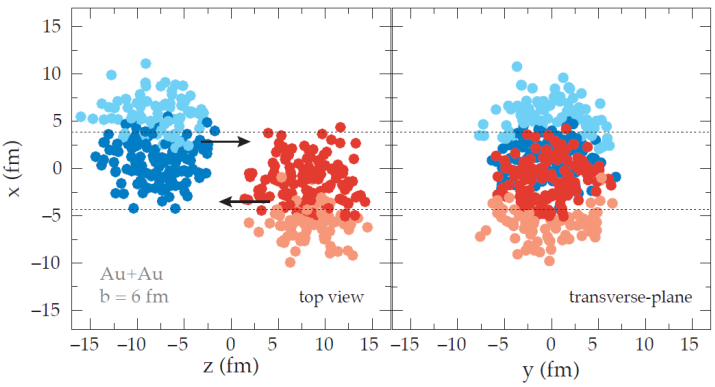

Figure 4.3: Colliding nuclei from two different perspectives. Due to the finite impact parameter b = 6 fm, the nuclei are not overlapping completely. Spectators are nucleons without interactions. They are marked by paler colors.

A comparison of the particle production for different centralities allows to trace physical effects dependent on the track multiplicity per event. Considering the event activity helps to obtain more precise results on particle production.

Fig. 4.3 shows two colliding nuclei and sketches the impact parameter b, that describes the distance of the collinear ion trajectories. A smaller impact parameter corresponds to a larger overlap area resulting in a high particle multiplicity in the detector acceptance. Consequently, a higher number of measured particles is correlated on average to a more central event. In the Au+Au beam time the PT3 (see section 2.4.3) with a minimum of 20 hits measured with TOF was used as minimum criteria for event selection.

One of the approaches to model the particle multiplicities of two colliding nuclei is the *Glauber Model* [137]. Its basic assumption are that all nucleons travel on straight trajectories throughout the collision. Each nucleon is expected to move as a straight line and is excited due to the collisions. This assumption is valid at low collision energies, since the Glauber model results agree with those obtained from Au+Au collisions at $1.23A$ GeV simulated with UrQMD. Every nucleon that had at least one collision is called wounded or participating nucleon. Nucleons that collided are tagged as wounded nucleons, while all others are tagged as spectators (see Fig. 4.3). A comparison of the model results to data helps to connect the multiplicity in a single event to its centrality.

For the centrality estimation in Au+Au data, at first the impact parameter is generated randomly according to a probability distribution. In the following, nucleons inside the nucleus are generated randomly according to the radial density distribution (e.g. *Woods-Saxon* shape). The repulsion inside a nucleus is modeled by requiring a minimum distance between each nucleon. During the collision step, a check, whether a reaction with another nucleon took place, is executed. In the final step, quantities like the number of wounded nucleons or number of binary collisions are extracted. But those quantities are not directly measurable and therefore called *pseudo-observables*. In any case, using the assumption that the particle production scales monotonically to those observables, one can use the number of participants in convolution with a particle production model to calculate the multiplicity distribution.

As a result, the reaction centrality is obtained in dependence of the impact parameter (see Fig. 4.4 (left)) [138]. But, due to the limited number of particles the different centrality classes

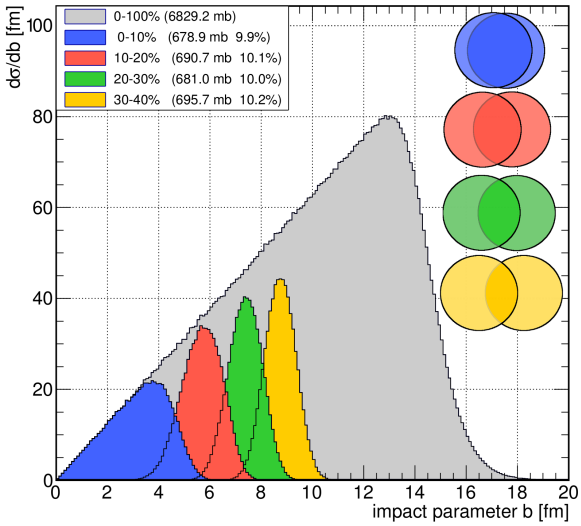

Centrality class [%]	Range [META hits]
0–10	160–250
10–20	121–160
20–30	88–121
30–40	60–88

Figure 4.4: Left: The impact parameter distributions for Au+Au minimum bias collisions and 10% centrality classes are shown. The overlapping circles indicate an average overlap between two nuclei of events from the corresponding centrality class. **Right**: Relation of centrality class to number of META hits.

are overlapping. Anyhow, 10% centrality classes are separated well enough to analyze centrality dependent trends of various physics observables. In order to define the centrality classes in experimental data, the impact parameter must be related to a real observable, e.g. number of particle tracks, number of META hits or hits in the forward wall detector. All three observables are applied as centrality estimator, but the number of META hits is the most precise and therefore chosen for centrality estimation in this analysis (see Fig. 4.4 (right)).

4.4 Preselection of tracks

During the track reconstruction, detector hits in all systems were assigned to track candidates and stored in DST files (see section 3.1). In this procedure, all matching candidates were combined and the usage of a single MDC segment for multiple track candidates was allowed. For that reason, a large number of combinations is available. The aim is to reject fake matches and select only true tracks, for which reason the track parts are only allowed to be used once. In order to reject fake matches of detector signals, track candidates using the same detector hits are sorted by their Runge-Kutta quality χ^2_{RK}. Finally, only the candidate with the best matching quality (χ^2_{RK}), out of all candidates using the same track part, is chosen. In addition, selection criteria can be applied to pre-select a specific particle species. For example, hadronic tracks can be removed in first place by conditions on physics observables, e.g. velocity β.

4.4.1 Track-sorting procedure

List Position	Inner seg. ID	Outer seg. ID	RICH Ring	Velocity
~~1.~~	1	1	✓	β= 0.60
~~2.~~	1	2	X	β= 0.93
3.	1	1	✓	β= 0.98
4.	1	3	✓	β= 0.91

Figure 4.5: This is an example list that shows how the track sorting criteria modify the chosen track. Requiring a RICH ring and a velocity $\beta > 0.9$, removes the first two candidates. Out of the remaining two, only the one with better quality (no. 3) is used in further analysis.

Every track candidate is required to have an inner and outer MDC segment with a successful Runge-Kutta fit as well as a META hit. However, every inner MDC segment can be used for multiple track candidates by combinations with different outer MDC segments. All track candidates sharing the same inner MDC segment are sorted in a list by track quality χ^2_{RK} (see Fig. 4.5). χ^2_{RK} is a good measure of quality since it provides information whether the segment combination is well described by the particle trajectory through the magnetic field. Since the usage of every track hit is allowed only once, solely the first track of the list is chosen. This list is modified by removal of candidates due to application of additional requirements to the track properties. There exists a standard set of selection criteria for electrons and hadrons. Those criteria limit the velocity to $\beta > 0.9$ and the matching in the META detectors in direction along the rod (`MetaQa` < 3). Furthermore, the track position of the electron or positron candidate is required to match with the one of a RICH ring. As a consequence, the number of candidates in the list is reduced and therefore rearranged. Finally, the track candidate at the top of the list is chosen as particle candidate (see Fig. 4.5).

4.4.2 Impact of track sorting on simulated and experimental data

The impact of the track sorting in experimental and simulated data is checked to estimate the quality of the simulation. Therefore, the track candidates are compared before and after applying the track sorting to simulated and to experimental data for the 40% most central events.

Before the track sorting, the fraction of tracks with certain input characteristics is plotted in Fig. 4.6 (left). In experimental data, 12% of tracks candidates not contain an outer segment, while 18% tracks do not comprise of a signal in the META detector. Only 2.6% of the tracks do have any signature in the RICH because most of the tracks are of hadronic origin. Less tracks (0.6%) contain RICH information obtained by backtracking (see chapter 5), since the RICH rings are allowed to be matched in a larger area ($8°$) around the track position.

The comparison of experimental to simulated data reveals differences in the occurrence of tracks with META signal in the order of 9%. Another discrepancy appears in case of backtracking information. Less track candidates have a ring information in simulation. A measure of the quality of simulation is provided by comparison of track quality (χ^2_{RK}) in experimen-

tal and simulated data which is presented for different centrality classes (see Fig. 4.6 (right)). The number of tracks with large χ^2_{RK} values in the most central events is enhanced. Due to the fact that more tracks complicate the track reconstruction, they enhance the probability of fake combinations. Consequently, the track quality depends on the particle multiplicity in the event. Furthermore, the simulation underestimates the number of tracks with large χ^2_{RK} values due to a lack of reproduction of cross talk in simulation. However, the region with small χ^2_{RK} values shows good agreement.

In order to investigate the track selection performance for electrons, the cuts on observables are applied and show a strongly reduced number of particle candidates per event in Fig. 4.7 (left). Besides the removal of events with an artificially high number of tracks, also the agreement between the number of tracks in simulation and experimental data improves dramatically. This allows to perform the analysis in simulated data in order gain a better interpretation of the analysis steps. The comparison of the fit quality of used to rejected tracks reveals a reduction of tracks with bad quality values Fig. 4.7 (right). However, the deviation between simulated and real data at high χ^2_{RK} values is still present for which reason an additional constraint of the quality value for further analysis is indicated (see section 7.2).

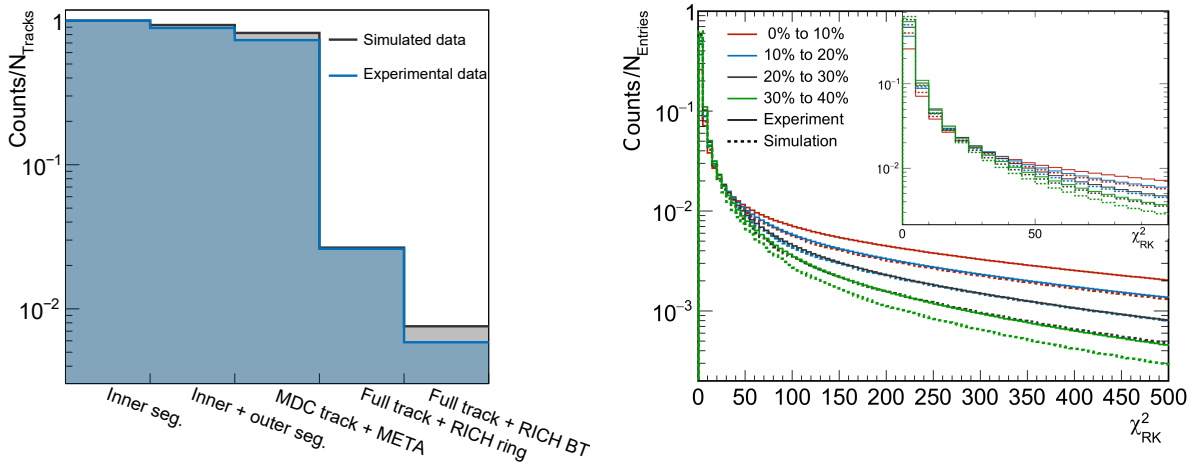

Figure 4.6: Left: Number of tracks with signal in each specific detector normalized to the number of all tracks with inner track segment. Results for experimental and simulated data are shown. **Right:** Quality of the Runge-Kutta track fitting (χ^2_{RK}) for simulated (dotted) and experimental (solid) data.

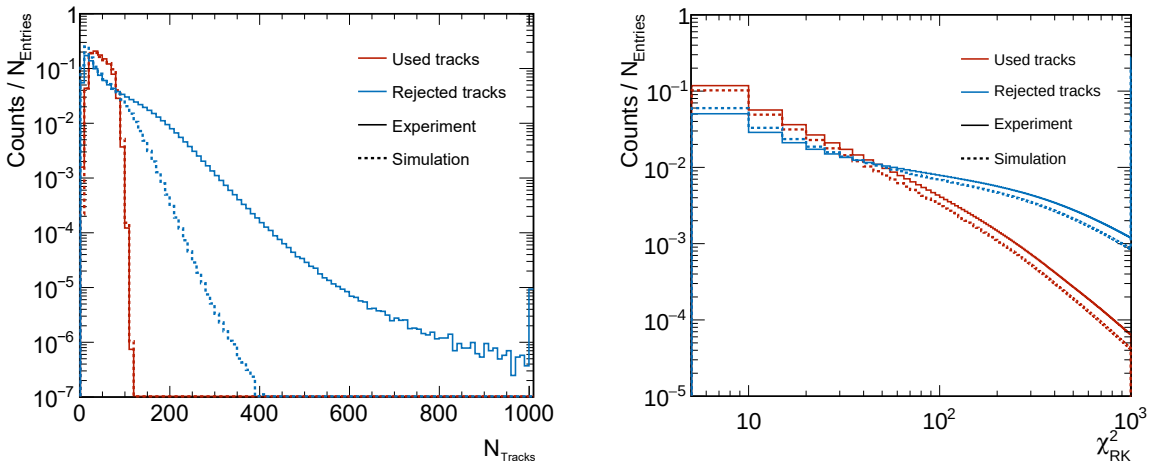

Figure 4.7: The number of tracks (**left**) and the quality of the momentum fitting χ^2_{RK} (**right**) for used and rejected tracks in simulated (dotted) and experimental data (solid). Both figures show the results before (blue) and after (red) applying track selection criteria.

Chapter 5

Backtracking for electron identification

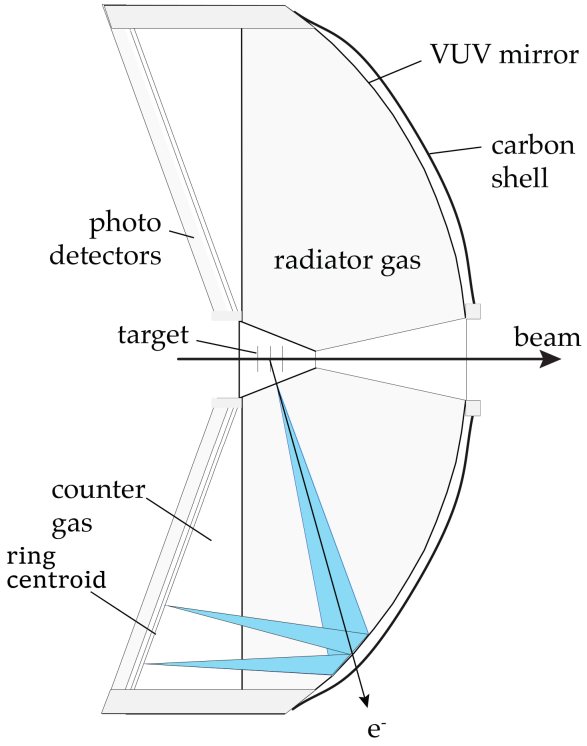

Figure 5.1: Side view of the RICH detector demonstrating the detection mechanism with backtracking. A e^- track emits Cherenkov radiation (blue) and the ring centroid can be estimated using the angular information reconstructed by the MDC chambers.

Measurements of dileptons are dominated by hadron tracks and suppressed by a branching ratio of $\approx 10^{-5}$ with respect to hadronic decay channels of vector mesons. Additionally, dileptons are produced below the elementary particle production threshold at SIS18 energies and therefore produced in approximately one out of 100 heavy-ion collisions only. An investigation of such rare probes requires a high efficiency electron and positron[1] identification and a proper background subtraction in order to obtain a high purity data sample. The actual electron identification with HADES is mainly based on the RICH detector (see section 2.3.1). As described

[1] In the further course denoted as electrons.

in section 3.6, electrons create ring distributed signals that are identified by a pattern search algorithm. Further particle reconstruction combines the measurements of the RICH detector with the MDC tracks. If the position of the ring centroid and a track match, this combination is considered as a electron candidate. This identification procedure was applied successfully in previous experiments and in the Au+Au beamtime [139]. Due to challenges of the high multiplicity environment in Au+Au collisions, possible improvements in efficiency and purity might be helpful. Another challenge for the ring finder is the identification of electron pairs with a small opening angle. Since rings start to overlap for opening angles smaller than 4°, the ring shape gets distorted. In this case, only one or even only one distorted ring is reconstructed and the electron partner will not be identified. This is one of the most dangerous sources of the combinatorial background.

Therefore, a new concept to improve ring finding by usage of tracking information, obtained from the inner MDC segment, has been developed. This concept is called *backtracking*. In this approach, the track position is used to predict regions of interest in which the RICH response is evaluated. This method is expected to enhance the electron identification efficiency, due to decreased degrees of freedom by fixing the ring position. Moreover, the reconstruction efficiency for pairs with small opening angles should improve since with this approach, instead of one, two tracks can be identified as electrons and used to reconstruct the electron pair.

5.1 Concept

Instead of using the RICH detector as an isolated system, backtracking uses information from tracking and time-of-flight detectors in HADES for electron identification. Before the electron signal search in the RICH, criteria on the specific energy loss measured in the drift chambers and the velocity measured by the time-of flight detectors are applied to preselect electron candidates. Only for selected electron candidates, the position information provided by the tracking detectors is used to estimate the position of a possible signal in the RICH (see Fig. 5.1). The *region of interest* (ROI) in which photon hits are expected is defined and compared to the RICH response. An analysis of RICH hits in the region interest allows the identification of good electron candidates.

5.2 Implementation

5.2.1 Candidate preselection

The main challenge for the electron identification with backtracking is the contamination by hadrons. Since the calculation time of backtracking information increases linearly with the number of tracks, the performance worsens significantly with high track multiplicity. Moreover, also

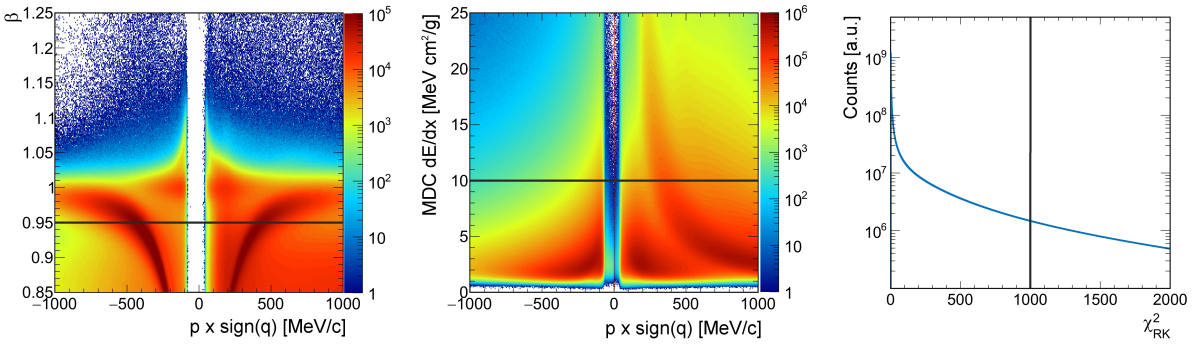

Figure 5.2: Observables for backtracking candidate preselection. The particle velocity (**left**), the energy loss in the drift chambers (**center**) and the Runge Kutta fit quality (**right**) values are restricted to preselect electrons. The lines indicate the chosen thresholds.

the probability of wrongly identified hadrons increases with the track multiplicity, since random matches of hadrons to background hits in the RICH become more likely.

This problem is solved by a pre-selection of good electron candidates. Different particle species are separated by their velocities. Electrons have a velocity close to that of light (i.e. $\beta \approx 1$) while the velocity of hadrons, at the same momentum, is smaller than the one of the electron (see Fig. 5.2 (left)). For the backtracking procedure, all track candidates with $\beta >$ 0.95 (0.93) are chosen for the RPC (TOF) system. Also, the specific energy loss measured in drift chambers is larger for hadrons and therefore constrained to values below 10 (see Fig. 5.2 (center)). In order to have a good track quality, an upper limit of 1000 for the χ^2_{RK} of the Runge-Kutta fit is required as well (see Fig. 5.2 (right)). Track candidates with larger χ^2_{RK} can only be created by fake matches and are therefore rejected. To avoid the rejection of good candidates, the multiple usage of inner and outer MDC segments is allowed. In summary, a rejection of obvious hadrons by preserving almost the full electron signal is achieved.

5.2.2 RICH pad plane position determination

The advantage of backtracking is the application of a given MDC track position to predict a region of interest for photon hits on the RICH pad plane. The track position is provided by the Runge-Kutta tracking algorithm. The track is used to calculate the point of intersection with the mirror of the RICH detector, which is translated to a position on the RICH pad plane (see Fig. 5.1). The track parameters at the interaction vertex and its position along the beam axis is needed for a precise position determination of the region of interest on the pad plane.

5.2.3 Parametrization of the region of interest

A starting point for the ring signature search was given by the pad plane position estimated with the MDC track. However, the region in which photon hits are expected is not yet determined and requires a parametrization of the ring radius (R) and width (σ). This is done using simulated

electrons that create Cherenkov radiation. The Cherenkov photons are emitted in a fixed polar angle relative to the particle's velocity vector, imaged as rings at the focal plane. Due to the construction of the experimental setup, rings are not perfectly circular and vary in radius and width. These effects are caused by the following detector parts:

- **Segmented target:** The target has a length of ≈6 cm. Due to different reaction vertices the source of emitted electrons is not always perfectly centered in the focal point of the RICH mirror. Consequently, the ring shape is modified as a function of the vertex position.

- **RICH mirror:** Deviations from a perfectly spherical mirror generate a smearing of the photon distribution. Therefore, the width of the photon distribution increases. However, this effect should be small.

- **Pad plane:** The most important reason for distortion of rings is the sector-wise planar RICH pad plane (see Fig. 5.3). Due to this approximation, ring shapes become more elliptical. This effect is partially reduced by a tilted pad plane and rectangular shaped pads of varying sizes (see section 2.3.1). However, this effect is still present and more pronounced at larger polar angles (see Fig. 5.4).

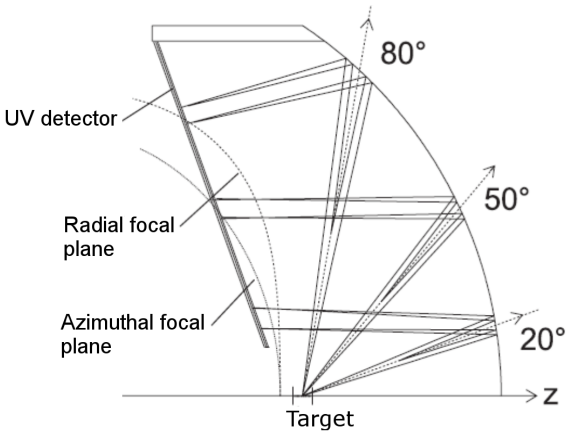

Figure 5.3: Electron or positron tracks (arrows) and their Cherenkov radiation is displayed schematically. The side view includes the ideal focal planes to display spherical rings on the pad plane. In addition, the simplified flat plane is shown. Large differences between both pad planes result in distorted rings [140].

As a consequence, the region of interest is determined using a ring parametrization depending on a vertex position, polar angle and azimuthal angle. Furthermore, the parametrization should be described by a small set of parameters and be flexible enough to adapt for changes in the future, e.g., modified target position or RICH geometry. Due to internal symmetry, the parametrization has to be done only for one sector and can be adjusted to all the others.

As a starting point, simulated electrons are transported through GEANT and the pad plane position of their Cherenkov photons is investigated. Moreover, the electron sources are divided in different bins of reaction vertex, polar angle and azimuthal angle. In order to get a precise knowledge about the rings shapes, photon distributions of many rings from the same angular and vertex region are overlayed. The resulting photon distributions are presented in Fig. 5.4 and demonstrate the distortion of the ring shapes with growing polar angle (Θ). In order to

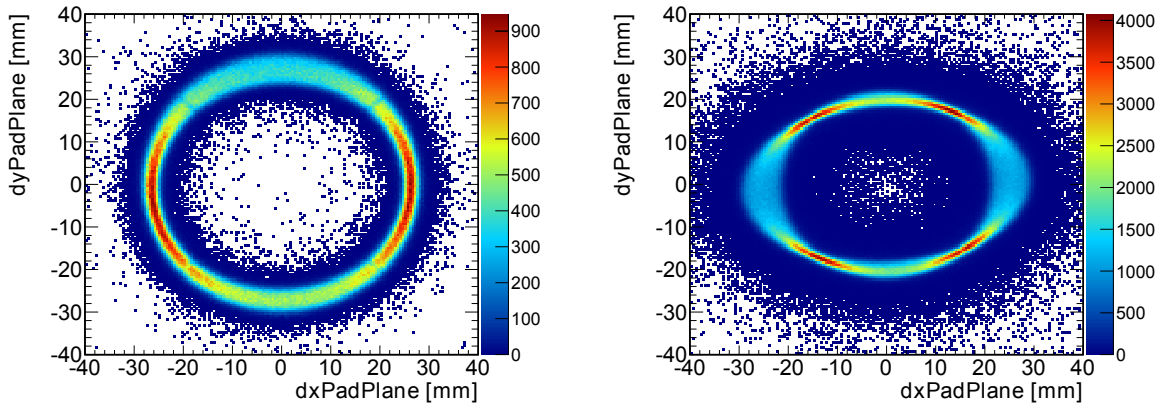

Figure 5.4: Ring shapes generated by overlaying photon hits from rings generated with GEANT. The **left** ring is located at a polar angle of $\Theta \approx 31°$ and the **right** is located at a polar angle of $\Theta \approx 77°$ while their azimuthal position is in the center of a RICH sector. A comparison reveals deformations of rings at high Θ.

simplify the analysis, the photon distributions are converted to a linear representation by the application of formulae 5.1 and 5.2:

$$dx \geq 0 : \begin{pmatrix} \alpha \\ r \end{pmatrix} = \begin{pmatrix} \arctan(\frac{d_y}{d_x}) + 90 \\ \sqrt{d_x^2 + d_y^2} \end{pmatrix} \tag{5.1}$$

$$dx < 0 : \begin{pmatrix} \alpha \\ r \end{pmatrix} = \begin{pmatrix} \arctan(\frac{d_y}{d_x}) + 270 \\ \sqrt{d_x^2 + d_y^2} \end{pmatrix} \tag{5.2}$$

where *dx*, *dy* is the relative position to the ring center in Cartesian coordinate system, α is the inscribed angle and *r* the radius in the circular representation. An offset factor of $90°$ and $270°$ is added to obtain a function from $0°$ to $360°$. In the r and α representation, changes in the ring radius and width as a function of α become more obvious.

The aim is to obtain a polynomial function that is able to describe modifications of the radius and width as a function of the polar and azimuthal track angles. Therefore, an approach focusing only in one inscribed angle ($\Delta\alpha = 8°$) bin is used (see Fig. 5.5). The radius and width is plotted as a function of

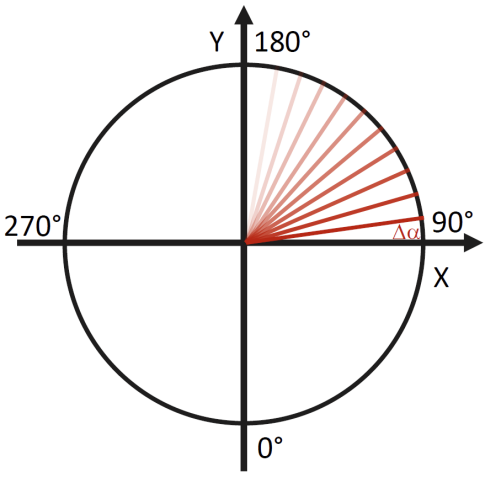

Figure 5.5: Schematic division of the ring in inscribed angle regions of $8°$. The red lines in the upper right part of the ring demonstrate the size of the inscribed angle regions.

polar and azimuthal angles in Fig. 5.6. In total $45 \times 15 \times 2 = 1350$ polynomial 2D functions are applied to describe all 45 angular bins, 15 vertex bins, ring radius and ring width.

All functions contain terms as a function Θ and Φ and the correlation of both. The correlation terms are needed to have a proper agreement between the function values and the data. The radius distribution is very smooth and has no strong modification for different inscribed angles and is described by a function with eight parameters (see equation 5.3). A description of the width values is more complicated since for different inscribed angle bins changes are much larger. In total 13 parameters are required to assure a good description in all regions (see equation 5.4). The following functions are used to describe the radius and width of the ring:

$$R(\Theta, \Phi) = a_0\Theta^3 + a_1\Theta^2 + a_3\Theta + a_4\Phi^2 + a_5\Phi + \Phi(a_6\Theta^2 + a_7\Theta) + a_8, \tag{5.3}$$

$$\sigma(\Theta, \Phi) = b_0\Theta^3 + b_1\Theta^2 + b_3\Theta + b_4\Phi^4 + b_5\Phi^3 + b_6\Phi^2 + b_7\Phi + \Phi * (b_8\Theta^2 + b_9\Theta + b_{10}) + b_{11}, \tag{5.4}$$

where a_n and b_n are free fit parameters.
Finally, both distributions are well described and the errors are obtained by comparing the mean deviation between the values estimated with $R(\Theta, \Phi)$ and $\sigma(\Theta, \Phi)$ and the data values. The average deviations are chosen as errors and result in $\Delta R \approx 0.2$ mm for the radius and $\Delta\sigma \approx 0.15$ mm for the width. Large deviations at the sector edges are caused by low statistics and are therefore negligible. The error of the photon search in a 3σ interval around the radius sums up to $\Delta Tot = \Delta R + 3\Delta\sigma = 0.65$ mm which is far below the pad size and will allow a precise region of interest determination.

Since the size of the errors is only 10% of the pad size, it allows to describe the parameters a_n of $R(\Theta, \Phi)$ and b_n of$\sigma(\Theta, \Phi)$ analytically to reduce the number of parameters that need to be stored. However, this will increase the errors for the calculated radius and width slightly. Therefore, every parameter a_n and b_n is plotted as a function of the inscribed angle bin (α) and vertex (z) (see Fig. Fig. 5.7). As a result, one two-dimensional distributions for each parameter is obtained. In total, eight distributions for the radius and 13 two-dimensional distributions for sigma need to be described.

Those distributions are fitted by a two-dimensional polynomial function (see Fig. 5.7). This results in eight functions with 20 parameters each to describe the radius $f_R(\alpha, z)$ and 13 functions with 20 parameters each to describe the ring width $f_\sigma(\alpha, z)$. Finally, the error is estimated, by comparing the radius and width from data to the radius and width estimated with $R(\Theta, \Phi)$ and $\sigma(\Theta, \Phi)$, for which the parameters a_n and b_n were estimated using the functions $f_R(\alpha, z)$,$f_R(\alpha, z)$. A check of the error shows that $\Delta\mathrm{Tot} \leq 1$ mm and thus still much smaller than the pad size itself. This justifies the description of R and σ by analytical functions.

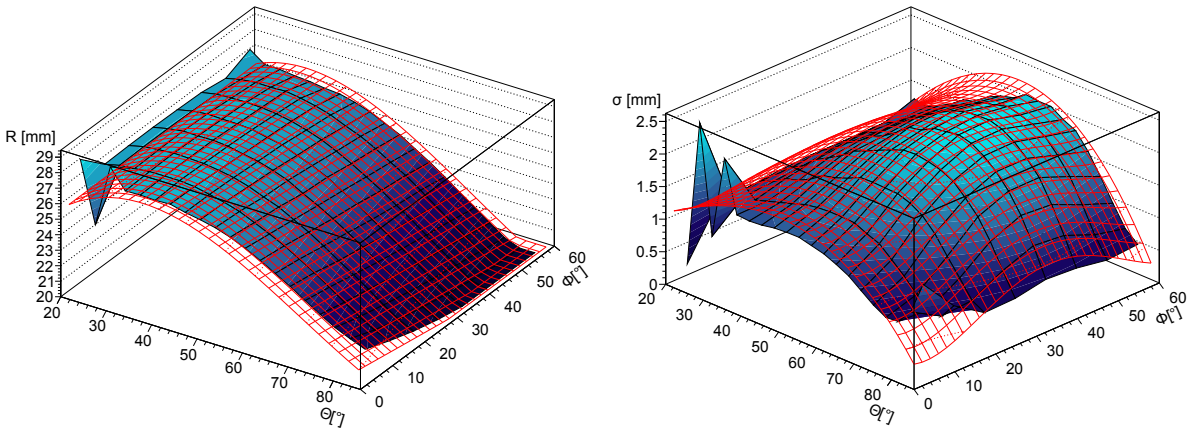

Figure 5.6: First and second moment of the UV photon's radial distribution in a given angular region of the ring circumference ($\Delta\alpha = 8°$), as a function of the location of ring center. Both distributions show a smooth gradient which allows a fit by a two-dimensional polynomial function. Deviations at the edges result from large statistical errors or edge effects of partially identified rings.

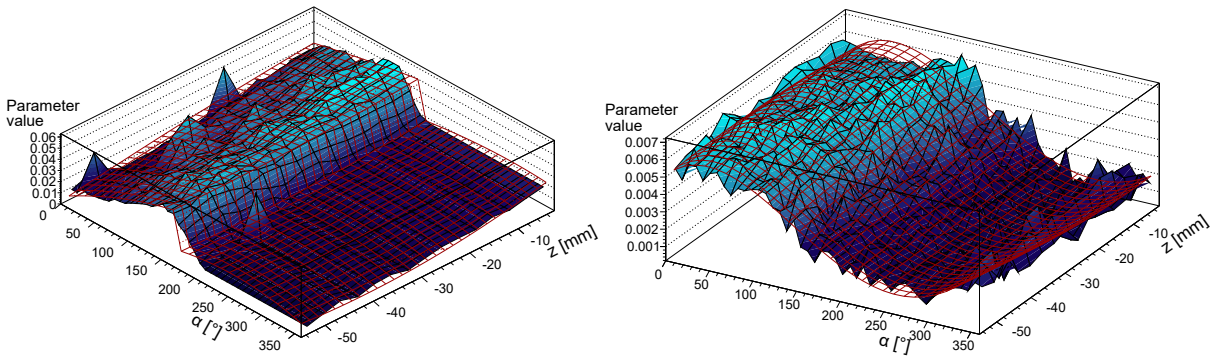

Figure 5.7: Example of a two-dimensional parameter fit for one parameter describing the radius (**left**) and width (**right**). The largest errors appear on steep rises of one parameter but are still reasonable.

5.2.4 Ring feature extraction

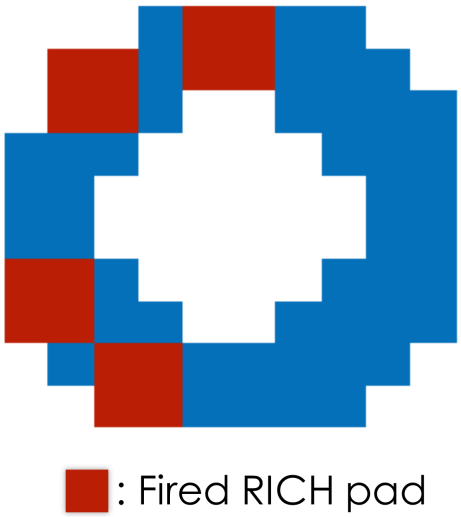

Figure 5.8: Evaluated region of interest on the RICH pad plane (blue). A comparison of hit position with the region of interest is performed for the basic electron candidate search.

After determining the region of interest, a method to identify good rings is needed. In the beginning, regions of interest are evaluated using the parametrization based on simulated rings (see section 5.2.3). The region of interest is determined as $R \pm 3\sigma$. Those regions are transformed into RICH pad addresses. In order to avoid pad gaps, which might appear if the region of interest is at the edge of a pad, additional smoothing is applied. Finally, the region of interest is compared to the fired RICH pads (see Fig. 5.8). Subsequently, fired pads matching with the region of interest are used to estimate meaningful observables for electron identification (see section 5.4).

5.3 Software design

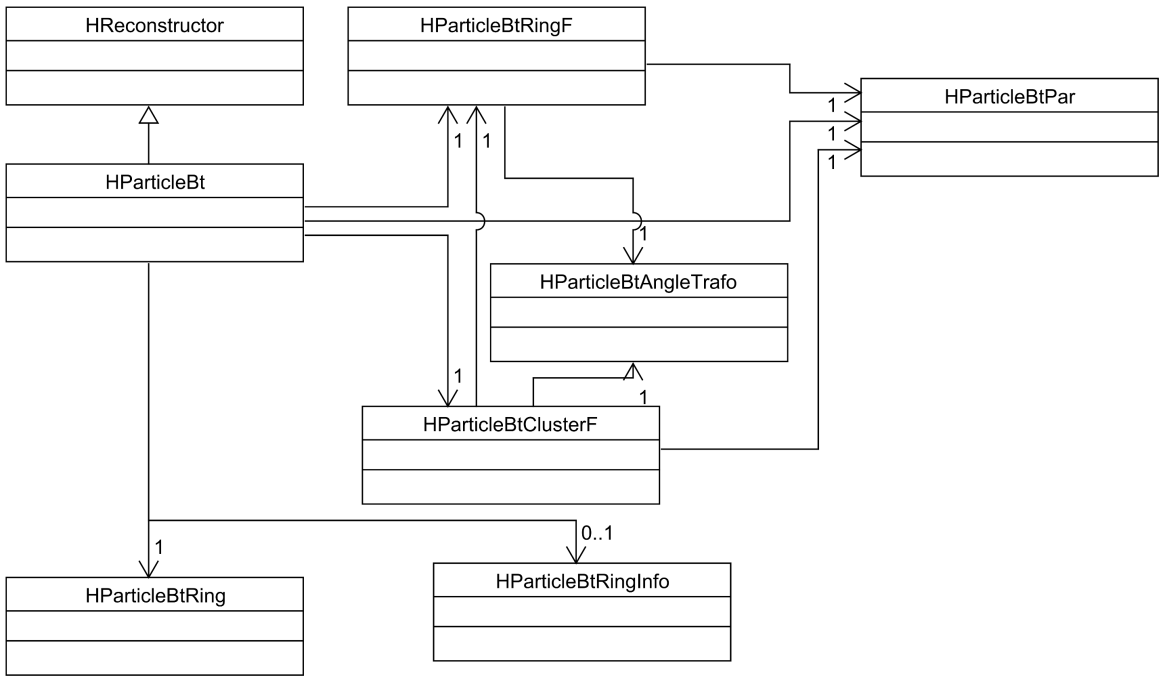

Figure 5.9: UML diagram of classes used by the backtracking procedure. `HParticleBt` performs the main task by looping over the particle candidates and calling sub-tasks.

The goal is to provide, in addition to the RICH ring finder, refined observables for electron identification with the RICH. Therefore, backtracking has to be integrated in the HYDRA analysis framework [105]. A major requirement is a flexible algorithm which can be easily adapted and maintained for future beamtimes, where the detector setup might be slightly different. Also the events are different in their track candidate and RICH hit multiplicity, which requires flexible handle regarding data storage. As output, a set of observables with a good ring identification power is needed. Furthermore, the code should allow for future extensions or improvements of the procedure and the output observables. The understanding of electron signal properties is important. For this reason, information for visualization should be provided as well.

In general, functions are grouped by their tasks and stored in various classes. `HParticleBt` is the main class to manage the backtracking procedure. It is inherited from `HReconstructor` to allow a simple integration into the DST production task list (see Fig. 5.9). The tasks which access the RICH detector information and estimate the region of interest are summarized in `HParticleBtRingF`. This class stores the information of pads matching with the region of interest. Often, those pads are grouped with other pads, so-called clusters. The calculation of cluster information itself is executed in `HParticleBtClusterF`, which obtains all necessary input information from the ring finder class. Calculations for cluster properties are done stepwise for each region of interest and the results are stored in vectors to be flexible regarding the number of tracks or clusters. All parameters needed for backtracking are accessible via `HParticleBtPar`. Since the estimation of the RICH pad plane position from the track position is complex and used by `HParticleBtRingF` and `HParticleBtClusterF`, an additional class `HParticleBtAngleTrafo` stores the methods containing geometrical transformations and corrections. After the evaluation of the fired pads in the region of interest, a check for a noisy RICH sector is performed. If an event contains a noisy RICH sector and a track with backtracking information in the same sector, the event will be skipped. In case no candidate is identified in the respective sector, all candidates with backtracking information are stored. The information is stored in `HParticleBtRing` and included in the standard DSTs. Additionally, `HParticleBtRingInfo` stores the information for visualization of rings, but it is only stored if the output is requested specifically by the user.

5.4 RICH response evaluation

A proper electron identification needs powerful observables to distinguish between an electron signal and background hits. The RICH response is evaluated in multiple steps to provide meaningful observables for electron identification.

1. A search of pads matching with the region of interest is executed (see section 5.4.1).

2. Clusters are estimated, by using the fired pads matching with the region of interest (see section 5.4.1).

3. The local maxima for each cluster are searched and their photon position is estimated with a cluster fit. (see section 5.4.2)

4. A ring quality is estimated utilizing the cluster positions. (see section 5.4.3)

5. The sharing of local maxima with other regions of interest is evaluated to identify overlapping rings (see section 5.4.4)

All of those steps and the extracted observables[1] will be explained in detail in the following sections.

5.4.1 Sum of pads and charge

The starting point for the RICH response evaluation is the comparison of the region of interest with fired RICH pads. However, the amount of the measured pads and charge per candidate varies since the photon emission and its signal amplification is a statistical process. In general, pads created by noise have on average lower charges than the ones created by Cherenkov photons. This helps separating background from signal measurements. Pads above the charge threshold of $q > 65$ a.u. provide the best separation between signal and background and are thus chosen as minimum charge threshold for pads.

Often, measured photon signals do not only consist of a single pad but form *clusters* (see Fig. 5.8). Therefore, clusters are identified by searching and grouping adjacent pads matching with the region of interest. In addition, pads outside the region of interest, but adjacent to pads matching with the region of interest, are added to the cluster as well.

Based on the obtained RICH response, observables are constructed. The sum of pads and charge in the region of interest ($\texttt{N}_{\text{BT Pads ROI}}$ and $\texttt{Sum}_{\text{BT Q ROI}}$) as well as the sum of pads and charge of clusters matching with the region of interest ($\texttt{N}_{\text{BT Pads Cluster}}$ and $\texttt{Sum}_{\text{BT Q Cluster}}$) is estimated. In addition, the number of clusters is counted and provided by $\texttt{N}_{\text{BT Cluster}}$.

5.4.2 Number of local maxima

The clusters matching with the region of interest were identified in the previous section. Their size reaches up to four pads per cluster mostly, but some clusters are much larger (see Fig. 5.10 (left)). The abundance of large clusters decreases as a function of their size but the number of large clusters is still above the expectation (see Fig. 5.10 (right)). Regarding to a previous investigation, clusters should have sizes up to three pads per cluster at maximum [136]. An explanation of such clusters are multiple photon signals merging to one large cluster. In that case, multiple local maxima per cluster (*seed pads*) are expected. Consequently, a local maxima search will be executed and the position of the photon will be estimated by a cluster fit.

[1] store in `HParticleBtRing` category

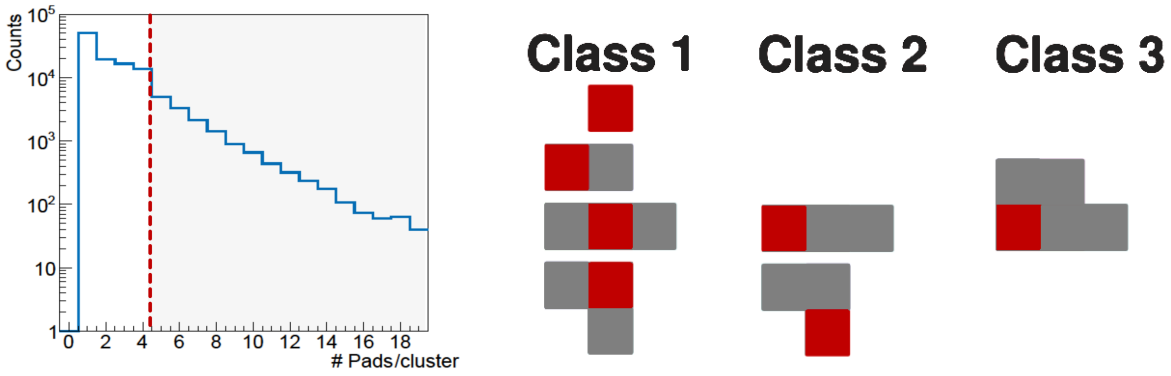

Figure 5.10: Left: Measured cluster sizes in the Au+Au beamtime. All clusters right to the red line can not be explained by single photon clusters. **Right:** Typical cluster shapes that are expected to be measured by the RICH detector. The red color indicates the pad with the maximum charge. Class 1 clusters are produced by single photons while class 2 clusters are produced by two close photons and Class 3 clusters are produced by more than two photons.

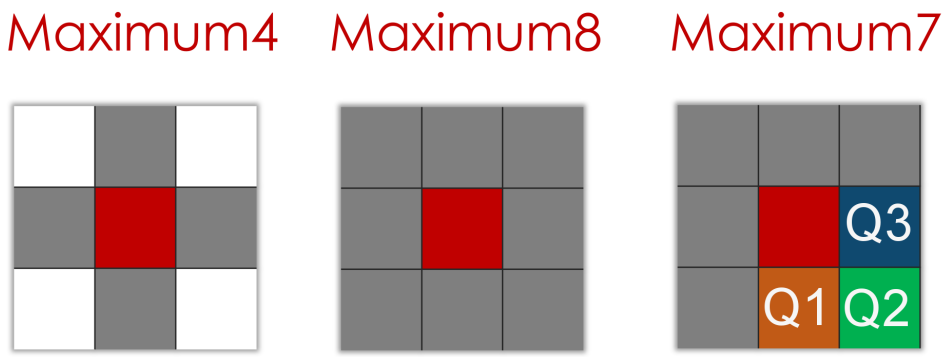

Figure 5.11: Search masks for the maximum identification criteria. The red pad corresponds to the position of the seed pad. The charge of the seed pad has to be larger than the charge of every gray pad (in case of Maximum4 and Maximum8).

For the local maxima identification, a search mask to scan the identified clusters is used. Three different search masks are shown in Fig. 5.11 and demonstrate the requirements of the different search methods:

- **Maximum8:** Requires a seed pad that measured a charge larger than in every of the 8 surrounding pads. This method is the most secure. However, neighboring maxima will not be identified.

- **Maximum4:** Requires a seed pad that measured a charge larger than in every of the vertically or horizontally adjacent pads. This method allows maxima that are diagonally adjacent. However, vertically or horizontally adjacent maxima will not be identified with this method.

- **Maximum7:** Maximum7 comprises all maxima identified as Maximum4. In addition, this procedure searches for additional diagonally adjacent maxima. This method is based on the assumption that the charge shared to vertically or horizontally adjacent pads is always larger than to diagonally adjacent pads.

  In case a Maximum4 is identified and the charge of a diagonally adjacent pad is larger than the one from a vertically or horizontally adjacent pad, an additional Maximum is expected. For example, Q1 is a maximum if the condition $Q2 > Q3$ is fulfilled (see Fig. 5.11). However, the charge of Q1 has to be larger in every surrounding pad besides the local maximum previously identified with Maximum4.

Since only the Maximum7 search mask is able to identify all adjacent maxima, it is applied for maximum identification. Up to now, those maxima are only defined by their pad position. A more precise maximum position provides further information for the determination of the quality of the ring signature.

This position is estimated by fitting a 2D Gauss function to each local maximum in the cluster. Hence, every maximum is described by a function having five parameters. In order to the reduce the number of parameters, the width in x and y direction of the 2D Gaussian function is restricted. The width is obtained by a fit of 1D Gaussian functions to single photon clusters that have only one local maximum. In addition, the height of the Gauss peak is restricted to values close to the charge of pad with maximum charge. Finally, only the x and y position of the maximum are left as free parameters. Their only restriction is to be inside the maximum pad range.

For the cluster fit, a combined function of one Gaussian distribution per maximum is fitted to the cluster distribution in order to evaluate more precise maxima positions (see Fig. 5.12). The resulting maximum position, obtained by the fit within a RICH pad, indicates structures instead of a smooth distribution (see Fig. 5.12). This indicates a limitation of the fit resolution due to a systematic error of the fitting procedure. Therefore, the position resolution is assumed to be the distance of half a pad.

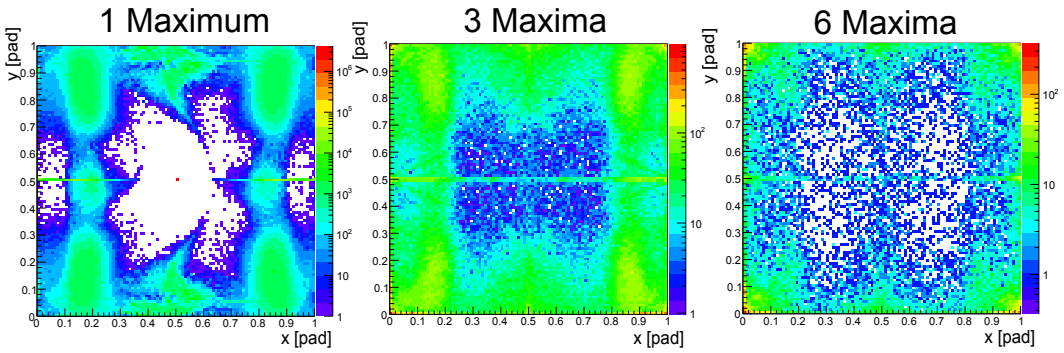

Figure 5.12: *x* and *y* position distribution inside the seed pad obtained from the the cluster refit. The distribution gets more continous for a larger number of maxima per cluster. Based on the worst case, a position resolution of a half pad size is determined for the position of the maximum.

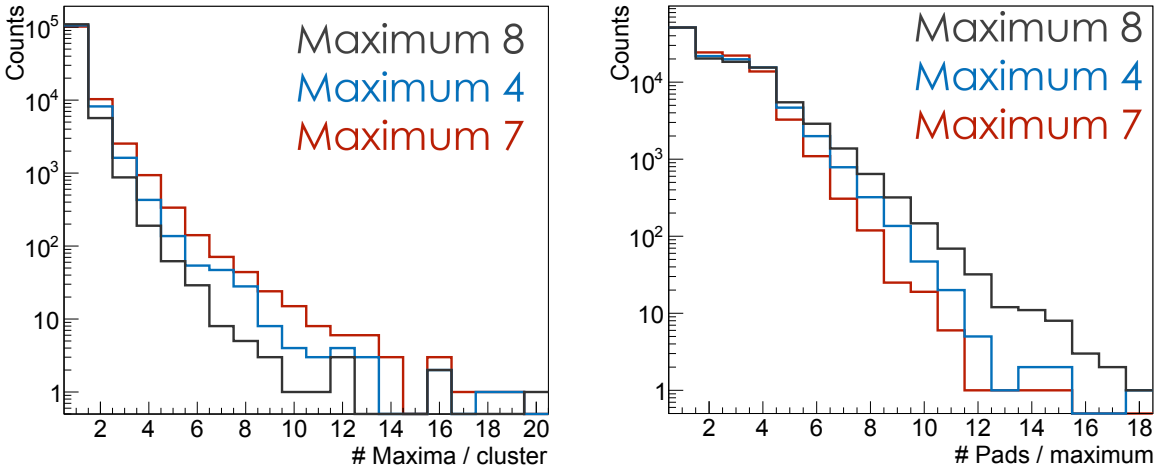

Figure 5.13: Left: Comparison of the number of pads per local cluster maximum between the different approaches. Both plots demonstrated that Maximum7 method is able to detect more maxima. **Right:** Comparison of the number of cluster pads per local maximum for three different local maxima search approaches.

This resolution must be considered if the relative position to the region of interest is estimated, Also the width of the photon distribution needs to be considered, since the photon distribution is smeared. Consequently, the deviation of the maximum position from the most likely photon position (Δx^2 and Δy^2) is normalized with the width of the photon distribution (σ_{geom}) and the local maximum position resolution (σ_{res}) to obtain a weighted distance measurement (σ):

$$\sigma = \frac{\sqrt{\Delta x^2 + \Delta y^2}}{\sqrt{\sigma_{geom}^2 + \sigma_{res}^2}}, \tag{5.5}$$

As output, the number ($\mathtt{N}_{\mathrm{BT\ \ Maxima}}$) and charge ($\mathtt{N}_{\mathrm{BT\ \ MaximaQ}}$) of local maxima per region of interest is provided. Moreover, the position resolution allows to sum up maxima that are only 3σ region from the most likely ring position ($\mathtt{N}_{\mathrm{BT\ \ Maxima\ \ 3}\sigma}$). The approach using local maxima is successful and reduces the cluster sizes to more reasonable values (see Fig. 5.13). However, there are still clusters with a large number of pads. Those clusters are generated from background and are excluded by removing clusters with more than seven maxima.

5.4.3 Ring quality

MDC tracks can be matched to large numbers of fired pads or maxima of background hits. Hence, further observables describing the ring quality are needed. In total, three observables for ring quality estimation are presented in this section.

The first observable is based on the position of the local maxima relative to the region of interest (see section 5.4.2). The region of interest was reconstructed by determining the ring radius and the with of the photon distribution. A Gaussian function was assumed for the photon distribution. Consequently, the most likely photon position is at the position of the radius. The

distance between the local maximum and the most likely position is summed up quadratically and inserted in equation 5.6 to calculate the quality of the RICH response in the region of interest:

$$\chi^2_{BT} = \frac{\sqrt{\sum_{n=1}^{N} \frac{\sqrt{\Delta x^2 + \Delta y^2}}{\sqrt{\sigma^2_{geom} + \sigma^2_{res}}}}}{N}, \tag{5.6}$$

where N is the number of maxima per region of interest, Δx^2 and Δy^2 are the deviations in x and y direction respectively, σ_{geom} is the width of the photon distribution and σ_{res} is the resolution of the maximum position determination. A second approach of estimation of a ring quality checks the distances in x and y direction separately. In case of small momenta, the reconstructed track might differ from the real particle trajectory due to bending in the inner MDC chambers and multiple scattering. In that case, a common shift of maxima positions in one direction would be expected. Therefore, a new center position with minimized $\mathcal{X}^2_{BT}$ is calculated. The difference between the original and shifted ring center is used as an mean distance observable.

Another approach is to include the surrounding area in order to detect noise. Therefore, the `BT Pattern matrix` observable is introduced. For this observable, pads in a circular area with radius of eight pads around the ring center are summed up. The fraction of pads directly matching to the region of interest to the ones in the circular region is calculated:

$$\text{BT Pattern matrix} = \frac{\text{N}_{\text{BT Pads ROI}}}{\text{N}_{\text{Pads circ}}} \tag{5.7}$$

An application of these observables, reveals that the mean distance is not very powerful to distinguish between background and ring shifts. The pattern matrix and $\mathcal{X}^2_{BT}$ observables are more useful but are only efficient for rings with a large number of maxima.

5.4.4 Extension to double-rings

One of the motivations of backtracking is to improve the identification of close pairs with overlapping rings. Close pairs are typical for a electron pair resulting from conversion in the detector material. For those electrons, a small opening angle is characteristic. Additionally, they have low momenta. For this reason, it is likely that one partner was bend by the magnetic field out of the detector acceptance. Therefore, the conversion partner is often only partially reconstructed.

After the first iteration of the basic backtracking information, candidates with at least one fired pad and sufficient charge are declared as possible electron candidates. These electron candidates are selected to search for close neighbors. The search is restricted to an opening angle range of $4°$. The backtracking information is calculated for all partially reconstructed tracks within this range. These are tracks without META hit or missing outer MDC segment and META hit. An estimation of the overlap area of two rings (see Fig. 5.14 (left)) is given by the number of shared maxima and shared charge of maxima between the two regions of interest.

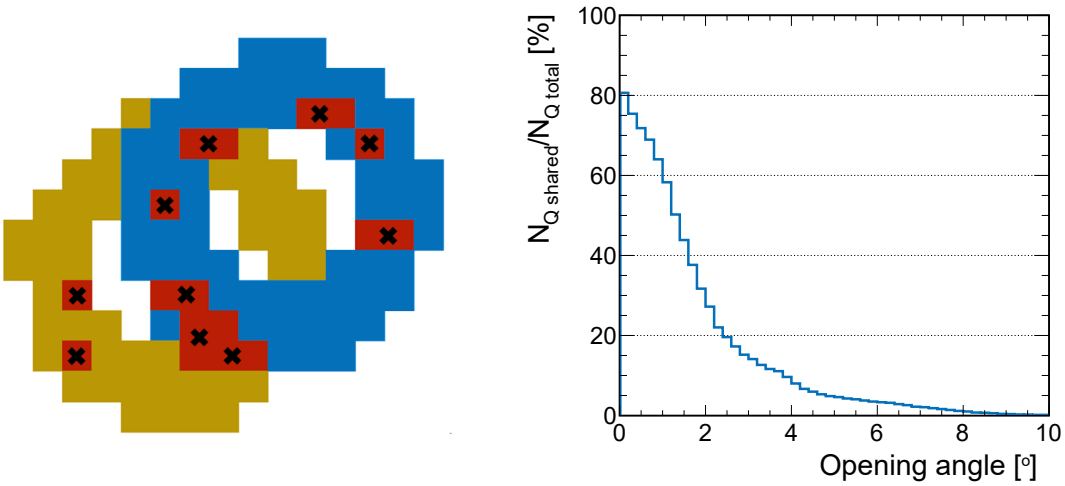

Figure 5.14: Left: Region of interests (blue, yellow) of overlapping rings. Fired pads are shown in red and maxima of clusters are illustrated by black crosses. Maxima that match with both prediction regions are counted as shared maxima. **Left:** Fraction of charge from local maxima matching to a region of interest of a close track.

The observables describe the number maxima ($\mathbb{N}^{\text{shared}}_{\text{BTMaxima}}$) and charge of maxima pads ($\mathbb{N}^{\text{shared}}_{\text{BTMaxQ}}$) that is shared with all close by tracks or track fragments. In addition, the number of maxima and charge of maxima pads shared to one specific track or track fragment is provided. Furthermore, only the number of shared maxima, within a 3σ range around the radius, with other tracks or one specific track is provided.

5.5 Summary and Outlook

The backtracking algorithm has been successfully integrated in the analysis framework HYDRA. The end user is able to apply backtracking information for electron identification based on the observables stored in DST files. The set of observables includes the ones used for single lepton identification and observables for close pairs. The observables for close pair identification are a unique feature of backtracking and are not provided by the standard RICH ring finder. In summary, the following output observables are provided by HParticleBtRing:

Single Observables

- $\mathtt{N}_{\mathrm{BT\ \ Pads\ \ ROI}}$
- $\mathtt{Sum}_{\mathrm{BT\ \ Q\ \ ROI}}$
- $\mathtt{N}_{\mathrm{BT\ \ Pads\ \ Cluster}}$
- $\mathtt{Sum}_{\mathrm{BT\ \ Q\ \ Cluster}}$
- $\mathtt{N}_{\mathrm{BT\ \ Cluster}}$
- $\mathtt{N}_{\mathrm{BT\ \ Maxima}}$
- $\mathtt{N}_{\mathrm{BT\ \ Maxima\ \ 3}\sigma}$
- $\mathtt{N}_{\mathrm{BT\ \ MaximaQ}}$
- $\mathcal{X}^2_{BT}$
- `BT Mean ring shift`
- `BT Pattern matrix`

Pair Observables

- $\mathtt{N}^{\mathrm{shared}}_{\mathrm{BTMaxima}}$ with other tracks
- $\mathtt{N}^{\mathrm{shared}}_{\mathrm{BTMaxQ}}$ with other tracks
- $\mathtt{N}^{\mathrm{shared}}_{\mathrm{BTMaxima}}$ with other track fragments
- $\mathtt{N}^{\mathrm{shared}}_{\mathrm{BTMaxQ}}$ with other track fragments
- $\mathtt{N}^{\mathrm{shared}}_{\mathrm{BTMaxima}}$ with other tracks (within 3σ)
- $\mathtt{N}^{\mathrm{shared}}_{\mathrm{BTMaxima}}$ with one specific track
- $\mathtt{N}^{\mathrm{shared}}_{\mathrm{BTMaxQ}}$ with one specific track
- $\mathtt{N}^{\mathrm{shared}}_{\mathrm{BTMaxima}}$ with one specific track (within 3σ)

The application of the observables has shown, that $\mathtt{N}_{\mathrm{BT\ \ Pads\ \ ROI}}$, $\mathtt{Sum}_{\mathrm{BT\ \ Q\ \ ROI}}$ and $\mathtt{N}_{\mathrm{BT\ \ Maxima}}$ are the best to identify a good RICH response. However, the other observables provide small improvements by rejection of fake matches of MDC tracks to RICH background hits. The pair observables were also succesfully tested. They become more efficient for overlapping rings with opening angles larger 2° since the rings below are nearly completely overlapping (see Fig. 5.14).

Furthermore, backtracking can be easily applied for future beamtimes since modifications like a different electron preselection can be introduced. The parametrization can be used in further beamtimes with the same geometry, but requires a reevaluation for the upgraded RICH detector. The planned upgrade of the RICH read out plane will change the inclination of the read out plane, pad size and number of readout pads. All modifications can be reproduced by new parameters. Due to the different inclination of the readout plane, ring shapes will become more elliptical. Since backtracking is independent from a certain pattern, it can be easily applied to identify more deformed rings because the search procedure is only based on the parametrized region of interest.

Chapter 6

Detector performance studies

A good agreement between simulated and experimental data is of importance, since simulated data is applied to correct for inefficiencies due to track reconstruction and particle identification. Once the events are reconstructed, the tracks can be applied to tune the digitizers of the sub detectors. Therefore, a measurement of the MDC layer efficiency is presented in section 6.1 and the results will be applied to improve the agreement between experimental and simulated data by adjusting the efficiency parameters of the MDC digitizers.

Furthermore, detector effects influence the creation of signal and background tracks. An investigation of those effects is important to identify changes in signal efficiency or the level of background contamination. For this reason, several studies concerning the RICH signal stability, signal and background characteristics and their implementation in simulation are conducted in section 6.2.

6.1 MDC layer efficiency

This chapter deals with the efficiencies of wire planes of the drift chambers, which are used for tracking in HADES. After a brief overview of the signal reconstruction with MDC, the data sample selection as well as the efficiency calculation of separate MDC cell layers is explained and the results will be discussed in the last section.

6.1.1 Particle detection mechanism in MDC

As explained in section 2.1.2, the MDC detector consists in total of four modules with one chamber per sector. Each chamber is filled with gas and consists of 13 wire planes forming six drift cell layers for track identification. The layers are arranged in different angular orientations (see Fig. 6.1). For particle identification, the gas inside a MDC chamber is ionized by traversing particles, which typically cross one cell per layer (see Fig. 6.2(left)). The energy loss within a cell of a traversing particle, is dependent of the track length in the cell. Hence, the deposited energy in a cell depends on the

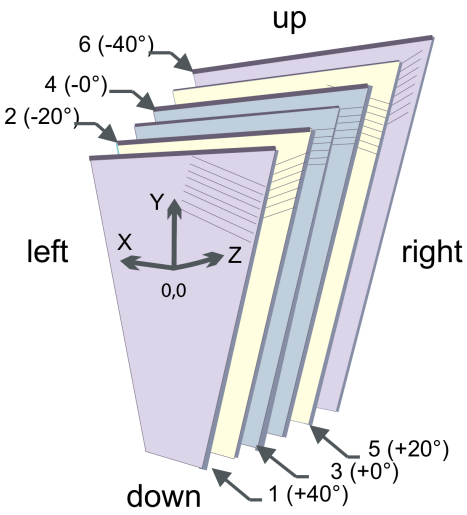

Figure 6.1: Orientation of wires for different MDC layers.

inclination of the track with respect to the layer plane. An inclination can also lead to tracks crossing two cells per layer in which a length dependent charge is measured.

The electrons, created by ionization, in the drift cell are pushed by the field, induced by field wires, towards the sense wire located in the middle of a cell while the electron signal is amplified by the gas. Due to the layer structure, the field gradients are varying as function of the x and y position inside the cell (see Fig. 6.2 (right)). This results in a position dependent electron and ion acceleration. Consequently, the drift times towards the sense wire vary with the topology of the track inside the cell. The charge is detected by the sense wire and registered as a signal in case the charge sum is above a pre-defined threshold. The measurement stops if the charge below this threshold. For particle reconstruction start and stop times are recorded and their absolute signal length *time-over-threshold* (ToT) is utilized for further hit reconstruction. The ToT depends on both, the track topology and the amount of ionization caused by the traversing particle. Hence, the ToT carries information about the specific energy loss of the particle and can augment particle identification, but is also an instrumental noise rejection.

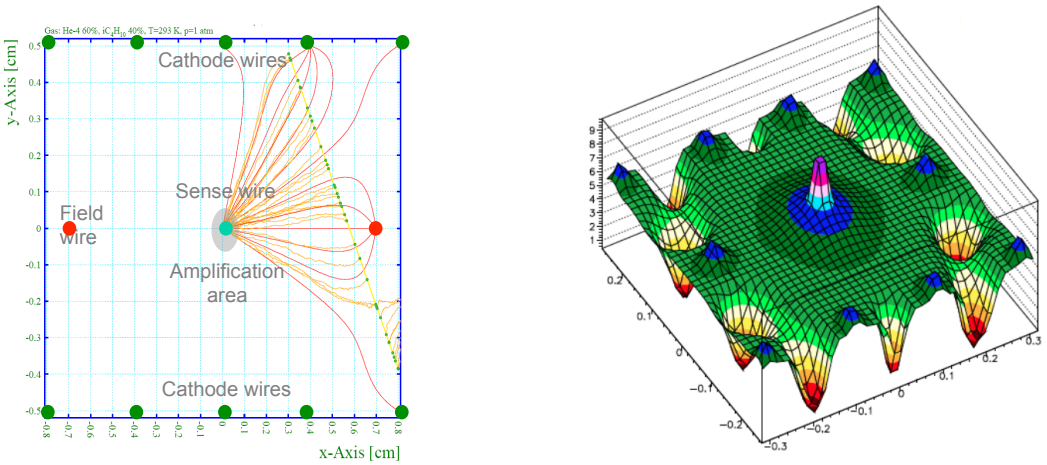

Figure 6.2: Left: Simulated electron signal within a drift cell simulated by Garfield [141]. The small green dots indicate the cluster origin. Drifting electrons (ions) are indicated by orange (red) lines. **Right:** Drift velocity in a cell filled with $ArCO_2$ as a function of position inside a cell. The field magnitude varies and depends on the used drift gas. For that reason, an electron emission close the field and sense wires results in slow drift velocities.

6.1.2 Data sample selection

An analysis of the data requires a pure data sample. In order to reduce correlated background the efficiency is analyzed using isolated tracks. For that, low-multiplicity events are selected (see Fig. 6.3) to minimize effects of detector cross talk and ambiguities in the track reconstruction. The MDC tracks for efficiency estimation are selected from fully reconstructed particle tracks and must comprise a reconstructed MDC segment in the inner and outer modules as well as a hit in one of the META detectors. The track candidate multiplicity is even lower compared to the one of META hits (see Fig. 6.3). A relation of approximately 2.5 hits in TOF and RPC to one particle candidate is indicated. The number of tracks for the chosen META hit multiplicity is around two or three tracks per chamber and allows a clean efficiency estimation with a low double hit probability.

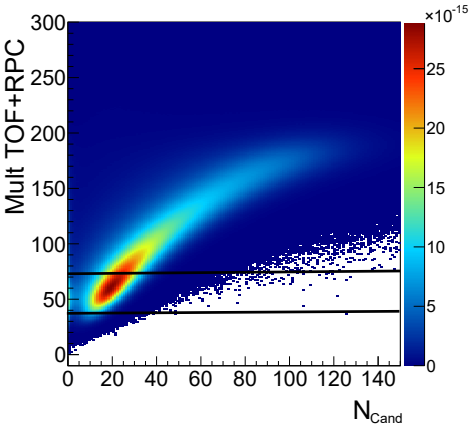

Figure 6.3: Correlation of candidate to META multiplicity. **Below first line:** META hit multiplicity / sector < 7 **Below second line:** META hit multiplicity / sector < 14.

6.1.3 Efficiency calculation method

An important parameter used in the digitizer is the probability, that a traversing particle fires at least one cell in a given layer. This so-called *layer efficiency* depends on the specific energy loss of the particle and is otherwise a feature of a drift cell layer governed, e.g. by threshold settings, applied high voltage or gas quality. As options for the layer efficiency estimation method itself, the MDC detector provides several objects after track reconstruction including MDC cell, cluster and segment hit. To achieve realistic results the MDC hit type used for calculation, should exclude hits caused by noise, while signals created by particles should be kept in the data sample. The different objects have the following advantages and disadvantages:

- **MDC Cell:** This object contains single fired MDC cells which probably include a significant amount of noise. It is already biased due to ToT restraints, which are applied to minimize noise contributions.

- **MDC Cluster:** MDC Cluster hits are the sum of correlated wires from different wire layers. This observable includes a reduced amount of noise, but has an increased probability to reject a good track signal from the sample.

- **MDC Segment:** An MDC segment requires a fit of nine out of 12 fired layers, in the two modules in front of and behind the magnet. Therefore, the number of rejected MDC signals from real particles is increased.

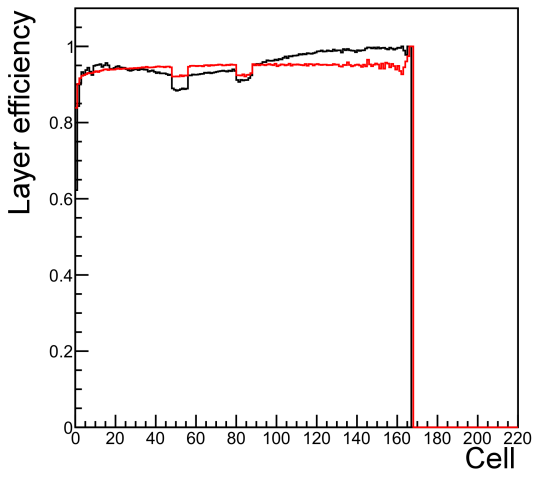

Figure 6.4: Layer efficiency for simulated (red) and experimental (black) data.

Based on the mentioned advantages and disadvantages, MDC clusters are chosen as hit type, since a major fraction of noise is excluded while a small number of good MDC signals is removed.

At the beginning of the layer efficiency estimation procedure, also MDC segments from a fully reconstructed particle track are chosen. The MDC segment hits assume the particle track as a straight line inside a MDC segment. Those segments are used to estimate which MDC cells were crossed in each wire plane. In case two cells of the same layer are crossed by a particle track, only one cell is used for efficiency calculation. Otherwise a cell-wise efficiency would be estimated. Finally, the efficiency is calculated as the ratio of hit cells to crossed cells (see Fig. 6.4). In order to calculate an efficiency of a whole wire plane, the mean value is determined out of efficiencies from single cells and will be denoted as layer efficiency in the further course.

6.1.4 Resulting efficiencies

The data sample for layer efficiency estimation was chosen to reduce background contributions. However, the estimated efficiency might still not be a pure measure of layer efficiency and comprise the following effects:

- **Layer efficiency**: Influenced by gas quality, high voltage and load on the chamber.
- **Hardware failure**: Missing measurements, due to broken mother boards.
- **Event characteristics**: Uncorrelated noise and correlated noise.
- **Tracking**: The selection of MDC hits per segment is biased by tracking.

These sources of inefficiency can not be distinguished from each other. Consequently, they are accounted to the layer efficiency. However, the same effects are present in experimental and simulated data and the measurements can be compared to each other to adjust the digitizers (see Fig. 6.4).

6.1.4.1 Layer efficiency

To identify systematic behaviors, the efficiencies of all layers from all chambers are compared in Fig. 6.5. The comparison reveals that the outer segment chambers have higher efficiencies than the inner segment chambers. Besides minor deviations, the layer efficiency of sectors in

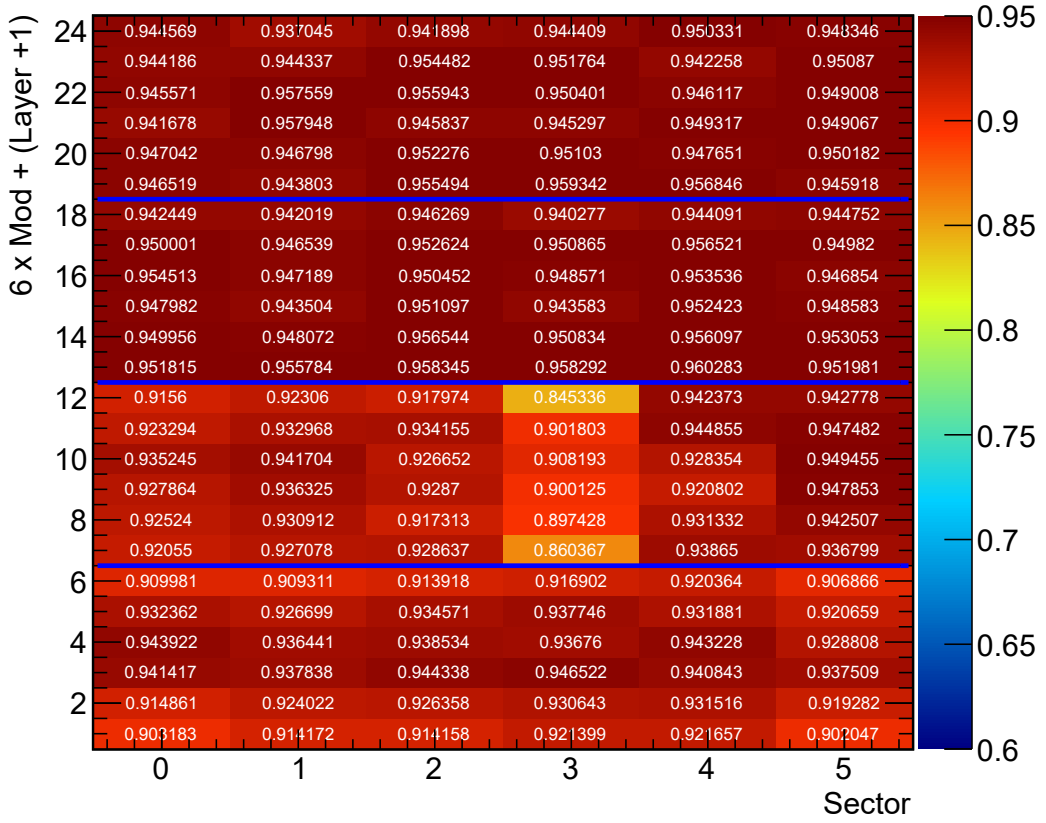

Figure 6.5: Layer efficiency separately shown for all sectors and all layers.

the outer drift chambers is around 95%. This value is slightly lower for the 40° layers at the back of the chambers (Layer 18 and 24).

The same observation is seen for the chambers of the inner MDC segment. The sectors of the first MDC module show similar trends, but have a reduced efficiency. In general, the efficiency is worst for 40° layers, it rises for 20° and is the best for 0° layers. The efficiency differences between wire planes with different orientations are up to 4% but depend slightly on the sector. For the second drift chamber module, a similar but less pronounced trend is visible. Sector 3 shows significantly reduced efficiency values in all layers. A comparison of the layer efficiencies in all chambers to the ones with an input sample containing higher META multiplicities (7–14 hits per sector) reveals similar results, but a general efficiency decrease of around 0.5% due to inefficiencies caused by double hits.

6.1.4.2 Energy loss dependence

Due to the fact that the MDC particle detection is based on the ionization principle, the correlation of energy loss to layer efficiency is investigated. The energy loss in a MDC cell is directly dependent on the particle velocity β and reaches a minimum at a velocity $\beta = 0.96$. For a detailed investigation, particles are categorized in three bins: (I) minimum ionizing particles (MIPS), (II) medium ionizing particles (MEPS) and (III) maximum ionizing particles (MAPS) (see Fig. 6.7 (left)).

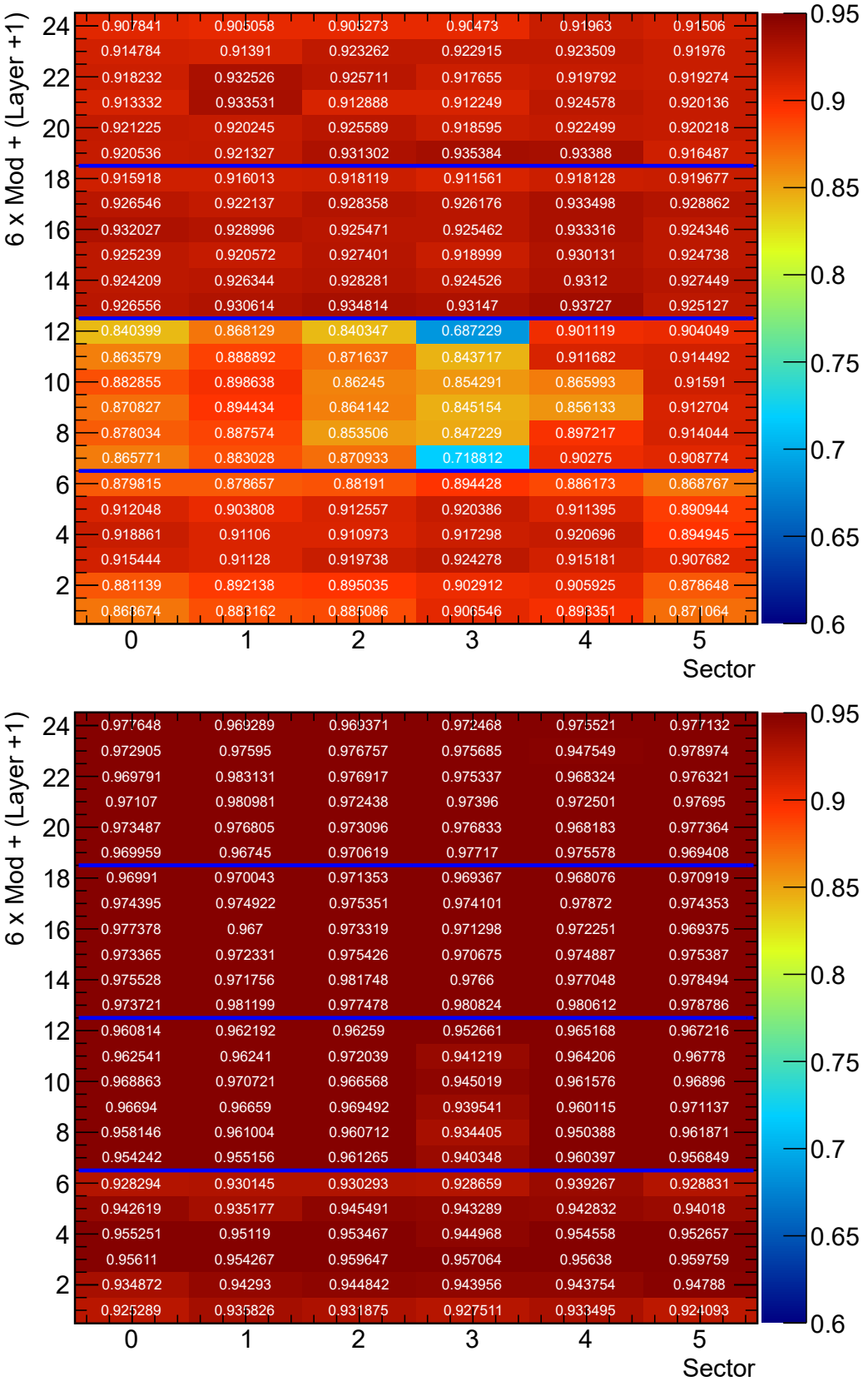

Figure 6.6: Efficiency for MIPS (**upper**) and MAPS (**lower**). The plots show efficiency values for different sectors (x-Axis) and layers (y-Axis). By comparison of MAPS to MIPS a systematically increased efficiency in case of MAPS is visible.

Category	β_{Min}	β_{Max}
MIPS	0.90	0.98
MEPS	0.45	0.90
MAPS	0.00	0.45

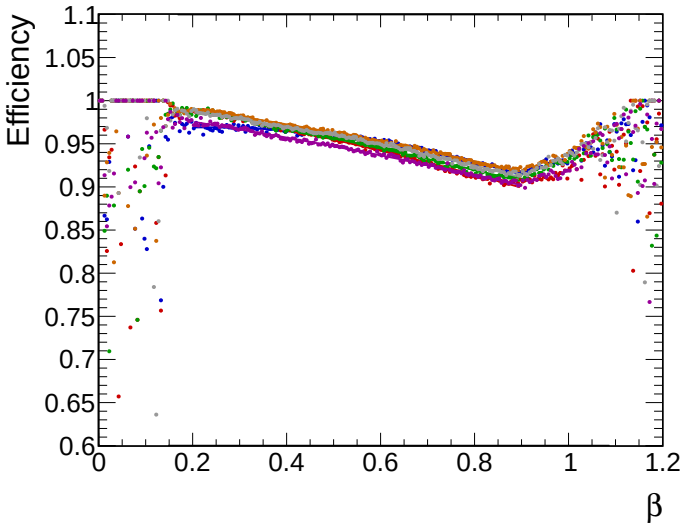

Figure 6.7: Left: Particles categorized into three groups with different ionization. The column Min and Max shows lower and upper β limits for the corresponding group. **Right:** Efficiency as a function of the particle velocity β. The efficiency decreases with rising velocity which corresponds to a smaller ionization.

By comparison of the layer efficiencies presented in Fig. 6.6, a difference between MIPS and MAPS of the order 5–10% is visible. In case of MAPS, efficiency values above 98% and a more stable efficiency value in all MDC modules is obtained. Even sectors from the inner segment show efficiencies above 97%. In contrary to MAPS, MIPS show large efficiency differences between the inner and the outer segment with deviations up to 8%.

The β dependent efficiency value in Fig. 6.7 (right) confirms the results estimated by the comparison between MIPS and MAPS. Measurements at β values around 0 and 1 are more rare and their statistical uncertainties are enhanced. This causes the fluctuations of these data points. In the velocity range from 0.1 to 1, the efficiency curve shows a continuous decrease towards higher velocities. A layer efficiency minimum is reached below β values of one, which fits to the energy loss minimum expected based on the Bethe Bloch formula [142].

6.1.4.3 Layer efficiency in the course of the run

Despite the estimation of the layer efficiencies, their stability is influenced by external and detector effects (e.g. gas quality, temperature, pressure and beam quality) and might vary during the beam time, for which reason their stability is investigated. The stability study requires a short time interval for a precise analysis but sufficient statistics to calculate a stable efficiency value. Therefore, the layer efficiency is plotted in two hour steps for tracks that are accumulated over a five minute time period.

As a result, the efficiency variations plot (see Fig. 6.8) indicates layer efficiency differences below 1% during the beamtime. The efficiency during the last two days is higher compared to previous days. This data belongs to measurements with a reversed magnetic field. A comparison

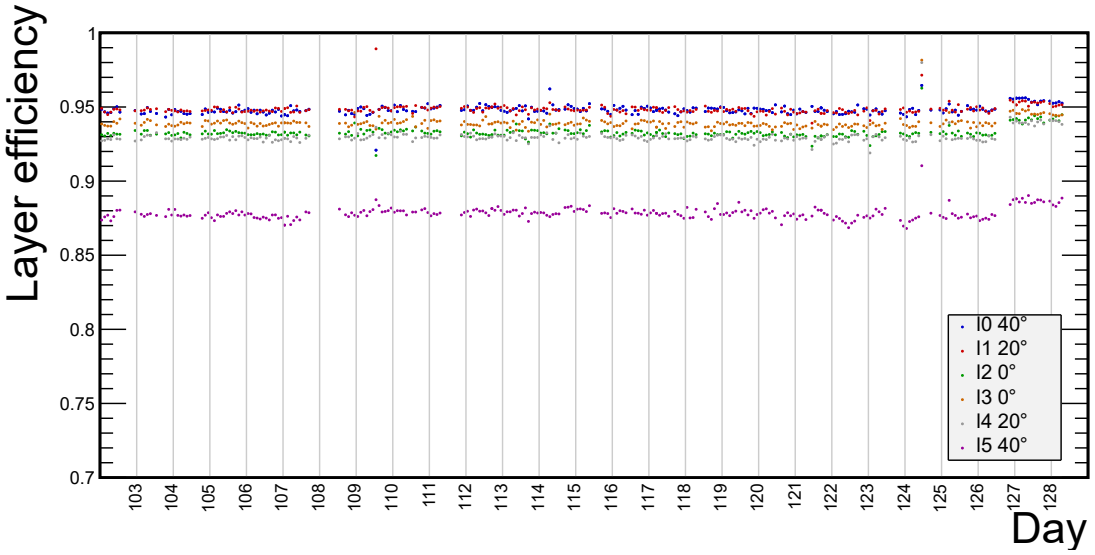

Figure 6.8: Time dependence of the layer efficiency for wire layers (l0-l6) with different orientations. Only small variations within the whole measurement period appear. Errors are not plotted to enhance the visibility.

between different sectors and different MDC modules displays an efficiency decrease for the -40° and 40° layers. The strength of this decrease is sector dependent and more pronounced for 40° layers in module 0 and 2 and -40° layers in module 1 and 3.

Sector 2 of module 1 reveals unstable layer efficiency values due to high voltage problems during the beamtime. For short time periods, this sector indicates layer efficiencies above 50 %. A comparison of the number of reconstructed tracks for all sectors within this time periods reveals, that less than of 90% tracks compared to other sectors are reconstructed in this specific drift chamber. Consequently, this drift chamber has a very low efficiency. Since the applied layer efficiency estimation method is only valid for layer efficiencies close to 100%, it can not be applied in sector 2.

In conclusion, the overall results show a stable behavior during the beamtime. Smaller variations are caused by changes of the gas quantities or the gas pressure inside the MDC chambers. Strong rises of efficiencies are caused by intensity differences of the provided Au beam. At these time intervals a short break of the incoming beam caused the efficiency differences. As the measurement was started again the efficiency rose strongly. A systematic decrease for one of the 40° layers in each MDC module is seen. The ToT measurements for these wires are as good as in all other layers. As a consequence, the decrease must be induced by the tracking procedure.

6.1.5 Conclusion

The layer efficiencies are implemented as single cell efficiencies in simulation in order to reproduce experimental results for the track reconstruction. Therefore, each layer of each chamber was tuned separately based on the estimated layer efficiency values. In addition, the dependence of the layer efficiency on ionization was estimated by a fit to the data points. The estimated ef-

ficiency dependence was implemented in simulated data as well. This modification improved the simulation and decreased differences between track reconstruction in experimental and simulated data. But, the application to simulation has also shown, that the reproduction is not yet sufficient (see Fig. 6.4). This issue is solved by an inclusion of δ-electrons in simulation (see Fig. 6.9 (left)). Their integration reduces the efficiencies mainly for detector regions more far away from the upper and lower detector edge, which correspond to medium cell numbers. After their inclusion, the layer efficiencies in simulation agree with those estimated in experimental data. This can be explained by δ-electrons passing a cell and creating a signal. This leads to a dead time in the cell in which no further signal can be reconstructed. As a consequence, the layer becomes more inefficient. Using the estimated layer efficiencies their impact on track reconstruction efficiency is investigated. Via a binomial distribution, the probability for having at least nine layers is calculated (see Fig. 6.9 (right)). Since the obtained layer inefficiency is below 10% the probability to have at least nine layers as input for track reconstruction is close to 1. Consequently, the study indicates a good performance of the MDC detectors for track reconstruction.

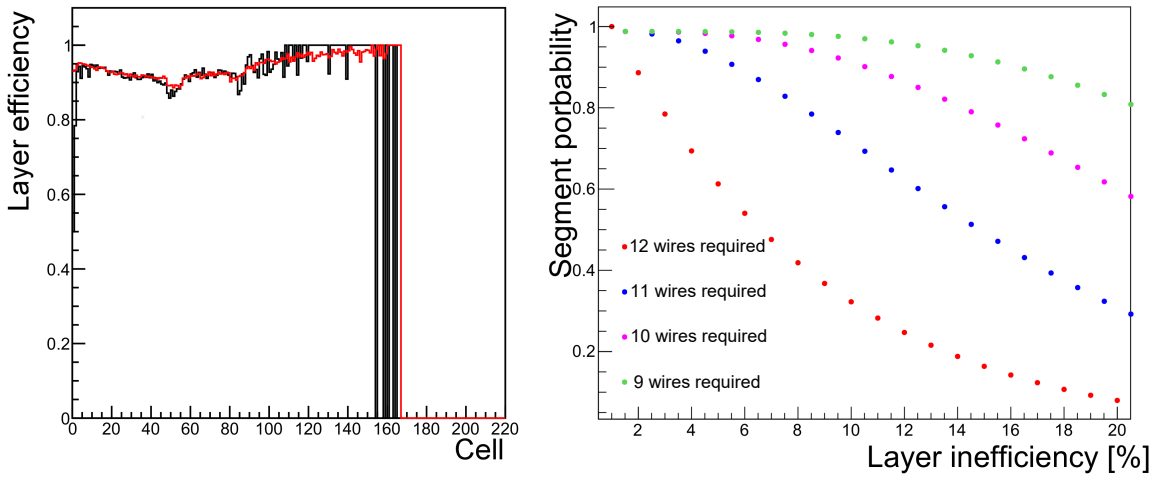

Figure 6.9: Left: Layer efficiency including for simulated data including δ electrons (red) and experimental (black) data. **Right:** Probability of MDC segment reconstruction for a given layer inefficiency.

6.2 RICH performance study

This study focuses on the RICH detector since this detector is the most important one for the dielectron analysis. The characteristics of signal and background hits in real data are analyzed and compared to simulated data. Furthermore, also the stability of the detector response in the course of the run is investigated.

6.2.1 Pad plane cluster properties

The electron and positron reconstruction can be an improved by knowing characteristics about the RICH response and situation with noise. This knowledge will lead to a more advanced electron and positron identification resulting in an improved identification efficiency as well as purity. A starting point is provided by a previous analysis of cluster shapes measured with the RICH detector. Three different classes of clusters were identified [136] (see Fig. 5.10 (left)):

- **Class 1**: Created by one single photon,
- **Class 2**: Created by two photons,
- **Class 3**: Created by three or more photons.

The applicability of this categorization for the high multiplicity in Au+Au collisions has to be verified. A way to access the RICH hit information is using the backtracking output[1]. All common cluster shapes are counted and plotted, as shown in Fig. 6.10. This distribution agrees with the expectation in general but has some interesting additional features. One observation is the similar occurrence of vertically and horizontally straight clusters. This is not expected, since the vertical orientation of wires might favor vertically oriented clusters due to enhanced charge sharing.

Another significant feature is the frequent appearance of the square shaped clusters. Since it appears nearly as frequent as the corner cluster of type six it has to originate from single photon hits as well. Additionally, many clusters with shapes not belonging to class 1 or class 2 are measured and support the assumption of several local maxima per cluster, which was already discussed in section 5.4.2.

Hence, the approach to search the number of local maxima per cluster and try to disentangle reasonable cluster sizes is applied. The visualizations in Fig. 6.11 demonstrate that the Maximum7[2] approach method is necessary to achieve reasonable cluster sizes of up to three pads per maximum. However, some clusters still cannot be explained by such an approach. The middle example in Fig. 6.11 indicates a cluster with only one local maximum but consisting out of seven pads. It is striking that such configurations mostly appear for a single pad with high charge. It is important to keep in mind, that the amount of signal amplification in the RICH

[1] `HParticleBtRingInfo`, See chapter 5
[2] See section 5.4.2

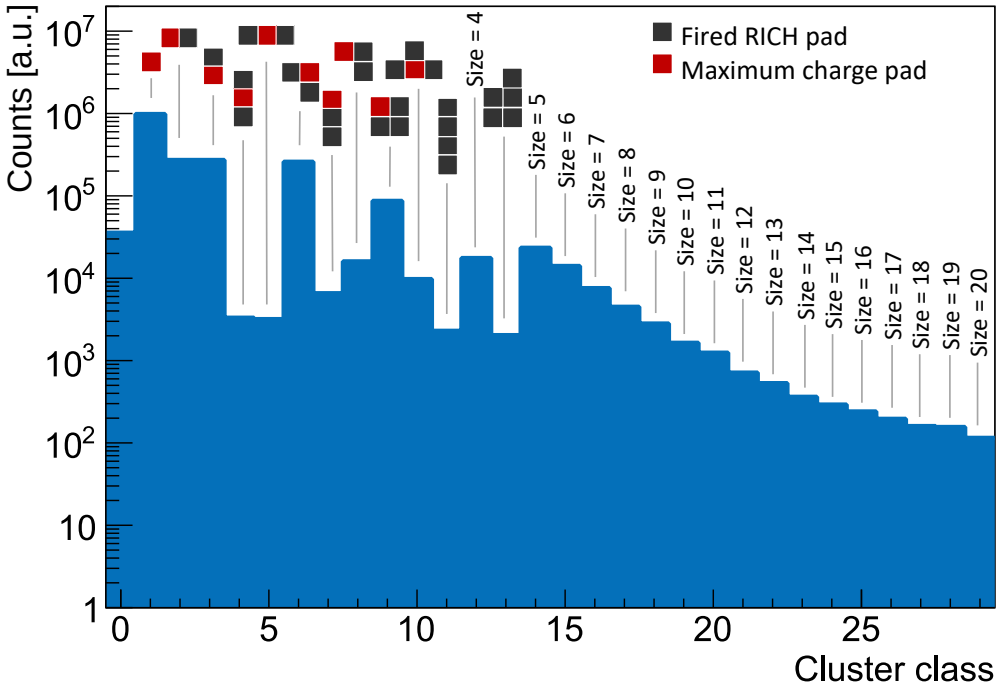

Figure 6.10: Distribution of cluster shapes identified with backtracking. A cluster type includes all orientations besides for types where several orientations are plotted separately.

varies strongly. As a consequence, the charge per photon varies and the deposited charge of a photon signal could be hidden, by the charge distribution of the strongly amplified signal of a second photon. In this case, only one local maximum is found but the cluster size is enhanced. Such large clusters do mostly contain up to three pads with a charge below 65 a.u.. Removing pads below this charge threshold decreases the number of pads per cluster to reasonable sizes of three or four pads per local maximum.

Although large clusters are explained by this effect, their frequent occurrence is still unexpected. An explanation for clusters with up to 10 pads is the larger amount of charge sharing or cross talk between the pads. But the number of very large cluster comprising about 20 pads cannot be explained by this mechanism. Those clusters must be created by background hits.

Figure 6.11: Three examples of large clusters measured by the RICH detector. The gray arrows indicate positions of local maxima identified with the Maximum7 search mask. The numbers depict the charge of each pad.

6.2.2 RICH background hit distribution

In the previous chapter, the presence of background hits, influencing the electron reconstruction, was identified. Those might sum up and create a signal similar to the one of true electron, which can be falsely matched to a hadron track. In case this track has a velocity close the speed of light, it might be identified as good electron or positron. The aim of this section is to identify background hit patterns and exclude these hits from the electron signature search in the RICH detector.

A source of background is identified by the number of backtracking maxima per electron candidate (see Fig. 6.12 (left)). In case of true electrons, the distribution is expected to follow a Poisson distribution. In order to select electron and positron candidates, tracks are constrained to large velocities ($\beta > 0.95$) and small momenta ($p < 300$ MeV/c). A fit to the $\mathtt{N}_{BTMax}$/Cand distribution shows a good agreement between the distribution and a Poisson fit for candidates having more than two local maxima. The fact that the number of local maxima attached to a electron track candidate agrees with a Poisson distribution, justifies identifying photons with local maxima detections.

However, a clear overshoot of data is present for candidates with only one local maximum. The latter typically have small charges and consist only of a single fired pad. These pads are caused by noise.

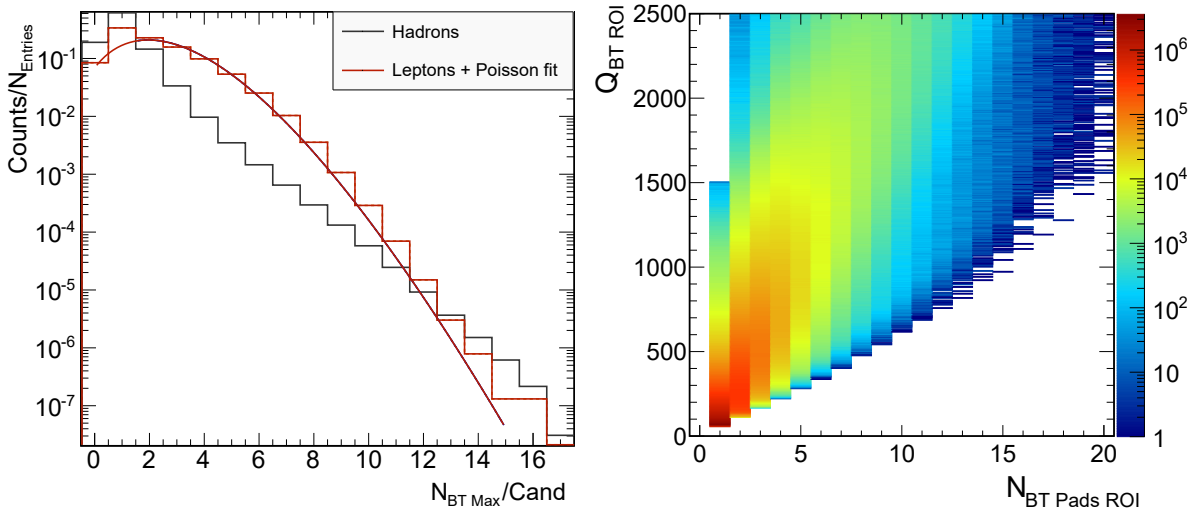

Figure 6.12: Left: Number of local maxima per candidate estimated with backtracking and plotted for hadrons and the sum of electrons and positron. Both particle species are selected by limitation of velocity and momentum. **Right:** Charge per candidate as a function of pads per candidate from backtracking after restriction of a minimum charge per pad to 55 a.u. (sector 3) and 65 a.u. (other sectors).

On the other hand also very large clusters are an origin of background. Those clusters are created by particles crossing the RICH pad plane directly. In this case, a lot of charge is created and distributed over a large area. This charge pattern is unexpected for real photon hits.

Additionally, large clusters can originate from partially "flashing" RICH sectors due to problems of the readout electronics. Also electrons originating away from the focal point of the mirror and crossing the radiator create a background. In this case, emitted Cherenkov photons are not focused to ring shapes but will be measured as a spray-like distribution of small charged clusters.

The different effects influencing a clean electron and positron identification should be removed. The following criteria are applied to remove background contributions and are already included in backtracking (see chapter 5):

- **Large clusters:** Large clusters as shown in Fig. 6.13 can be easily rejected by setting a upper limit of the 7 of local maxima per cluster.

- **Flashing RICH sectors:** Flashing RICH sectors are removed by setting an upper limit of fired RICH pads in one third of the RICH sector. In case of a electron or positron candidate within the flashing RICH sector, the event is disregarded.

- **Single pads:** The amount of noise in form of single pads is reduced by setting an lower charge limit of 65 a.u. inside the backtracking procedure. This limit is adjusted to 55 a.u. in sector three since in this sector the operating voltage was reduced from 2420 V to 2230 V.

The resulting pad and charge per candidate distribution is presented in Fig. 6.12 (right). Further background removal should be performed by the end user due to restriction of the backtracking observables, e.g. charger per candidate and pattern matrix.

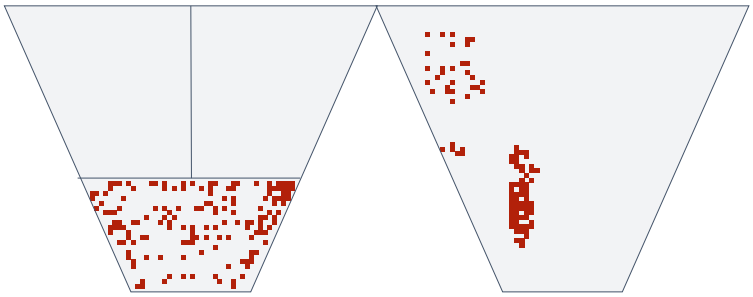

Figure 6.13: Sketch of RICH pad planes indicating different types of noise of RICH events. The left example shows a partially flashing sector. Borders of this effect are indicated by the lines crossing the sectors. Correlated background spray from electrons in the radiator gas and large clusters from direct impacts are presented in the right example.

6.2.3 Reproduction of RICH hit distributions in simulation

Besides checking and understanding of the RICH hit distribution in experimental data, the adaption of simulated to experimental data needs to be checked as well. Therefore, the average occupancy of fired pads in simulated and experimental data is investigated. To obtain comparable results, both data are normalized to the number of events. Various cleaning criteria are applied to exclude background hits from the ring signature search. For the standard ring finder three different removal procedures are applied (see section 3.6):

- **Single Pads:** Removes single pads that are isolated by seven pads. (`getIsCleanedSingle()`)
- **Large Clusters:** Removes large clusters which are produced by direct impacts of particles. (`getIsCleanedHigh()`)
- **Sector:** A sector is excluded if too many pads in the corresponding sector were fired. (`getIsCleanedSector()`)

The criteria are different in case of backtracking (see section 6.2.2):

- **Low charge pads:** Removes every pad with a charge q < 65 a.u.[3].
- **Large clusters:** Removes clusters with more than six local maxima (see Fig. 6.13 (right)).
- **Many hits per sector:** Removes sectors if many pads are fired randomly in one third of the sector (see Fig. 6.13 (left)).

In order to test the agreement between experimental and simulated data and the effects of the removal, a ratio of the RICH signal distribution between both data samples is calculated. The ratios are investigated for simulated data that include δ-electrons which create additional hits in the RICH detector.

The results for the different sectors without application of any cleaning procedure are presented in Fig. 6.15. All ratios differ from one significantly and show a similar trend in all sectors. The hits in the small y pad number[4] region are underestimated in simulation while the ratio is more similar at larger y pad numbers. Furthermore, a pattern, caused by effects of the read out electronics, is visible in all the sectors. The strength of deviations is varying for different sectors. However, these ratios do not include the cleaning criteria for the RICH ring finder or backtracking. The results after applying the ring finder pad cleaning criteria is shown stepwise in Fig. 6.16. The removal of large clusters removes 18% of pads in real and 16% of pads in simulated data. A stronger reduction of the number of fired pads of in the order of 20% in real and 40% in simulated data is caused by the single pad removal. In contrast, the application of the sector cleaning has an effect below 1%. The comparison of the three ring finder cleaning

[3] q < 55 a.u. in case of sector 3

[4] The polar angle Θ increases for larger y pad numbers.

procedures, reveals that the application of the single pad removal shows the largest differences between experimental and simulated data. The stronger removal in simulation is explained by the high multiplicity of fired pads in real data. Due to the higher occupancy, less single pads are isolated by seven surrounding pads. Therefore, more pads are removed in simulation.

The comparison before and after removal of the ring finder cleaning methods indicates the strongest differences between simulated and experimental data after the application of the cleaning methods. Using the backtracking pad cleaning results in an improvement compared to the ring finder cleaning, since the ratio is closer to one and more flat. Similar to the distributions after the RICH cleaning, the backtracking pad cleaning criteria reduces the number of fired pads by 56% in real data and 62% in simulated data. The single pad removal leads to the strongest pad removal of all backtracking cleaning criteria.

The comparison of the simulation including δ-electrons to one without δ-electrons shows a worse agreement for the simulation without δ-electrons (see Fig. 6.14). The inclusion of random background hits by δ-electrons increases the number of fired pads in simulation, for which reason the ratio gets closer to one. This proves that δ-electrons need to be included into simulation.

Although the comparisons show a deviation in simulation, the impact on the analysis is not known precisely, since a matching of the pads to the rings is not required. Therefore, the differences for identified rings should be checked in the final analysis again. Especially, the validity of the efficiency correction, that will be based on simulation, has to be evaluated in detail (see section 9.2).

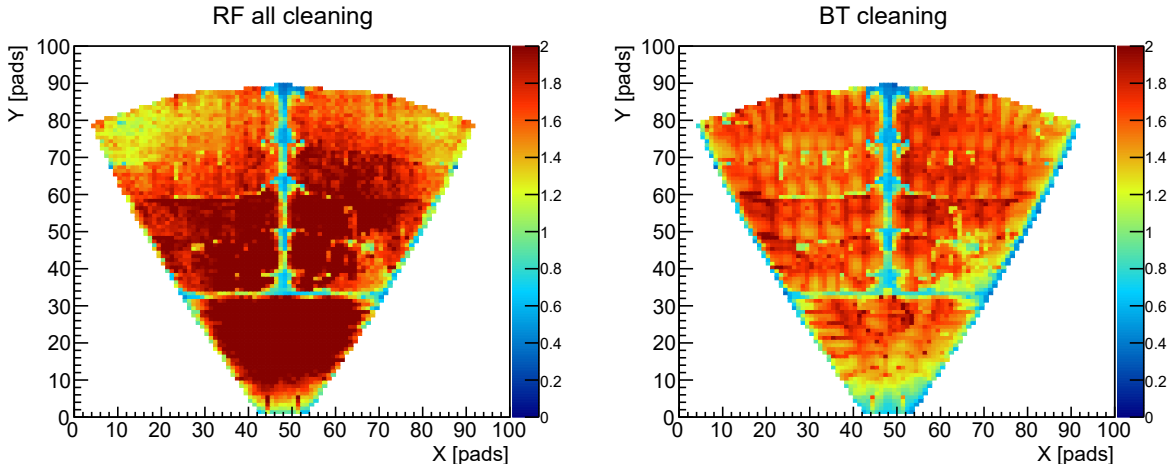

Figure 6.14: Ratio (exp./sim.) of fired pads for all RICH sectors. The same cleaning criteria as in 6.16 (lower) are applied. However, the simulated events used for these plots does not include a contribution from δ-electrons.

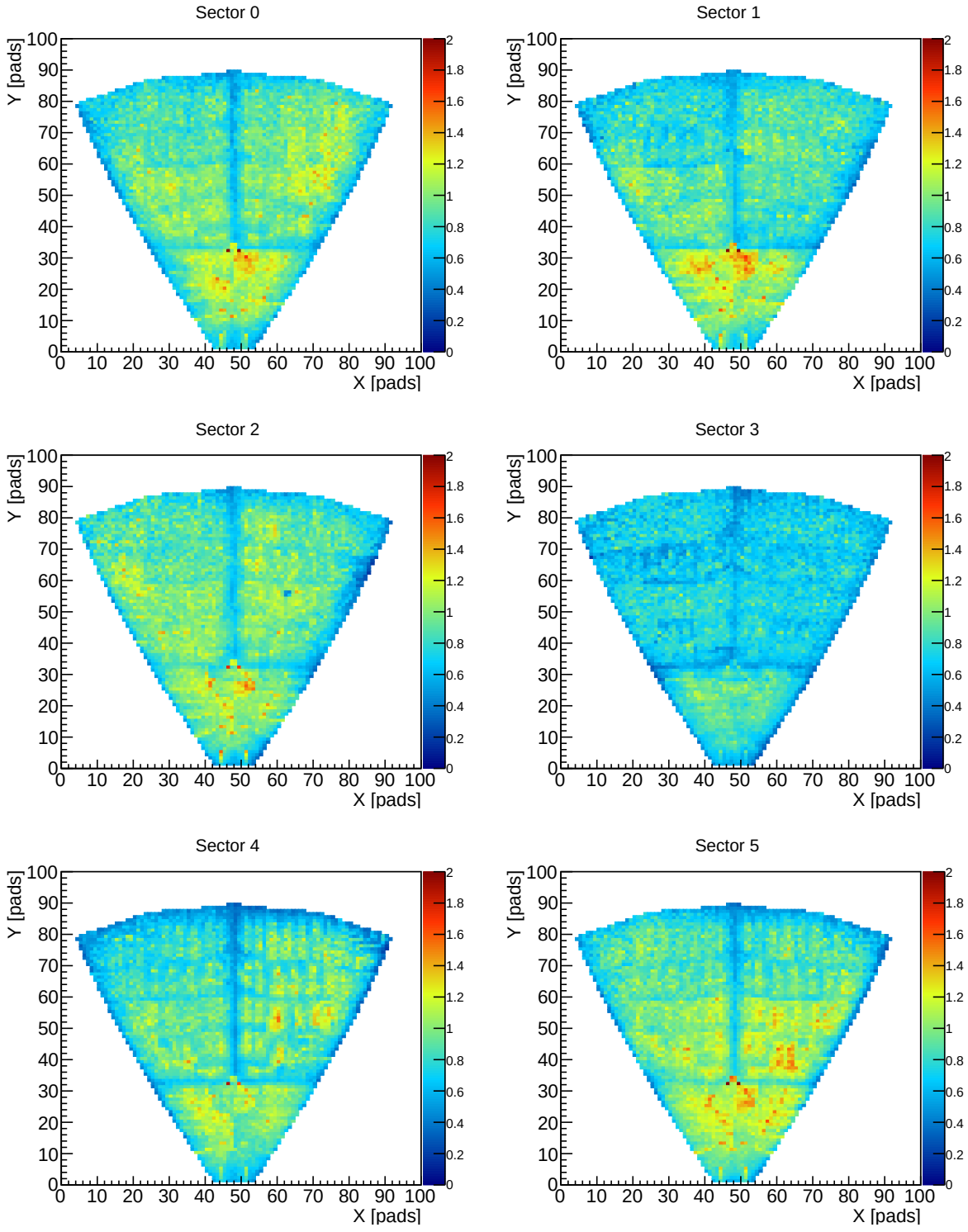

Figure 6.15: Ratio (exp./sim.) of fired pads for all RICH sectors. The small y pad number region shows a higher occupancy in experimental than in simulated data. Furthermore, specific patterns caused by the read out electronics are visible.

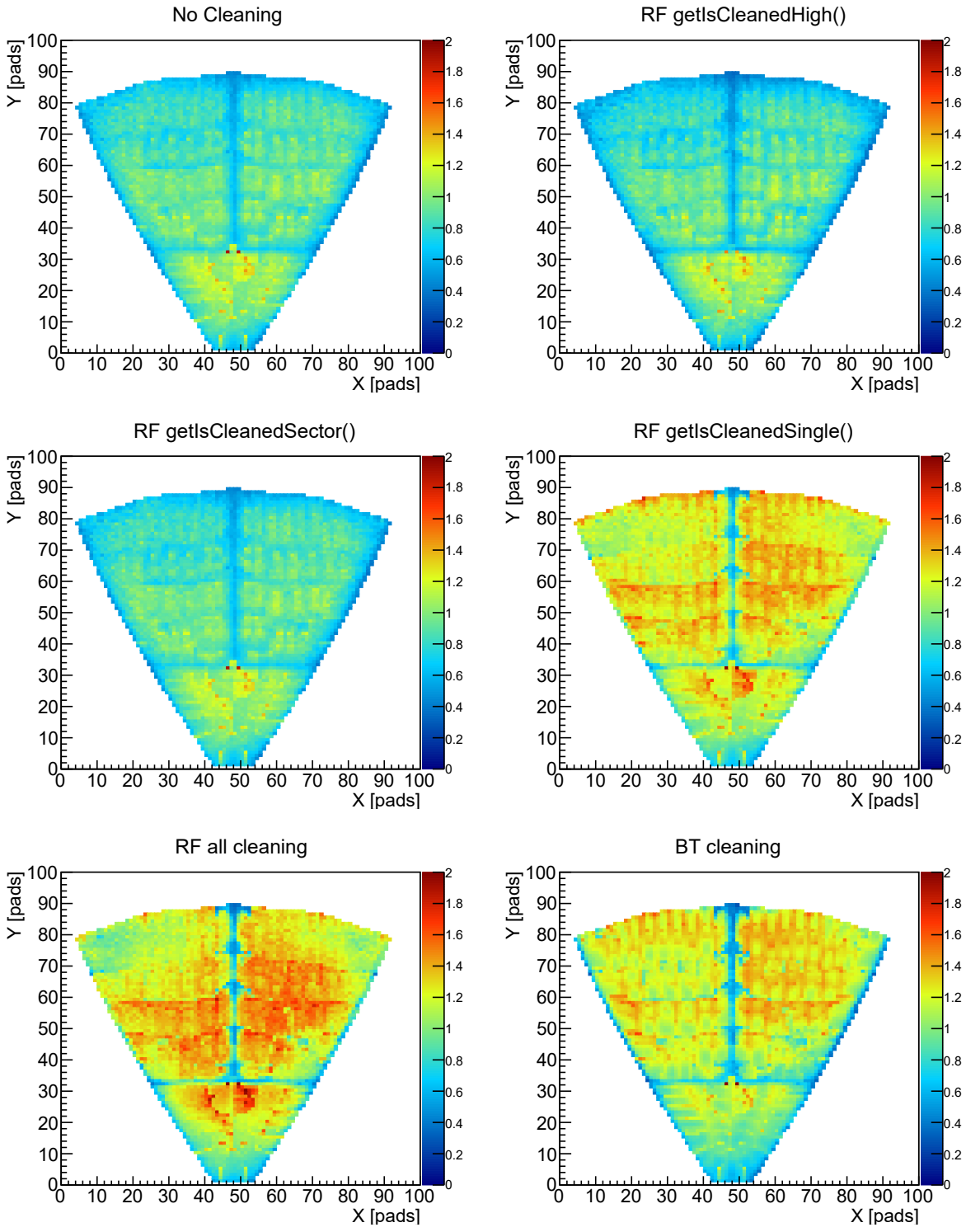

Figure 6.16: Ratio (exp./sim.) of fired pads for all RICH sectors. The different RICH ring finder (RF) cleaning procedures are compared. All (**lower left**) summarizes the three `IsCleaned()` flags presented above. The cleaning with backtracking (**lower right**) achieves a more smooth distribution than the application of all RICH ring finder cleaning flags.

6.2.4 RICH performance in the course of the run

The RICH response in simulation is tuned to events recorded with a well operating RICH detector. A well reproduced simulation is important to correct for inefficiencies due to electron and positron reconstruction and identification. Unfortunately, voltage changes occurred in the course of the run. In detail, five sectors were operating stably with constant high voltage, while sector three was operated at a lower voltage. Therefore, the impact of the performance variations on the electron identification is of interest.

An overview is obtained by checking the mean number of reconstructed $e^{\pm}$ candidates per event. Those candidates are identified via an analysis including the backtracking observables. A detailed overview of the analysis is given in section 7.3. An identification of $\pi^{\pm}$ via a velocity and momentum selection threshold is performed in parallel. The $\pi^{\pm}$ beam time scan serves as a reference since their identification relies on the drift chambers and time-of-flight detectors only. This helps to disentangle RICH detector effects from effects of the other HADES detector systems. By comparing $\pi^{\pm}$ and $e^{\pm}$ spectra (see Fig. 6.17 top and middle), a reduction of reconstructed $e^{\pm}$ per event towards the end of the beam time is present while the number of $\pi^{\pm}$ is constant (see section 4.4.2). Moreover, sector three shows large fluctuations but seems to have a similar behavior with a reduced number of reconstructed $e^{\pm}$ candidates. Drops for a short time period are present in all detectors but appear are the most common in sector three. This behaviour is caused by the voltage ramping procedure which influences the number or reconstructed rings per event (see Fig. 6.17 (bottom)). A drop for a short time period in sector three is clearly visible. The trend of reconstructed rings in sector two shows a clear correlation to the voltage in the corresponding period. Also small changes of $\Delta U \approx 100$ V around the nominal voltage of $U \approx 2420\ V$ show a large decrease in the number of reconstructed rings. On the other hand, the noise is reduced as well and leads to a similar signal-to-background ratio.

In conclusion, the average number of reconstructed rings shows a smooth trend, but indicates a continuous decrease with time. However, the simulation is tuned to match with the average detector performance in experimental data during the run and can therefore be applied for comparisons to experimental data.

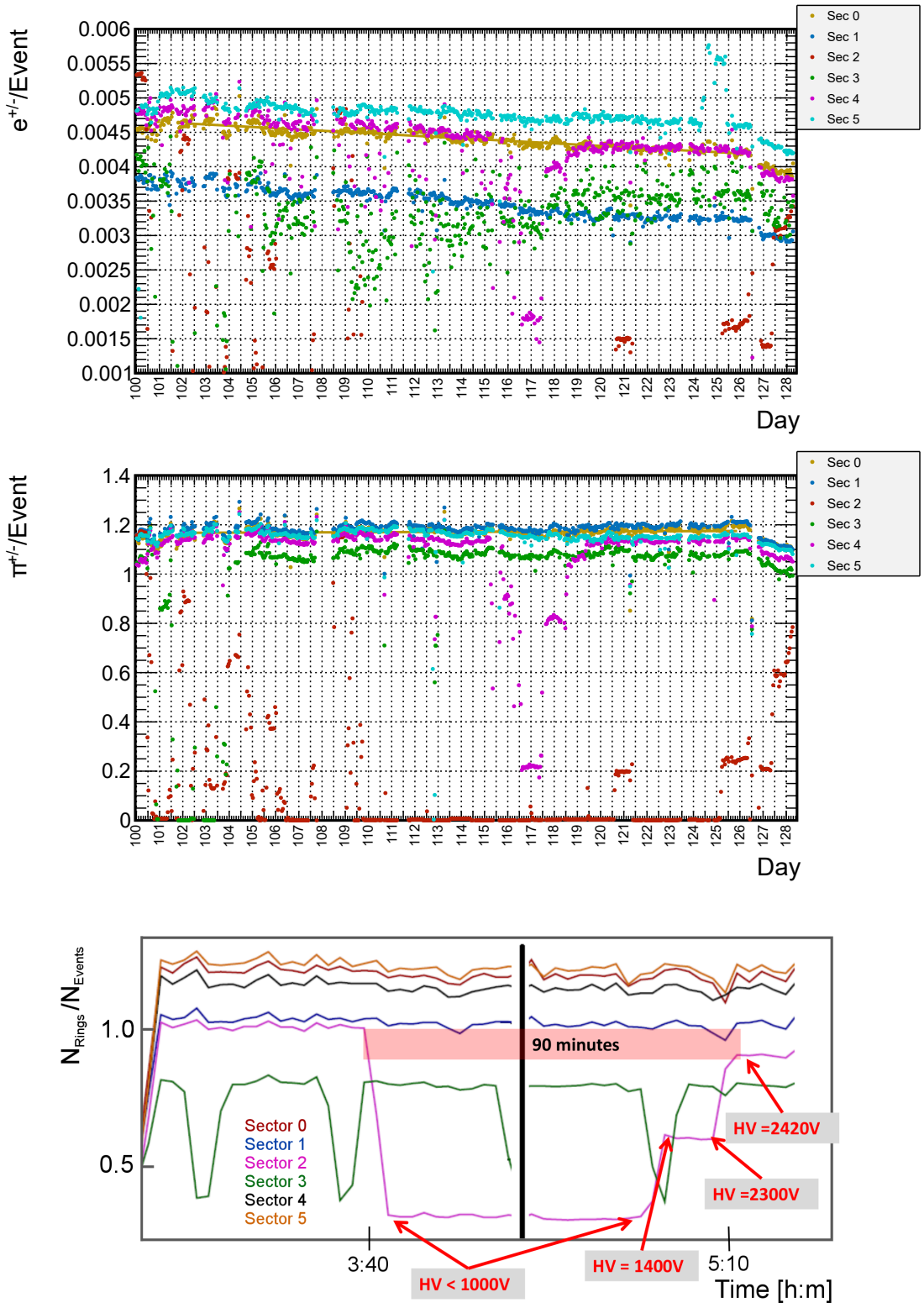

Figure 6.17: Upper: Mean raw multiplicity of reconstructed electrons averaged over one hour of operation. A degradation of the electron multiplicity towards the end of the beam time is observed. **Middle:** Mean raw multiplicity of reconstructed pions per event. Besides short-time drops, a stable mean multiplicity is observed. **Lower:** Mean number of reconstructed rings per sectors. This plot demonstrates the dependence between RICH high voltage and reconstructed particles.

Chapter 7

Single electron identification

Dielectrons are obtained by combining the individually reconstructed electron and positron[1], originating from the same particle. For the electron reconstruction, a high efficiency is essential to reconstruct both daughter particles, i.e. e^+ and e^-, with high probability. On the other hand, a high purity of electrons is important, since any falsely reconstructed electron or positron will increase the background because it has to be paired with any opposite-sign identified electron. Consequently, the combinatorial background increases. The major combinatorial background originates from hadron tracks, fake tracks, that are created by wrong combinations of single detector hits, and conversion electron tracks. In order to keep the combinatorial background as small as possible, specific selection criteria are applied to the electron candidates before the tracks are paired. All criteria are applied in the following order in the analysis:

- **Electron candidate selection:** Reduction of fake tracks and hadronic background.
- **Multivariate electron identification:** The electron selection is based on a multivariate analysis (MVA), which considers multidimensional correlations between the observables.
- **Close pair rejection:** Rejection of electron candidates which appear to originate from incompletely reconstructed conversion pairs.

In the following, these analysis steps are explained in detail.

7.1 Particle identification observables

Track quality parameters

Observables, determining the quality of single detector hits or the matching between inner and outer MDC track segments and hits from PID detectors, respectively, are summarized as track quality parameters. A measure of reconstruction accuracy of the inner and outer MDC segments

[1] In the further course, electrons and positrons will be denoted as electrons.

is given by the χ^2_{Seg} value obtained by the segment fit. Furthermore, the quality of the whole MDC track is estimated by the χ^2_{RK} from the Runge-Kutta fit, that applied is to reconstruct the momentum of a particle (see section 3.3). The matching of the MDC track to the META detectors is constrained to a single META rod[2]. Additionally, the matching accuracy between MDC segments and hits in the META detectors is estimated by the distance between the reconstructed MDC track and a hit in the META detectors in units of the resolution in the META detector (`MetaQa`)[3]. Acceptance differences at sector edges between simulated and experimental data are reduced by applying a fiducial volume cut. The area is chosen by restrictions in the x and y direction in the detector coordinates[4]. All mentioned observables are applicable for hadron and electron identification and their main purpose is to reject fake tracks.

Particle identification observables

Observables for the identification of specific particle species are based on physical properties of particle tracks. The most important observable is the momentum reconstructed with MDC (p) and the velocity β that is determined by the particle trajectory and its time-of-flight provided by the TOF and RPC detector. Since the TOF and RPC differ regarding their time-flight-resolution, the analysis will sometimes be presented for TOF or RPC separately. Additionally, the energy loss of particles is estimated in the drift chambers and gives information about the energy loss of particles traversing the MDC (`MDC dE/dx`). The energy loss information in each drift chamber plane is accessible. However, only combining the measurements of all drift chamber planes provides a significant energy loss measurement. In addition, an energy loss estimation is provided by the TOF detector (`TOF dE/dx`) and therefore only available for polar angles larger than 45°. In the region of smaller polar angles additional hadron rejection capability is provided by the Pre-Shower detector. The Pre-Shower measures the electromagnetic shower that particles produce while traversing the detector (see section 2.3.2). Since the electromagnetic shower is larger for electrons, they can be separated from hadrons. In contrast to previous observables, which are applicable to all particle species, Pre-Shower information is only applicable to distinguish electrons from hadrons.

Ring variables

The most powerful selection criteria for electrons are based on the RICH ring finder information, since only electrons generate a ring signal[5]. Especially, the so-called RICH matching quality (`RichQa`), describing the angular distance between the MDC track and the RICH ring centroid, is important for hadron rejection. However, the matching resolution decreases due multiple

[2] `GoodMetaCell=kTRUE`
[3] See section 3.4
[4] Removes tracks in case `isAtAnyEdge=kFALSE`
[5] Only up to a momentum of 1800 MeV/c since for larger momenta muons can produce Cherenkov radiation as well.

scattering of electrons in the RICH mirror. Therefore, the multiple scattering is corrected by fixing the source position of the track to the estimated collision vertex. This is valid, since the dielectrons of interest are expected to be emitted close to the reaction vertex. As a consequence, the matching resolution of electron tracks improves. Electrons are identified by removal of tracks with large matching distances, which reduces the number of fake matches of hadron tracks to RICH rings strongly. The ring quality can be further estimated by the number of fired pads per ring or the ring amplitude. Additionally, the pattern matrix sums up fire RICH pads that are outside the expected ring area to estimate the amount of background hits around a reconstructed ring. Its application reduces the number of rings created by noisy RICH pad plane areas.

Backtracking variables

Since backtracking is less demanding on the quality of a ring signature in the RICH, it provides additional electron candidates compared to the standard ring finder. However, there is no single observable that is as decisive as the `RichQa`. A proper ring identification with backtracking always requires a combination of the backtracking RICH response observables (see section 5.5). Typically, the most decisive backtracking observables are number of local maxima, number of pads and the charge per candidate. Moreover, the additional backtracking pair observables are suited to search for signatures of pairs with small opening angles. This is a unique feature of backtracking, since the standard ring finder does not provide a similar observable.

7.2 Electron candidate selection

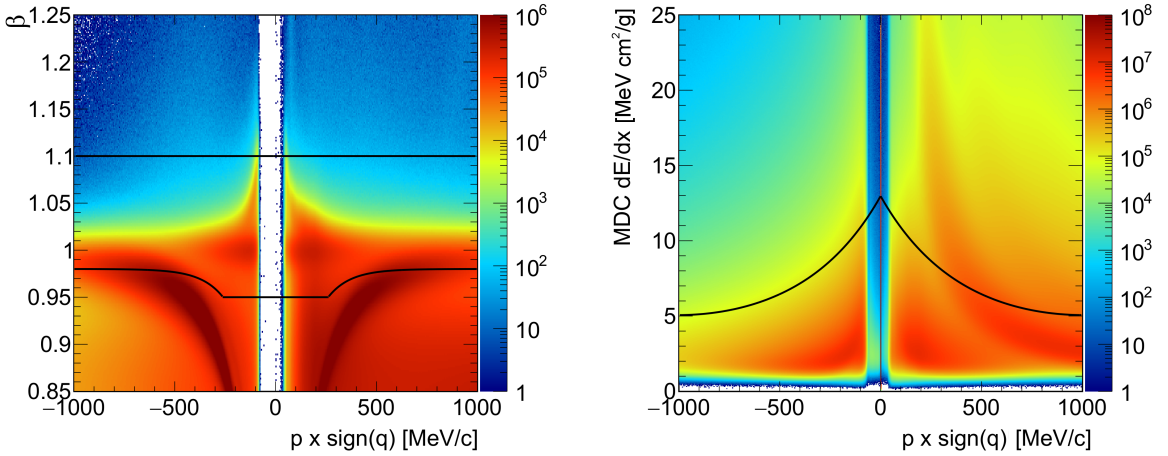

Figure 7.1: Left: Velocity as a function of momentum for all selected tracks. The selected electron candidates around $\beta \approx 1$ are indicated by the black line. **Right:** Energy loss in MDC as a function of momentum.

As already explained in section 4.4, a track sorting procedure is applied to remove fake tracks from the sample of track candidates. In case of electrons, their identification can be improved by rejection of hadronic background already at the stage of the track sorting. For this reason, the standard criteria, that were already presented during event reconstruction, are applied and extended by additional criteria to reject hadrons. Since protons and pions are heavier than electrons at the same momenta, electrons move faster. Therefore, the velocity can be applied to separate the electron signal from the hadron tracks up to momenta of $\approx$ 400 MeV/c^2. For momenta above, the velocity of electrons can not be separated from the one of pions due to the limited time resolution of the time-of-flight detectors. However, electrons can be separated from pions by the specific energy loss estimated in MDC. Due to the relativistic rise, the electrons have a larger energy loss than pions at $\approx$ 400 MeV/c^2, which allows to reject the major pion contribution by the specific energy loss. In detail, the following criteria are applied:

- 2D velocity selection function (see Fig. 7.1 (left)), lower limit: $\beta = 0.95$ ($\beta = 0.92$) for RPC (TOF), upper limit: $\beta = 1.1$ (see Fig. 7.1 (left)),
- Upper limit on the specific energy loss measured in MDC: 2D selection function (see Fig. 7.1 (right)),
- Only signals of the ToF rod at which the reconstructed track is pointing to are selected (`MetaQa`$_y$),
- Spatial matching of ToF signal and Track position (`MetaQa`$_x$`<` 3σ),
- Apply fiducial volume (`isAtAnyMDCEdge=`kFALSE),
- Track segment fit succeeded (χ_{RK} `<` `200`),
- $100 < p < 1000$ MeV/c,
- Require significant RICH response ($\mathrm{N_{BT\ Maxima}}$ `>` `0`).

As shown above, the selection criteria are extended by track quality restrictions. A minimum track candidate requirement is a MDC track matched to a hit in the META detectors. The MDC track must point exactly to the META cell that its matched with. Moreover, along the rod the matching distance is limited to $\mathrm{MetaQa_x} < 3$. Tracks at the detector edges are removed by applying a fiducial volume cut. In addition, the number of fake tracks is reduced by limiting χ^2_{RK} to 100 at maximum, which is not very strict but removes obvious fake contributions. Also, the momentum is restricted to a lower limit at p = 100 MeV/c, since tracks with smaller momenta show a decreased track quality due to their curvature. Tracks with momenta above 1000 MeV/c are also removed, due to fact that the number of electrons decreases exponentially while the hadrons are still abundant. As additional hadron rejection, a minimum ring signature is required.

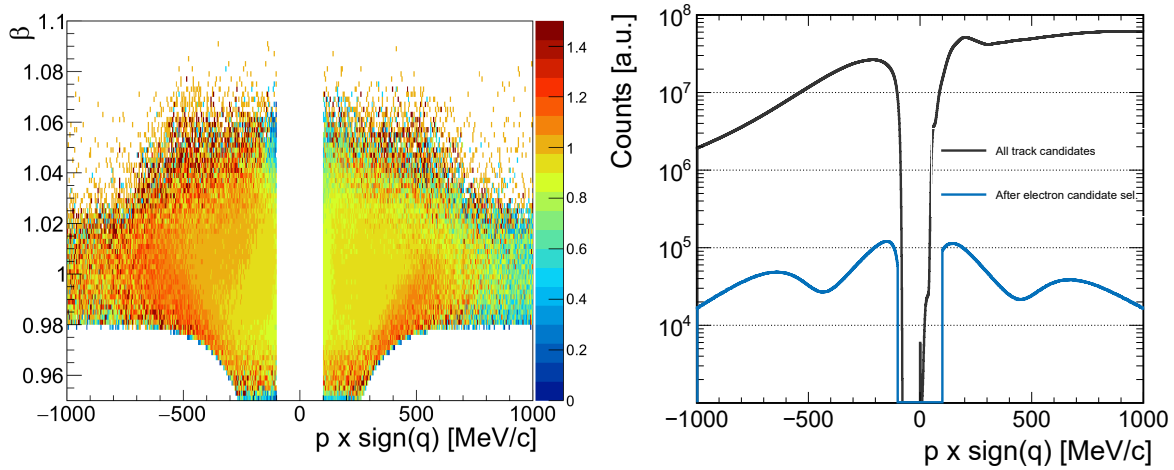

Figure 7.2: Left: A ratio of identified electrons for two different track selections is presented. The results obtained from an analysis including a stricter track selection function is divided by the electrons obtained by a simple track selection function. Values above one indicate an increased number of tracks for the analysis with a stricter selection. **Right:** Momentum distribution for tracks in the RPC acceptance before and after application of the electron candidate selection.

A detailed investigation of the impact of the electron candidate selection on the track sample is shown in Fig. 7.2 (left). It reveals that stricter selection criteria enhance the number of electron track candidates compared to a selection with only basic requirements (see section 4.4).
This is explained by wrongly matched MDC segments. In that case, MDC segments belonging to an e^+/e^- have a worse χ^2_{RK} than a segment belonging to a hadron. As a consequence, the hadron segment will be selected for a electron track and a fake match is created. Those fake matches are removed by requiring a minimum velocity. Hence, only the segment created by the electron is available and the true electron track is reconstructed. After applying all the selection criteria, the number of track candidates is strongly reduced from the mean number of 112 to 0.1 tracks per event (see Fig. 7.2). This reduction is achieved by prohibition of the multiple usage of track parts and requirement of a full track. Furthermore, the selection criteria are tuned for electron identification. Therefore, the strong reduction of the mean number or track candidates is mainly due to rejection of hadron tracks. This indicated in Fig. 7.2 (right) by removal of a lot of candidates with large momenta. After their removal, an exponential drop-off towards large momenta is expected and seen. However, the bumps above 500 MeV/c are created by background tracks and have to be further removed by additional analysis steps.

7.3 Multivariate approach to electron identification

7.3.1 Multivariate analysis toolkit

The advantage of a *multivariate analysis* (MVA) method is to consider multi-dimensional correlations, which enhances the particle identification performance. The Toolkit for Multivariate

Data Analysis (TMVA) [143] is an add-on to the ROOT framework and provides such algorithms for particle identification. Those methods are used for regression with a continuous output value or categorization, which is applicable for particle identification. Before application, all methods need to be trained using signal and background samples. Afterwards, the trained machine learning approaches can differentiate between signal and background tracks out of a data sample containing not yet categorized tracks. The largest challenge, regarding the application of machine learning algorithms, arises during the training procedure, especially in the case of a high number of input variables. Due to the high dimensionality of the attribute space, a large input data sample has to be provided to cover the full phase space during the training procedure. Moreover, a training with a specific data sample might lead to an exact description of signal and background, the so-called *overfitting*. In that case, an application of the trained MVA method to a more general sample would perform badly. For this reason, overfitting has to be avoided by choosing an appropriate data sample for training.

The decision, in order to select the best MVA method, is governed by the classification quality, time of training, time of classification and storage capacity. In the presented analysis, three different MVA methods will be applied and compared. All of them are expected to achieve a high prediction power, but might differ in their capability of handling a different number or type of observables. The first machine learning approach is a *decision tree*. It consists of nodes, whereof everyone has a condition which categorizes the results in two groups. A large number of conditions on attributes leads to a final decision on the output value. Several approaches for training improvements of trees or the decision-making process are available e.g., usage of a large number of classification trees with a small decision strength. A second classification method is a *Bayesian network classifier*. It consists of nodes that represent events. Latter ones are connected via arcs, which represent the conditional probabilities between the nodes. They describe the probability of an event correlated with the occurrence of a second event and are evaluated during the training procedure. Finally, the trained network is used to categorize the output.

A third machine learning method is an *artificial neural network*, which is motivated by the structure of the human brain. A neural network consists of neurons which are represented by a mathematical function, that receives input and delivers output. In a *multilayer perceptron* (MLP), the neurons are assigned to an input layer, output layer and at least one hidden layer in between (see Fig. 7.3). All neurons are connected with every neuron from adjacent layers. The importance of each input connection strength is given by a weight of each connection. An improved identification power arises due to the multiply usage of neurons, which allows to model complex classification functions (see Fig. 7.3).

All three approaches were applied to the data sample for electron identification. As a result, the neural network reaches a better performance, in case of identified electrons and rejected hadrons, than the Bayesian one. However, the decision tree approach achieves a similar electron identification efficiency in case of small training samples. But a large training sample with more

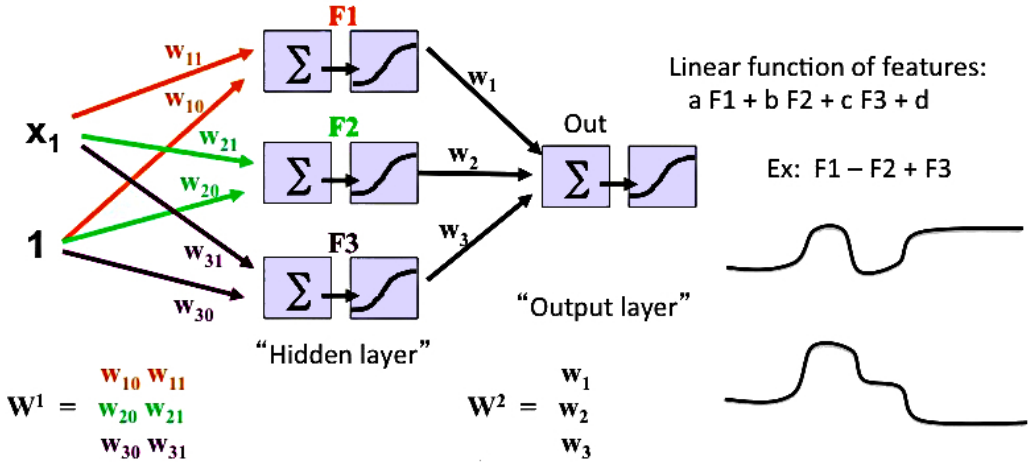

Figure 7.3: Schematic overview of an multilayer perceptron. The values x1 and 1 serve as input for the hidden layer which serve as input for the output layer. w_{xx} depicts the weight of each connection. A combination of the hidden layer nodes creates a more complex function for decision making process. (Picture taken from [144])

signal and background events enhances the identification power of the neural network. Since a large training sample is available and the training time is not limited, the neural network is chosen as the method for particle identification.

7.3.2 A neural network for electron identification

The application of a neural network for electron identification requires three tasks. At the beginning, the analysis approach is trained by a known data sample. Once the method is trained, it is applied for particle identification and a response value is obtained. In the final step, a decision of a response value threshold, to differentiate between signal and background, needs to be set.

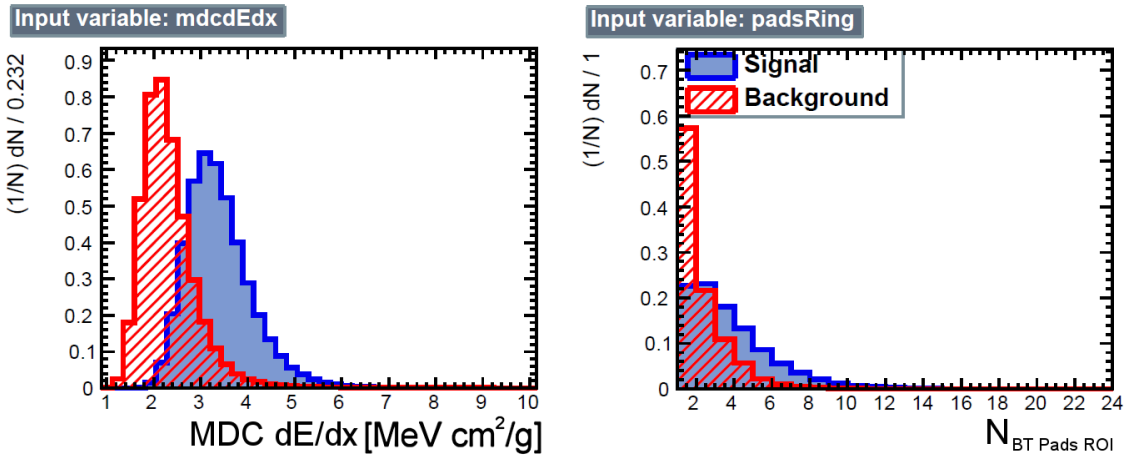

Figure 7.4: MDC dE/dx (**left**) and the number of fired backtracking pads per candidate (**right**). Those are the distributions after electron candidate selection and are used as input for the MVA procedure.

In this analysis, a multilayer perceptron is used. The method is trained with a signal and background sample of simulated data containing tracks that passed the electron candidate selection. As signal sample, electrons equally distributed in momentum, θ and ϕ are generated and identified via Monte Carlo particle ID information to select only true electrons. Moreover, a minimum RICH response ($N_{BT\ \ Maxima} > 0$) is required. As background, a sample of pions and protons, identified via Monte Carlo particle ID, with physical momentum distributions is used. Two examples of input variable distributions are presented in Fig. 7.4. The amount of fired pads in the region of interest does not show a clear separation of signal and background while the MDC dE/dx distribution shows a stronger separation. Both observables are included in the neural network since the separation improves by consideration of multidimensional correlations between all observables. Therefore, the following variables are included in the neural network:

- $\mathrm{N_{BT\ Pads\ ROI}}$
- $\mathrm{Sum_{BT\ Q\ ROI}}$
- $\mathrm{N_{BT\ Pads\ Cluster}}$
- $\mathrm{Sum_{BT\ Q\ Cluster}}$
- $\mathrm{N_{BT\ Cluster}}$
- $\mathrm{N_{BT\ Maxima}}$
- $\mathrm{N_{BT\ Maxima\ 3\sigma}}$
- $\mathrm{N_{BT\ MaximaQ}}$
- $\mathcal{X}^2_{BT}$
- `BT mean ring shift`
- `BT Pattern matrix`
- `METAQa`
- `MDC dE/dx`
- $\mathcal{X}^2_{RK}$
- ϕ inside sector
- Velocity β
- Momentum
- Shower difference (RPC only)
- `TOF dE/dx (TOF only)`

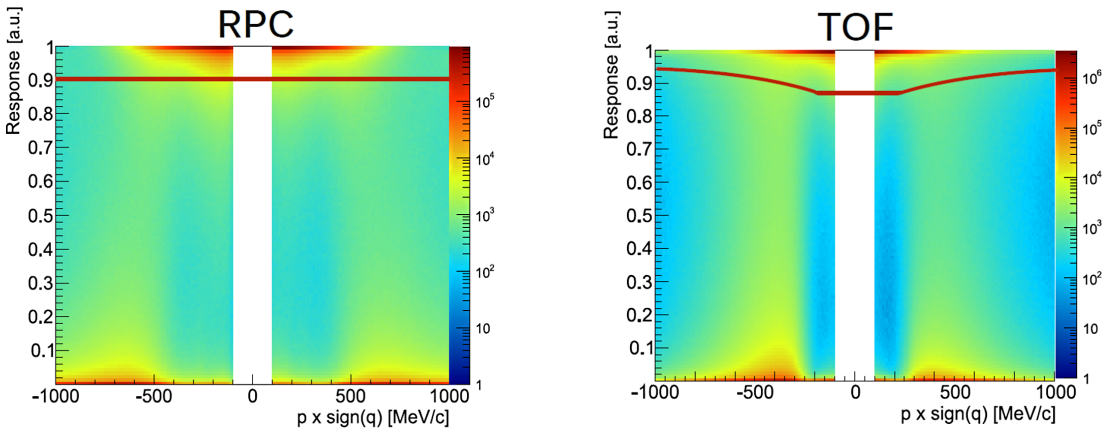

Figure 7.5: MVA response value in the RPC (**left**) and TOF (**right**) regions. The red line indicates the lower boundary for electron and positron selection.

Based on the training results, every variable included to the MVA method enhances the performance of the e^+e^- identification. Further optimization is achieved by variation of the training sample sizes. Enhancing the number of background compared to the signal input events, results in reduction of background in the high momentum region. However, also good electron candidates in the high momentum region are reduced. A variation of the training sample sizes lead to the selection of a training sample containing 100 million signal events and 20 million background events. However, even after application of the neural network identification in the high momentum region (p > 700 MeV/c), hadron tracks are present. This background is not rejected because electrons in the simulated training sample do not have an exponential drop-off towards large momenta. Therefore, the number of electrons is artificially increased in the high momentum region. Consequently, the signal-to-background ratio is much higher than in real data and the neural network underestimates the hadron track rejection. In order to remove the hadrons, the particle identification is extended and a more significant RICH response ($N_{BTMaxima} > 1$) is required to reduce the enhanced hadronic background.

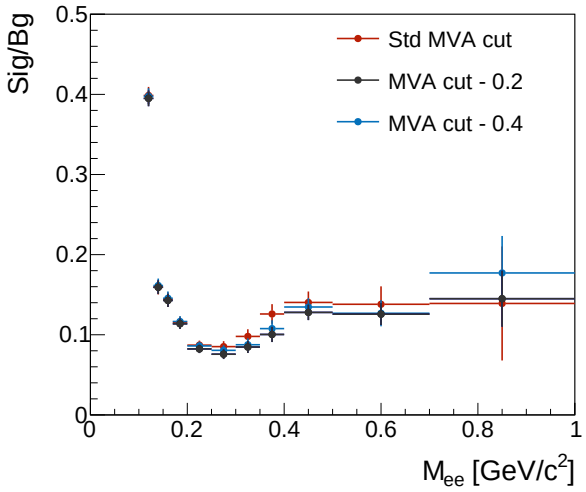

Figure 7.6: Signal-to-background ratio for three different MVA response value cuts. The Sig/Bg value is estimated as the invariant mass signal divided by the combinatorial background. [6]

Finally, the trained MVA method is applied to real data. A response value distribution is retrieved and presented as a function of momentum (see Fig. 7.5). In order to select good electron candidates, a threshold on the response value is applied. Entries with a response value close to 1 correspond to signal and those close to 0 to background. Both cases are well separated, but there are response values between 0 and 1 that are not directly assignable. Those candidates are not negligible and rise towards higher momenta. For the distinction of signal and background in the sample of single candidates, a constant (see Fig. 7.5 (left)), a linear rising or a curved (see Fig. 7.5 (left)) threshold were defined and varied in their threshold limit. The variation is optimized to achieve a good signal-to-background ratio in the invariant mass signal [7] above the π^0 mass. Based on the results, a signal response value limit, in form of a constant (curved) threshold for RPC (TOF), close to 1 improves the purity compared to thresholds at lower response values. This is indicated by Fig. 7.6 in which the standard (Std) cut (see Fig. 7.5) is compared to thresholds that are 0.2 or 0.4 lower. Slight variations of the threshold between 0.9 and 0.95 do not change the result drastically. The resulting thresholds are indicated in Fig. 7.5 as solid lines, for both systems separately.

[7] See chapter 8 for invariant mass reconstruction.

7.4 Reference analysis

The multivariate analysis is expected to achieve a high efficiency and purity. However, the identification is hidden and not easy to interpret by the user. Therefore, a simpler analysis is performed as reference to validate the output of the multivariate analysis. In the reference approach, hadrons are rejected by setting thresholds on one- and two-dimensional observable distributions. The rejection power of this analysis is limited, but the analysis is easy to interpret and defines a baseline for the identification efficiency. Consequently, it is perfectly suited to serve as reference analysis for more complex identification procedures.

Two different analyses, one using the standard ring finder and one using backtracking, are executed. Since the electron candidate selection thresholds removed a lot of background tracks already, only a few additional RICH criteria are applied. In the backtracking analysis restrictions on the following observables, to enhance the significance of the RICH response, are applied:

- **Number of pads (BT)**: Lower limit: $\mathtt{N}_{\mathrm{BT\ \ Pads\ \ ROI}} = 3\ (4)$ for RPC (TOF)
- **Number of maxima (BT)**: Lower limit: $\mathtt{N}_{\mathrm{BT\ \ Maxima}} = 2\ (3)$ for RPC (TOF)
- **Pattern matrix (BT)**: Lower limit: $\mathrm{PM}_{\mathrm{BT}} > 0.3$

The chosen thresholds vary for the RPC and TOF acceptance. In the TOF acceptance, an additional backtracking pad and local maximum in the region of interest is required since more photon hits per electron are expected due to the extended flight path of electrons in the RICH at larger polar angles [8]. Moreover, fake electron candidates, having many fired pads outside the region of interest, are removed by the pattern matrix condition.

A second analysis uses the standard ring finder only. In this analysis, a ring needs to be reconstructed and the RICH matching quality is restricted to select only good rings ($\mathtt{RichQa} < 1.5$). The results of the two reference analyses will follow in section 7.6 and will be compared to the results obtained from the multivariate analysis.

7.5 Close pair rejection

The close pair rejection procedure aims at removal of electrons that are not of physical interest to decrease the combinatorial background. Those are mainly produced by photons converting in the detector material. Those electrons enhance the combinatorial background and should be removed. The photon conversions are characterized by small opening angles, they are so-called *close pairs*. The detection of close pairs is limited by the MDC position resolution of 1-2° [9] and the fact that two separate rings in the RICH detector do not overlap for opening angles smaller than 4°. Consequently, a search of tracks and track segments around identified electrons to search for true close pairs is performed.

[8] See section 2.3.1

[9] 60–100 μm (120–200 μm) in polar (azimuthal) angle direction

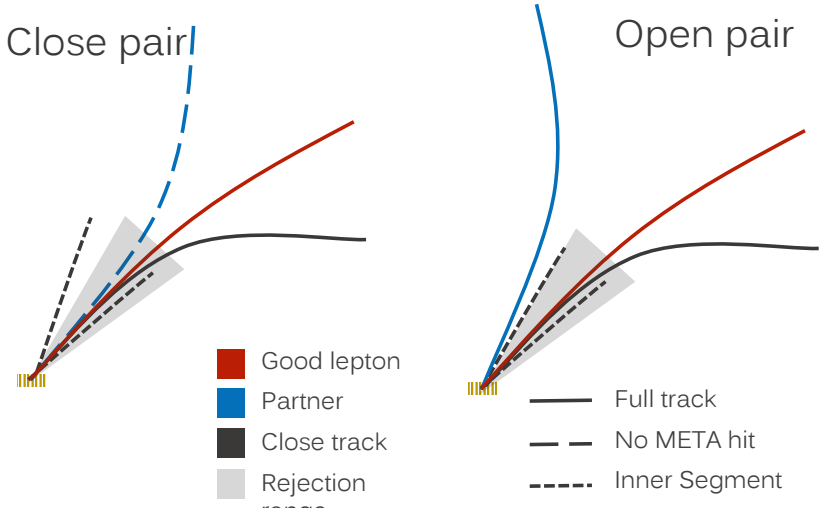

Figure 7.7: Example of a close and open pair surrounded by close hadron track or track segments. A close pair rejection area is indicated by the gray triangle.

In Fig. 7.7 (left), a close pair is rejected properly since the conversion partner is within the rejection range. However, random matches to a close by hadron might lead to false removal of electrons from open pairs (see Fig. 7.7 (right)). This can be avoided by a preselection of the close partner which is aiming for hadron rejection. This reduces the probability of matching an identified electron from an open pair to a random close by hadron. Consequently, the probability that only true close pairs are removed is enhanced.

The implementation of the rejection is based on a search for track signatures within a restricted angular range around identified electron tracks. The opening angle (α) range rises with the polar angle to account for the reduced track density dependence at larger polar angles (Θ) and increases linearly from $\alpha = 3.46°$ at $\Theta = 20°$ to $\alpha = 4.5°$ at $\Theta = 85°$.

Due to the small opening angles, close tracks will mostly share fired RICH pads (see section 5.4.4). Hence, only information provided by the drift chambers and time-of-flight detectors is used. In the first step, every candidate in the opening angle range is considered as possible conversion partner. Since the opening angle might be below the tracking resolution, even the usage of the same MDC segment for multiple for track combinations is allowed. The electron like conversion partners are then selected by applying the following criteria:

- **Mass**: $m < 10$ MeV/c^2
- **Track Quality**: $\chi^2_{RK} < 50$
- **Velocity**: $\beta > 0.9$
- **Momentum**: $p < 700$ MeV/c
- **Energy loss**: MDC dE/dx < 10
- **Charge**: $q_1 \neq q_2$

Candidates that survive the rejection criteria are considered as electrons. Consequently, the identified electron and the close by electron candidate might originate from a conversion pair. In this case, the identified electron is removed from the sample.

7.6 Results

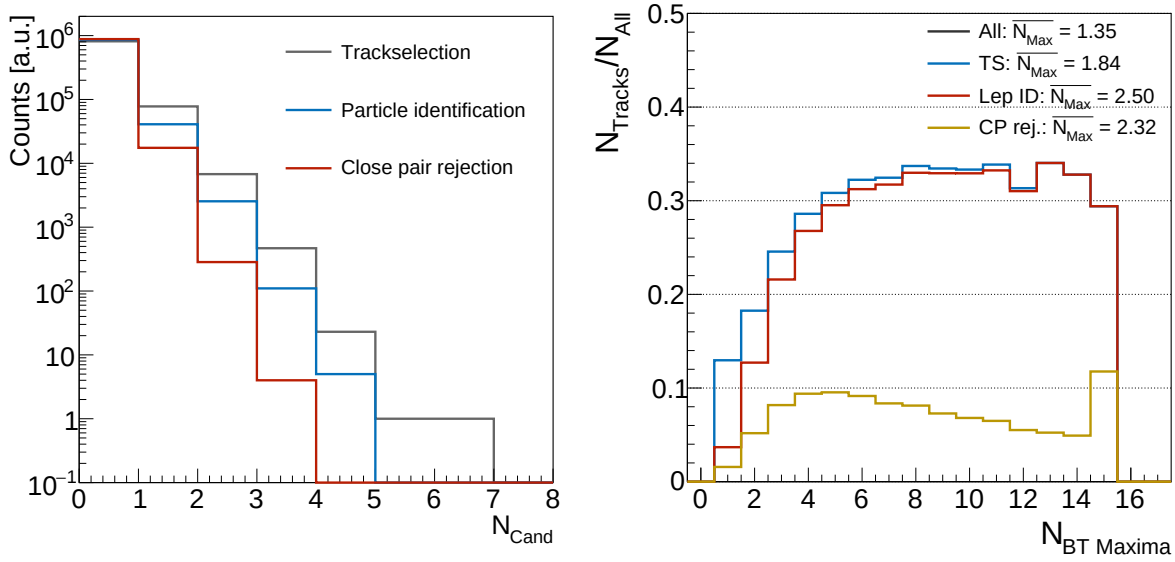

Figure 7.8: Left: Number of identified electrons presented for a reduced data sample with six active sectors. Track candidates before the electron candidate selection are not shown, since they exceed the scale. **Right:** Number of backtracking maxima per candidate divided by the number all track candidates. This ratio provides information about the change of the number of local maxima per candidate. The legend depicts the average number of maxima in each data sample.

In order to check the quality of each single selection step and also the combination of all selection criteria steps, their electron identification performance is assessed. Therefore, the number of electron candidates per event after each selection step is displayed in Fig. 7.8 (left). The strongest reduction of the number of candidates arises from the electron candidate selection. Additionally, the particle identification rejects hadron tracks which reduces the number of particle candidates further. The close pair rejection, has a stronger effect on the number of tracks than the electron identification. This indicates that a large number of electrons from conversion pairs contribute to the sample of identified electron candidates. Finally, the number of electrons is reduced to four tracks per event at maximum.

The result discussed above does not provide any measure of the quality of rejected and accepted electron candidates. To provide a measure of quality, Fig. 7.8 (right) compares number of local maxima per candidate after each selection step. Since the number of local maxima corresponds to the number of identified Cherenkov photons per electron, a high number indicates a better ring quality. As a result, the mean number of maxima increases after the electron

candidate selection and multivariate electron identification procedure. Although the multivariate particle identification removes less tracks than the electron candidate selection, a stronger increase in the maxima number is achieved after application of the multivariate electron identification criteria. In contrast to the previous analysis steps, the close pair rejection shows a small reduction of the mean number of maxima. This can be explained by the removal of tracks with small opening angles, which are matched to partially or fully overlapping regions of interest. In case of overlapping rings, the RICH hits of both tracks are accumulated and the sum is assigned to both tracks as their backtracking information. Those tracks have more maxima than a typical single electron has. As a consequence, this selection step removes tracks with more maxima than average and results in a reduced mean number of maxima.

Besides the estimation of the number of candidates per event and their quality, a comparison of the MVA analysis to the reference analysis monitors its identification performance. The momentum distributions of the reference analyses are compared to the one of the MVA analysis in Fig. 7.9 (left). A clean electron identification is expected to provide an exponentially decaying spectrum. Any deviations from such a shape are caused by impurities due to hadrons or momentum dependent selection criteria. In the low momentum region, all analyses show an exponential drop-off. The MVA analysis shows a much larger number of reconstructed electrons up to a momentum of $p = 500$ MeV/c than the other analyses. The strong efficiency increase of the MVA analysis, is based on the reduced RICH response requirements. They are sufficient, since most of the charged pion background is already rejected by the particle velocity criterion. Above 500 MeV/c, both reference analyses deviate from the exponential shape, due to hadron contamination. This effect is stronger for the backtracking reference analysis, since the single backtracking observables are less decisive than the RICH matching quality of the standard ring finder. In contrast to the reference analysis, the MVA analysis shows still an exponential behavior, due to its enhanced identification quality. However, a step at $p = 700$ MeV/c is present and induced by requiring a more significant RICH response ($\mathtt{N}_{\mathrm{BT\ Maxima}} > 1$), which is necessary to further suppress hadron tracks. To examine the rejected hadrons in more detail, Fig. 7.9 (right) shows the ratio of identified single electrons to input candidates. While electrons are dominant in the low momentum region at high velocities, the charged pion background is mostly present in the velocity region below $\beta = 1$ at higher momenta. The strongest reduction of tracks is present in the area with less pion isolation capability by velocity. Moreover, the selection of at least two maxima above $p = 700$ MeV/c is also visible due to a reduction in the ratio.

For the quality estimation of close pairs, different observables are needed. An effective rejection should remove tracks stemming from conversions pairs, to reduce the background. Furthermore, the number of electron pairs with a large opening angle should be unaffected. In order to check the rejection quality, one simulated electron per sector is embedded in real events. Those electrons can be seen as belonging to an open pair, which should not be rejected by the close pair removal criteria. The embedding quantifies the number of rejected electrons in an environment of realistic background track contribution. Fig. 7.10 (left) shows the removal of

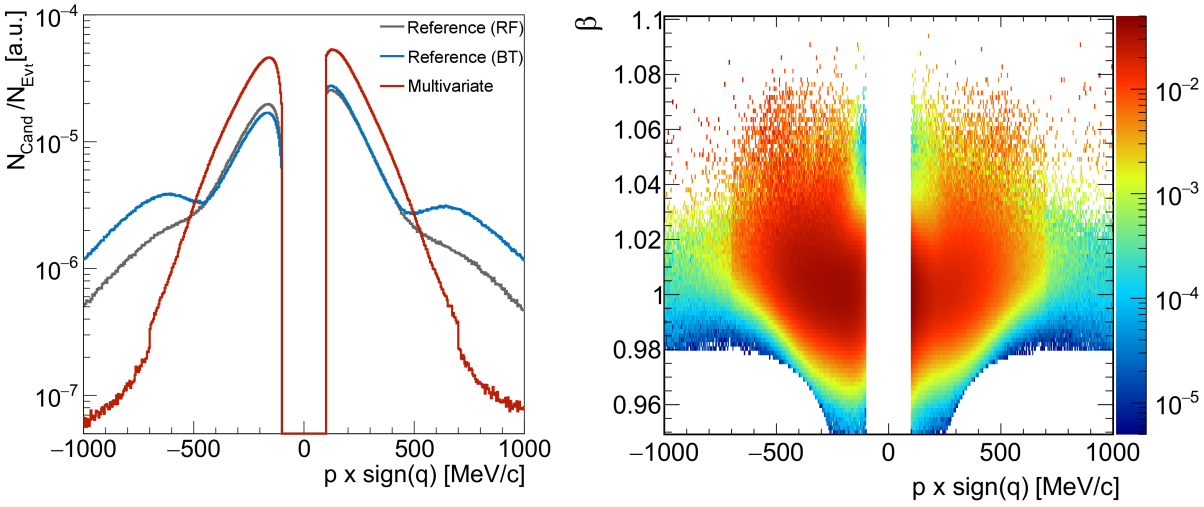

Figure 7.9: Left: Momentum distribution, in the acceptance of the RPC detector, presented after the single electron identification for the multivariate analysis as well as the reference analyses using backtracking (RF) and the standard ring finder (RF). **Right:** Ratio of tracks after single electron identification to all input tracks. It demonstrates the background rejection for tracks in the acceptance of the RPC detector.

electrons due to the close pair rejection criteria. The rejection is stronger in the acceptance of the RPC detector. This is expected due to combinations of electrons with random close by hadron tracks, which are more abundant in the low polar angular region. Therefore, the search range for close by tracks is reduced linearly towards smaller polar angles. However, the decreased search range does not compensate the reduction due to combinations with hadrons completely. Further results are obtained by reconstruction of electron pairs in experimental data since an assessment of the reconstructed pair spectra provides direct information about the dielectron signal quality [11]. The reconstructed combinatorial background is reduced to approximately 20% over the full mass range (see Fig. 7.10 (right)). In contrast to the background, the signal is only reduced to values around 55% in the mass region up to M_{ee} = 0.1 GeV/c^2. As a consequence, the signal-to-background ratio is enhanced and this results in an improved signal quality.

Due to the large statistical error, the signal in the high mass region fluctuates more, but it is still less reduced than the background. An additional cross-check comes from the fact, that the reduction of the pairs should be the product of the reduction of single electrons. An assumption of an equally distributed number of electrons in TOF and RPC, would result in a single electron reduction factor of approximately 0.8 which corresponds to a pair signal reduction factor of 0.64. Latter one is comparable to the value estimated with the pair spectra, especially by consideration of the large statistical errors and the uncertainty due to the approximation of the electron momentum distribution.

In order to demonstrate the standard selection as optimal solution, a variation of the pair rejection criteria is performed (see Fig. 7.11). In this figure, the close pair rejection explained

[11] See chapter 8 for explanation of the pair reconstruction.

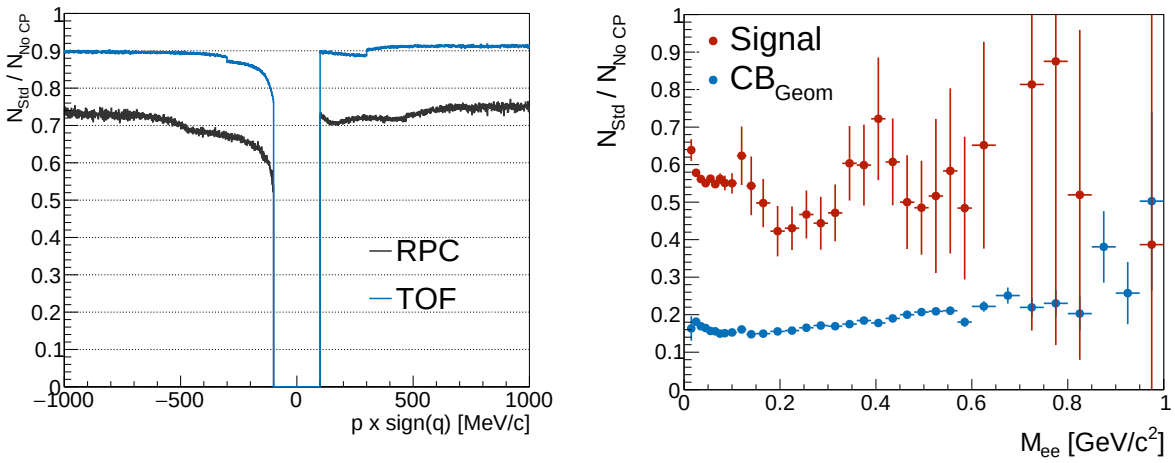

Figure 7.10: Left: Ratio of the number of identified electrons with and without close pair rejection. As electron source, one electron per sector is embedded in real events and analyzed along with the real data sample. **Right:** The signal and background (CB_{Geom}) yield is obtained from reconstructed pair spectra.

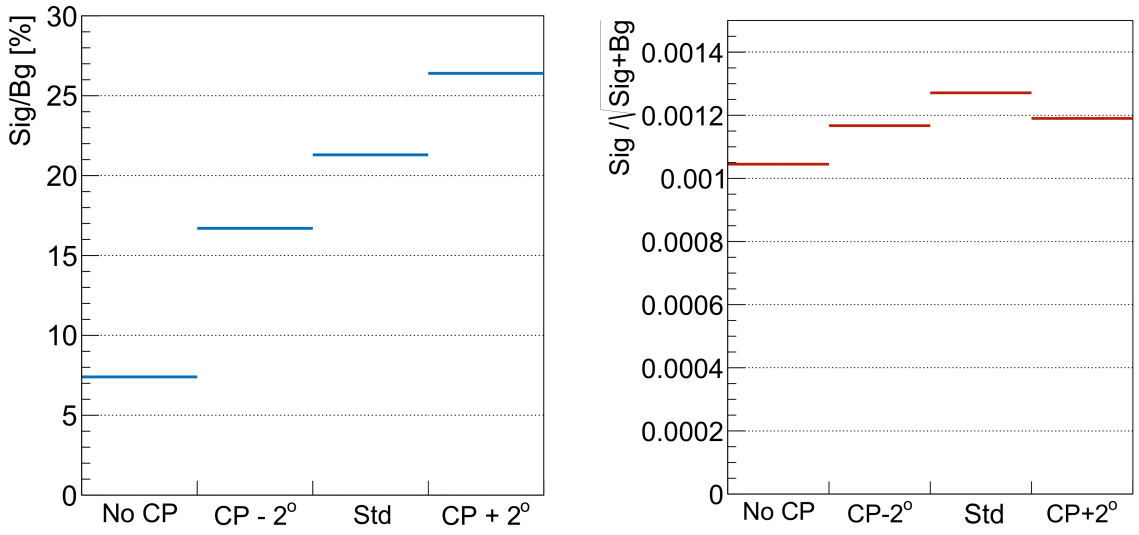

Figure 7.11: The significance (**left**) and signal-to-background ratio (**right**) are estimated with invariant mass distributions [10] in the mass range from 300 MeV/c^2 to 700 MeV/c^2. In both figures, results after a variation of the close pair rejection criteria are presented. The standard (Std) selection is compared to others with varying the upper angular limit (CP$\pm$2°) and without close pair rejection.

in section 7.5, the so-called standard (Std) analysis, is compared to results obtained with variations of the rejection criteria. The signal-to-background ratio rises strongly with an increasing rejection angle limit. Although the signal-to-background ratio is rising steadily, the signal yield is reduced. Therefore, the significance of the signal is investigated in addition and shows a maximum for the standard rejection criteria. Stronger rejection criteria remove signal, because of fake combinations, which are more likely due to increased search range for close partners. Consequently, the applied selection performs the best in order to improve the signal quality together with small losses of signal.

In addition to the quality checks based on experimental data, the selection is tested with simulated data as well. This study is motivated by the RICH performance investigation in section 6.2.3. As an example, the number of cluster pads per candidate observable is chosen to demonstrate the level of agreement between experimental and simulated data (see Fig. 7.12). In order to obtain more conclusive results, the distributions are plotted separately for tracks with good ($0 < \texttt{RichQa} < 1.5$, see Fig. 7.12 (left)) and bad ($0 > \texttt{RichQa}$ or $\texttt{RichQa} > 1.5$, see Fig. 7.12 (right)) matching quality. The candidates with good matching qualities show only a shift of 0.6 pads in the overall distribution, while the yield for the distribution of candidates with bad matching qualities deviates strongly. Especially, the number of tracks with a small number of pads per candidate in simulated data exceeds those in experimental data strongly. This results from the tuning of the RICH simulation, which was based on well identified electrons with good rings only. Therefore, electrons with bad ring signatures are not modeled properly.

In summary, the single electron identification gains in efficiency when applying the MVA method. A large number of hadron tracks and fake combinations are removed properly by the electron candidate selection and multivariate electron identification. This is indicated by the pion suppression factor (see Fig. 7.13 (left)) revealing that at maximum two out of 10000 pions are reconstructed as good electron candidate. Afterwards, the close pair rejection improves the signal quality which is indicated by a maximized significance. However, a comparison between experimental and simulated data reveals deviations between the two. This is of major importance for the efficiency correction of tracks. Finally, the reconstructed tracks of events that are used for pair reconstruction are presented in Fig. 7.13 (right). The distribution is dominated by one e^+e^- pair per event.

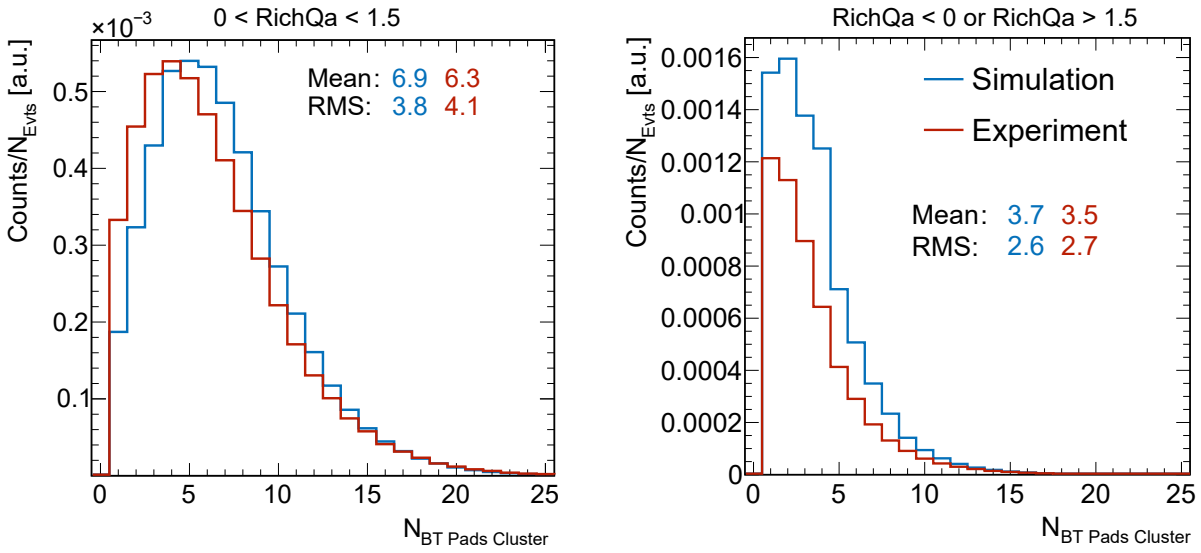

Figure 7.12: Number of pads in clusters per candidate shown for rings with good (**left**) and bad (**right**) matching quality.

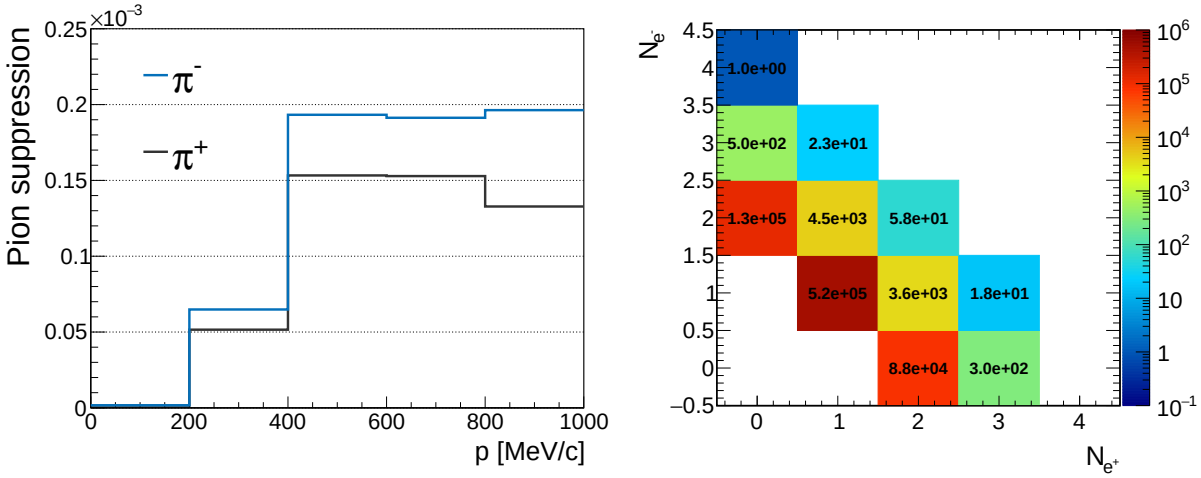

Figure 7.13: Left: Pion suppression as a function of invariant mass. The value is estimated using $\pi^{+/-}$ embedded in real events and constructed as ratio of pions identified by the electron identification to pions in the HADES acceptance. **Right:** The number of reconstructed electrons and positrons per event. Only events with at least two candidates are used for pair reconstruction.

Chapter 8

Reconstruction of dielectron signal

In the previous chapter, the results for the single electron identification were presented. The next step of this analysis is focused on pair reconstruction, including the determination of the invariant mass, p_T, rapidity and helicity distributions of the emitting source. Since there is no information of the relation between particles available, all possible unlike-sign pair combinations on event-by-event basis are calculated. Unfortunately, a large amount of combinatorial background (see Fig. 8.1) is created in this approach. This background contribution must be subtracted from all pair combinations in order to estimate the true signal pairs. A high quality background description is necessary for a well estimated signal contribution. The signal quality can be improved by increasing the signal-to-background ratio. Hence, a recursive minimum opening angle restriction is applied to reduce the background. Each lepton having at least one opposite-sign partner below the opening angle limit is removed before pair combination. The remaining combinatorial pairs are estimated by two approaches for background calculation. Systematic deviations in the background estimation will be corrected by an additional correction factor.

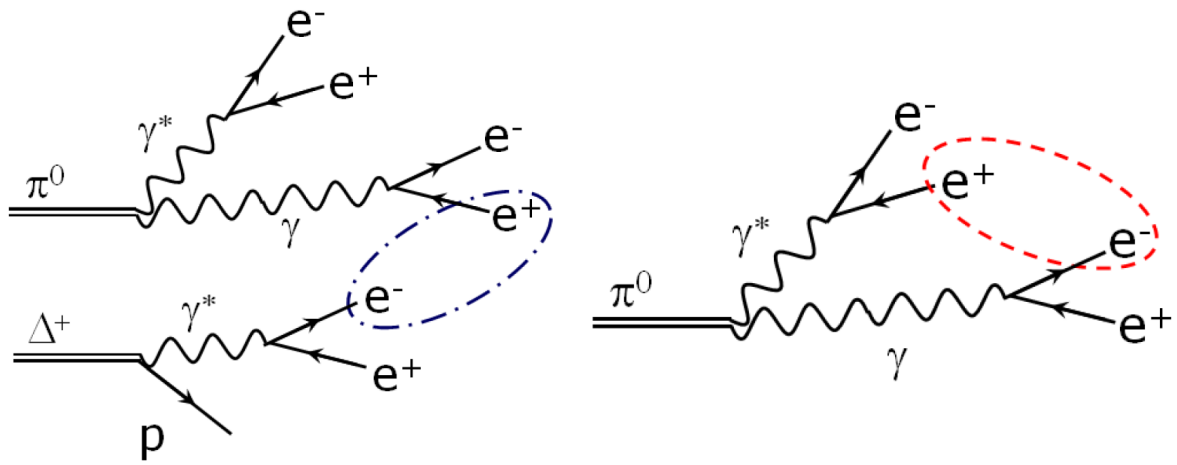

Figure 8.1: Illustration of two different background types. In case of uncorrelated background (**left**), the paired leptons originate from different sources. Semi-correlated background (**right**) is caused by leptons from an identical source.

8.1 Methods for combinatorial background estimation

8.1.1 Phenomenology of the combinatorial background

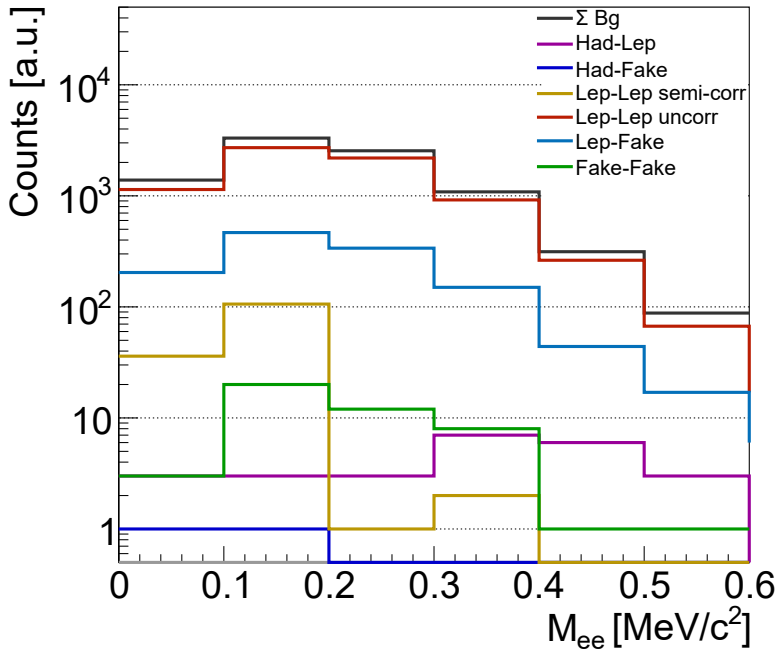

Figure 8.2: Fractions of different pair combinations that form combinatorial background pairs. The sum of all background contributions is indicated by the black line. The identified single leptons are scaled by a factor of 0.5 to accounted for the overestimated efficiency in simulation (The value is obtained as average correction factor estimated in section 9.2).

The background comprises wrong pair combinations of tracks, that can be subdivided into various background sources of different origin. Besides real leptons, also a small number of hadrons or fake tracks, created due to wrong combination of detector hits, are reconstructed and contribute to the background. In case of uncorrelated pairs (see Fig. 8.1 (left)), each lepton that originates from different "mother" particles, leading to a structureless background contribution. In contrast, semi-correlated background (see Fig. 8.1 (right)) is created in case two tracks with different "mothers", but the same "grand mother", are paired. Due to their correlation, the background shape can show bump-like structures.

To estimate the sources of background contributions, a simulated cocktail containing π^0, η and dielectrons from a coarse-grained transport approach is embedded in UrQMD events. The particles are identified as described in chapter 7 and categorized in electrons (LEP), hadrons (HAD) and fake matches (FAKE) using Monte Carlo information. The results in Fig. 8.2 compare the background sources contributing to the combinatorial background and show, that pairs of two electrons are the most abundant background source. Moreover, uncorrelated electron pairs have a larger contribution than semi-correlated ones. Latter ones are mostly present in the low-mass region, since they are formed by decay products from π^0-Dalitz or $\pi^0 \rightarrow \gamma\gamma$ de-

cays. At higher masses, their relative contribution reduces. Also, fake tracks contribute to the background in the full mass range. They are mostly paired with a true electron and form uncorrelated background. Pairs with one or two hadrons are very rare. This indicates a high purity of the single electron sample.

In conclusion, the low-mass region (M_{ee} <0.15 GeV/c^2) requires consideration of semi-correlated background while the higher mass region comprises mostly of uncorrelated background. In the following section, two methods for estimation of appropriate background contributions will be discussed.

8.1.2 Same-event like-sign background

One approach for background estimation is based on combination of two electrons from the same event. In this approach, like-sign pairs are used for the background description. For implementation, the geometrical (CB_{geom}) or arithmetical (CB_{arith}) mean of like-sign pairs is calculated to estimate the combinatorial background:

$$CB_{geom} = 2\sqrt{N^{++}N^{--}}, \tag{8.1}$$

$$CB_{arith} = N^{++} + N^{--}. \tag{8.2}$$

A check of the validity of this method was investigated in [145] for muon contributions in the dilepton spectrum of the NA50 experiment. The presented background estimation approach is based on the assumption of an independent production of muons from semi-leptonic decays. Moreover, the number of leptons per event is assumed to follow a Poisson distribution, while the momentum correlation for semi-correlated background contributions is neglected. The procedure was tested for examples with absence and presence of semi-correlated background. It is concluded, that the subtraction procedure works well without semi-correlated background contribution but deviates for an increasing contribution of semi-correlated background.

In HADES, semi-correlated background has only a small contribution in the π^0 mass range. In the mass range above π^0, the amount of semi-correlated background is completely negligible. Comparing the background estimated with CB_{geom} and CB_{arith} shows differences in the background yield. The yield of the combinatorial background using the geometrical mean is always lower or equal to the one using the arithmetical mean. However, only the geometrical mean does consider deviations due to imbalance of the number of charged particles and is therefore chosen as method for same-event like-sign background estimation.

8.1.3 Mixed-event background

Instead of using electrons from the same event, uncorrelated pairs can also be reproduced by mixing particles from different events. The so-called event-mixing procedure offers the advan-

tage of large statistics due to multiple usage of electrons from a given event. However, semi-correlated background is not reproduced by this technique. An accurate background description requires the consideration of the event characteristics. The following four event properties are considered:

- **Centrality**: The electron reconstruction efficiency is centrality dependent.
- **Reaction vertex**: The acceptance is modified due to variations in the vertex position.
- **Reaction plane**: Flow effects modify particle distributions as a function of their emission angle.
- **Time**: Small efficiency losses of detectors systems for a limited time period modify the particle reconstruction efficiency.

Technically, the event mixing [139] consists of two buffers for electrons and positrons, that are filled with identified electrons. Once the buffers are filled, the first particle in each buffer is combined with every particle of the oppositely charged particle buffer. After all combinations, the first element in each buffer is removed. This procedure is executed iteratively every time the buffer is filled completely. As already mentioned, the electron properties depend on the event characteristics and electron candidates with the similar event properties should be categorized in the same event class. Consequently, two buffers for each event class are implemented, whereby electrons are only mixed within their specific event class.

For the application, the granularity of the event classes for a sufficient background description is estimated. The amount of event classes is a trade-off between the precision of background description and many pairs to reduce statistical fluctuations in each event class. To check the differences, due to variation of the event mixing setup, the number of event vertex classes and reaction plane classes as well as the number of input files is varied. Furthermore, the input electrons are selected out of events with at least one electron, two electrons or two electrons with opposite charge. The different variations are compared to a standard event class setup using four multiplicity, seven vertex and four reaction plane classes, calculated using 250 input files and events with at least two identified particles. The deviations from the standard background are estimated by building up a ratio of the yield estimated with a modification of the event mixing setup to the yield estimated with the standard setup.

In the result presented in Fig. 8.3 (left), the black points have the strongest deviations from unity in the mass region above 0.20 GeV/c^2. Therefore, more than three event vertex classes should be considered for the mixed-event background calculation. The setup with 15 vertex classes does not have significant systematic deviations from unity over a broad mass range. A comparison of a different number of reaction plane bins shows a deviation of the order of 1% above a mass of 0.20 GeV/c^2 in case only one reaction plane class is used. In contrast, the setup with 8 reaction plane classes does not show a systematic deviation. In conclusion, the standard event mixing setup describes the background shape sufficiently.

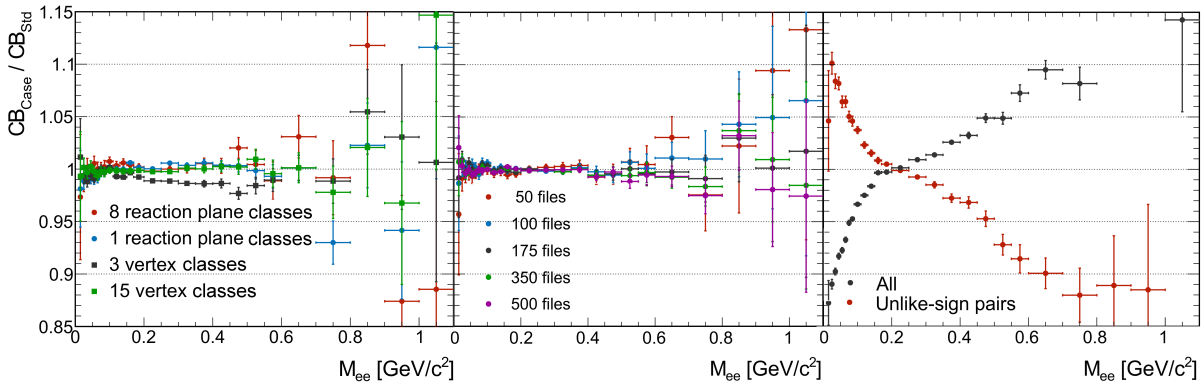

Figure 8.3: Variation of the combinatorial background (CB) when applying more refined event classes ($N(Mee)/N^{Std}(Mee)$). A variation of the event vertex classes and reaction plane (**left**), the number of input files (**center**) and the input event types (**right**) is shown.

In addition, the impact of varying the number of input events is determined. Since the detection efficiency might vary over time, the background is reproduced the best for short timescales. Using large time scales might smear those detector effects and modify the background shape. A comparison of setups with a different number of input files in Fig. 8.3 (center) reveals no significant deviations of multiple neighboring bins from unity for the setup using 50, 100 or 175 input files. There is a slight indication that the setup using 350 and 500 input files underestimates the background yield of the standard setup above a mass of 0.4 GeV/c. This hints that the impact of the number of input files to the background shape is small. Finally, 250 is chosen as number of files to assure a high statistic coverage in the high mass region.

An impact of using events with at least one electron or at least two oppositely charged electrons are compared to the standard setup in Fig. 8.3 (right). The different input types modify the slope of the event mixing background strongly. Since the same-event background estimation is based on events having at least two electrons, these are also chosen for the mixed-event background estimation.

The mixed-event background has to be properly normalized. For that we use the same-event like-sign. The mass range between 0.20 GeV/c^2 and 0.30 GeV/c^2 is chosen for normalization. The range is tuned to avoid the application of the mixed-event background in the semi-correlated background region. Moreover, the statistical fluctuations in the same-event like-sign background should be small. Finally, the combinatorial background consists of the same-event like-sign background below and the mixed-event above a mass of 0.2 GeV/c^2.

8.2 Correction for unlike-sign/like-sign pair differences

In HADES, the particles are bend by a magnetic field to determine their momentum. Electrons and positrons are bend in different directions. This effect is of importance for the particle acceptance but also for their detection efficiency. Since the same-event like-sign background is

estimated using a different charge combination than for the actual unlike-sign background, the background distribution needs to be corrected for these efficiency and acceptance differences.

The correction is based on like-sign and unlike-sign pair distributions estimated with event mixing. For the estimation of the acceptance and efficiency difference, the so-called *k-factor* [146] is constructed as a ratio of unlike-sign pairs to the geometrical mean of like-sign pairs:

$$k = \frac{N^{+-}}{2 \cdot \sqrt{N^{++} \cdot N^{--}}}, \tag{8.3}$$

where the N^{+-},N^{++} and N^{--} are the number of pairs with respective charge obtained from event mixing. The resulting k-factor is presented as a function of opening angle and mass in Fig. 8.4 (left). At low masses, two areas with a strong deviation from unity are clearly visible. More specifically, the k-factor at an opening angle $\alpha \approx 20^{\circ}$ is smaller than 1. This arises in case of a pair close to the detector edge (see Fig. 8.5 (Case 1)). At one detector edge, only particles with one specific charge are bend out. For this reason, the unlike-sign yield is reduced at the small and large polar angle edge of HADES. Therefore, like-sign pairs are more likely than unlike-sign pairs for combinations of electrons from the same detector edge. Consequently, the combinatorial background is overestimated.

The second significant deviation from unity is present at opening angles above $\alpha > 60^{\circ}$. It is caused by combinations of an electron from the inner with one from the outer detector edge. Since one specific charge is bend out at a given edge, mostly unlike-sign pairs will be reconstructed in case of a combination of electrons from opposite detector edges (see Fig. 8.5 (Case 2)). As a consequence, like-sign pairs are reduced. Therefore, the like-sign yield needs to be increased. At larger masses the k-factor is flat but still slightly above unity.

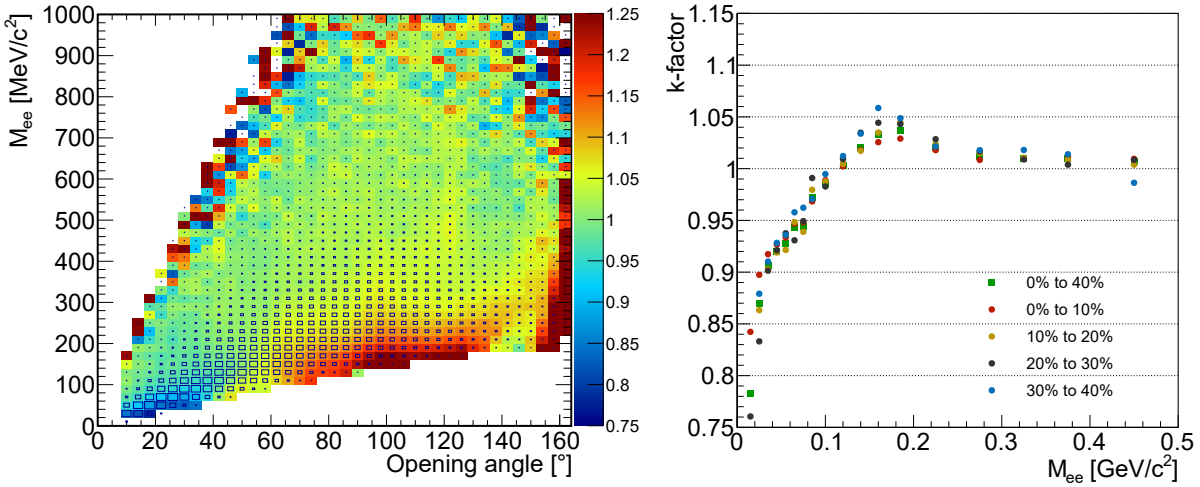

Figure 8.4: Left: k-Factor as a function of mass and opening angle for 0-40% centrality. The relative frequency of pairs in each bin is indicated by the size of the blue boxes. **Right**: Centrality dependent k-factor, where the statistical errors are neglected to enhance the visibility. The statistical errors rise towards larger masses and reach $\approx 1\%$ at $M = 0.15$ GeV/c^2 and $\approx 1.5\%$ at $M = 0.45$ GeV/c^2.

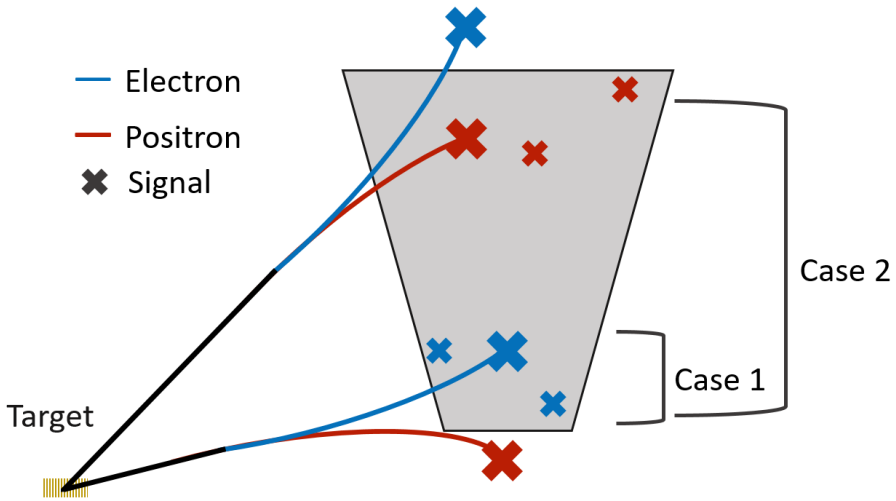

Figure 8.5: Two cases that create pair sign sign efficiency and acceptances differences. Example tracks are indicated by lines and will be bend differently in dependence of their charge. Consequently, hits of one charge are accumulated at one detector edge.

Finally, the combinatorial background distribution of a one dimensional observable (e.g. mass) is multiplied with the respective one dimensional k-factor. The k-factor is evaluated and applied for each centrality class, separately (see Fig. 8.4 (right)). All k-factors show a similar trend, which is expected since the effects from acceptance and efficiency are the same for all centrality classes. However, a general decrease of the k-factor towards more central events is clearly visible. This effect might be explained by fake tracks. Since the number of outer segments is larger in more central collisions, it is more likely to build a fake match of an inner MDC segment with a random outer MDC segment and create a fake track. In this case, the charged particle imbalance is reduced and more like-sign pairs are reconstructed. A more differential application (e.g., mass and opening angle) does not modify the resulting total background distribution compared to k-factor application in one dimension (e.g. mass) only.

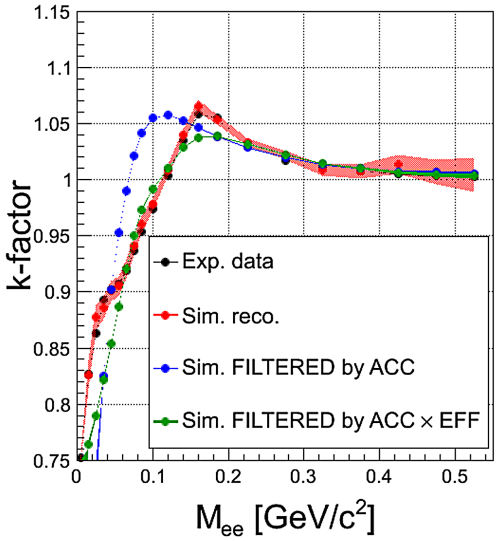

Figure 8.6: k-Factor estimated with simulated an experimental data. The Exp. and Sim. results are obtained with reconstructed tracks. The filtered curves are estimated by weighting of GEANT tracks with efficiency and acceptance. (See chapter 9 for efficiency and acceptance estimation.) Statistical errors are only noticeable using simulated data and are indicated by the red band. (Picture taken from [139])

In order to understand the systematic behavior of the k-factor, the reconstruction was studied in experimental and simulated data (see Fig. 8.6). The curve that was only filtered by acceptance differs strongly from the other curves. This indicates that the efficiency has to be taken to account for corrections. All other cases do not differ much among them. The largest deviations be-

tween the different methods appear in the low-mass region $M_{ee} < 0.2$ GeV/c^2. This is expected, since the acceptance and reconstruction differences are the strongest for single electrons with small momenta, that result in small invariant masses for pairs.

8.3 Results

The combinatorial background was reconstructed and the k-factor for correction of pair-sign dependent efficiency and acceptance effects was estimated. For signal reconstruction, the same-event like-sign background is multiplied by the k-factor for each centrality class separately. To adjust the background contribution in the high mass region, the mixed-event background is matched to the same-event background in the mass range between 0.20 GeV/c^2 and 0.30 GeV/c^2. All pair distributions are limited to a minimum opening angle of a pair. An application of different opening angle thresholds resulted in a 9° limit as the best option. A restriction to opening angle limits below 9° results in worse background rejection while the application of opening angle limits above results in an increased reduction of the signal over the whole mass range. Finally, the background is subtracted from the spectrum of all unlike-sign pairs and results in the signal spectrum.

In order to check the background estimation quality, the same-event and mixed-event background are reconstructed in experimental data (see Fig. 8.7). The overlapping distributions agree over a broad mass range and the largest deviation arises in the mass region $M_{ee} > 0.40$ GeV/c^2. Those deviations are still within the statistical errors. The only deviation beyond, arises due to semi-correlated background in the low-mass region around 0.10 GeV/c^2.

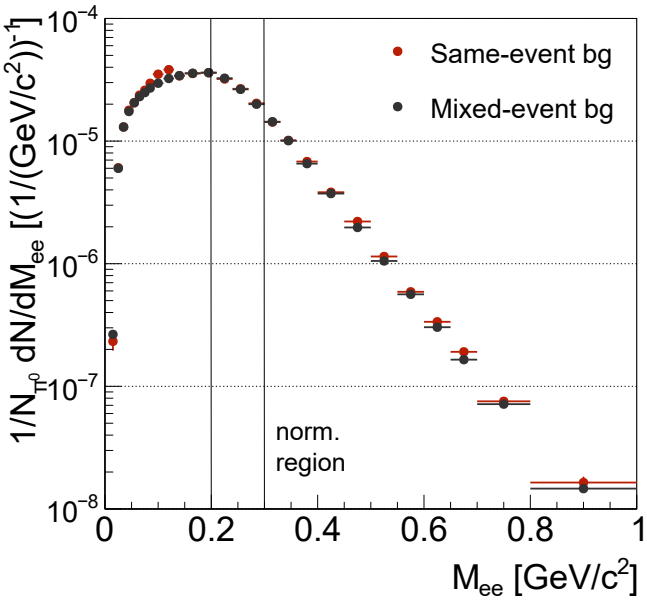

Figure 8.7: Same-event and mixed-event background estimated based on real data.

Finally, the signal spectrum is presented in Fig. 8.8. In the mass region up to 0.15 GeV/c^2, π^0-Dalitz decays are the dominant contribution. The distribution does not follow a Dalitz shape towards smaller masses, due to the 9° restriction on the opening angle of pairs. In contrast to the low-mass region, the distribution at the higher mass region is rather continuous. The corresponding signal-to-background ratio is shown Fig. 8.9 (left). At low masses the signal-to-background ratio is high and gets lower for larger masses. A minimum of the ratio is present in the mass region between 0.15 GeV/c^2 and

0.30 GeV/c^2. As a consequence, the background knowledge in this specific region must be very precise, since the background quality has a stronger influence on the signal yield. The ratio is enhanced in the high mass region to approximately 20%. However, the signal quality does not improve further due to the statistical error of the unlike-sign pair spectrum. Therefore, further improvements of the statistical error of the mixed-event background will not lead to an improved signal quality. Additionally, the significance, i.e. $Sig/\sqrt{Sig+Bg}$, is shown in Fig. 8.9 (right). It drops towards higher masses due to the decreased number of signal pairs. The rise of the signal-to-background ratio around M_{ee} = 0.30 GeV/c^2 is reflected in the significance curve by a small increase. But in total, the quality of the spectrum is mainly guided by the number of produced pairs.

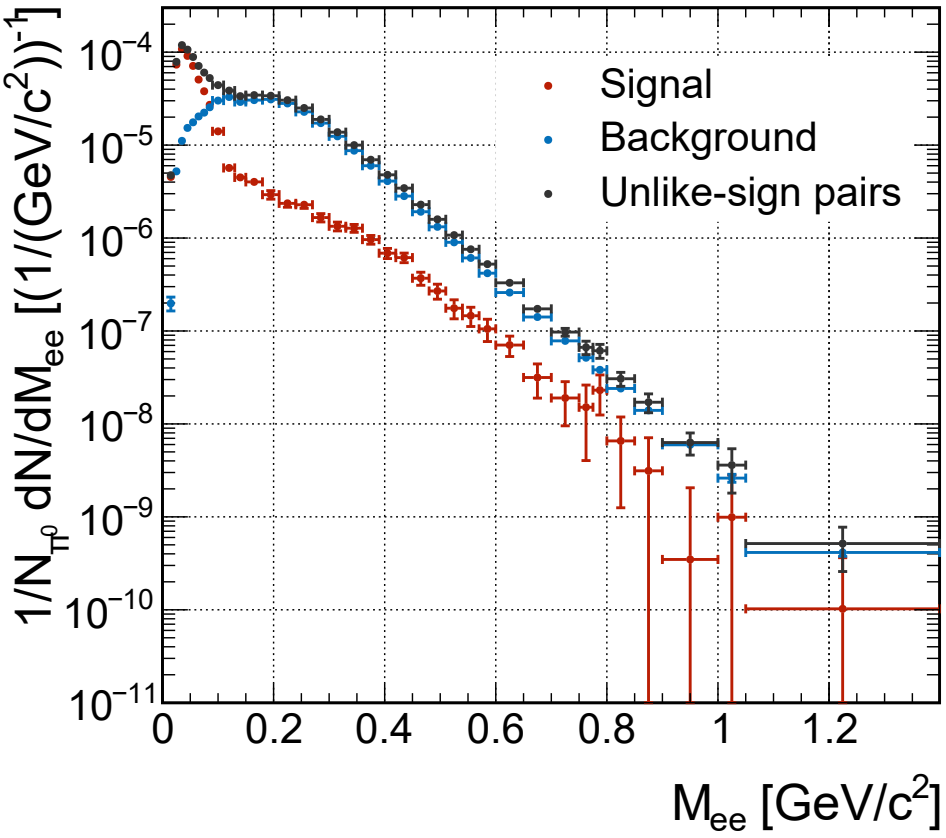

Figure 8.8: Reconstructed signal (red circles) after background subtraction is shown together with the sum of unlike-sign pairs (black circles) and the estimated combinatorial background (blue circles).

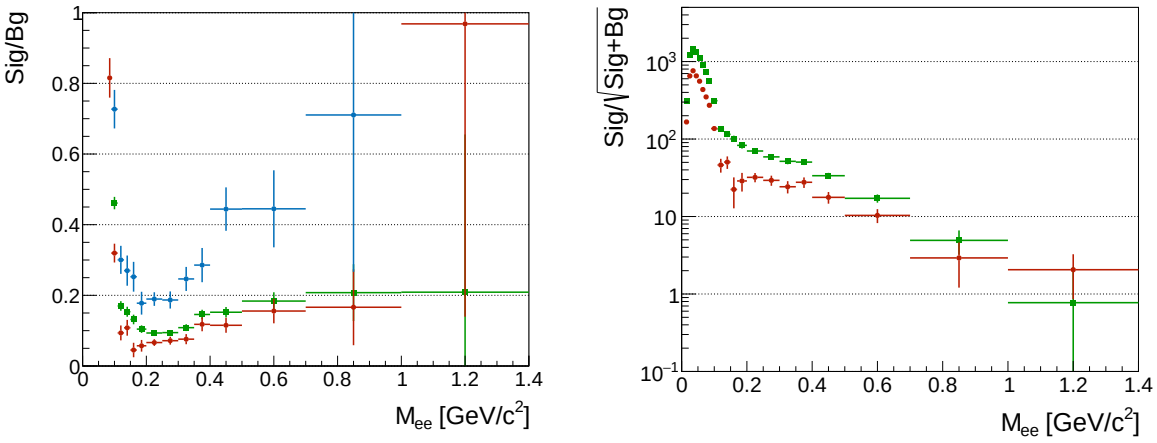

Figure 8.9: Left: Signal-to-background ratio as a function of invariant mass for $0-40\%$ (green squares), $0-10\%$ (red circles) and $30-40\%$ (blue circles) centrality. **Right:** Significance as a function of invariant mass for $0-40\%$ (green squares), and $0-10\%$ (red circles) most central collisions. It is mainly guided by the lower number of pairs towards higher masses.

8.4 Systematic errors due to combinatorial background subtraction

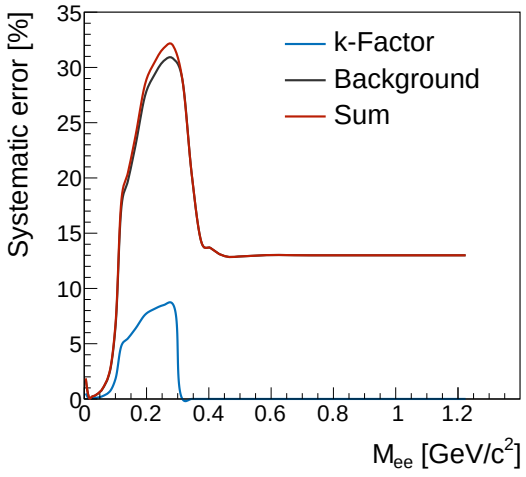

Figure 8.10: Systematic error arising from the background estimation method. All curves are scaled by the signal-to-background ratio to propagate the background error to the signal.

The resulting combinatorial background distribution has been presented section 8.3 [139]. Every method applied for background estimation contains systematic uncertainties which have to be evaluated. In general, there are two uncertainties, one arising from the uncertainty of the k-factor determination and a second one from the background estimation itself.

The error of the k-factor is estimated by a comparison of the k-factors derived from experimental and simulated data (see Fig. 8.6). The deviations between the different generation approaches are used to evaluate the errors. Only the approaches based on reconstructed data are used. Otherwise, the efficiency and acceptance error of filtering would be also considered. An estimation of the maximum differences between the methods using simulated and experimental data reveals, that the methods differ within 0.5% in mean. This error is set in the range at which the k-factor is applied ($M_{ee} < 0.3$ GeV/c^2). As second systematic uncertainty is caused due the variation of the background yield. This error arises, due to systematic deviations in the evaluation procedure of the same-event like-sign and the mixed-event unlike-sign

background. The differences in the yield are estimated by choosing two different normalization regions, namely the mass ranges of 0.2–0.3 GeV/c^2 and 0.3–0.4 GeV/c^2. A comparison of the background obtained with the two-different normalization regions results in a variation by 1.8% of the background. Since the origin of the deviations can not be assigned to the same-event or mixed-event background, it is used as a general uncertainty of the background over the full mass range.

Both background errors are added quadratically and have to be scaled by the signal-to-background ratio in order to be used as error on the signal:

$$\frac{\Delta N_{BgTot}}{N_{BgTot}} = \left(\sqrt{\frac{\Delta N_k}{N_k}^2 + \frac{\Delta N_{Bg}}{N_{Bg}}^2} \right) / \frac{Sig}{Bg} \tag{8.4}$$

The result of systematic error due to the background contribution is shown in Fig. 8.10. In conclusion, the errors are dominated by the signal-to-background ratio. Therefore, a maximum error is reached in the mass region between 0.2–0.3 GeV/c^2.

Chapter 9

Efficiency and acceptance correction

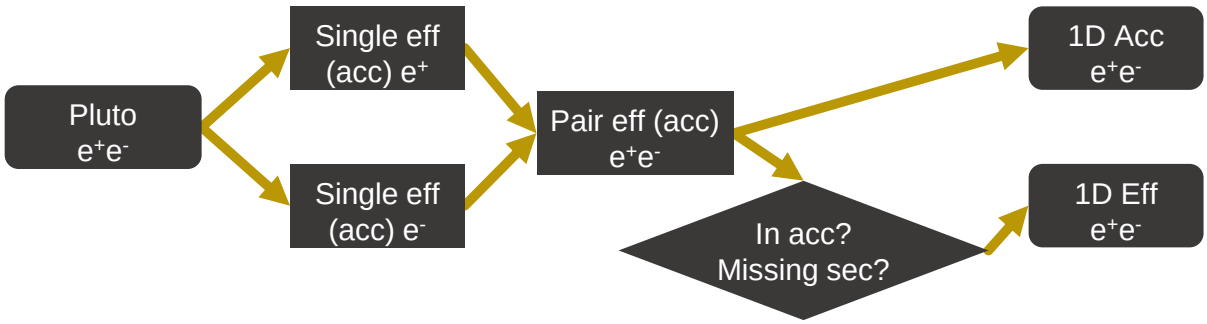

Figure 9.1: Flow of the efficiency and acceptance factor estimation. The single electron efficiencies serve as input for the pair efficiency and pair acceptance estimation. A pair efficiency is estimated only if both tracks are in acceptance. In case a track passes at the position of a sector excluded from analysis, the pair efficiency is set to 0.

The resulting invariant mass distributions, that were presented in chapter 8, are affected by the detector acceptance and the electron reconstruction efficiency. In order to compare the resulting data with other experiments or model calculations, the pair spectra have to be corrected for those effects. Simulated tracks, which were transported trough the detector using the GEANT package, are used to evaluate the correction factors. The corrections are split to acceptance and efficiency losses as follows:

- **Acceptance:** Accounts for losses if particles do not traverse active volumes at the detector. Furthermore, restrictions of momentum (0.10 GeV/c < p < 1.00 MeV/c) and the pair opening angle ($\alpha > 9°$) are also considered.

- **Efficiency:** Losses due to track reconstruction and electron identification criteria.

The corrections are estimated in two steps (see Fig. 9.1). In the first step, correction matrices for single electrons are evaluated as a function of polar angle (Θ), azimuthal angle (Φ) and momentum. To do so, one single electron per sector is embedded in real events. The estimated

single electron efficiency and acceptance matrices are used in a second step to estimate a one dimensional pair correction via an input distribution based on simulated pairs from realistic models.

9.1 Single track correction

The correction factors for single electrons or positrons are estimated using embedding of simulated tracks into real events. A definition of acceptance and efficiency of tracks has been defined previously. The definition translates to the following criteria to define the acceptance and efficiency for simulated tracks:

- **Accepted tracks (N_{Acc}):** Generated electron tracks that are crossing at least four MDC layers per chamber and one of the time-of-flight detectors.
- **Reconstructed tracks (N_{Reco}):** Generated electron tracks, that were identified as electron (see chapter 7). Furthermore, fake tracks are rejected by requiring, that at least 50% of MDC wire signals were created by the input track. This assures a pure electron efficiency estimation.

The acceptance factor ϵ_{Acc} and efficiency factor ϵ_{Eff} are defined as follow:

$$\epsilon_{Acc} = \frac{N_{Acc}}{N_{4\pi}}, \tag{9.1}$$

$$\epsilon_{Eff} = \frac{N_{Reco}}{N_{Acc}}, \tag{9.2}$$

where $N_{4\pi}$ stands for the number of simulated electrons in full phase-space. Simulated tracks are chosen as reference particles since they can be easily monitored. In order to cover the full phase-space with a sufficient statistic, electrons, distributed uniformly over momentum and Θ, Φ angles, are generated. Afterwards, one electron per sector is embedded in real events.

Accepted tracks are defined by checking the hits in the sub detectors as explained above. For particle identification, the selection criteria are applied in the same way to embedding data, as they are applied to real data and comprise the electron candidate selection, multivariate electron identification and close pair rejection criteria (see chapter 7). The true properties of reconstructed tracks can be used to check the reconstruction quality. This allows the identification of fake combinations that consist only partially of the original track. These are not considered as good identified tracks.

Once tracks are identified, they are assigned to the respective Θ, Φ and p bin. The true values and the reconstructed properties are available to fill the track in the corresponding bin. A comparison of efficiency estimation using true or reconstructed momentum values (see Fig. 9.2 (left)) reveals a significant increase of efficiency by using the reconstructed values of momentum. This effect is caused due to a general shift towards lower values of the reconstructed

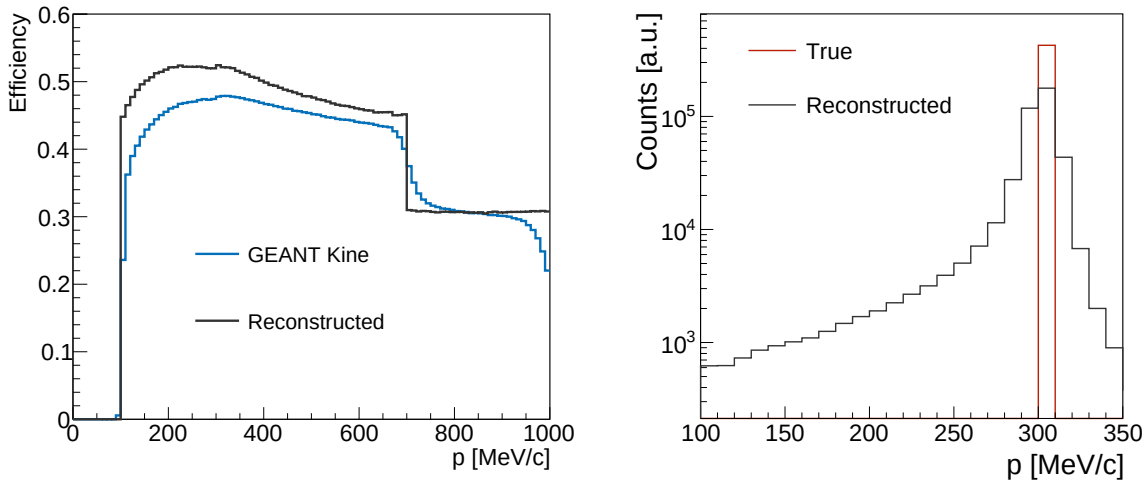

Figure 9.2: Left: Efficiency estimated with true (GEANT kine) and reconstructed momentum. The integrals of both distributions are different, since a different number of electrons is excluded by an lower and upper momentum limit ($100 < p < 1000$ MeV/c). **Right:** True and reconstructed momentum for a true momentum of $300 < p < 310$ MeV/c. The reconstructed momentum is smeared by detector resolution and bremsstrahlung of electrons. In total, only 40% of reconstructed tracks have the same momentum as the had as input. The bremsstrahlung causes that 40% of tracks have a smaller momentum than the true input momentum.

momentum caused by bremsstrahlung process (see Fig. 9.2 (right)). Because of the uniform distribution of the electron momentum (not exponential drop off), the amount of accepted tracks in the low momentum region is enhanced artificially. Due to the exponential decrease of a physical electron distribution towards large momenta, this effect will be strongly reduced in real data. Consequently, the true momentum (`GEANT kine`) is better suited to determine the momentum and is used to sort the electrons. Finally, histograms counting the number of input, accepted and identified tracks are obtained. The efficiency and acceptance matrices are estimated and a Savitzky-Golay noise filter is applied to those in order to smooth edge effects of detector regions with small statistics. The application of the noise filter has only a small impact, since the distribution is only smoothed slightly while the overall values are not modified.

The final efficiency matrices as a function of the polar, azimuthal angle and integrated over momenta are presented in Fig. 9.3. Both matrices indicate deviations between the sectors, which are caused by a lower performance of MDC or RICH. Furthermore, structures within the sectors, caused by a reduced performance of single cells of TOF or RPC, are also visible. The acceptance matrices are presented in Fig. 9.4. They show a constant acceptance value inside the sector and a reduced one at the sector edges. Outside the sector acceptance, a few tracks are visible. However, the probability of having such tracks is very low. Consequently, their contribution to the pair spectra is negligible.

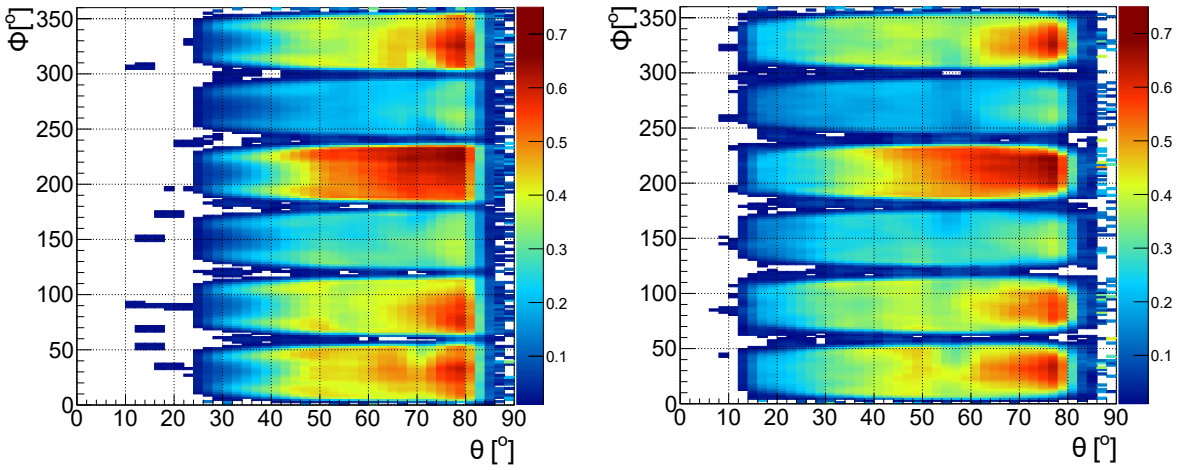

Figure 9.3: Single electron efficiencies (ϵ_{Eff}) for positive (**left**) and negative (**right:**) electrons in the momentum range $p = 0.15 - 0.20$ GeV/c.

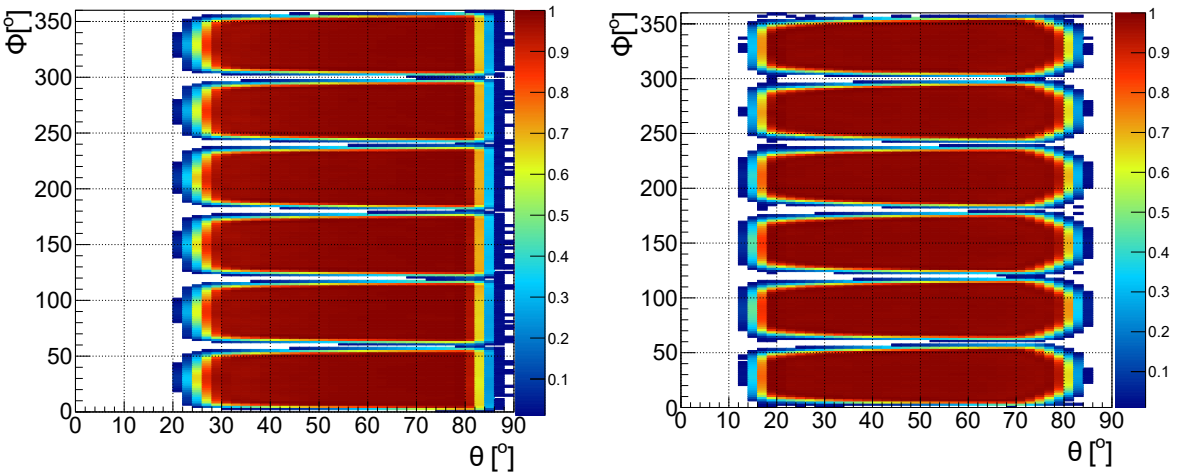

Figure 9.4: Single electron acceptance (ϵ_{Acc}) for positive (**left**) and negative (**right**) tracks in the momentum range $p = 0.15 - 0.20$ GeV/c.

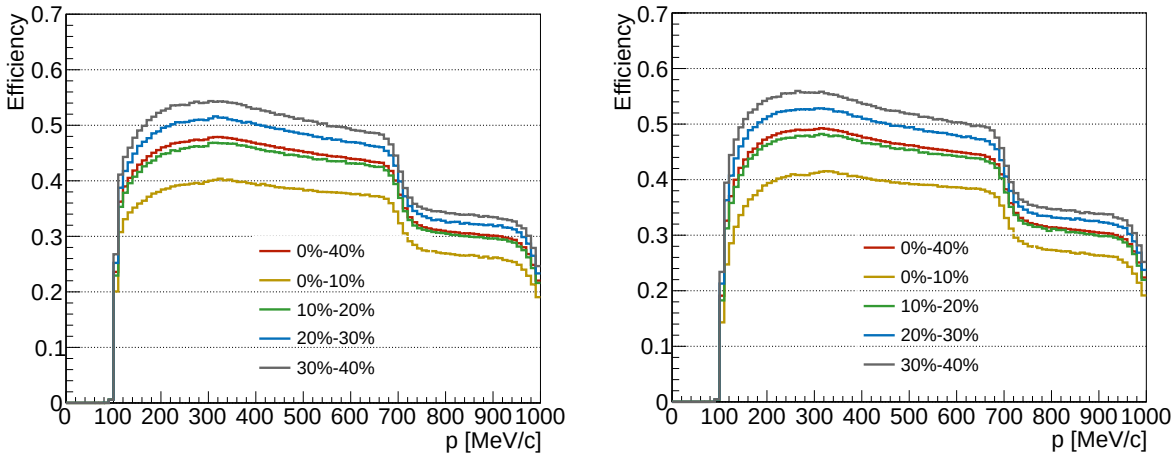

Figure 9.5: Multiplicity dependence of efficiency (ϵ_{Eff}) for positrons (**left**) and electrons (**right**).

Differences in acceptance of electrons and positrons are caused by their deflection in the magnetic field. Since electrons are bend towards larger polar angles, their acceptance is higher in the small polar angle region. Besides the angular and momentum dependence, the centrality dependence of the electron efficiency is also of interest. For that reason, the efficiencies of different multiplicity classes are compared in Fig. 9.5. The efficiency is decreasing with track multiplicity. All curves show a reduced efficiency at higher momenta, due to the stronger electron identification criteria beyond momenta of p = 700 MeV/c.

9.2 RICH efficiency correction factor

The correction of the single electron yield is based on simulated electron tracks embedded to real data. Therefore, the correction is only valid as much as the embedding procedure and the digitizer are close to reality. Especially, the response of the RICH detector is of importance for the electron reconstruction. The RICH digitizer was adjusted to reproduce the response based on a sample of good rings and shows deviations in the number of reconstructed electrons for rings with low quality (see section 6.2.3). This has also been seen during single electron identification. A comparison of the number of pads per ring between good[1] and bad[2] rings showed a large difference in the yield between simulated and experimental data for tracks with bad ring signatures (see Fig. 7.12).

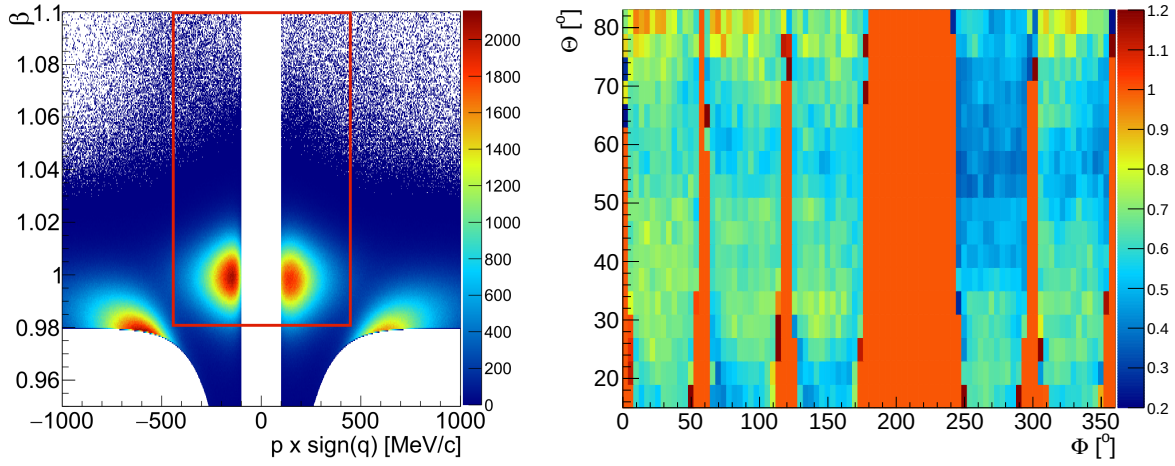

Figure 9.6: Left: Velocity as a function of momentum of electrons used for estimation of the RICH correction factor. The sample contains all tracks passing the standard track sorting (see section 4.4). The red box indicates the selected particles. **Right:** Ratio of identified tracks in real data to the ones identified in simulation. It is presented for tracks with two backtracking maxima. The red area corresponds to the MDC sector which was not operating properly during data taking.

[1] 0 < `RichQa` < 1.5
[2] 0 > `RichQa` or `RichQa` > 1.5

Therefore, the impact of bad reproduced events in simulation on the efficiency estimation will be checked. This analysis is based on electrons selected with a basic electron identification. Therefore, the standard track sorting (see section 4.4) requiring a minimum RICH response[3], is chosen. In addition, the velocity is restricted to high β values while only low momentum ($p < 500$ MeV/c) tracks are chosen (see Fig. 9.6 (left)).

A ratio between the number of experimental and simulated tracks is calculated as a function of the number of backtracking maxima, Θ and Φ angles. An investigation as a function of the significance of the RICH response, reveals rings with bad ring signatures[4], as the ones with the largest deviations. However, those electrons are the dominant fraction of the identified electrons. In contrast, the difference between simulated and experimental data for good rings is only small.

In order to search for differences as a function of polar (Θ) and azimuthal (Φ) track angle, a two dimensional distribution is shown in Fig. 9.6 (right). The distribution indicates, that the differences depend on both angles. In general, a strong deviation between the number of simulated and experimental tracks is seen in each sector. Consequently, an additional correction factor needs to be applied for a proper efficiency correction of tracks with bad ring signatures. The following properties should be incorporated in the correction factor:

- Independent from the electron identification analysis.
- Spatial dependence to consider position dependent effects.
- Averaged correction value to secure stable single track corrections.

As the results from Fig. 9.6 (right) are obtained from an independent analysis, they provide an ideal basis for the discussed RICH correction factor. Furthermore, the three dimensional ($\Theta,\ \Phi,\ p$) dependence assures a precise description of the effect. However, the statistics of simulated events is limited and rings with a large number of maxima are rare. Consequently, the correction is limited to four backtracking maxima per candidate in order to provide a stable correction value. This restriction has only a small impact, since the relative contribution of tracks with more backtracking maxima is small and shows less deviations between simulated and real data.

For application, the correction factor is incorporated to the single electron efficiency calculation process. Therefore, the number of backtracking maxima and RICH matching quality of every electron, that is tagged as reconstructed, is obtained. In case of a bad ring signature, the corresponding correction factor is obtained from the input matrix ($\Theta,\ \Phi$ and $\mathtt{N}_{\mathrm{BT\ Maxima}}$) and is filled in a three dimensional matrix as a function of $\Theta,\ \Phi$ and p. Consequently, an averaged correction factor is obtained. Finally, the efficiency matrix, estimated with single electrons, is multiplied by the correction factor matrix. As a consequence, a more realistic efficiency correction matrix for the backtracking electron identification is obtained. The strength of the correc-

[3] 1 backtracking maximum per candidate.
[4] Corresponds to a small number of backtracking maxima per candidate.

tion is already seen on the mass dependent electron pair efficiency curve in Fig. 9.8 (left). As a result, large differences are obtained and stress the importance of this correction procedure.

9.3 Pair correction

Single electrons could be corrected by efficiency as discussed in section 9.1. However, this method has several weak points:

- **Combinatorial background**: The correction factor is applied on event by event basis to each single track before the combinatorial background pair is built. However, the estimation of combinatorial background is fully based on counting statistics and does not incorporate scaling factors due to efficiency corrections.
- **High mass range**: Only a few pairs are reconstructed in the high mass range. For this reason, small statistical deviations in the spectrum of reconstructed pairs are corrected by large correction factors and thus might result in large deviations in the corrected pair spectrum.
- **Low performance sectors**: The data sample contains events, whereof sectors, where at least on of the sub detectors had a lower performance, were temporarily excluded from the analysis (see section 4.2). The final pair spectrum must be corrected for sectors, that were excluded from analysis.

A way to overcome all those disadvantages is to apply a pair correction procedure. Its basic concept is the generation of events containing one random electron pair per event. The pairs are generated as a function of mass, transverse momentum and rapidity, while all other degrees of freedom are averaged. The generated single electrons of each pair are checked for acceptance. The pair efficiency itself is estimated by multiplication of the two single electron efficiencies, which are retrieved from the three dimensional efficiency matrix (see section 9.1). 10 million π^0 and η as well as 1 billion coarse-grained dielectron events are generated with Pluto and used as input pairs. Based on these events, a one

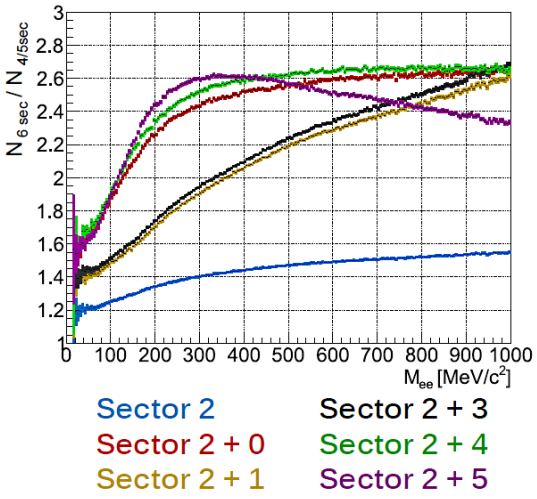

Figure 9.7: Impact of sector combinations excluded from analysis on the pair efficiency. Combinations of the sectors are depicted in the legend. Relative to sector 2, sector 1 and 3 are neighboring and 5 is the opposite sector. The correction is much stronger for two than for one missing sector and does depend on the sector combination. Small differences (e.g. between black and yellow) are induced by efficiency differences between sector 1 and 3.

dimensional (e.g. mass, p_t or y) efficiency curve is estimated as the average efficiency of pairs. An acceptance correction curve is modeled analogously. In this case, every generated electron pair is chosen. Furthermore, the three dimensional acceptance matrix obtained with single electrons is chosen for estimation of the pair acceptance.

This procedure does not yet incorporate sectors, that were excluded from analysis. To consider the effects due to missing sectors, every combination has to be considered separately, since each correction factor has a different mass dependence (see Fig. 9.7). Therefore, all missing sector combinations with at least 4 active sectors are extracted from the data sample of the entire beam time. Later on, those distributions are used to sample the missing sectors for events with generated Pluto pairs. In case a sector is missing, the efficiency of a track from that sector is set to 0. By this, the electron efficiency is reduced and will account for sectors excluded from the analysis.

The efficiency and acceptance corrections are presented in Fig. 9.8 (left). The curve including the RICH factor is enhanced by approximately two, but the difference between both is rather flat over the whole mass range. In contrast, the acceptance correction has a strong mass dependence. It has much smaller values at small masses due to the acceptance losses of low momentum tracks and pairs with opening angles smaller than $9°$. Additionally, a centrality dependent efficiency is estimated (see Fig. 9.8 (right)). As expected, the largest corrections are extracted for the $0 - 10\%$ most central collisions.

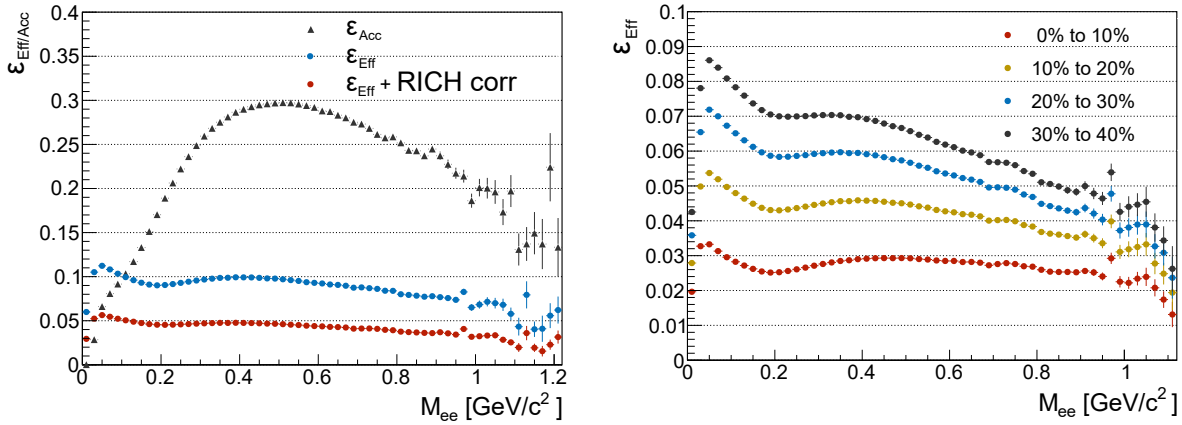

Figure 9.8: Left: The efficiency with and without RICH correction factor is estimated with thermal electrons as input and shows a similar shape. Additionally, the acceptance correction is shown. **Right:** Pair efficiency as a function of invariant mass for four centrality classes. This efficiency includes the RICH correction factor.

9.4 Quality assessment of corrections

Before the efficiency corrections are applied to real data, the validity and quality of the method needs to be proven. Therefore, tracks are reconstructed in simulation and compared to the cor-

responding input information. This approach will be presented for the reconstructed mass distribution as an example.

As simulated data sample, UrQMD events, containing one embedded electron pair per event, are used. The sample contains events whereof 10 million π^0, η and electrons from coarse-grained transport model are embedded, resulting in a total event sample of 30 million. This sample contains a much larger fraction of π-/η-Dalitz decays than the event sample used for efficiency estimation. Identical to real data, the electrons are identified using the same identification criteria (see chapter 7), but only embedded electrons are used. Furthermore, the additional RICH correction factor is not required since only simulated events are used. The simulation does not incorporate bad performance sectors. For this reason, the missing sector correction within the pair efficiency is neglected.

The identified electrons are corrected for efficiency as well as for acceptance. Afterwards, the corrected spectra are compared to the generated input distributions (see Fig. 9.9). The efficiency corrected mass distribution agrees with the input distribution within 5% in the mass range of $M_{ee} = 0.20 - 0.40$ GeV/c^2. The maximum deviation is present at the low-mass (M_{ee} < 0.20 GeV/c^2) and the high-mass (M_{ee} > 0.40 GeV/c^2) region of the distribution. At low masses, mostly low momentum electrons and pairs with small opening angles contribute to the spectrum. Electrons with p < 100 MeV/c^2 and $\alpha_{e^+e^-}$ < 9 are removed by cuts. The momentum of particles is smeared due to the detector resolution. Consequently, sometimes a track can not be clearly assigned to acceptance or efficiency losses. This results in uncertainties of the efficiency correction. The deviation at higher masses (M_{ee} > 0.40 GeV/c^2) is partially explained by the large statistical errors, due to the limited number of tracks with large masses. But some of those deviations arise of the efficiency estimation method itself. This might be induced by the unknown composition of the dielectron sources. In detail, different decays have different kinematics, which might result in a different pair efficiency and acceptance. Therefore, the results might depend on the cocktail composition. However, the used cocktail comprises a larger amount of Dalitz decays, which is not expected in real data. In real data, pairs from two-body decays are assumed to be the dominant source. Therefore, the scenario using a increased number of Dalitz decays is assumed to be the worst case with large deviations of the phase space distribution from the experimental one. Consequently, this quality check depicts an upper limit of deviations in case the cocktail contributions for the pair correction are not known precisely.

Finally, a mean deviation of the ratio from unity of 11% is estimated for the efficiency corrections. For the acceptance correction, the deviation is larger is for masses up to $0.15\ GeV/c^2$ around 20%. This deviation is induced by the strong correction, for tracks with low momentum and small opening angle.

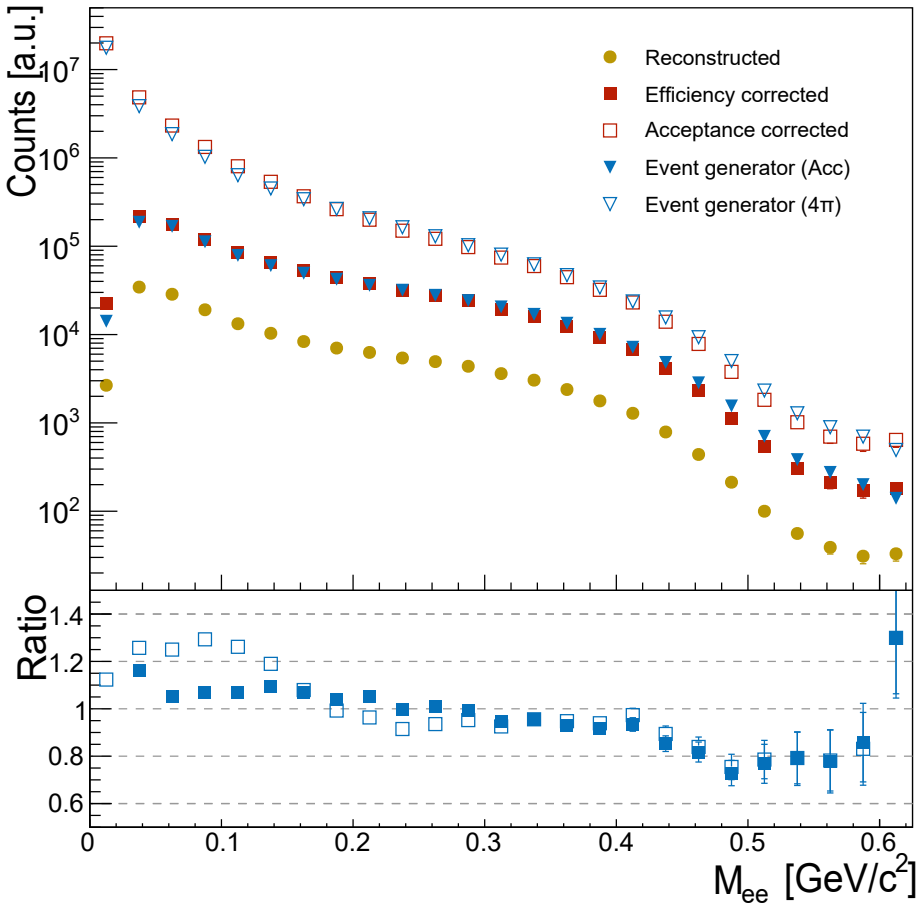

Figure 9.9: Evaluation of efficiency correction method. The upper plot shows the identified pairs corrected for acceptance and efficiency as well as the pair input distribution in the HADES acceptance (see section 9.1). The ratios in the lower plot compare the corrected yield to the simulated input. They are presented for yields in acceptance (filled squares) and full phase space (open squares).

9.5 Corrected spectrum

Finally, the estimated efficiency and acceptance corrections are applied to the reconstructed signal spectrum (see section 8.3). Therefore, the pair efficiency (ϵ_{Eff}^{Pair}) and acceptance (ϵ_{Acc}^{Pair}) is estimated with the single electron efficiency ($\epsilon_{Eff}^{e^{\pm}}$) and acceptance ($\epsilon_{Eff}^{e^{\pm}}$) and RICH correction factors ($c_{Rich}^{e^{\pm}}$):

$$\epsilon_{Eff}^{Pair} = \epsilon_{Eff}^{e^-} c_{Rich}^{e^-} \cdot \epsilon_{Eff}^{e^+} c_{Rich}^{e^+} \tag{9.3}$$

$$\epsilon_{Acc}^{Pair} = \epsilon_{Acc}^{e^-} \cdot \epsilon_{Acc}^{e^+} \tag{9.4}$$

The final yield within the HADES acceptance is estimated by dividing the reconstructed pairs (N_{Reco}) by the pair efficiency. To correct the yield to the full phase space, the pair acceptance has to be divided additionally:

$$N_{4\pi} = N_{Reco} \cdot \frac{1}{\epsilon_{Eff}^{Pair}} \cdot \frac{1}{\epsilon_{Acc}^{Pair}} \tag{9.5}$$

The effect of the efficiency and acceptance correction is shown as a function of mass, but the method is identical for different observables. As a first check, the Au+Au spectrum is compared to the *reference spectrum* (see section 10.2.2), which is estimated with elementary collisions and constructed as $\frac{1}{2}(np + pp)$ (see Fig. 9.10). The final spectrum is displayed by the red points. To demonstrate the effect of the RICH correction factor, a corrected spectrum without this factor is plotted as well. As expected, a comparison of both reveals a large difference among them. Furthermore, the Au+Au yield without using RICH correction is below the one of the reference spectrum in the π^0 mass region. However, the efficiency corrected Au+Au yield is expected to be larger than the reference spectrum yield over the whole mass range, since additional sources of medium radiation are contributing to the dielectron spectrum. Due to differences between simulated and real data, the efficiency estimated using simulated data is larger than the real efficiency in experimental data. Consequently, the correction factor is too small. After inclusion of the RICH correction factor, the dielectron yield increases and exceeds the one of the reference yield. However, the shape of the spectrum is not modified strongly due to the correction.

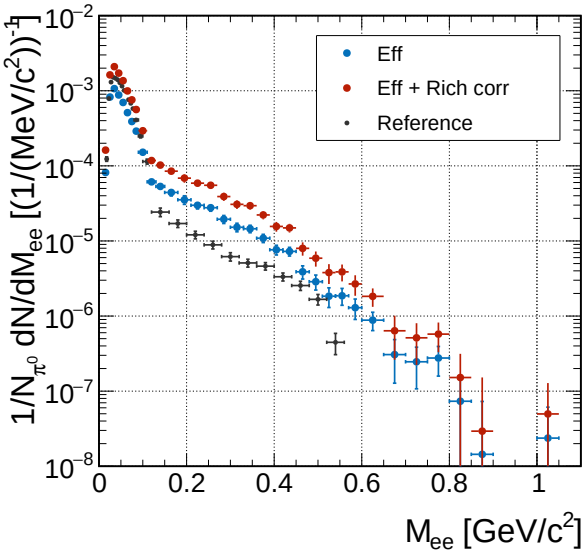

Figure 9.10: Comparison of efficiency corrected spectra with and without RICH correction factor. The reference of elementary collisions is plotted in addition.

The efficiency corrected spectrum obtained with the standard analysis is compared to the one without using close pair rejection criteria (see Fig. 9.11 (left)). The mass region above 0.15 GeV/c^2 and below 0.30 GeV/c^2 reveals a general underestimation of the reconstructed dielectron yield for the standard analysis compared to the analysis without close pair rejection. This might be caused by deviations between embedding events and experimental events using e^+ and e^- tracks embedded in real events. However, each single electron track might cause correlated background, which is not reproduced in simulation and therefore not present in embedding events. This source of noise might create signals in the drift chambers that result in reconstruction of a MDC segment. In case this segment is close by to the electron track, an application of the close pair rejection will remove the electron only in experimental data but not in embedding files. As a consequence, the efficiency is assumed too large and will not corrected for the removal of tracks in experimental data. To account for those uncertainties between the different analyses, the average yield of both spectra is chosen up to a mass of 0.30 GeV/c^2. For masses above, the standard spectrum is chosen, since it has a better signal-to-background ratio, which is important in the mass range with less reconstructed pairs to obtain a high signal quality.

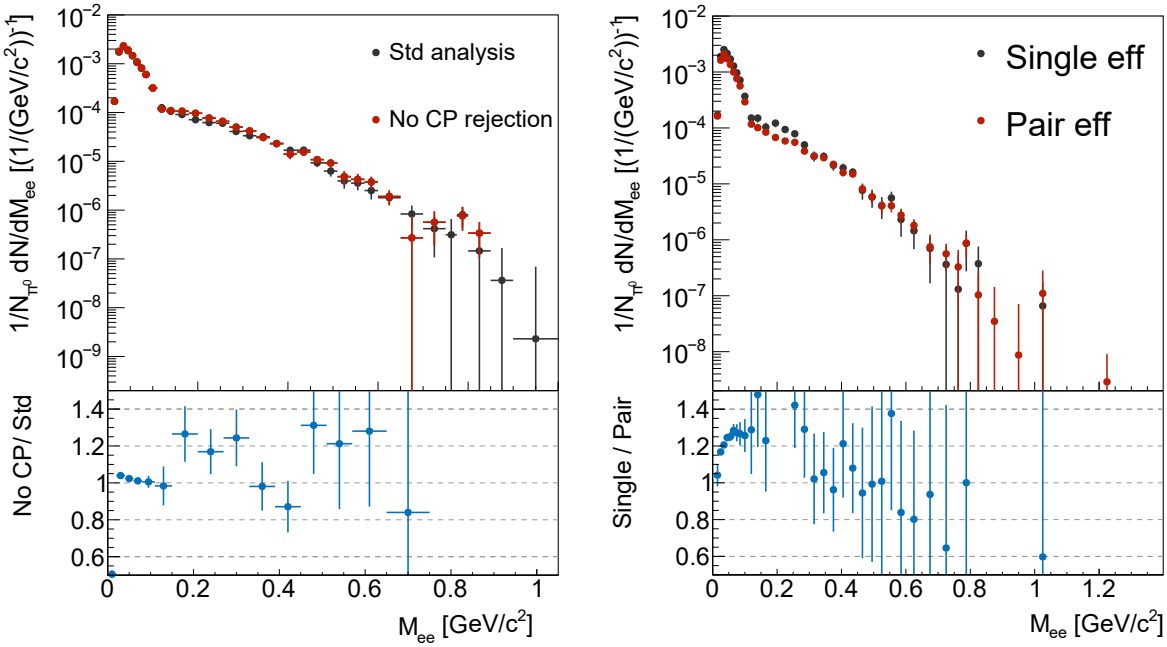

Figure 9.11: Left: Comparison of the spectra with and without close pair rejection. **Right:** Resulting mass spectra after applying the efficiency to each electron separately (black) and pair-wise (red).

To check the improvements of the pair efficiency correction with respect to the one estimated for single electrons, both spectra are compared in Fig. 9.11 (right). In general, the spectra are in agreement. The most significant deviations are present at masses around $0.10 - 0.20$ GeV/c^2. In the high mass range, the pair efficiency corrected spectrum is of higher quality, due to less points fluctuating. Theses improvements could be explained by two reasons. Since the background subtraction, in case of pair correction, is not affected by efficiency correction, a more precise background contribution is estimated and subtracted. A second advantage are the more stable efficiency values. In the analysis of single electron efficiency correction, the high mass region contains only a few electrons that are corrected by large correction factors of the order of 20. A small error in the correction factor might lead to large deviations in the corrected spectrum. The pair correction is better, since an efficiency, averaged over numerous pairs, is estimated for correction.

9.6 Systematic errors due to efficiency and acceptance correction

As a final step, the systematic uncertainties of the correction method are determined. One uncertainty arises from the reconstruction method, containing the single and pair efficiency method (see section 9.4). A second uncertainty arises due to the simulation which is not ideal. In order to identify differences of the efficiency and acceptance correction method itself, a self consis-

tency check was performed. In case of the single electron efficiency corrections, differences might arise due to:

- Deviations in the definition of acceptance and efficiency between experimental data and simulated data.
- Usage of ideal instead of reconstructed momentum values to sort the correction factors. In reality, the smearing of momentum values is caused by the detector resolution and bremsstrahlung.

Moreover, also the pair efficiency method introduces uncertainties:

- Phase space differences of the generated electron cocktail compared to the real distribution in experimental data.

All those differences are summarized by the self consistence check (see Fig. 9.4). A relative difference of 11% is estimated as mean deviation for the efficiency correction. However, the acceptance correction introduces additional deviations, which are dominantly present in the π^0 mass region. These errors arise due to the challenging extrapolation of the momentum and opening angle distribution at invariant masses close to zero. As a result, 20% is chosen as mean deviation error in the mass region up to $0.15\ \mathrm{GeV/c^2}$.

A second error, considering deviations between simulated and real data, needs to be added as well. Most of the differences are taken into account by the correction factor already (see section 9.2). In order to estimate the remaining differences, the calculation of the correction factor is varied by modifying the track selection criteria. In one case the standard track sorting (see section 4.4) is chosen while in the second approach more strict selection criteria are used (see section 7.2). A ratio between both analyses methods reveals differences of 0.5%, but further evaluation of the systematic errors would be important. Finally, the relative errors obtained by the self consistency check $\frac{\Delta N_{SC}}{N_{SC}}$ and relative deviations between experimental and simulated data $\frac{\Delta N_{Sim}}{N_{Sim}}$ are added quadratically:

$$\frac{\Delta N_{EffTot}}{N_{EffTot}} = \sqrt{\frac{\Delta N_{SC}}{N_{SC}}^2 + \frac{\Delta N_{Sim}}{N_{Sim}}^2} = \sqrt{11\%^2 + 0.5\%^2} \cong 11\% \tag{9.6}$$

As a result, a flat error distribution is obtained for the efficiency correction. In case of acceptance correction, the error is increased in the low-mass region correspondingly.

Chapter 10

Results and discussion

In the previous chapters, the methods for electron and positron identification were discussed. These electrons and positrons were paired to unlike-sign pairs and a combinatorial background was estimated. The resulting signal spectra were corrected for efficiency and acceptance effects.

The reconstructed spectra will provide insights to the particle production and propagation in heavy-ion collisions. To isolate contributions from the hot and dense stage of the heavy-ion collision, the contributions from the others stages need to be identified and subtracted. Afterwards, the reconstructed pair properties will be interpreted.

10.1 Resulting invariant mass, transverse mass, rapidity and angular distributions

Fig. 10.1 shows the resulting efficiency corrected e^+e^- invariant mass distribution normalized to the number of neutral pions. The dielectron spectrum includes systematic uncertainties[1], which were discussed in section 8.4 and 9.6. The systematic errors due to background subtraction ($\Delta N_{Bg}/N_{Bg}$), efficiency (acceptance) correction ($\Delta N_{Eff}/N_{Eff}$) and normalization to π^0 ($\Delta N_{\pi^0}/N_{\pi^0} = 10\%$) are independent from each other and therefore added quadratically to estimate the total systematic error (ΔN_{Sys}):

$$\frac{\Delta N_{Sys}}{N_{Tot}} = \sqrt{(\frac{\Delta N_{BG}}{N_{Bg}})^2 + (\frac{\Delta N_{Eff}}{N_{Eff}})^2 + (\frac{\Delta N_{\pi^0}}{N_{\pi^0}})^2}. \tag{10.1}$$

The resulting systematic errors are presented in Fig. 10.2. The first indication of a medium effect is the observation that dielectrons are emitted with invariant masses far beyond the kinematic limit of free NN collisions at the same beam energy. The integral pair multiplicities per produced π^0 in selected mass bins are:

[1] Shown with gray boxes around the central value.

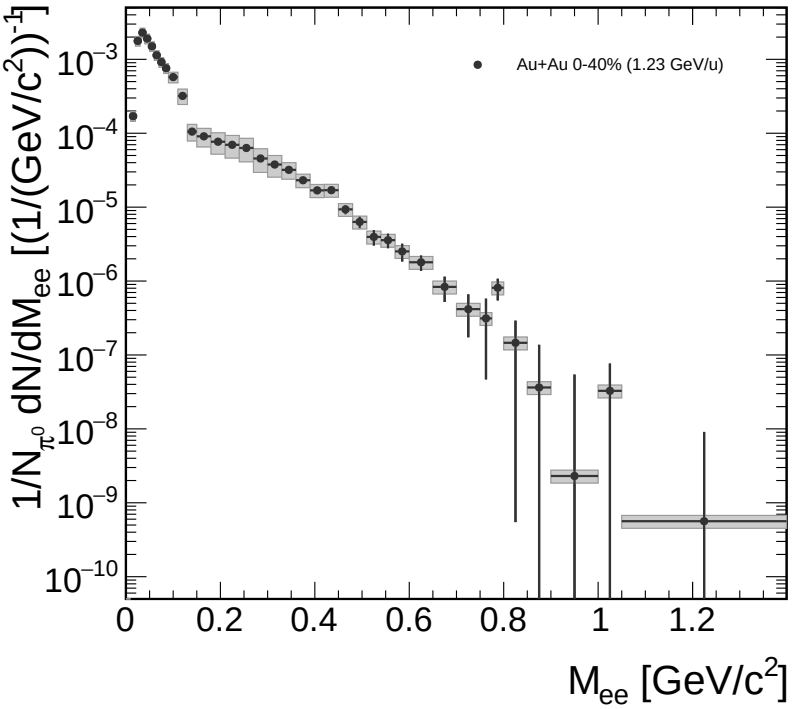

Figure 10.1: Efficiency corrected mass spectrum.

- $M_{ee} < 0.15$ GeV/c^2: $1.9 \cdot 10^5$ pairs,
- $0.15 < M_{ee} < 0.30$ GeV/c^2: $1.3 \cdot 10^4$ pairs,
- $0.30 < M_{ee} < 0.70$ GeV/c^2: $4.3 \cdot 10^3$ pairs,
- $M_{ee} > 1.40$ GeV/c^2: 50 pairs.

Fig. 10.3 shows the electron pair signal as a function of invariant mass and transverse momentum. It demonstrates the high acceptance of HADES with only a small area of p_T < 0.1 GeV/c and M_{ee} < 0.1 GeV/c^2 that is not covered. Moreover, HADES has a large rapidity coverage (-0.5 < y < 0.6) around mid rapidity (see Fig. 10.4 (lower left)). The medium effects are expected to be more prominent at low p_T, and here HADES has a good coverage. Different dielectron sources contribute to different mass regions. To isolate their properties, the e^+e^- spectrum is split in three different mass bins:

- 0.00 GeV/c^2 - 0.15 GeV/c^2 (π^0 region)
- 0.15 GeV/c^2 - 0.30 GeV/c^2 (Excess bin I)
- 0.30 GeV/c^2 - 0.70 GeV/c^2 (Excess bin II)

The ranges are motivated by the strong contribution of π^0 in the low-mass region. In the mass range above 0.15 GeV/c^2, contributions from the medium are expected to be dominant, but this mass region is challenging due to the small signal-to-background ratio. At higher masses, the yield is still expected to be dominated by medium effects and the signal-to-background

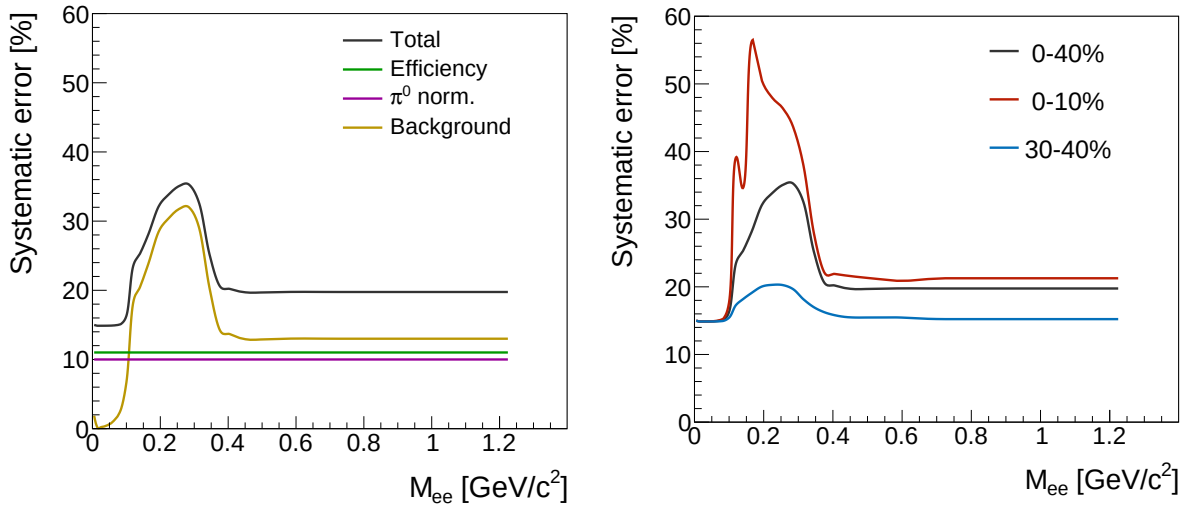

Figure 10.2: Left: The different contributions to the systematic error and the total systematic error. **Right:** Total systematic errors for different centrality classes.

ratio improves. However, the number or reconstructed pairs is reduced, which results in larger statistical errors.

Observables can be analyzed in the indicated mass ranges to investigate properties of different sources. One of these observables is the transverse momentum (p_T) (see Fig. 10.4 (upper left)) or the transverse mass (m_T) (see Fig. 10.4 (upper right)). For an easier comparison, m_{ee} is subtracted from m_T. In the mass range of π^0, $m_{ee} = 0.135$ GeV/c^2 is subtracted, while in the higher mass range the mass of the pair itself is subtracted. In addition, the rapidity distributions (y) are shown in Fig. 10.4 (lower left) with the mid rapidity $y_0 = 0.74$ subtracted. The spectra are expected to be symmetric around mid rapidity. Due to the limited acceptances of HADES, the spectra are not perfectly symmetric. Additionally, the angular distributions of dielectrons were reconstructed (see Fig. 10.4 (lower right)). The helicity describes the angle of the electron with respect to the virtual photon in the reference frame of the virtual photon. A more flat distribution towards higher masses is clearly visible.

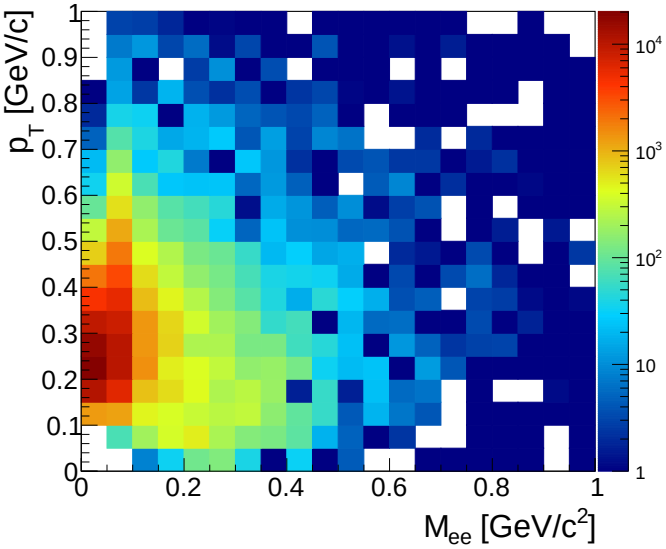

Figure 10.3: Transverse momentum as a function of invariant mass for the identified dielectrons. The signal after combinatorial background subtraction is shown.

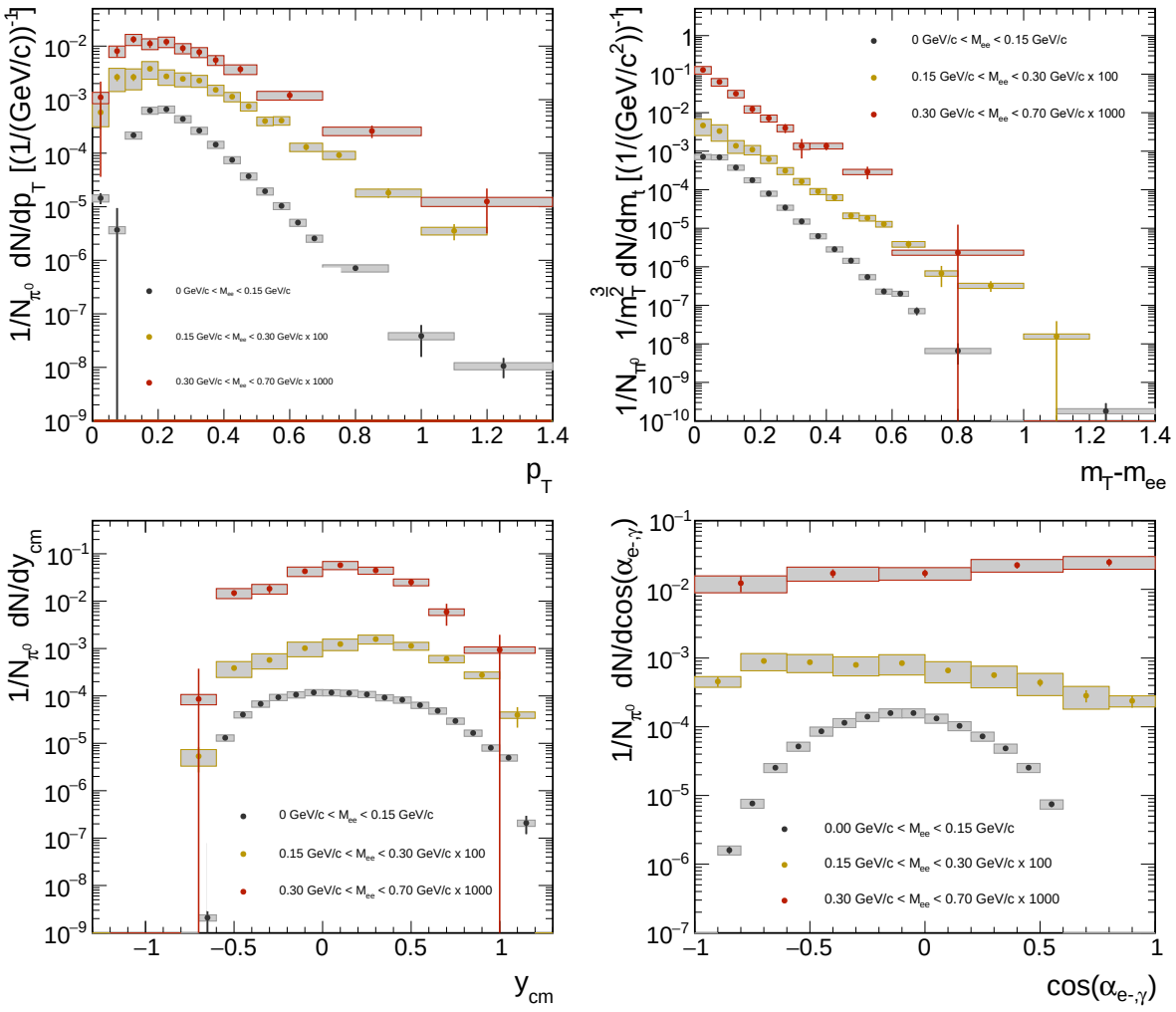

Figure 10.4: Reconstructed pair observables for three different mass regions. The transverse momentum (**upper left**), transverse mass (**upper right**), rapidity (**lower left**) and helicity are presented (**lower right**) after efficiency correction. All observables are normalized to π^0. The transverse momentum (p_T) and transverse mass (m_T) spectra are presented for acceptance corrected pairs.

10.2 Dielectron contributions from the initial and freeze-out stages

The analysis of dielectrons is aiming for extraction of signals from the hot and dense stage of the heavy-ion collision. However, a physical background from the initial and freeze-out stage contributes to the spectrum as well (see section 1.2.3). An extraction of the signal from the hot and dense stage requires a precise knowledge of all contributions from initial and freeze-out stages. The contributions from the initial stage are constructed by means of elementary collisions while the freeze-out contributions are estimated on the basis of observed meson multiplicities in Au+Au collisions. Both distributions will be derived in the following sections.

10.2.1 Spectra normalization

In order to ease comparisons of the results with data obtained for other collisions systems, the dielectron yields are normalized to the number of produced π^0 in the respective centrality class. In that way trivial volume effects are taken out as well as to first order also effects due to different collision energies. Indeed the pion multiplicity shows a monotonous rise as a function of the beam energy (see Fig. 1.23 (right)) [97].

Neutral pions can be reconstructed via an electromagnetic decay channel, namely their double photon decay: $\pi^0 \rightarrow \gamma\gamma$. Since HADES does not contain a detector for γ detection, only the γ that converted in the detector material can be identified. Those photons convert in the detector material and produce an e^+e^- pair which is identified by its kinematics. However, HADES is optimized for a low material budget to reduce the background, created by conversion pairs, in the dielectron measurement. Therefore, only in 0.78% of the cases both photons from a π^0 decay convert in the detector. Nonetheless, a four lepton analysis is performed to identify π^0. A four electron invariant mass is reconstructed. The yield in the peak is estimated and corrected for efficiency as well as acceptance to estimate the number of produced π^0 in the collision (see Table 10.1). However, the precision of the result is limited due to statistical and systematical uncertainties.

An indirect way to derive the multiplicity of neutral pions is to use the charged pion multiplicities and to apply isospin symmetry arguments. The number of π^0 corresponds to the mean number of π^+ and π^-. Charged pions are most abundant and can be identified by restriction of the identified particle velocity in combination with momentum. A resulting rapidity distribution of π^- is shown for each centrality class (s.t. Fig. 4.4) in Fig. 10.5 (left). The yield in full phase space is estimated by extrapolation of the measured data to 4π and is summarized in Table 10.1 for each centrality class. The errors are much smaller than the ones obtained from the conversion analysis of π^0. They consist of a statistical, systematical and an additional error from the extrapolation of the yield to the full phase space. Finally, the yield of isospin average elementary collisions (1/2(pp+np)) is scaled with A_{part}. This is realized by scaling the Au+Au

spectra by the number of π^0 and 1/2(pp+np) by the corresponding number of π^0 and results in the so-called *reference spectrum*.

10.2.2 Contributions from the initial collision stage

In the early collision stage of heavy-ion collisions, incoming nucleons scatter with the ones from the target and present the production processes for dielectrons. Therefore, baryonic resonances, namely Δ and N^*, as well as bremsstrahlung are most important dielectron sources at this stage of the collision. Those processes are identical to the ones in elementary collisions. Previous experiments by HADES have shown, that results from pp and np collisions differ significantly (see Fig. 1.24). In order to incorporate this effect, the average yield of np and pp collisions is estimated as contribution from first chance collisions, which are scaled by the number of π^0 per event.

10.2.3 Dielectron contributions from the late collision stage

Dalitz decays from $\pi^0,\ \eta$ and ω as well as two body decays of ω and ϕ contribute to the dielectron spectrum up to $1.1\ \mathrm{GeV/c^2}$. Some of those mass distributions are broad, which makes their identification in the e^+e^- channel challenging. A way to overcome this problem, is to identify their yield in another decay channel and scale it with the corresponding branching ratio to the e^+e^- decay channel.

The estimation of the π^0 yield was already presented in section 10.2.1. The contribution of η was identified in the same way like π^0 (by using the photon conversion method). The conversion probability of η is different to the one of π^0 and rises to 1.15%. The resulting η peak is shown in Fig. 10.5 (center). It allows the reconstruction of the number of η in 0-40% most central Au+Au collisions.

The estimation of the ϕ yield is more complicated, since it is more rarely produced. As decay channel, the one to K^+ and K^- is chosen since it has the highest branching ratio. The reconstructed rapidity distribution is presented in Fig. 10.5 (right). Even an estimation of the centrality dependence is available due to the signal reconstruction for two different centrality classes (see Table 10.1).

An estimation of the ω yield is challenging. It also needs to be identified via its decay products, but most of its abundant decay channels contain neutrals in the final state. The parity violating decay into two charged pions has only a branching ratio of 1.5% and the signal does not emerge from respective invariant mass distribution due to the huge combinatorial background. Therefore, its yield is estimated via the thermal model fit to the data (see section 1.1.3). The data set used comprises $A_{part},\ p,\ \pi^-,\ \eta,\ K^+, K^0_s,\ K^-\ \phi$ and Λ. After fixing the temperature and baryon chemical potential of the system at freeze-out, the yields for ω and various particles are predicted.

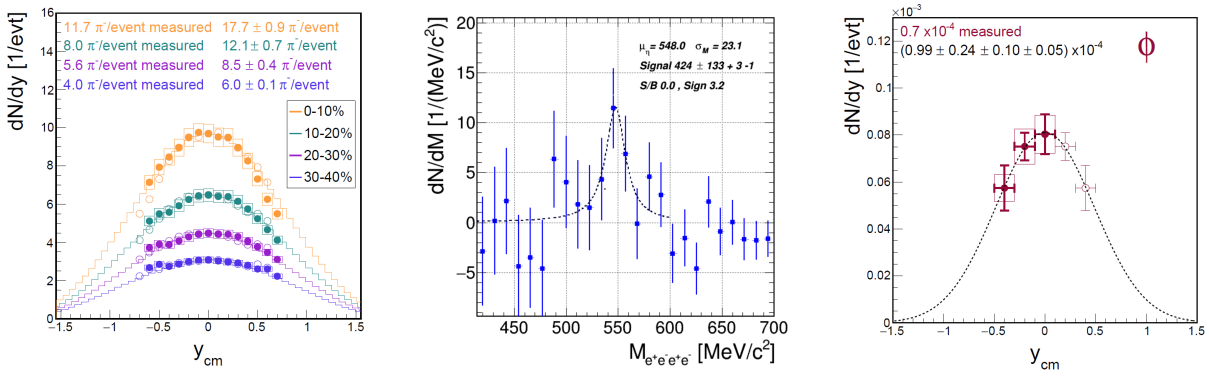

Figure 10.5: Reconstructed π^- (**left**), η (**center**) and ϕ (**right**) obtained from conversion and hadronic decay channels.

All the yields are summarized in Table 10.1. Additionally, a centrality scaling to estimate an A_{part} dependence is provided for all particles but η and ω. Finally, the particles are generated as a thermal distribution (the radial expansion velocity is set to 0) with the event generator Pluto and smeared with the HADES momentum resolution. As a result, a cocktail of freeze-out contributions is estimated.

Centrality	A_{Part}	π^0	η	ω	φ
0-40%	191	8.7	0.08	3 x 10^{-3}	1.94 x 10^{-4}
0-10%	303	13.4	-	-	3.36 x 10^{-4}
10-20%	215	9.5	-	-	
20-30%	150	6.8	-	-	1.28 x 10^{-4}
30-40%	103	4.9	-	-	

Table 10.1: Extracted hadronic cocktail yields. A centrality dependence of η and ω could not be estimated in Au+Au data.

10.3 Isolation of the excess yield

Information about the medium radiation is obtained by the comparison of the Au+Au data to the elementary reference spectrum as well as to the hadronic cocktail at freeze-out. The reference or cocktail yield is of the order of the Au+Au yield in the π^0 mass region. For higher masses, the Au+Au data shows a clear enhancement above the reference spectrum (see Fig. 10.6 (left)). This excess is attributed to radiation from the hot and dense stage.

This *excess yield* can be directly estimated by subtraction of the known sources from the Au+Au spectrum. However, ϕ and ω are not subtracted since their yield has larger uncertainties. Only the η and properly scaled isospin averaged reference spectrum (1/2(pp+np)) contribution is subtracted from the Au+Au spectrum. The acceptance corrected e^+e^- excess spectrum,

normalized to the number of π^0 is shown in Fig. 10.6 (right). Due to the large statistical and systematical errors arising from corrections for an opening angle cut ($\alpha > 9°$) and a single electron momentum cut (p_e > 100 MeV/c) the spectrum is presented for M_{ee} >150 GeV/c^2. To extend the acceptance corrected spectra to zero masses requires additional investigations.

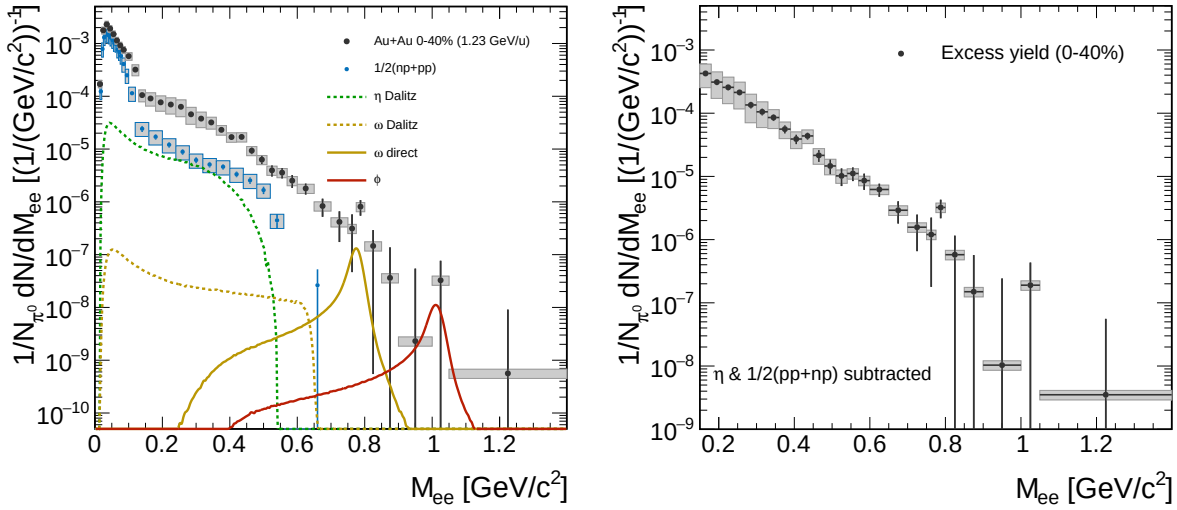

Figure 10.6: Left: Efficiency corrected invariant mass distribution together with the dielectron contributions from the first chance collisions and the freeze-out stage. **Right:** Acceptance corrected excess yield after subtraction of η and reference spectrum. Both spectra are normalized to the number of π^0.

10.4 Centrality and system size dependence of the excess yield

In order to investigate the in-medium properties systematically, the acceptance corrected excess yield is presented for four different centrality classes in Fig. 10.7. The yield is not normalized to π^0 and the error due to normalization is not included to the total systematic error. Each spectrum is scaled by factor of 50 for a better presentation. Due to large statistical and systematic uncertainties, a significant conclusion can not be drawn, for which reason the excess yield is integrated. The integration range between 0.3 GeV/c^2 and 0.7 GeV/c^2 was chosen (see section 10.1) and results in an excess yield with smaller relative errors compared to the single mass bins. The propagation of the systematic error is more complicated since the correlation from bin to bin is unknown. The error itself consists of a correlated and an uncorrelated fraction. Only the correlated error is of importance and estimated as average bin error weighted by the corresponding yield:

$$\Delta_{Tot} = \frac{\sum \Delta_i x_i}{\sum x_i}. \tag{10.2}$$

Since only a fraction of the total systematic error is correlated, it is assumed that only 50% of the total systematic error is correlated.

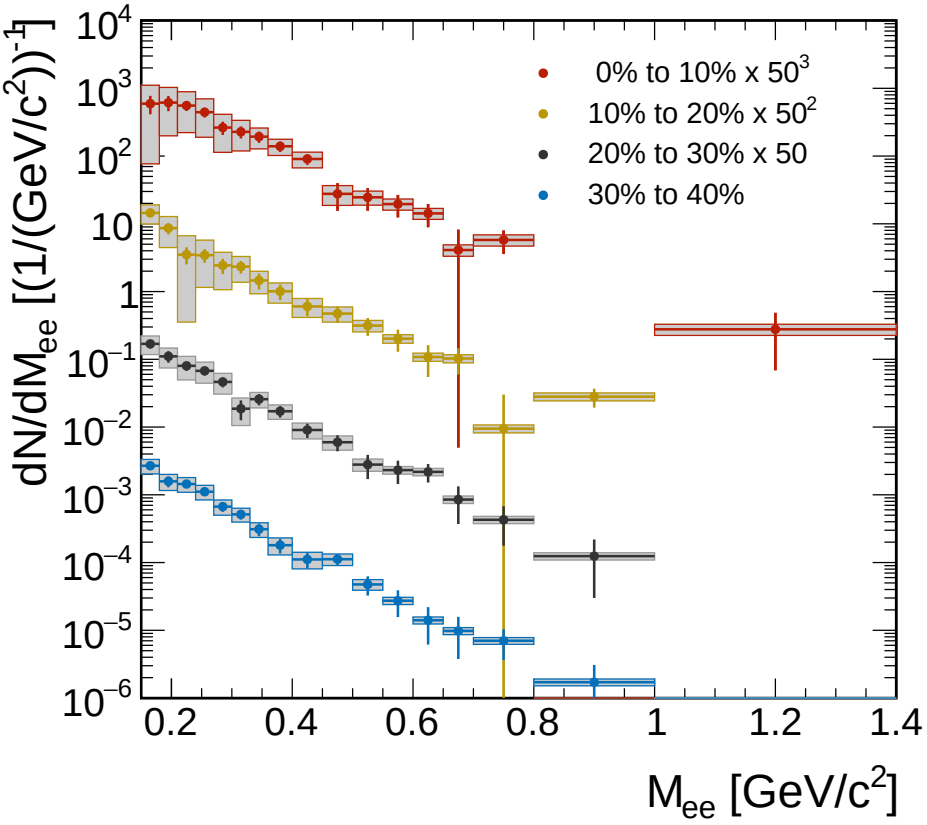

Figure 10.7: Excess yield for four centrality classes after subtraction of the reference spectrum and η. The excess yield is not normalized to the number of π^0 in each centrality class to reduces the systematical errors.

Finally, an integrated excess yield of $1.065 \cdot 10^{-4} \pm 0.057 \cdot 10^{-4}(stat) \pm 0.17 \cdot 10^{-4}(sys)$ is estimated in the mass range between 0.3 GeV/c^2 and 0.7 GeV/c^2 for the 40% most central events. The yields for four different centrality classes are plotted as a function of A_{part} in Fig. 10.8 (left) after π^0 and η subtraction only and in Fig. 10.8 (right) for subtraction of η and reference spectrum. Both results indicate a similar rise as a function of A_{part}, which is modeled by the following function:

$$N_{4\pi}^{Excess} \propto \cdot A_{part}^{\alpha}. \tag{10.3}$$

A fit of this function to data is applied, considering the statistical and systematical uncertainties. It is assumed that some of the systematic uncertainties are the same for the different centrality classes. Consequently, they will not influence the resulting scaling factor and can be neglected. To account for this common systematic differences, the systematic error of the yield estimated in the most peripheral class is subtracted from the systematic error of each centrality class. As a result, only the systematic errors exceeding the one from the most peripheral class are considered. This shall account for differences that vary between the centrality classes only, since only those are relevant for a modification of the A_{part} dependence. In case of π^0 and η subtraction, $\alpha = 1.32 \pm 0.15$ is estimated as scaling factor (see Fig. 10.8 (left)), while $\alpha = 1.44 \pm 0.17$ is estimated in case the reference spectrum and η is subtracted (see Fig. 10.8 (right)).

The systematic studies can be extended by previous HADES measurements, namely C+C at $2A$ GeV and Ar+KCl at $1.76A$ GeV which are compared to the 40% most central Au+Au collisions. The excess yield for Au+Au for the 40% most central events is estimated as $1.322 \cdot 10^{-4} \pm 0.056 \cdot 10^{-4}(stat) \pm 0.16 \cdot 10^{-4}(sys)$ for the case with π^0 and η subtraction, just as it has been done for former runs. In order to compare the Au+Au excess yield to the previous HADES measurements, C+C and Ar+KCl data is scaled with the incident beam energy. The scaling is based on an excitation function of π^0, η and excess yield from previous experiments (see Fig. 10.9 (left)). It reveals a scaling of the excess yield similar to the scaling of the π^0 yield. The resulting yields after scaling and subtraction of the π^0 and η contribution are compared to Au+Au data in Fig. 10.9 (right). A fit to HADES data results in an excess scaling of $\alpha = 1.15 \pm 0.10$, which is lower somewhat than within Au+Au data, but still in agreement within errors. Besides the A_{part} dependence, the systematic evolution of the data with collision energy is shown in Fig. 10.10 together with the results obtained by the STAR collaboration in the RHIC beam energy scan.

Both, centrality and system size dependence of the excess yield, indicate a stronger than linear rise with the number of participants. In contrast, the collision energy indicates a rather moderate evolution of the excess yield. Those effects can be explained by the following collission properties:

- **System size:** A larger number of participating nucleons enhances the volume in which a medium is created.
- **Temperature and density:** Collisions with a larger number of participating nucleons are assumed to have higher temperatures and densities, that modify the thermal production rates.
- **Lifetime:** The medium lasts longer and the production rates accumulate over a longer system lifetime.

The most significant property regarding the excess yield scaling is the size system, which rises strongly with A_{part}, in convolution with the lifetime of the system. Those properties are assumed to have to strongest contribution to the enhanced excess in more central events. But also the temperature might contribute to the larger yield since a small indication for a higher temperature in more central collisions was given (see Fig. 10.13). Additionally, the temperature increases with collision energy. For this reason, a smaller excess yield would be expected for smaller collision energies. However, the yield at lower collision energies is rather constant and is assumed to be compensated by an increased life time or volume of the fireball .

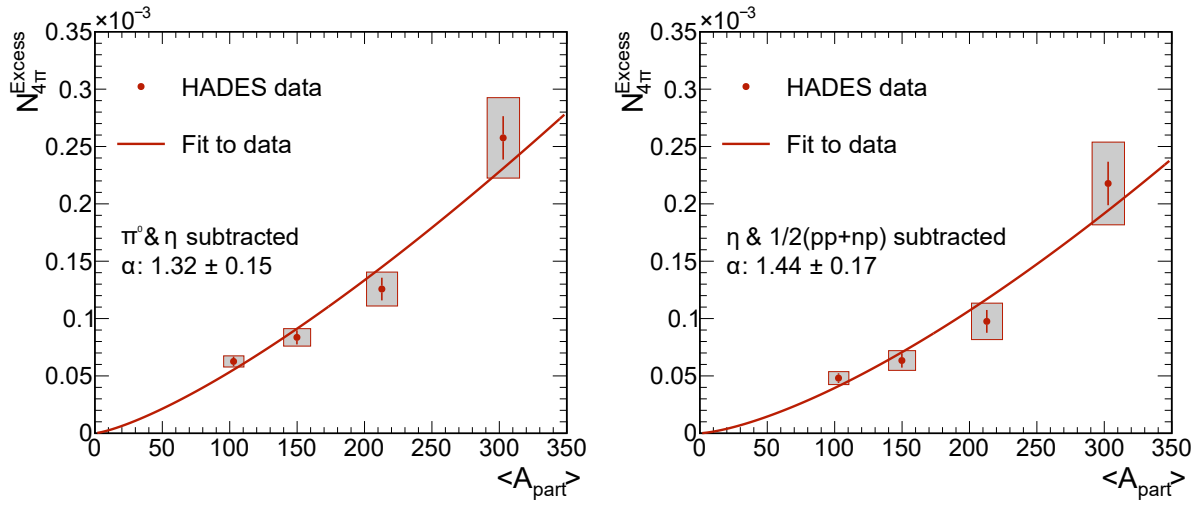

Figure 10.8: Integrated excess in the mass region $0.30 < M_{ee} < 0.70$ GeV/c^2 yields as a function of A_{part}. The excess yield is estimated by subtraction of the π^0 and η (**left**) as well as by subtraction of the elementary reference and η (**right**).

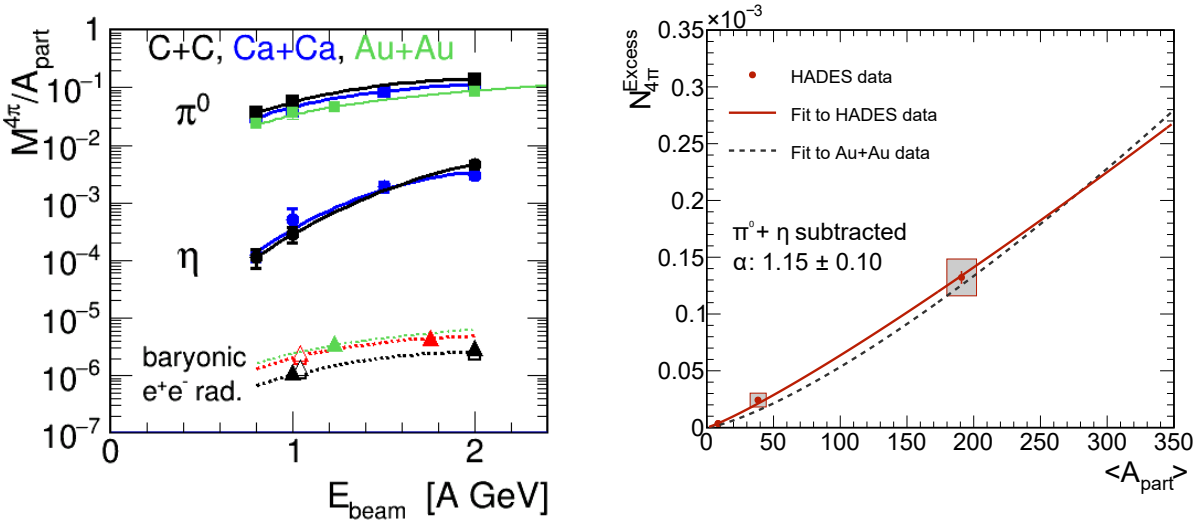

Figure 10.9: Left: Excess scaling with beam energy. It scales similar to the number of produced π^0 per event. **Right:** Integrated excess yields of HADES experiments with π^0 and reference spectrum subtracted. The excess yields evolution is scaled to the collision energy of Au+Au data based on the scaling in the left plot.

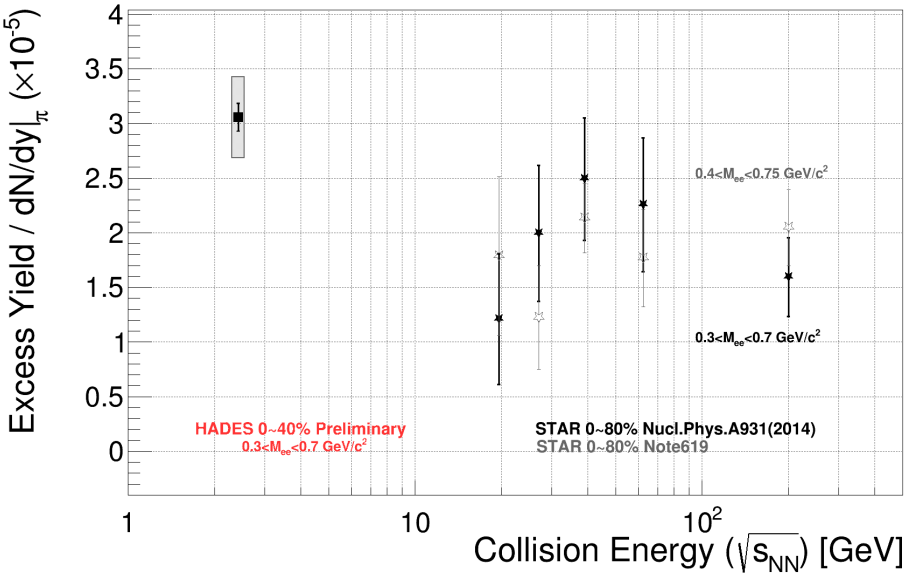

Figure 10.10: Excess yield measured by STAR together with the one measured by HADES (η and reference spectrum subtracted) as a function of collision energy.

10.5 Properties of matter created in Au+Au collisions

In heavy-ion collisions, a high energy is deposited within a volume, much larger than the particle size itself. This system is assumed to be in thermal equilibrium during the hottest collision stage in which particles are produced. Based on these assumptions, this system can be expected to be an ideal gas in which particle velocities are described by Maxwell-Boltzmann distributions [147]. Therefore, to estimate the temperature of the system the pair m_T spectra are fit with the Boltzmann distribution:

$$\frac{dn}{dm_T} \propto m_T^{3/2} e^{\frac{-m_T}{T}}, \tag{10.4}$$

where m_T is the transverse mass and T_{eff} the inverse slope, the so-called *effective temperature*. The latter is a convolution of the particle temperature and the radial expansion of the system. Such a fit is applied to the transverse mass spectrum for five different mass ranges (see Fig. 10.11 (left)). π^0 and η or 1/2(pp+np) and η are not subtracted from the data. Each mass range is expected to comprise multiple sources for particle production, having one slope per source. The mass ranges up to 0.45 GeV/c indicate at least two slopes, while the higher mass range indicates a single slope. Consequently, each distribution is fit in a m_T range from 0.07 GeV/c^2 [2] to 1.0 GeV/c^2 [3]. The fits are indicated by the colored lines and provide an effective temperature for each mass range (see Fig. 10.11 (right)). Errors of the fit results arise due to statistical uncertainties of each single points resulting an uncertainty of the determined fit parameter.
The results in Fig. 10.11 (right) reveal an increase of the effective temperature as a function of mass. The estimated temperature in the π^0 mass range needs to be corrected to account for

[2] 0.1 GeV/c^2 for the lowest mass range
[3] 0.6 GeV/c^2 for the highest mass range

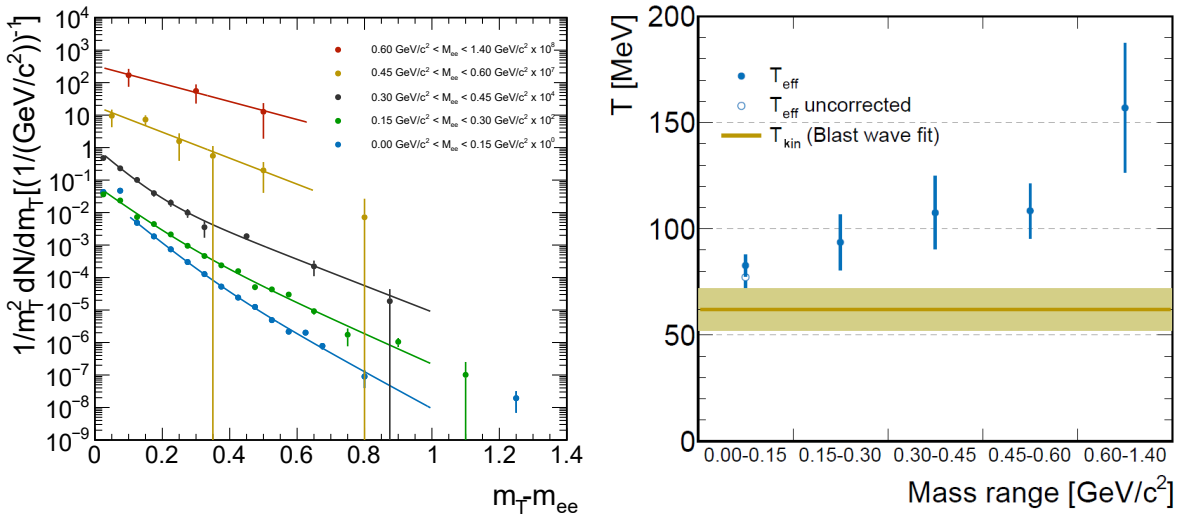

Figure 10.11: Left: Transverse mass spectra for five different mass regions together with their Boltzmann fit. No π^0, η and 1/2(pp+np) subtraction has been done. **Right**: Resulting effective temperatures obtained by a one slope Boltzmann fit. They are compared to the kinetic freeze-out temperature estimated with a blast wave fit [148].

the photon of the Dalitz decay which is not considered for the mother particle reconstruction. This is done by comparing the estimated slopes of $\pi^0 \rightarrow \gamma e^+e^-$ with $\pi^0 \rightarrow e^+e^-$ and using the differences of the estimated T_{eff} as correction factor. As a result, a correction of 5.5 MeV is estimated. A comparison of the extracted effective temperatures shows the largest deviations from the trend for the 0.45 GeV/c^2 $< M_{ee} <$ 0.60 GeV/c^2 range. However, they are still consistent within errors. The kinetic freeze-out temperature is not expected to vary strongly with particle mass. As a consequence, the steady rise of the effective temperature is accounted to the contribution by radial expansion. Particles with a higher mass a more affected by the radial expansion of the systems. The rise of their β_T manifests itself in a larger temperature enhancing T_{eff} for particles with larger masses:

$$T_{eff} = T_{kin} + 1/2m < \beta_T^2 >, \tag{10.5}$$

where T_{kin} is the kinetic freeze-out temperature. The kinetic freeze-out temperature is estimated by a blast wave fit using protons, charged pions, K$^+$, K^0_s, ϕ and Λ. As a result of the fit a kinetic freeze-out temperature of 62 $\pm$ 10 MeV is estimated [148]. This value is smaller than the T_{eff} value due to the radial expansion of the collision system.

A second approach of temperature estimation within the collision systems is provided by the slope of the excess yield (properly scaled 1/2(pp+np) and η are subtracted). This approach assumes the fireball as object emitting thermal radiation in form of virtual photons following Planck's law [149]. The temperature of the radiator can be extracted by a fit to the invariant mass distribution of the excess spectrum. A temperature extraction requires a proper scaling of the mass spectrum by $1/M_{ee}^{\frac{3}{2}}$ [54].

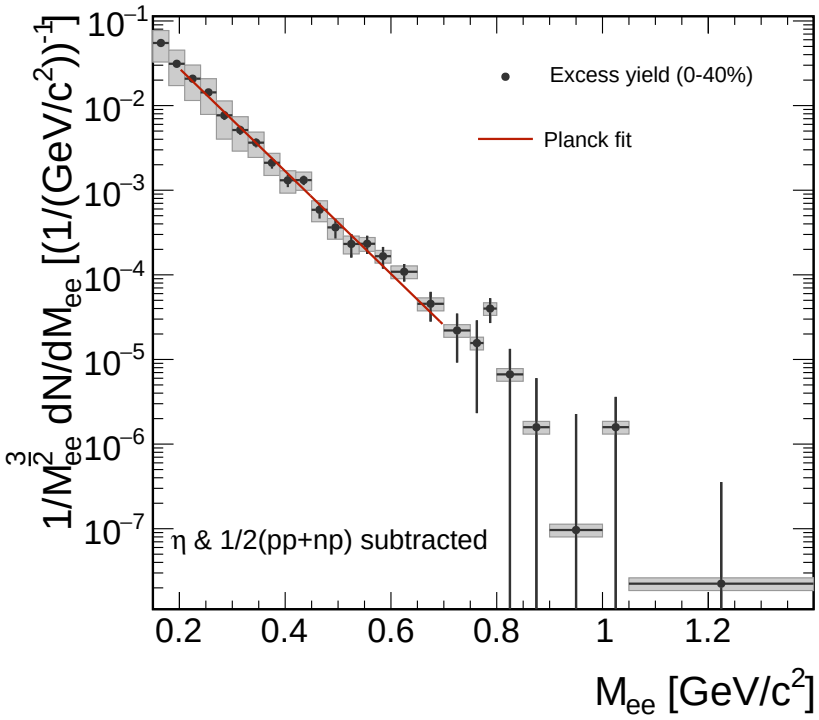

Figure 10.12: Planck fit to the excess yield. The excess is estimated for the case with η and reference spectrum subtraction.

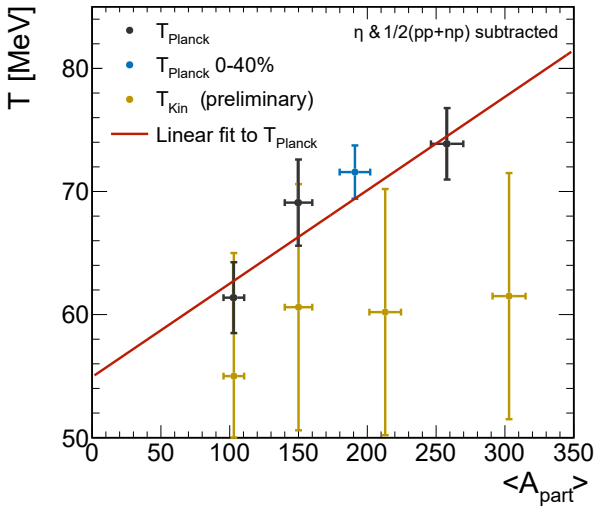

Figure 10.13: Temperatures estimated by slope fit to the excess yield in the mass range between 0.2 GeV/c^2 and 0.7 GeV/c^2. The errors in x-direction depict the error of A_{part}. The centrality dependence is indicated by a fit of a linear function to data from the different centrality ranges. The temperature of $0-40\%$ centrality is shown as reference. T_{kin} is estimated by a blast wave fit to the hadron spectra. The conservative error of 10 MeV is assumed.

The resulting distribution is presented in Fig. 10.12 and a fit is applied in the mass range 0.2 GeV/c^2 to 0.7 GeV/c^2. As a result a temperature of 71.6±2.2 MeV is extracted. This estimated temperature is the real source temperature of the radiation during the hot and dense phase. However, it does not indicate the maximum temperature but the average temperature. The peak temperatures are definitely higher. A comparison to the model calculations in Fig. 1.30 (right) indicates a maximum temperature of 80 MeV. Assuming a lifetime τ=15 fm/c of the hot and dense stage, results in a temperature matching with the average of the simulation. Moreover, the temperatures have been extracted for $0\%-20\%$, $20\%-30\%$ and $30\%-40\%$ centrality classes. The results, shown in Fig. 10.13, indicate a rise of the temperature towards more central events. This fact suggests a higher initial temperature in more central collisions. The estimated temper-

atures are slightly higher than the kinetic freeze-out temperatures in every centrality class. In conclusion, the dielectrons must be produced in a collision stage before the freeze-out and are a probe of the hot and dense collision stage.

10.6 Assessment of excess characteristics using model calculations

The efficiency corrected mass spectrum is compared to the experimentally deduced cocktail (see Fig. 10.1). An enhancement above the cocktail, the so-called excess yield, has been extracted. The origin of the e^+e^- excess could be identified by comparison to model calculations. Each model uses different production and propagation mechanisms. Therefore, a comparison to various models might give insides to a certain production scenario and the in-medium propagation of hadrons.

In Fig. 10.14, the efficiency and acceptance corrected spectrum is presented in comparison to cocktail contributions of π^0, η [4], ω, ϕ, as discussed in chapter 10.2.3, and additional dielectron yield from coarse-grained transport model calculations [4]. Two single points in the vector meson mass region have a larger yield than their neighboring points and their mass matches with the one of ω and ϕ.

The indication of the ω meson motivates the determination of its yield. The yield is estimated by a fit of the invariant mass spectrum (see Fig.10.15) with an exponential function to model the physical background and a Gaussian function to estimate the ω yield. To reduce the number of fit parameters, the mean and width of the Gauss function was estimated by a fit to a simulated (after the full analysis chain) ω distribution. The estimated values are fixed as parameters of the Gaussian and the fit is applied to the data while considering statistical errors. The integral of the resulting Gaussian distribution provides the number of ω decaying to dielectrons only. Hence, the yield has to be divided by the branching ratio ($BR_\omega = 7.28 \cdot 10^{-5}$). However, as indicated in the insert figure in Fig.10.15 the Gaussian function does not estimate the full yield of the reconstructed ω. Therefore, the yield has to be scaled up by the ratio of the both integrals (Reconstructed/Gaussian). Consequently, the yield is scaled up by 30% to $\omega_{4\pi} = 9.9 \cdot 10^{-3} \pm 6.4 \cdot 10^{-3}$. For a comparison, the ω of the cocktail is scaled up to match with the curve of the fit (see Fig. 10.15). A scaling factor of 3.2 is used and results, together with the input yield of $3 \cdot 10^{-3}$ (resulting from a SHM fit to hadron yields), a yield of $\omega_{4\pi} = 9.6 \cdot 10^{-3}$ which agrees with the one estimated with the Gaussian + background fit.

An additional contribution to the spectrum is the in-medium ρ. It does not show any peak structure in the spectrum (blue line). Therefore, its production must be strongly affected by the medium. The underlying mechanism is attributed to the strong ρ-baryon coupling. The e^+e^-

[4] Due to the smaller errors, the η yield is taken based on the extrapolation of TAPS measurements (s.t. Fig. 1.23) [97].

medium contribution is the dominant contribution above the π^0 mass range and describes the data reasonably well.

A comparison of various models to the efficiency corrected spectrum is presented in Fig. 10.16. All models are scaled to the same yield in the mass range between 0.05 GeV/c^2 and 0.1 GeV/c^2. One of the models is a coarse graining [65] approach that has a similar magnitude as the one of [4]. Both models apply the same thermal rates [54] and use different ways to extract T, μ_B, β_T of the system. The largest deviations are present in the mass region around the ω pole mass.

Another model calculation is provided by HSD, in which dielectrons are dominantly produced due to the decay of the $\Delta(1232)$ resonance. Medium effects are introduced by a broadening and mass shift of the vector meson spectral function. Additionally, the regeneration of the Δ resonance, increases the dielectron yield. The matching to data in the mass range up to 0.3 GeV/c^2 is better than for both coarse gaining approaches. However, the yield is overestimated for the mass range above 0.4 GeV/c^2. The spectrum with medium effects shows a better agreement, since the one without underestimates the yield in the mass range between 0.4 GeV/c^{2}and 0.6 GeV/c^2. A fourth model (GiBUU) is also used and is based on contributions from various baryonic resonances, but fails to describe the mass range up to 0.7 GeV/c^2. This could be caused by the missing in-medium spectral function in this model.

A further comparison of models to p_T spectra is performed to check the description quality of the coarse-grained (GSI-Texas A&M) and HSD model calculation (see in Fig. 10.17). Both model results are very similar and have less steep shape than the data in the π^0 mass range. They match with the data points in the excess mass ranges. The best agreement is obtained for the mass range above 0.3 GeV/c^2.

All of those results lead to the conclusion, that a thermal source is relevant for the description of the excess yield. This argument could be strengthen by a check of the helicity distribution. Helicity describes the angle of the electron (positron) to the virtual photon in the rest frame of the virtual photon. A thermal source is expect to have random emission resulting in a flat helicity distribution. A challenge arises due to the strong helicity dependence of the acceptance correction (see Fig. 10.18 (upper)). For this reason, the assumption of an e^+e^- source with a flat helicity distribution is filtered by acceptance and compared to data in Fig. 10.18. The worst agreement is obtained in the π^0 mass range, which fits to the expectation that the helicity of π^0 is not flat. The better agreement in the higher mass region supports the assumption of a thermal dielectron source. This fact together with the observation, that only models using an in-medium spectral function do describe the data, strengthens the argument of thermal radiation as source of the excess.

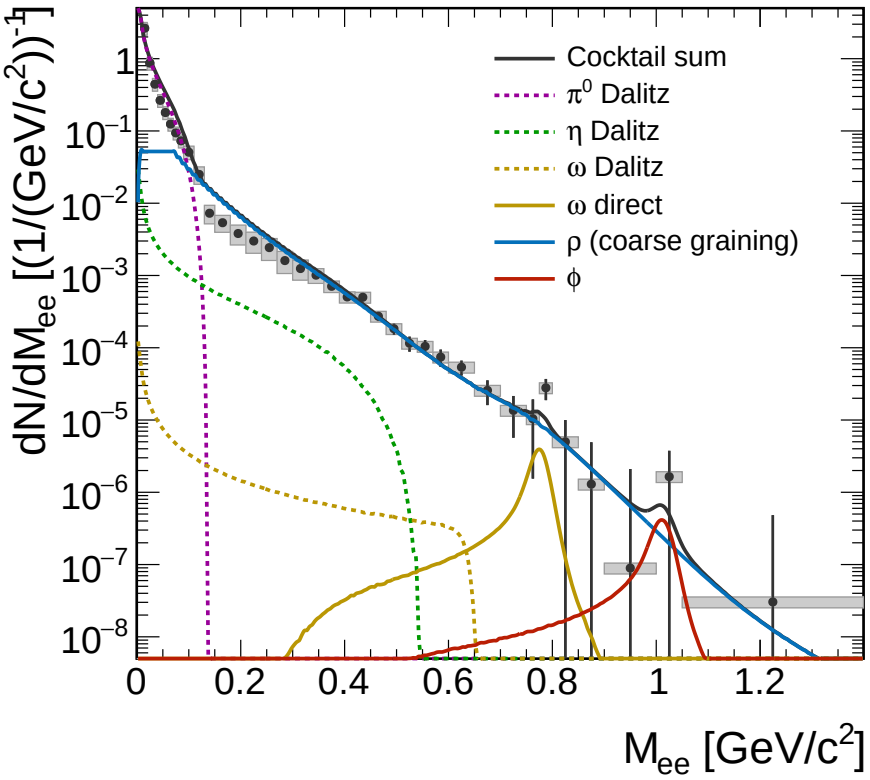

Figure 10.14: Acceptance corrected mass spectrum together with the hadronic cocktail and in-medium contribution.

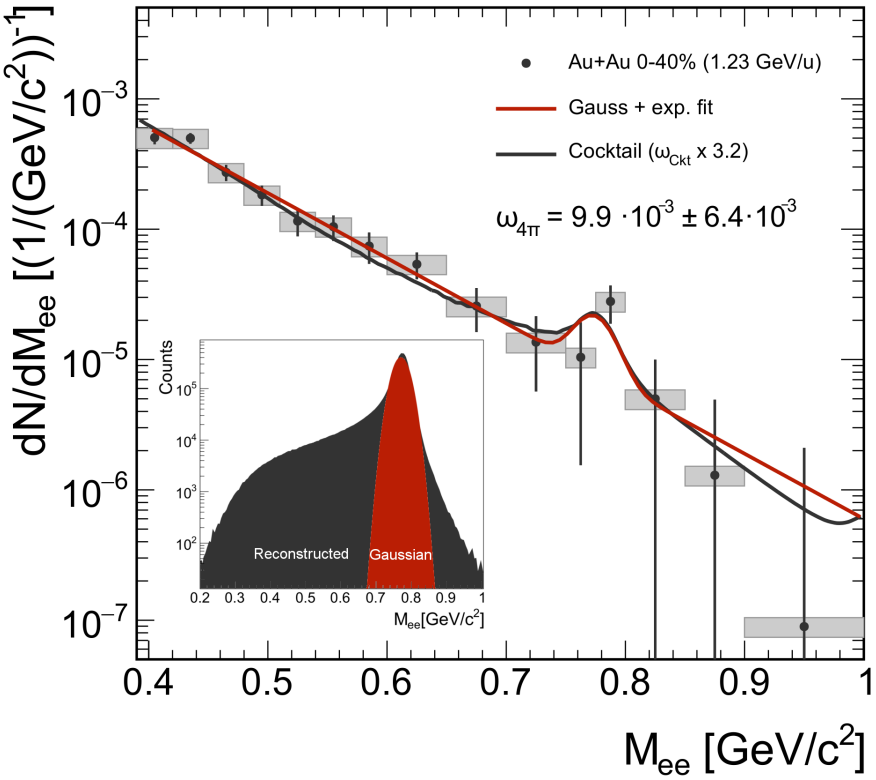

Figure 10.15: Fit of a Gaussian + exponential function to the data. The ω yield of the cocktail is scaled up to match with the yield of the fit function. The insert figure sketches how the Gaussian fit covers only a fraction of the actual ω meson distribution, which is broadened due to momentum resolution and bremsstrahlung.

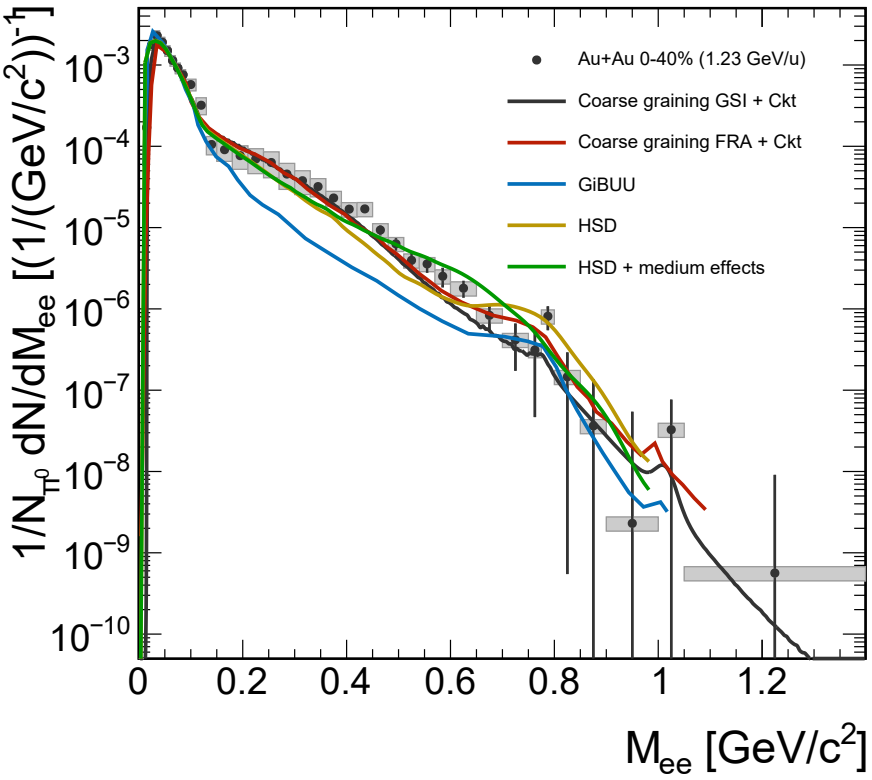

Figure 10.16: Model calculations compared to the efficiency corrected spectrum. GiBUU: [150], CG Fra: [65], HSD: [86], CG GSI: [4]

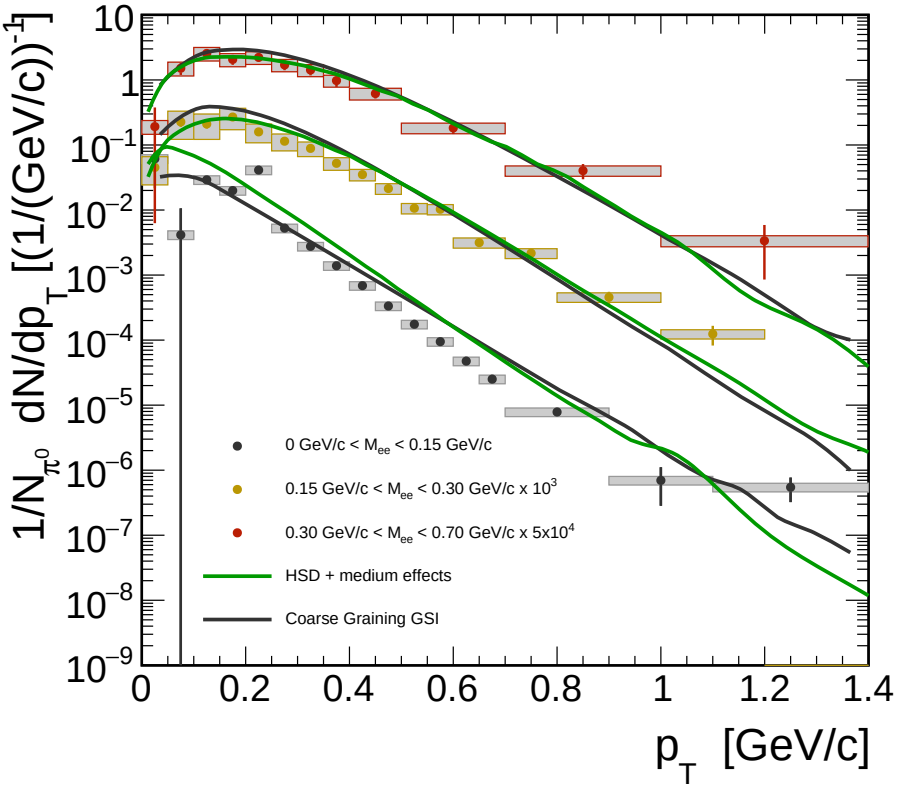

Figure 10.17: p_T for three different mass ranges compared to model calculations of HSD and coarse-grained (GSI) calculations.

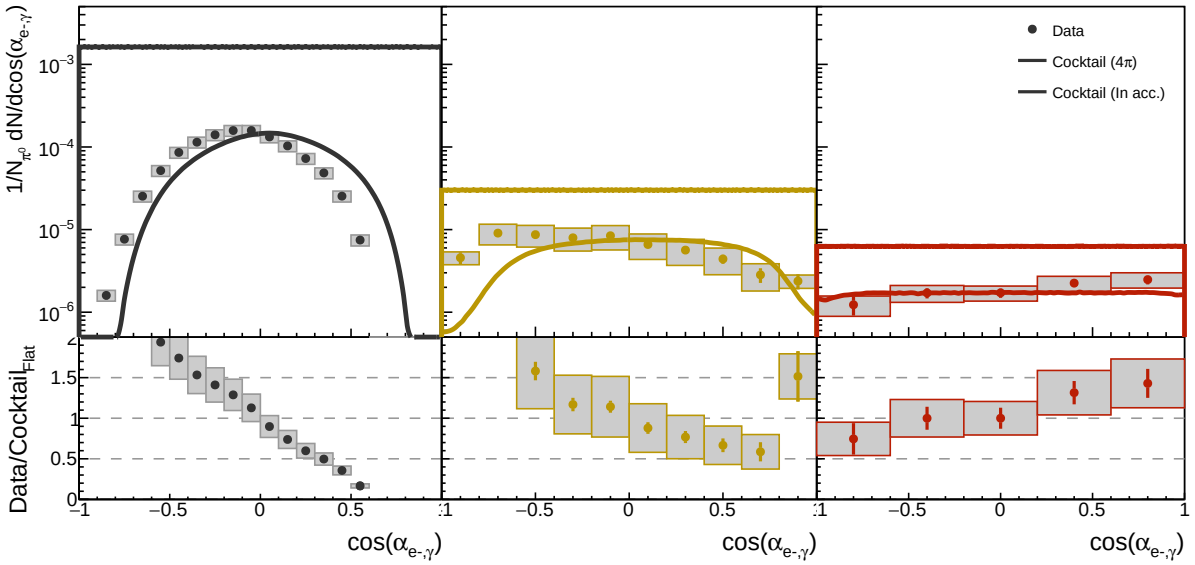

Figure 10.18: Comparison of helicity distributions to a Cocktail with flat helicity. The cocktail is scaled to match with the data at $cos(\alpha_{e^-,\gamma}) = 0$. Since the acceptance correction is strongly helicity dependent a comparison in acceptance is preferred. A ratio (lower) of data to a cocktail assuming a flat helicity distribution is presented for data in acceptance.

Chapter 11

Summary and Outlook

11.1 Summary

In this thesis, the measurement of dielectrons in Au+Au collisions was presented. In total, $7.3 \cdot 10^9$ of the 47% most central events were recorded at a kinetic beam energy of $1.23A$ GeV and have been used for the analysis.

In order to improve the separation of electrons and positrons from hadronic background and the close pair rejection, a backtracking algorithm has been developed to enhance the detection capability of the RICH detector. Observables provided by various detectors, were applied in a three step signal identification procedure: (I) track selection, (II) particle identification and (III) close pair rejection. Subsequently, the identified lepton candidates were paired within events. The background of uncorrelated combinations was estimated by a same event like-sign and mixed unlike-sign background. Finally, a correction for efficiency and acceptance effects of the detector and the identification procedure was evaluated and applied to the reconstructed signal pairs.

As a result, the properties of the dielectron signal were presented, whereof their invariant mass is of major importance since it is directly related to the spectral function of vector mesons. The reconstructed invariant mass spectrum is nearly structureless. Small yields of ω and ϕ contribute to the spectrum. An indication for a ρ peak is not present, suggesting a strong broadening of the spectral function due substantial depletion of the chiral condensate. The medium radiation was isolated by subtraction of the sources from the initial and freeze out stages from the full invariant mass spectrum. An excess yield of $1.322 \cdot 10^{-4} \pm 0.056 \cdot 10^{-4}(stat) \pm 0.16 \cdot 10^{-4}(sys)$ was estimated in the mass range between 0.3 GeV/c^2 and 0.7 GeV/c^2 for events with 0% to 40% centrality. This dilepton source is dominant compared to all other contributions and therefore a clear indication of a medium created within the collision is possible. Its evolution was also investigated as a function of 10% centrality classes. A scaling of the excess yield was confronted with assumption of an evolution like $C_0 \cdot A_{part}^{\alpha}$. As a result, a scaling with $\alpha = 1.44 \pm 0.017$ has been observed, indicating a larger, hotter and/or more dense system in more central events. A comparison to the excess yield estimated at collision energies up to 200 GeV shows a rather

moderate collision energy dependence. This indicates, that the a larger system size convoluted with the fireball lifetime ($V \otimes \tau$) compensates for the reduced excess yield due to the lower temperature at SIS18 collision energies.

To characterize some of the system properties, an effective temperature was estimated for five mass bins and indicates a rise towards higher masses. This effect is explained due to the radial expansion of the fireball. Additionally, a true fireball temperature was extracted by a "Planck"-like fit to the excess yield. A temperature of 71.6$\pm$2.2 MeV was estimated for the 40$\%$ most central events. The temperature was also estimated for three separate centrality classes. As a result, a hotter temperature for more central events has been found. These temperatures are higher than the kinetic freeze-out temperature in the corresponding centrality class. Finally, the data were compared to model calculations from GiBUU, HSD and two coarse-grained approaches. It showed, that only models including medium radiation are able to describe the Au+Au dielectron spectrum.

11.2 Future experiments

HADES plans to continue the systematic studies of dielectrons and strangeness production in heavy-ion and elementary collisions. An upgrade of the SIS18 will be finished in the beginning of 2018 and will allow new measurement campaigns. In the so-called FAIR Phase-0, the upgraded HADES detector will be in operation. HADES plans to measure Ag+Ag collisions at the highest available energy at SIS18 (1.65A GeV). This will provide further studies of the excess excitation and allow to access ω and ϕ with higher statistics (see table 11.1). The intermediate mass range might be accessible as well. Due to the top SIS18 energy, strangeness will be more abundant and the measurement of Ξ^- is identified as one of the major topics. Additionally, π^- induced reactions are planned to scan the heavier resonances compared to the first pion beam measurements in 2014.

HADES will also operate at FAIR Phase-1, at the SIS100 accelerator. Therefore, the experiment has to be moved to the new cave, which is shared with the CBM experiment. A measurement of heavy systems at highest energies is not possible due to the larger number of produced particles, but HADES will perform important reference measurements. Moreover, Ag+Ag can be measured at 3.5A GeV to investigate the excess yield scaling with collision energy. More important, the increased energy allows to access the dielectron invariant masss range above the ϕ mass. At these low energies the structureless intermediate mass range is dominantly produced by in-medium sources, since the background of charm and Drell-Yan decays is rather small. Therfore a measurement of the slope of the spectrum in the intermediate mass range could provide a measure of system temperature [54].

Observable	Counts/day (Ar+CL)	Counts/day (Ag+Ag)
Excess ($0.15 < M < 0.55$ GeV/c^2)	690	55200
η ($M > 0.15$ GeV/c^2)	275	13200
ω	1.7	82
Φ	~0.25	12
$1.1 < M < 1.5$ GeV/c^2	~5×10^{-4}	0.2

Table 11.1: Dielectron yields per day in Ag+Ag at 1.65A GeV. The yields are estimated based on the Ar+KCl beam time, with an increased event rate by factor eight, increased yield due to Apart scaling of a factor three to five and an enhanced efficiency of a factor of two. A comparison to the Ar+KCl beam time indicates the better performance.

11.3 Upgrades

Several experiments are proposed to continue the investigation of QCD matter at SIS18 energies and increased energies at the upcoming FAIR accelerator SIS100 with HADES. For this purpose, several detector upgrades are needed and being realized.

Detector upgrades

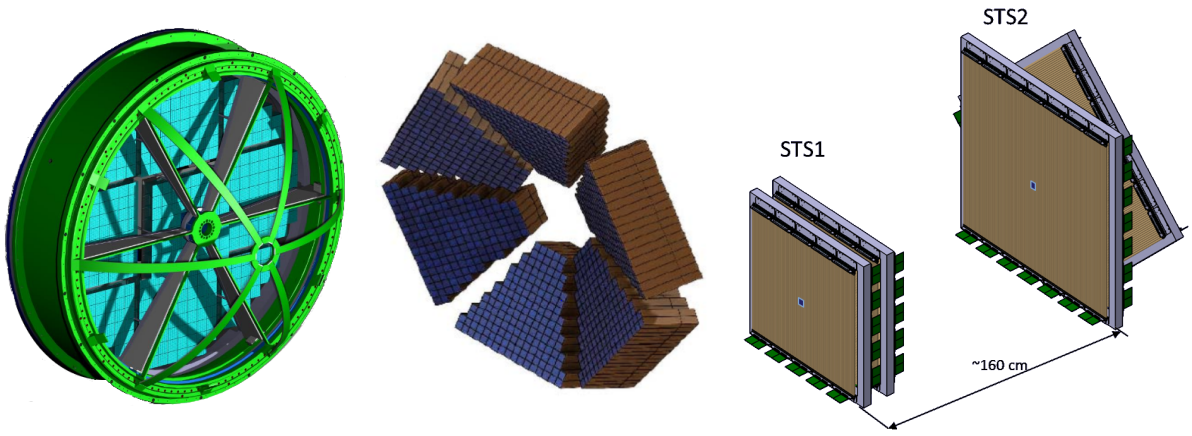

Figure 11.1: Sketch of RICH detector (left), ECAL (center) and STS (right).

RICH

A high efficiency of the RICH detector is essential for the dielectron analysis. During the Au+Au beam time, a loss of detection efficiency compared to previous beam times has been observed. As a consequence, a new UV photon detector will be installed by the end of 2017 (see Fig. 11.1 (left)). The current photon detector will be replaced by 428 photo multipliers

(MAPMT), that are the same type, which will be used for the CBM RICH detector at FAIR. The ring reconstruction is tested with the CBM algorithm and will enhance the e^+/e^- identification efficiency substantially [151]. Once backtracking is adjusted to the new RICH geometry, it is anticipated that the lepton identification will become more efficient. Further improvements are expected due to the close pair rejection with backtracking which might be more efficient with an increased number of photons (see Appendix).

Electromagnetic calorimeter

The dilepton analysis requires knowledge about the π^0 and η yields as reference. Up to now, HADES is only able to identify photons via the conversion method, which is not very efficient due to the low conversion probability of around 1%. Therefore, an electromagnetic calorimeter, replacing the PreShower detector and covering the polar angular region $16^\circ < \theta < 45^\circ$, is under construction. It will be equipped with 978 modules comprising a lead glas Cherenkov counters and photomultipliers (see Fig. 11.1 (center))). Four out of the six sectors are planned to be operational in 2018. Besides the possibility to detect π^0 and η directly, further decay channels of baryonic resonances, including photons as decay products, will be accessible. Moreover, the dilelectron analysis will profit from a significantly improved e^+/e^- to hadron separation for momenta above 0.4 GeV/c [152].

Forward detector

Collisions of π^- and p with nucleons or nuclei provide the baseline for heavy ion collisions. In order to increase the HADES acceptance in forward direction ($0.5^\circ < \Theta < 6.5^\circ$) for light collision systems, a new forward detector will be installed. It consists of two Straw tube tracking stations (STS) (see Fig. 11.1 (right)), which apply the technology that will be used in PANDA at FAIR. Additionally, the ToF will be measured by an RPC detector and a segmented scintillator will provide an energy loss information. Simulations have shown that measurements of centrality or event plane, using SSTS in heavy-ion collisions, will not be possible due to the high occupancy [153].

MDC upgrade

In order to be able to comply the requirements of high rates and occupancy, the MDC detector read out electronics have to be upgraded. The reduction of crosstalk between neighboring wires, and an increased bandwidth will increase the capability to operate at high hit occupancies [154].

Zusammenfassung

Einleitung

QCD-Materie kann verschiedene Zustände annehmen, deren Auftreten von der vorherrschenden Temperatur und Dichte abhängt. In solchen Zuständen wird eine Modifikation von Eigenschaften der Hadronen, im Vergleich zu denen bei Normaldruck und Normaltemperatur, erwartet. Schwerionenkollisionen bei (ultra-)relativistischen Energien bieten eine Möglichkeit solch extreme Materiezustände im Labor zu untersuchen. Eine Schwerionenkollision entwickelt sich dynamisch, was zu einer Änderung der Temperatur und Dichte führt. Ihre Entwicklung kann in drei Stufen unterteilt werden:

- I: Erste Kollisionen
- II: Heiße und dichte Phase
- III: Ausfrierphase

Von diesen drei Phasen ist die heiße und dichte Phase am interessantesten, da dort neue Materiezustände erwartet werden. Diese zeichnen sich durch eine Verbreiterung der Spektralfunktion von Hadronen aus. Ein Nachweis dieses Effekts lässt sich durch eine erhöhte Teilchenproduktion unterhalb/oberhalb der Polmasse des jeweiligen Teilchens nachweisen.

Die Stärke dieser Effekte ist von der Temperatur, Größe und Dichte des Kollisionssystems abhängig. Generell lassen sich hohe Temperaturen mit hohen Kollisionsenergien erzeugen, während niedrigere Temperaturen jedoch hohe baryonchemische Potentiale (ein Maß der Antisymmetrie zwischen Materie und Antimaterie) bei niedrigeren Kollisionsenergien erzeugt werden. Diese Zustände können z.B. am SIS18 Beschleuniger am GSI Helmholtzzentrum für Schwerionenforschung erzeugt werden. Dabei herrschen etwa dreimal so hohe Dichten wie die normaler hadronischer Materie und Temperaturen bis etwa 80 MeV vor. Der dabei erzeugte Feuerball besitzt eine Lebensdauer von etwa 11 fm/c. Sie ist vergleichbar mit denen bei höheren Kollisionsenergien. Eine Besonderheit dieser Kollisionsenergien ist jedoch der dominante Beitrag der hadronischen Resonanzen ($\Delta,\ N^*$) zur Teilchenproduktion.

Eine Extraktion der Zustände während der Kollision ist durch die Messung der produzierten Teilchen möglich. Die starke Wechselwirkung von Hadronen innerhalb der Kollision verdeckt jedoch die Hadroneneigenschaften. Daher werden Teilchen, die mittels eines virtuellen Photons

in ein e^+e^- Paar zerfallen, sogenannte Dileptonen (Dielektronen), verwendet. Der Produktionsprozess wird jedoch nicht durch eine simple elektromagnetische Wechselwirkung beschrieben, sondern ist modifiziert und wird von einem Formfaktor beschrieben. Eine Beschreibung dieses Formfaktors liefert das *Vector Meson Dominance* (VMD) Modell. Es sagt aus, dass die virtuellen Photonen die Identität eines Vektormesons annehmen können. Dies ist möglich da beide Teilchen den gleichen Spin und die gleiche Parität besitzen. Die Wahrscheinlichkeit für ein bestimmtes Vektormeson ist durch das Gell-Mann und Zweig Quarkmodell gegeben. Daher ist ρ das dominante Vektormeson und ist zudem am besten geeignet, da es eine Lebensdauer von nur 1.3 fm/c besitzt. Dadurch zerfällt es innerhalb des Feuerballs in ein e^+e^- Paar . Dieses wechselwirkt nur elektromagnetisch und daher sehr selten, sodass die Informationen über deren Eigenschaften nahezu unverändert transportiert werden.

Eine Detektion von e^+e^- ermöglicht die Rekonstruktion des Mutterteilchens. Der dielektronische Zerfall ist jedoch mit einem Faktor $\approx 10^{-5}$ unterdrückt. Zudem sind solche Paare bei SIS18 Energien noch seltener, da sie unterhalb der elementaren Produktionsschwelle produziert werden. Eine Estimation der Teilchenproduktion im Mediums setzt die Bestimmung der Beiträge der Phasen vor und nach der heißen und dichten Phase voraus.

Bisher wurden verschiedene Dielektronenmessungen für verschiedene Kollisionssysteme und Kollisionsenergien durchgeführt. Dazu zählen die Experimente am Bevalac/SIS18, SPS und RHIC Beschleuniger. Alle beobachteten einen starken Beitrag von Dielektronen die im Medium produziert wurden. Dabei wurde eine Verbreiterung der ρ Spektralfunktion festgestellt. Ansätze zur theoretischen Beschreibung wurden von einem Modell, dass eine thermisch Produktion annimmt, geliefert und waren in der Lage, alle Messungen zu beschreiben. Jedoch wurden schwere Kollisionssyteme nur bei hohen Kollisionsenergien gemessen. Eine Erweiterung der systematischen Untersuchung wird durch High Acceptance DiElectron Spectrometer (HADES) durchgeführt, indem im Jahr 2012 Au+Au Kollision bei 1.23A GeV am SIS18 Beschleuniger gemessen wurden.

Das HADES

HADES führt Messungen am SIS18 Beschleuniger durch. Es ist für Dielektronenmessungen in Schwerionenkollisionen bis zu einer Strahlenergie von 2A GeV optimiert. Dies setzt die Aufzeichnung hoher Datenraten, große räumliche Akzeptanz, Leichtbauweise zur Reduktion von Konversion sowie Vielfachstreuung und eine gute Massenauflösung im Bereich der Vektormesonen voraus. HADES besteht aus mehreren Unterdetektoren (Siehe Fig. 11.2 (links)), welche jeweils einen spezifischen Beitrag zur Teilchenrekonstruktion leisten. Die Hauptkomponente ist ein Magnetspektrometer, bestehend aus vier Vieldrahtdriftkammern (MDC) Ebenen sowie einem supraleitenden Magneten, welches zur Spurrekonstruktion verwendet wird. Die Flugzeit einer Spur wird bestimmt indem eine Startzeit vom START Detektor und eine Stoppzeit vom RPC (Polarwinkel < 45°) oder TOF (Polarwinkel > 45°) Detektor gemessen und da-

raus die Differenz gebildet wird. Die Anzahl der Treffer im ToF Detektor wird zusätzlich zur Zentralitätsbestimmung der Kollision verwendet. Für die Elektronen- und Positronenidentifikation wird der RICH Detektor verwendet. Im Polarwinkelbereich unter 45° ist der PreShower Detektor für eine zusätzliche Hadronenreduktion installiert. Nachdem die Detektoren kalibriert wurden, werden die aufgezeichneten Messwerte mittels der Analyseumgebung HYDRA zu vollständigen Spuren rekonstruiert. Diese Informationen werden in *data summary tapes* (DST) gespeichert und für die Analyse bereitgestellt.

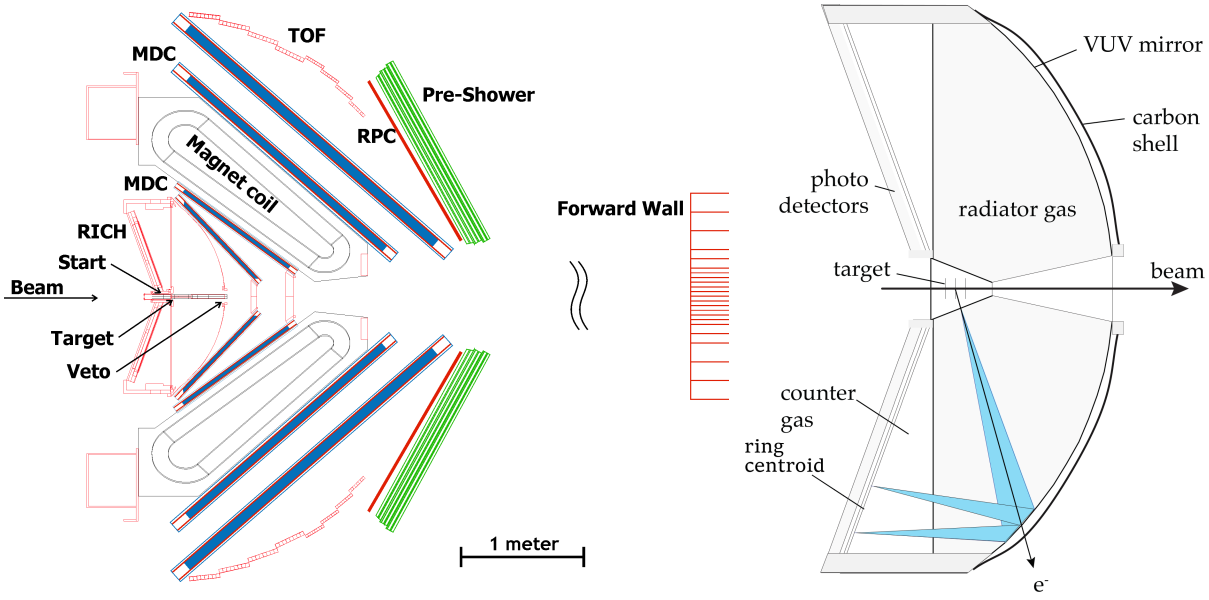

Figure 11.2: Links: Querschnitt des HADES Detektors. Der einkommende Strahl trifft von links auf ein Ziel bestehend aus 15 Goldfolien. Die Signale der erzeugten Teilchen werden von den Subdetektoren aufgezeichnet. **Rechts:** Querschnitt des RICH Detektors. Ein Elektron erzeugt beim Durchqueren des Radiators Tscherenkow Strahlung, welche durch die pad plane detektiert wird. Im Fall des Backtrackings wird die Positron Spur verwendet um den erwarteten Ringmittelpunkt (ring centroid) der Spur zu bestimmen.

Backtracking

Der RICH Detektor ist auf Identifikation von e^+/e^- Spuren ausgelegt. Jene emittieren in dem RICH Radiator Tscherenkow-Strahlung, welche kegelförmig um die Teilchenspur abgestrahlt wird. Durch den verwendeten Spiegel werden im Photonendetektor kreisförmige Photonenansammlungen für den e^+/e^- Kandidat aufgezeichnet. Als standardmäßiges Ausleseverfahren wird eine Ringsuche durchgeführt. Nachdem die Ringe identifiziert wurden, werden sie mit rekonstruierten Teilchenspuren gepaart und als e^+ oder e^- Kandidat bezeichnet, falls ein räumliche Überstimmung beider Positionen vorhanden ist.

Zur Steigerung der Effizienz wurde ein neuer Ansatz für eine effizientere Ringrekonstruktion entwickelt. Bei dem sogenannten Backtrackingverfahren wird die Geschwindigkeit und der Energieverlust der rekonstruierten Teilchenspur verwendet, um die Anzahl möglicher e^+

und e^- Kandidaten zu reduzieren. Die verbliebenen Kandidaten werden verwendet, um eine Position des Ringmittelpunktes im Photonendetektor vorherzusagen (Siehe Fig. 11.2 (rechts)). In Abhängigkeit des Ringmittelpunktes kann der Bereich, in welchem Photonen zu erwarten sind, bestimmt werden. Observablen werden aus den gemessenen Signalen, welchen mit dem Vorhersagegebiet übereinstimmen, konstruiert. Jene werden der Ausgangsspur zugeordnet, um sie im weiteren Analyseverlauf zur e^+e^- Identifikation anzuwenden.

Analyse

Für die folgende Analyse werden Au+Au Daten verwendet, welche im Jahr 2012 gemessen wurden. Es wurden nur Ereignisse mit mindestens 20 Signalen im TOF aufgezeichnet, sodass $4.98 \cdot 10^9$ der 47% zentralsten Ereignisse gespeichert wurden. Von diesem Datensatz werden Ereignisse mit schlechter Qualität entfernt. Für die Analyse werden zudem nur 40% der zentralsten Ereignisse verwendet. Nach diesen Einschränkungen stehen somit $2.6 \cdot 10^9$ Ereignisse für die Analyse bereit. Diese ist unterteilt in eine Identifizierung einzelner Leptonen und deren Rekonstruktion zu paaren.

Leptonenidentifikation

Die größte Herausforderung zur Identifikation einzelner Leptonen aus Dielektronenpaaren, besteht in deren Seltenheit bei SIS18 Energien. Sie sind von einem großen Untergrund hadronischer Teilchen, aber auch von e^+ und e^- aus Photon Konversion im Detektormaterial umgeben.

Der hadronische Untergrund wird durch Einschränkungen von physikalischen Observablen entfernt. Dazu stehen die Qualität der rekonstruierten Spur, die Abweichung zwischen Teilchenspurposition und der Position in RPC oder TOF, Teilchenimpuls, Energieverlust in MDC und TOF, PreShower Information und RICH Informationen zur Verfügung. In dieser Analyse werden die RICH Observablen des Backtrackingverfahrens verwendet. Für eine Identifikation werden alle Observablen in einem multivariaten Analyseverfahren verwendet, wodurch multidimensionale Korrelation zwischen ihnen berücksichtigt werden und zu einer verbesserten Identifikation führen. Zu Beginn wird das Analyseverfahren mit simulierten Daten trainiert. Bei der folgenden Anwendung auf echte Daten wird ein Wert zwischen 0 (Untergrund) und 1 (Signal) ausgegeben. Alle Teilchenkandidaten mit einem Wert um 1 sind sogenannte Leptonenkandidaten. Viele dieser Kandidaten sind jedoch Konversionselektronen. Ein Konversionspaar zeichnet sich vorzugsweise durch kleine Öffnungswinkel aus. Daher können Konversionselektronen mit einer Limitierung des maximalen Öffnungswinkels entfernt werden.

Paarrekonstruktion

Um Rückschlüsse auf die Eigenschaften der heißen und dichten Kollisionsphase ziehen zu können, müssen die Mutterteilchen aus e^+e^- Paaren rekonstruiert werden. Jedoch ist keine präzise

Information über die Zugehörigkeit der Leptonen und ihren Ursprungsort vorhanden, sodass alle Paare mit ungleichnamiger Ladung gebildet werden. Dabei werden jedoch auch unkorrelierte Paare generiert, die einen Untergrund bilden und daher subtrahiert werden müssen. Die Signalqualität korreliert zu dem Signal zu Untergrund Verhältnis. Daher wird eine Einschränkung des Paaröffnungswinkels auf minimal 9° angewendet, um die Kombinatorik zu reduzieren. Durch das Öffnungswinkelkriterium wird ein Großteil der Konversionselektronen entfernt während das interessante Signal erhalten bleibt, da es sich durch größere Öffnungswinkel auszeichnet. Eine Abschätzung des Untergrundes im Massenbereich bis 0.30 GeV/c^2 basiert auf dem *same-event like-sign* Verfahren. Dazu werden Paare mit gleichnamiger Ladung aus demselben Ereignis miteinander kombiniert. Der kombinatorische Untergrund (Cb_{geom}) wird aus dem geometrischen Mittelwert beider Ladungskombinationen bestimmt ($Cb_{geom} = 2\sqrt{N^{++}N^{--}}$). Da die Effizienz und Akzeptanz von Paaren mit unterschiedlicher Ladung varriert, muss der Untergrund durch den sogenannten k-Faktor korrigiert werden. Er wird mithilfe von Paaren des im Folgenden erwähnten mixed-event Verfahrens bestimmt:

$$k = \frac{N^{+-}}{2 \cdot \sqrt{N^{++} \cdot N^{--}}}, \tag{11.1}$$

wobei N^{xx} die Anzahl der Paare mit der jeweiligen Ladung kennzeichnet. Im höheren Massenbereich, sind weniger Paare vorhanden und die statistische Genauigkeit des same-event like-sign Untergrundes sinkt. Daher wird in diesem Massenbereich das sogenannte *mixed-event* Verfahren verwendet. Dabei werden ungleichnamig geladene Paare aus verschiedenen Ereignissen kombiniert. Da die Höhe des Untergrunds, im Gegensatz zum same-event like-sign Verfahren, nicht normiert ist, wird der Beitrag des mixed-event Untergrund an den des same-event like-sign Untergrund im Massenbereich zwischen 0.20 GeV/c^2 und 0.30 GeV/c^2 angepasst. Der finale Untergrund setzt sich somit aus beiden Methoden zusammen und wird von dem Spektrum der Kombinationen ungleichnamiger Ladung abgezogen. Das erhaltene Spektrum beschreibt das gemessene Signal.

Der erhaltene Untergrund ist jedoch noch von Effizienz- und Akeptanzeffekten der Analyse und des Detektors behaftet. Diese Effekte müssen korrigiert werden und werden daher mittels simulierter Daten bestimmt. Dazu wird eine Identifikation für simulierte e^+/e^- Kandidaten in echten Ereignissen durchgeführt. Als Ergebnis erhält man die Korrekturwerte für einzelne e^+/e^- Spuren. Im Folgenden werden die Beiträge zum Dielektronenspektrum, mittels eines simplen Modells zur Teilchenproduktion in einem Feuerball (Pluto), simuliert. Mittels der Ortsinformationen und Eigenschaften der simulierten Teilchen kann der entsprechende Korrekturfaktor der einzelnen Teilchen erhalten werden. Die Kombination beider Korrekturfaktoren führt zu dem Paarkorrekturfaktor für Effizienz und Akzeptanz. Dieser wird verwendet, um die rekonstruierten Paare zu korrigieren und somit die finalen Paarspektren zu erhalten.

Ergebnisse

Zu Beginn ist es wichtig, die Beiträge der außerhalb der heißen und dichten Phase zu bestimmen. Mittels elementarer Kollision (1/2(pp+np)) werden die Dielektronenbeiträge der ersten Kollisionen bestimmt. Die Beiträge der Ausfrierphase werden durch andere Zerfallskanäle in Au+Au Kollisionen extrahiert und mit dem entsprechenden Dileptonenverzweigungsverhältnis skaliert. Für die Analyse der Eigenschaften der heißen und dichten Phase werden die rekonstruierten Paareigenschaften verwendet. Davon ist die invariante Masse von besonderer Bedeutung, da sie direkt mit der Spektralfunktion der Vektormesonen verknüpft ist. Das resultierende Spektrum (siehe Fig. 11.3 (links)) zeigt einen nahezu exponentiellen Verlauf und nur eine kleine Ansammlung von ω und ϕ um deren Polmasse. Ein Beitrag von ρ bei dessen Polmasse ist nicht eindeutig zu erkennen, da dessen Spektralfunktion in der heißen und dichten Phase am stärksten modifiziert wurde. Dies ist eine Anzeichen für eine erhebliche Schwächung der Chiralen Symmetriebrechung. Der Vergleich des Au+Au Spektrums zu den Quellen der ersten Kollisionen sowie denen der Ausfrierphase zeigt eine Überstimmung im π^0 Massenbereich. Im höheren Massenbereich ist ein klarer Überschuss des Au+Au Spektrums gegenüber den gezeigten Beiträgen vorhanden. Somit wurden diese Paare in der heißen und dichten Phase produziert. Der Teilchenüberschuss kann genauer spezifiziert werden, indem die Quellen von den vorherigen und folgenden Phasen abgezogen werden. Der Teilchenüberschuss, nach Abzug von den 1/2(pp+np) und η Beiträgen, beträgt $1.065 \cdot 10^{-4} \pm 0.057 \cdot 10^{-4}(stat) \pm 0.17 \cdot 10^{-4}(sys)$ im Massenbereich zwischen 0.3 GeV/c^2 und 0.7 GeV/c^2 für eine Zentralität zwischen 0% und 40%. Eine Unterteilung in vier verschiedene Zentralitätsklassen erlaubt eine Untersuchung des Teilchenüberschusses in Abhängigkeit von der Anzahl der kollidierenden Nukleonen (A_{part}) (siehe Fig. 11.3 (rechts)). Der Verlauf wird wie folgt angenommen: $C_0 \cdot A_{part}^{\alpha}$. Eine Anpassung dieser Funktion an die Datenpunkte ergibt einen Skalierungsfaktor $\alpha = 1.44 \pm 0.17$. Der Anstieg kann durch eine höhere Temperatur, Lebensdauer und ein größeres System hervorgerufen werden. Zusätzlich wird der Teilchenüberschuss der 40% zentralsten Ereignisse mit dem aus C+C und Ar+KCl Kollisionen verglichen. Dazu muss der Teilchenüberschuss korrigiert werden, um mit der Kollisionsenergie der Au+Au Daten übereinzustimmen. Als Ergebnis erhält man ein Skalierungsfaktor $\alpha = 1.15 \pm 0.10$. Dieser Wert ist zwar niedriger als in Au+Au, aber immer noch konsistent innerhalb der Fehler. Des Weiteren wird der Überschuss in Abhängigkeit der Kollisionsenergie untersucht. Dabei zeigt sich ein nahezu konstanter Wert. Basierend auf einer niedrigeren Temperatur bei niedrigen Kollisionsenergien, würde man einen reduzierten Überschuss erwarten. Dies ist nicht der Falls und lässt auf ein größeres Kollisionsvolumen und langlebigeres Kollisionssystem bei niedrigeren Kollisionsenergien schließen.

Um einen Einblick in weitere Kollisionseigenschaften zu erhalten, wird die effektive Temperatur bestimmt. Die extrahierten Temperaturen zeigen einen Anstieg für größere Massen, was auf die radiale Expansion, welche sich stärker auf große Massen auswirkt, zurückzuführen ist. T_{Eff} beschreibt daher nicht die Emissionstemperatur der Dielektronen. Eine Temperatur zu dem Zeitpunkt der Dileptonenemission kann durch eine sogenannte "Planck"-Anpassung be-

stimmt werden. Die Temperatur für die 40% zentralsten Au+Au Kollisionen ist 71.6±2.2 MeV. Eine zentralitätsabhängige Analyse zeigt zudem einen Anstieg zu hohen Massen an (siehe Fig. 11.4 (links)). In dem Histogramm wird ebenfalls angedeutet, dass T_{Planck} jeweils höher als die kinetische Ausfriertemperatur ist. Dies bedeutet, dass die Dielektronen in einer heißen Phase vor dem ausfrieren erzeugt wurden und sich somit eignen, um die heiße und dichte Kollisionsphase zu untersuchen. Zum Schluss werden, die Daten mit Modellrechnungen von mikroskopischen Transportmodellen verglichen (siehe Fig. 11.4 (rechts). Dabei zeigen Modelle, die eine im Medium modifizierte Dileptonenspektralfunktion beinhalten (CG, HSD), eine bessere Übereinstimmung als jenes ohne (GiBUU). Zusammen mit den extrahierten Kollisionseigenschaften ergibt sich die Schlussfolgerung, dass in den gemessenen Au+Au Kollisionen eine heiße und dichte Phase erzeugt wurde, in welcher thermische Dielektron emittiert werden die einen signifikanten Teilchenüberschuss im Dielektronenspektrum herbeiführen.

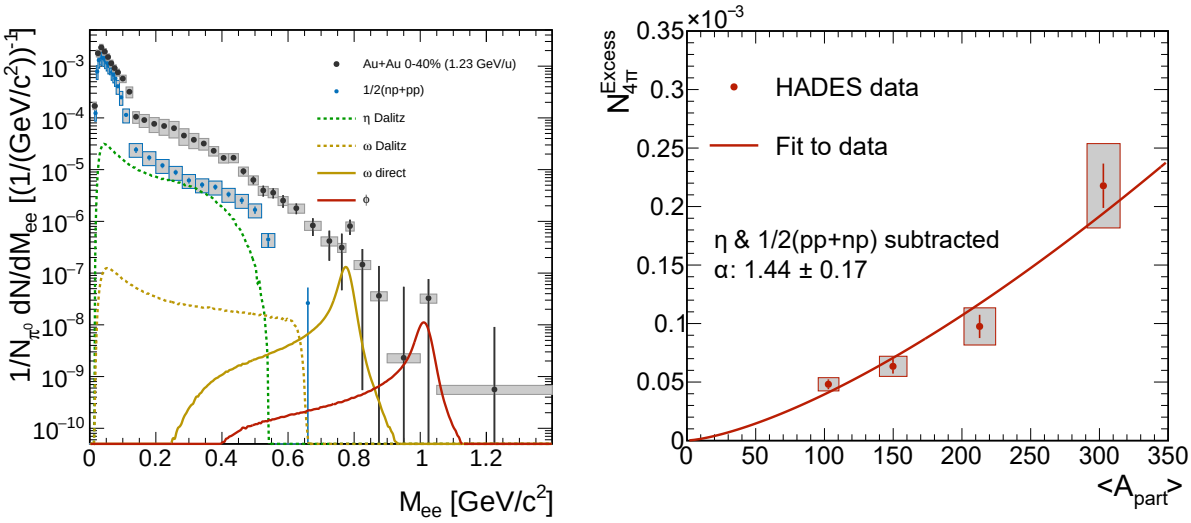

Figure 11.3: Links: Invariante Masse Verteilung für Au+Au Kollision. Die Beiträge aus elementaren Kollisionen (1/2(np+nn)) sowie die der Ausfrierphase sind zusätzlich dargestellt. π^0 ist dabei bereits in elementaren Kollisionen enthalten. **Rechts:** Akzeptanzkorrigierter Teilchenüberschuss für den Massenbereich zwischen 0.3 GeV/c^{2}und 0.7 GeV/c^2. Die rote Linie zeigt die Anpassung einer exponentiellen Funktion an die Datenpunkte.

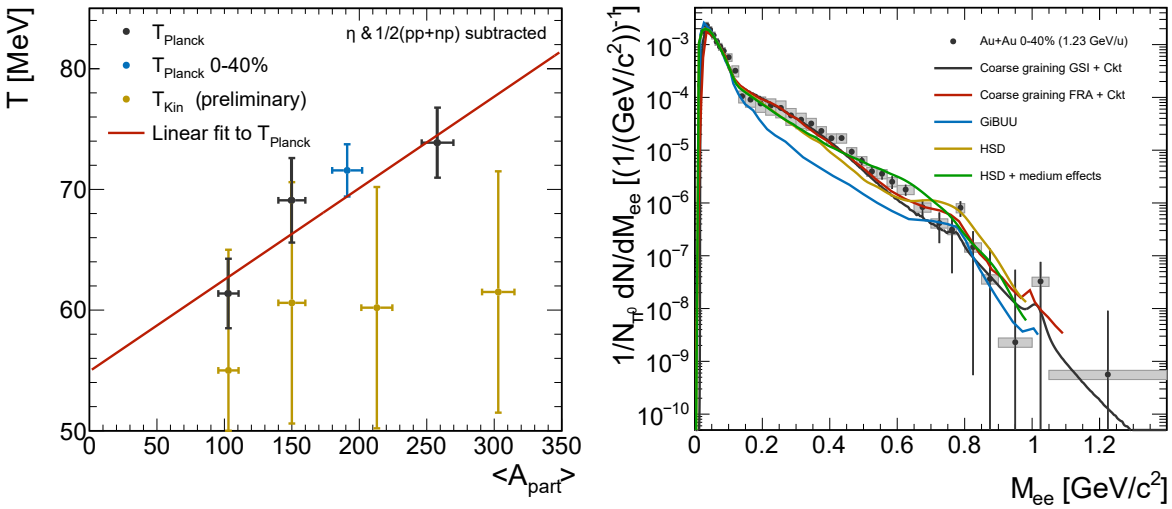

Figure 11.4: Links: Extrahierte T_{Planck} Temperaturen in Abhängigkeit von A_{part}. Zusätzlich ist die kinetische Ausfriertemperatur aufgetragen. **Rechts:** Vergleich des effizienzkorregierten Au+Au Spektrums mit verschiedenen Modellrechnungen. Alle Kurven wurden auf die Daten im Massenbereich zwischen 0.05 GeV/c^2 und 0.1 GeV/c^2 skaliert.

Appendix A

Application of backtracking at the upgraded RICH detector

An application of backtracking using the new RICH detector requires an adjustment of backtracking parameters. The geometry of the RICH photon detector changes the ring positions and therefore the shapes on the pad plane, for a given lepton track angle, are modified. Once the parameters are tuned, backtracking might profit from the higher efficiency. Especially the quality variable $\mathcal{X}^2_{Bt}$ (see section 5.4.3) will become more accurate. This is anticipated since an larger number of photons assure provide a better precision to evaluate how well the photon distribution matches with the predicted ring shape. Also the basic observables, e.g. the number of pads or number of maxima, will provide a better separation between signal and noise hits. Therefore, the lepton identification with backtracking is assumed to gain lepton identification efficiency. Based on the findings in Au+Au, lepton identification performs even better by using backtracking observables in combination with a neural network. Such an analyses might provide an even higher identification efficiency than a similar approach using the ring finder observables.

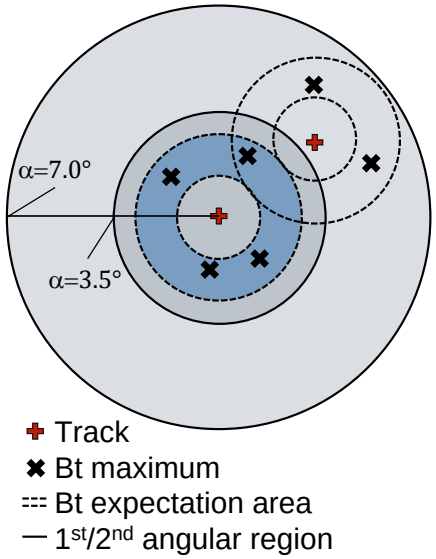

Figure A.1: Sketch of the close partner search including the two search regions. Besides an identified lepton track a possible conversion lepton partner is shown. Since the opening angle is quite large, the criteria for the outer angular region are applied. Due to the fact that both rings have unshared maxima, all are identified as leptons and marked as close pair.

Further improvements are expected due to the close pair rejection with backtracking. A rejection method applying backtracking observables was tested to improve the close pair rejection

was tested in Au+Au data but could not be implemented since the effect of the rejection was not reproduced well in simulation. Consequently, the spectra were not corrected properly by efficiency correction. The tested approached extends the application range of the close pair rejection by splitting it in two opening angle ranges (see Fig. A.1). The first range is restricted to $\alpha = 3.46°$ at $\Theta = 20°$ to $\alpha = 4.5°$ at $\Theta = 85°$ as upper threshold. A second opening angle range begins at these opening angles and is restricted by an upper opening angle limit of $\alpha = 7°$.

While the criteria in the inner range are kept as explained in section A.1, backtracking information is applied to the close pair search in the second opening angle range. The identification criterion is based on the charge of backtracking maxima per ring. Two cases of signal sharing in the RICH detector are distinguished:

1. **Case 1:** Both tracks are very close and their backtracking expectation regions overlap nearly completely, wherefore every RICH hit overlaps with the second ring as well. Consequently, this is not a reliable ring signature and could be created by matching with a random hadron track.

2. **Case 2:** The close by track candidate overlaps and besides shared hits, additional RICH hits are measured in the remaining ring region. Due to additional RICH hits, the track candidate is considered as a real lepton hit.

For rejection, only tracks having their own RICH hits are considered (Case 2) and selected via backtracking observables (see Fig. A.1). The number of isolated maxima reaches a value around 5 at maximum, while the isolated sum of maxima charge per ring offers a range from 75 up to around 2000. Since the charge has a more fine binning, it provides a more smooth selection criterion. For this reason, a minimum sum of maxima charge ($Q_{Maxima} > 150$), which is not shared with the adjacent ring is required. Finally, the rejection criteria in both angular ranges are applied to reduce further combinatorial background induced by conversion leptons.

List of Abbreviations

AGS Alternating Gradient Synchrotron

ALICE A Large Ion Collider Experiment (LHC)

ATLAS Experiment at LHC

BES Beam Energy Scan program at RHIC

BEVALAC Synchroton accelerator at Lawrence Berkeley Laboratory

BNL Brookhaven National Laboratory

BT Backtracking

CB Combinatorial Background

CERES ChErenkov Ring Electron Spectrometer

CERN European Organization for Nuclear Research

CG Coarse Graining: Theoretical approach for estimation Dielectrons yields

CMS Experiment at LHC

CP Close Pair

CTS Central Trigger System

DAQ Data Acquisition

DLS Dilepton experiment at the BEVALAC accelerator

DST Data Summary Tape

EPICS Experimental Physics and Industrial Control System

FAIR Facility for Antiproton and Ion Research

FW Forward Wall

GEANT Toolkit for the simulation of particles in matter

GiBUU Giessen Boltzmann-Uehling Uhlenbeck (Heavy-ion collision model)

HADES Hich Accpetance DiElectron Spectrometer

HBD Hadron Blind Detector

HERA File System at GSI

HLD HADES List-mode DATA

HSD Hadron String Dynamics (Heavy-ion collision model)

HYDRA Extension to ROOT framework

IMR Intermediate Mass Range

ITS Inner Tracking System

JINR Joint Institute for Nuclear Researc

LHC Large Hadron Collider

LHCb Experiment at LHC

LMR Low Mass Range

LQCD Lattice Quantum Chromo Dynamics (Model calculations)

MAPS Maximum ionizing particles

MDC dE/dx Energyloss in MDC

MDC Mini drift chamber detector

MEPS Medium ionizing particles

META Multiplicity Electron Trigger Array

METAQa META matching Quality

MIPS Minimum ionizing particles

MVA Multivariate analysis

NA60 North Area 60: Dimuon experiment at SPS

NICA Nuclotron-based Ion Collider fAcility

OBE One Boson Exchange (Model)

PHENIX Pioneering High Energy Nuclear Interactions eXperiment

PLUTO Simulation framework for heavy-ion and hadron reactions

PT3 Particle Trigger 3

PYTHIA Model for generation of high energy particle interactions

QCD Quantum Chromo Dynamics

QED Quantum Electro Dynamics

QGP Quark Gluon Plasma

RHIC Relativistic Heavy Ion Collider

RICH cal RICH calibrater: Parameter set

RICH Ring imaging cherenkov detector

RIChQa RICH matching quality

RK Runge Kutta

ROI Region Of Interest

ROOT Data Analysis Framework

RPC Resistive plate chamber

RQMD Relativistic Quantum Molecular Dynamics model (Heavy-ion collision model)

SIS100 Schwerionensynchrotron 100

SIS18 Schwerionensynchrotron 18

SMASH Simulating Many Accelerated Strongly-interacting Hadrons (Heavy-ion collision model)

SPS Super Proton Synchrotron

STAR Experiment at RHIC

TMVA Toolkit for Multivariate Data Analysis

TOF Time-of-flight Detector

ToF Time-of-flight

ToT Time over Threshold

TPC Time Projection Chamber

TRB Trigger Readout Board

UrQMD Ultrarelativistic Quantum Molecular Dynamics model (Heavy-ion collision model)

VMD Vector Meson Dominance model

List of Figures

List of Tables

Bibliography

[1] M. Gell-Mann, "A schematic model of baryons and mesons," *Physics Letters*, vol. 8, no. 3, pp. 214 – 215, 1964. 1, 1.2.2

[2] J. Friedman, "Deep inelastic scattering: Comparisons with the quark model," *Reviews of Modern Physics.*, vol. 63 (3), pp. 615–628, 1991. 1

[3] H. Bohr and H. Nielsen, "Hadron production from a boiling quark soup: A thermodynamical quark model predicting particle ratios in hadronic collisions," *Nuclear Physics B*, vol. 128, no. 2, pp. 275 – 293, 1977. 1

[4] Galatyuk, Tetyana, Hohler, Paul M., Rapp, Ralf, Seck, Florian, and Stroth, Joachim, "Thermal dileptons from coarse-grained transport as fireball probes at SIS energies," *Eur. Phys. J. A*, vol. 52, no. 5, p. 131, 2016. 1, 1.12, 1.2.4, 1.3.4, 1.30, 10.6, 10.16

[5] A. Kurkela and A. Vuorinen, "Cool Quark Matter," *Phys. Rev. Lett.*, vol. 117, p. 042501, Jul 2016. 1

[6] V. Khachatryan *et al.*, "Measurement of the inclusive 3-jet production differential cross section in proton-proton collisions at 7 TeV and determination of the strong coupling constant in the TeV range," *Eur. Phys. J.*, vol. C75, no. 5, p. 186, 2015. 1.1

[7] J. Sakurai, "Theory of Strong Interactions," *Annals of physics*, vol. 11, pp. 1–41, 1960. 1.1.1, 1.2.2

[8] F. Halzen and A. Martin, *Quarks & Leptons: An introductory course in modern particle physics*. New York, USA: John Wiley & Sons, 1984. 1.1.1

[9] O. W. Greenberg, "Spin and Unitary-Spin Independence in a Paraquark Model of Baryons and Mesons," *Phys. Rev. Lett.*, vol. 13, pp. 598–602, Nov 1964. 1.1.1

[10] L. Csernai", *Introduction to relativistic heavy ion collisions*. John Wiley and Sons Ltd., 1994. 1.1.1

[11] K. G. Wilson, "Confinement of quarks," *Phys. Rev. D*, vol. 10, pp. 2445–2459, Oct 1974. 1.1.1

[12] D. J. Gross and F. Wilczek, "Ultraviolet Behavior of Non-Abelian Gauge Theories," *Phys. Rev. Lett.*, vol. 30, pp. 1343–1346, Jun 1973. 1.1.1

[13] Z. Fodor and C. Hoelbling, "Light Hadron Masses from Lattice QCD," *Rev. Mod. Phys.*, vol. 84, p. 449, 2012. 1.1.1

[14] R. Gupta, "Introduction to lattice QCD: Course," in *Probing the standard model of particle interactions. Proceedings, Summer School in Theoretical Physics, NATO Advanced Study Institute, 68th session, Les Houches, France, July 28-September 5, 1997. Pt. 1, 2*, pp. 83–219, 1997. 1.1.1

[15] A. Bazavov et al., "Fluctuations and correlations of net baryon number, electric charge, and strangeness: A comparison of lattice qcd results with the hadron resonance gas model," *Phys. Rev. D*, vol. 86, p. 034509, 2012. 1.1.1

[16] Z. Fodor and S. D. Katz, "Critical point of QCD at finite T and mu, lattice results for physical quark masses," *JHEP*, vol. 04, p. 050, 2004. 1.1.1, 1.1.3

[17] V. Koch, "Aspects of chiral symmetry," *Int. J. Mod. Phys.*, vol. E6, pp. 203–250, 1997. 1.1.2

[18] B. Friman, C. Hohne, J. Knoll, S. Leupold, J. Randrup, R. Rapp, and P. Senger, "The CBM physics book: Compressed baryonic matter in laboratory experiments," *Lect. Notes Phys.*, vol. 814, p. pp. 980, 2011. 1.1.2, 1.1.3, 1.2.1, 1.3.1

[19] Y. Nambu, "Quasi-Particles and Gauge Invariance in the Theory of Superconductivity," *Physical Review*, vol. 117, pp. 648–663, Feb. 1960. 1.1.2

[20] J. Goldstone, A. Salam, and S. Weinberg, "Broken Symmetries," *Physical Review*, vol. 127, pp. 965–970, Aug. 1962. 1.1.2

[21] M. Gell-Mann, R. J. Oakes, and B. Renner, "Behavior of Current Divergences under $\mathrm{SU}_3 \times \mathrm{SU}_3$," *Phys. Rev.*, vol. 175, pp. 2195–2199, Nov 1968. 1.1.2

[22] S. Weinberg, "Precise Relations between the Spectra of Vector and Axial-Vector Mesons," *Phys. Rev. Lett.*, vol. 18, pp. 507–509, Mar 1967. 1.1.2

[23] S. Schael *et al.*, "Branching ratios and spectral functions of tau decays: Final ALEPH measurements and physics implications," *Phys. Rept.*, vol. 421, pp. 191–284, 2005. 1.2

[24] R. Rapp, "The Vector probe in heavy-ion reactions," *J. Phys.*, vol. G31, pp. S217–S230, 2005. 1.2

[25] R. Bellwied, S. Borsanyi, Z. Fodor, J. Günther, S. D. Katz, C. Ratti, and K. K. Szabo, "The QCD phase diagram from analytic continuation," *Phys. Lett.*, vol. B751, pp. 559–564, 2015. 1.3

[26] S. Borsanyi, Z. Fodor, C. Hoelbling, S. D. Katz, S. Krieg, C. Ratti, and K. K. Szabo, "Is there still any T_c mystery in lattice QCD? Results with physical masses in the continuum limit III," *JHEP*, vol. 09, p. 073, 2010. 1.1.3, 1.4

[27] H.-T. Ding, A. Francis, O. Kaczmarek, F. Karsch, E. Laermann, and W. Soeldner, "Thermal dilepton rate and electrical conductivity: An analysis of vector current correlation functions in quenched lattice qcd," *Phys. Rev. D*, vol. 83, p. 034504, Feb 2011. 1.1.3

[28] Z. Fodor and S. D. Katz, "Critical point of QCD at finite T and mu, lattice results for physical quark masses," *JHEP*, vol. 04, p. 050, 2004. 1.1.3

[29] F. Karsch, E. Laermann, and C. Schmidt, "The chiral critical point in 3-flavour QCD," *Physics Letters B*, vol. 520, no. 1-2, pp. 41 – 49, 2001. 1.1.3

[30] B. Friman, F. Karsch, K. Redlich, and V. Skokov, "Fluctuations as probe of the QCD phase transition and freeze-out in heavy ion collisions at LHC and RHIC," *Eur. Phys. J.*, vol. C71, p. 1694, 2011. 1.1.3

[31] P. Braun-Munzinger, V. Koch, T. Schäfer, and J. Stachel, "Properties of hot and dense matter from relativistic heavy ion collisions," *Physics Reports*, vol. 621, pp. 76 – 126, 2016. Memorial Volume in Honor of Gerald E. Brown. 1.1.3

[32] L. McLerran, "Quarkyonic Matter and the Phase Diagram of QCD," in *Continous advances in QCD. Proceedings, 8th Workshop, CAQCD-08, Minneapolis, USA, May 15-18, 2008*, pp. 125–134, 2008. 1.1.3

[33] A. Andronic, D. Blaschke, P. Braun-Munzinger, J. Cleymans, K. Fukushima, L. McLerran, H. Oeschler, R. Pisarski, K. Redlich, C. Sasaki, H. Satz, and J. Stachel, "Hadron production in ultra-relativistic nuclear collisions: Quarkyonic matter and a triple point in the phase diagram of {QCD}," *Nuclear Physics A*, vol. 837, no. 1-2, pp. 65 – 86, 2010. 1.1.3, 1.5, 1.1.3

[34] L. McLerran and R. D. Pisarski, "Phases of dense quarks at large Nc," *Nuclear Physics A*, vol. 796, no. 1-4, pp. 83 – 100, 2007. 1.1.3

[35] Z. Fodor, S.D. Katz, "Critical point of QCD at finite T and μ, lattice results for physical quark masses," vol. 050 [arXiv:hep-lat/0402006], 2004. 1.5

[36] B. Schaefer and J. Wambach, "Private communication." 1.5

[37] M. Lorenz, "Reviewing hadron production at SIS energies featuring the new HADES data," *Nuclear Physics A*, vol. 931, pp. 785 – 789, 2014. 1.5

[38] J. Cleymans and K. Redlich, "Chemical and thermal freezeout parameters from 1 A/GeV to 200-A/GeV," *Phys. Rev.*, vol. C60, p. 054908, 1999. 1.5, 1.1.3

[39] J. Stachel, A. Andronic, P. Braun-Munzinger, and K. Redlich, "Confronting LHC data with the statistical hadronization model," *J. Phys. Conf. Ser.*, vol. 509, p. 012019, 2014. 1.5

[40] P. Braun-Munzinger, K. Redlich, and J. Stachel, "Particle production in heavy ion collisions," 2003. 1.1.3

[41] F.Seck, "Centrality determination at 1.23 AGeV Gold-Gold collision and readout-electronics for the HADES electromagnetic calorimeter," Master's thesis, Technische Universitaet Darmstadt, 2015. 1.6

[42] P. M. Hohler and R. Rapp, "Massive Yang-Mills for vector and axial-vector spectral functions at finite temperature," *Annals Phys.*, vol. 368, pp. 70–109, 2016. 1.2.1, 1.7

[43] R. Rapp and J. Wambach, "Chiral symmetry restoration and dileptons in relativistic heavy ion collisions," *Adv. Nucl. Phys.*, vol. 25, p. 1, 2000. 1.2.1, 1.8, 1.2.1, 1.3.1

[44] R. Arnaldi *et al.*, "First measurement of the rho spectral function in high-energy nuclear collisions," *Phys. Rev. Lett.*, vol. 96, p. 162302, 2006. 1.2.1, 1.3.1, 1.3.1

[45] M. Herrmann, B. L. Friman, and W. Norenberg, "Properties of rho mesons in nuclear matter," *Nucl. Phys.*, vol. A560, pp. 411–436, 1993. 1.2.1

[46] G. Chanfray and P. Schuck, "The Rho meson in dense matter and its influence on dilepton production rates," *Nucl. Phys.*, vol. A555, pp. 329–353, 1993. 1.2.1

[47] M. Post, S. Leupold, and U. Mosel, "Hadronic spectral functions in nuclear matter," *Nucl. Phys.*, vol. A741, pp. 81–148, 2004. 1.2.1

[48] W. Peters, M. Post, H. Lenske, S. Leupold, and U. Mosel, "The Spectral function of the rho meson in nuclear matter," *Nucl. Phys.*, vol. A632, pp. 109–127, 1998. 1.2.1

[49] R. Rapp, G. Chanfray, and J. Wambach, "Medium modifications of the rho meson at CERN SPS energies," *Phys. Rev. Lett.*, vol. 76, pp. 368–371, 1996. 1.2.1

[50] P. Muehlich, V. Shklyar, S. Leupold, U. Mosel, and M. Post, "The spectral function of the ω meson in nuclear matter from a coupled-channel resonance model," *Nuclear Physics A*, vol. 780, pp. 187 – 205, 2006. 1.2.1

[51] L. G. Landsberg, "Electromagnetic Decays of Light Mesons," *Phys. Rept.*, vol. 128, pp. 301–376, 1985. 1.2.2

[52] J. Beringer et al. (Particle Data Group) *Phys. Rev. D*, vol. 86, p. 010001, 2012. 1.10

[53] K. A. Olive *et al.*, "Review of Particle Physics," *Chin. Phys.*, vol. C38, p. 090001, 2014. 1.1

[54] R. Rapp and H. van Hees, "Thermal dileptons as fireball thermometer and chronometer," *Physics Letters B*, vol. 753, pp. 586 – 590, 2016. 1.2.3, 1.2.4, 1.3.1, 1.3.4, 10.5, 10.6, 11.2

[55] T. Sjostrand, S. Mrenna, and P. Z. Skands, "A Brief Introduction to PYTHIA 8.1," *Comput. Phys. Commun.*, vol. 178, pp. 852–867, 2008. 1.2.4

[56] W. Cassing and E. L. Bratkovskaya, "Parton-Hadron-String Dynamics: an off-shell transport approach for relativistic energies," *Nucl. Phys.*, vol. A831, pp. 215–242, 2009. 1.13, 1.2.4

[57] S. A. Bass *et al.*, "Microscopic models for ultrarelativistic heavy ion collisions," *Prog. Part. Nucl. Phys.*, vol. 41, pp. 255–369, 1998. [Prog. Part. Nucl. Phys.41,225(1998)]. 1.2.4

[58] M. Bleicher, E. Zabrodin, C. Spieles, S. A. Bass, C. Ernst, S. Soff, L. Bravina, M. Belkacem, H. Weber, H. Stöcker, and W. Greiner, "Relativistic hadron-hadron collisions in the ultra-relativistic quantum molecular dynamics model," *Journal of Physics G: Nuclear and Particle Physics*, vol. 25, no. 9, p. 1859, 1999. 1.2.4

[59] H. Stöcker, H. Sorge, and W. Greiner, "Poincare invariant hamiltonian dynamics: modelling multi-hadronic interactions in a phase space approach," *Annals of Physics*, vol. 192, p. 266, 1989. 1.2.4

[60] O. Buss, T. Gaitanos, K. Gallmeister, H. van Hees, M. Kaskulov, O. Lalakulich, A. B. Larionov, T. Leitner, J. Weil, and U. Mosel, "Transport-theoretical Description of Nuclear Reactions," *Phys. Rept.*, vol. 512, pp. 1–124, 2012. 1.2.4

[61] J. Weil *et al.*, "Particle production and equilibrium properties within a new hadron transport approach for heavy-ion collisions," 2016. 1.2.4

[62] J. Weil, J. Staudenmaier, and H. Petersen, "Dilepton production with the SMASH model," *J. Phys. Conf. Ser.*, vol. 742, no. 1, p. 012034, 2016. 1.2.4

[63] D. M. Manley and E. M. Saleski, "Multichannel resonance parametrization of pi N scattering amplitudes," *Phys. Rev.*, vol. D45, pp. 4002–4033, 1992. 1.2.4

[64] G. Peach, *Collisional Broadening of Spectral Lines*, pp. 875–888. New York, NY: Springer New York, 2006. 11

[65] S. Endres, H. van Hees, J. Weil, and M. Bleicher, "Dilepton production and reaction dynamics in heavy-ion collisions at SIS energies from coarse-grained transport simulations," *Phys. Rev. C*, vol. 92, p. 014911, Jul 2015. 1.2.4, 1.3.4, 1.30, 1.3.4, 10.6, 10.16

[66] W. K. Wilson *et al.*, "Inclusive dielectron cross-sections in p + p and p + d interactions at beam energies from 1.04 GeV to 4.88 GeV," *Phys. Rev.*, vol. C57, pp. 1865–1878, 1998. 1.3.1

[67] R. J. Porter *et al.*, "Dielectron Cross Section Measurements in Nucleus-Nucleus Reactions at $1.0A$ GeV," *Phys. Rev. Lett.*, vol. 79, pp. 1229–1232, Aug 1997. 1.3.1, 1.15

[68] C. Gale and J. Kapusta, "Dilepton radiation from high temperature nuclear matter," *Phys. Rev. C*, vol. 35, pp. 2107–2116, Jun 1987. 1.3.1

[69] H. Huang, S. Beedoe, M. Bougteb, J. Cailiu, J. Carroll, T. Hallman, L. Heilbronn, G. Igo, P. Kirk, G. Krebs, A. Letessier-Selvon, B. Luttrell, F. Manso, L. Madansky, H. Matis, D. Miller, J. Miller, C. Naudet, R. Porter, G. Roche, L. Schoeder, P. Seidl, Z. Wang, R. Welsh, W. Wilson, and A. Yegneswaran, "Dielectron yields in p+d and p+p collisions at 4.9 gev," *Physics Letters B*, vol. 297, no. 3, pp. 233 – 237, 1992. 1.3.1

[70] W. K. Wilson *et al.*, "Dielectron measurements in p + p and p + d interactions from E (beam) = 1-GeV to 4.9-GeV," *Phys. Lett.*, vol. B316, pp. 245–249, 1993. 1.3.1

[71] A. Drees *et al.*, "First results of the CERES electron pair spectrometer from p + Be, P + Au and S + Au collisions," *Nucl. Phys.*, vol. A566, pp. 87C–94C, 1994. 1.3.1

[72] G. Agakichiev *et al.*, "Enhanced Production of Low-Mass Electron Pairs in 200 GeV/Nucleon S-Au Collisions at the CERN Super Proton Synchrotron," *Phys. Rev. Lett.*, vol. 75, pp. 1272–1275, Aug 1995. 1.3.1

[73] D. Adamova *et al.*, "Modification of the ρ meson detected by low-mass electron-positron pairs in central pb-au collisions at," *Physics Letters B*, vol. 666, no. 5, pp. 425 – 429, 2008. 1.3.1

[74] D. Adamová *et al.*, "Enhanced Production of Low-Mass Electron-Positron Pairs in 40-AGeV Pb-Au Collisions at the CERN SPS," *Phys. Rev. Lett.*, vol. 91, p. 042301, Jul 2003. 1.3.1

[75] F. Bellaiche, B. Cheynis, D. Contardo, O. Drapier, J. Y. Grossiord, A. Guichard, R. Haroutunian, M. Jacquin, F. Malek, and J. R. Pizzi, "The NA50 segmented target and vertex recognition system," *Nucl. Instrum. Meth.*, vol. A398, pp. 180–188, 1997. 1.3.1

[76] R. Rapp, "Dileptons, charm and charmonium at finite temperature and chemical potential," *arXiv:0908.3344v1*, vol. arXiv:0908.3344v1, 2009. 1.3.1

[77] R. Arnaldi *et al.*, "NA60 results on thermal dimuons," *Eur. Phys. J.*, vol. C61, pp. 711–720, 2009. 1.3.1

[78] H. J. Specht, "Thermal Dileptons from Hot and Dense Strongly Interacting Matter," *AIP Conf. Proc.*, vol. 1322, pp. 1–10, 2010. 1.3.1

[79] R. Arnaldi *et al.*, "First results on angular distributions of thermal dileptons in nuclear collisions," *Phys. Rev. Lett.*, vol. 102, p. 222301, Jun 2009. 1.3.1

[80] L. Adamczyk *et al.*, "Measurements of dielectron production in Au + Au collisions at $\sqrt{s_{NN}} = 200$ GeV from the STAR experiment," *Phys. Rev. C*, vol. 92, p. 024912, Aug 2015. 1.3.1

[81] A. Adare and others., "Detailed measurement of the e^+e^- pair continuum in $p+p$ and $\mathrm{Au}+\mathrm{Au}$ collisions at $\sqrt{s_{NN}} = 200$ gev and implications for direct photon production," *Phys. Rev. C*, vol. 81, p. 034911, Mar 2010. 1.3.1

[82] L. Adamczyk *et al.*, "Measurements of Dielectron Production in Au+Au Collisions at $\sqrt{s_{\mathrm{NN}}}$ = 200 GeV from the STAR Experiment," *Phys. Rev.*, vol. C92, no. 2, p. 024912, 2015. 1.3.1

[83] M. M. Aggarwal *et al.*, "An Experimental Exploration of the QCD Phase Diagram: The Search for the Critical Point and the Onset of De-confinement," 2010. 1.3.1

[84] P. Huck, "Beam energy dependence of dielectron production in Au+Au collisions from STAR at RHIC," *Nuclear Physics A*, vol. 931, pp. 659 – 664, 2014. 1.3.1, 1.4

[85] X. Zhangbu, "STAR BES-I results and BES-II Program, http://ift.uni.wroc.pl/~cpod2016/ZhanbuXu.pptx," 08 2016. 1.3.1

[86] W. Ehehalt, W. Cassing, "Relativistic Transport Approach for Nucleus-Nucleus Collisions from SIS to SPS Energies," *arXiv:hep-ph/9507274*, 1995. 1.3.1, 10.16

[87] P. Reichelt, "Low-Mass Dielectron Production in pp, p-Pb and Pb-Pb Collisions with ALICE," *J. Phys. Conf. Ser.*, vol. 612, no. 1, p. 012028, 2015. 1.3.1

[88] A. Calica, "Measurement of dielectrons in pp,p-Pb and Pb -Pb collisions with ALICE at the LHC,https://indico.cern.ch/event/403913/contributions/1849260/," 06 2016. 1.3.1

[89] G. Aad *et al.*, "The ATLAS Experiment at the CERN Large Hadron Collider," *JINST*, vol. 3, p. S08003, 2008. 1.3.1

[90] S. Chatrchyan *et al.*, "The CMS experiment at the CERN LHC," *JINST*, vol. 3, p. S08004, 2008. 1.3.1

[91] A. A. Alves, Jr. *et al.*, "The LHCb Detector at the LHC," *JINST*, vol. 3, p. S08005, 2008. 1.3.1

[92] M. Sumbera, "Results from STAR Beam Energy Scan Program," *Acta Phys. Polon. Supp.*, vol. 6, pp. 429–436, 2013. 1.3.1

[93] G. Odyniec, "Future of the beam energy scan program at RHIC," *EPJ Web Conf.*, vol. 95, p. 03027, 2015. 1.3.1

[94] V. Toneev, "The NICA/MPD project at JINR (Dubna)," *PoS*, vol. CPOD07, p. 057, 2007. 1.3.1

[95] G. Agakichiev, the HADES Collaboration, *et al.*, "Dielectron production in 12 C+ 12 C collisions at 2 A GeV with HADES," *Journal of Physics G: Nuclear and Particle Physics*, vol. 34, no. 8, p. S1041, 2007. 1.3.2

[96] G. Agakishiev *et al.*, "Study of dielectron production in C+C collisions at 1A GeV," *Phys. Lett.*, vol. B663, pp. 43–48, 2008. 1.3.2

[97] G. Agakishiev *et al.*, "Dielectron production in Ar+KCl collisions at 1.76A GeV," *Phys. Rev.*, vol. C84, p. 014902, 2011. 1.23, 1.3.2, 10.2.1, 4

[98] G. Agakichiev *et al.*, "Origin of the low-mass electron pair excess in light nucleus-nucleus collisions," *Physics Letters B*, vol. 690, no. 2, pp. 118 – 122, 2010. 1.3.2

[99] R. Shyam and U. Mosel, "Dilepton production in proton-proton and quasi-free proton-neutron reactions at 1.25 GeV," *Phys. Rev.*, vol. C82, p. 062201, 2010. 1.3.2

[100] M. Bashkanov and H. Clement, "On a Possible Explanation of the DLS Puzzle," *Eur. Phys. J.*, vol. A50, p. 107, 2014. 1.3.2

[101] G. "Agakishiev and others", "Inclusive dielectron spectra in p+p collisions at 3.5 GeV kinetic beam energy," *The European Physical Journal A*, vol. 48, no. 5, 2012. 1.3.2

[102] J. Weil and U. Mosel, "Dilepton production at SIS energies with the GiBUU transport model," 2012. [J. Phys. Conf. Ser.426,012035(2013)]. 1.3.3

[103] S. Endres, H. van Hees, J. Weil, and M. Bleicher, "Dilepton Production in Transport Calculations and Coarse-Grained Dynamics," *J. Phys. Conf. Ser.*, vol. 503, p. 012039, 2014. 1.3.3

[104] E.L. Bratkovskaya et al, "System size and energy dependence of dilepton production in heavy-ion collisions at sis energies," *arXiv:1301.0786v1 [nucl-th]*, 2013. 1.3.3

[105] G. Agakichiev et al., "The high-acceptance dielectron spectrometer HADES ," *Eur. Phys. J. A*, vol. 41, pp. 243–277, 2009. 2, 2.1.1, 2.1.2, 2.1.2, 2.2.2, 2.2.3, 2.3.1, 2.7, 2.3.2, 3.6, 3.3, 4.2, 5.3

[106] "http://www.gsi.de/," 08 2016. 2

[107] "SIS18, https://www.gsi.de/work/beschleuniger/schwerionensynchrotron_sis18.htm," 08 2016. 2

[108] H. Schoen , *Ein Dielektronenspektrometer hoher Akzeptanz für relativistische Schwerionenkollisionen*. PhD thesis, Gesellschaft für Schwerionenforschung,Germany, 1995. 2

[109] T.Bretz, "Magnetfeldeigenschaften des Spektrometers HADES," Master's thesis, Technische Universität München,Germany, 1999. 2.1.1

[110] C. Muntz *et al.*, "The HADES tracking system," *Nucl. Instrum. Meth.*, vol. A535, pp. 242–246, 2004. 2.1.2

[111] H. Bokemeyer *et al.*, "Development of low-mass drift chambers for the HADES spectrometer," *Nucl. Instrum. Meth.*, vol. A477, pp. 397–400, 2002. 2.1.2

[112] , "GSI Detektorlabor, https://www.gsi.de/work/fairgsi/rare_isotope_beams/detector_laboratory.htm," 2012. 2.4, 2.8

[113] J. Pietraszko *et al.*, "Diamonds as timing detectors for minimum-ionizing particles: The HADES proton-beam monitor and START signal detectors for time of flight measurements ," *Nucl. Instrum. Meth.*, vol. A618, pp. 121–123, 2010. 2.2.1, 2.4.1

[114] J. Pietraszko, "Beam detectors in Au+Au run and future developments https://indico.gsi.de/materialDisplay.py?contribId=9&sessionId=4&materialId=slides&confId=2142./." 2.2.1, 2.4.1

[115] G. Kornakov, *New advances and developments on the RPC ToF wall pf the HADES experiment at GSI*. PhD thesis, Universidad de Santiago de Compostela, 2012. 2.2.2, 2.5

[116] D. Belver, "The HADES RPC inner TOF wall," *Nuclear Instruments and Methods in Physics Research A*, vol. 602, pp. 687–690, 2009. 2.2.2

[117] A. Blanco *et al.*, "In-beam measurements of the HADES-TOF RPC wall," *Nucl. Instrum. Meth.*, vol. A602, pp. 691–695, 2009. 2.2.2

[118] C. Agodi et al., "The HADES time-of-flight wall," *Nuclear Instruments and Methods in Physics Research A*, vol. 492, pp. 14–25, 2002. 2.2.3

[119] K. Zeitelhack et al., "The HADES RICH detector," *Nucl. Instrum. Meth. A*, vol. 433, pp. 201–206, 1999. 2.3.1, 2.3.1

[120] T. Ypsilantis, J. Seguinot, "Theory of ring imaging Cherenkov counters," *Nuclear Instruments and Methods in Physics Research A*, vol. 343, pp. 30–51, 1994. 2.3.1

[121] A. Balanda et al., "The hades pre-shower detector," *Nuclear Instruments and Methods in Physics Research A*, vol. 531, pp. 445–458, 2004. 2.3.2

[122] B. Kindler, B. Lommel, A. Hübner, W. Hartmann, and J. Steiner, "Targets for the electron-positron pair spectrometer hades," *Nuclear Instruments and Methods in Physics Research Section A: Accelerators, Spectrometers, Detectors and Associated Equipment*, vol. 655, no. 1, pp. 95 – 99, 2011. Proceedings of the 25th World Conference of the International Nuclear Target Development Society. 2.4.1

[123] O. V. Andreeva, M. B. Golubeva, F. F. Guber, A. P. Ivashkin, A. Krasa, A. Kugler, A. B. Kurepin, O. A. Petukhov, A. I. Reshetin, A. S. Sadovsky, O. Svoboda, Y. G. Sobolev, P. Tlusty, and E. A. Usenko, "Forward scintillation hodoscope for nuclear fragment detection at the high acceptance dielectron spectrometer (hades) setup," *Instruments and Experimental Techniques*, vol. 57, no. 2, pp. 103–119, 2014. 2.4.2

[124] K. O. Lapidus, "Investigation of the production of electron-positron pairs in nucleon-nucleon interactions with the hades detector," *Physics of Atomic Nuclei*, vol. 73, no. 6, pp. 985 – 987, 2010. 2.4.2

[125] J. Michel, *Development and Implementation of a New Trigger and Data Acquisition System for the HADES Detector*. PhD thesis, Johann Wolfgang Goethe Universität, 2012. 2.4.3

[126] I. Fröhlich *et al.*, "A General Purpose Trigger and Readout Board for HADES and FAIR-Experiments," *IEEE Trans. Nucl. Sci.*, vol. 55, pp. 59–66, 2008. 2.4.3

[127] "HERA file system, https://www.gsi.de/work/forschung/it/hpc/data.htm," 08 2016. 2.4.3

[128] "Experimental Physics and Industrial Control System, http://www.aps.anl.gov/epics/docs/index.php," 08 2016. 2.4.3

[129] J. Michel et. al., "The upgraded hades trigger and data acquisition system," *TOPICAL WORKSHOP ON ELECTRONICS FOR PARTICLE PHYSICS*, 2011. 2.4.3

[130] I. Antcheva *et al.*, "ROOT: A C++ framework for petabyte data storage, statistical analysis and visualization," *Comput. Phys. Commun.*, vol. 180, pp. 2499–2512, 2009. 3

[131] M. Bleicher, E. Zabrodin, C. Spieles, S. A. Bass, C. Ernst, S. Soff, L. Bravina, M. Belkacem, H. Weber, H. Stöcker, and W. Greiner, "Relativistic hadron-hadron collisions in the ultra-relativistic quantum molecular dynamics model," *Journal of Physics G: Nuclear and Particle Physics*, vol. 25, no. 9, p. 1859, 1999. 3.1

[132] I. Fröhlich et al., "Design of the Pluto Event Generator," *arXiv:0905.2568v1*, 2009. 3.1

[133] R. Brun, F. Bruyant, M. Maire, A. C. McPherson, and P. Zanarini, "GEANT3," 1987. 3.1

[134] W. H. Press, S. A. Teukolsky, W. T. Vetterling, and B. P. Flannery, *Numerical Recipes 3rd Edition: The Art of Scientific Computing*. New York, NY, USA: Cambridge University Press, 3 ed., 2007. 3.3

[135] G. Kornakov *et al.*, "Time of flight measurement in heavy-ion collisions with the HADES RPC TOF wall," *JINST*, vol. 9, no. 11, p. C11015, 2014. 3.5

[136] L.Fabbietti , *Study of the e+e- pair acceptance in the dilepton spectrometer HADES*. PhD thesis, Technische Universität München, 2003. 3.6, 5.4.2, 6.2.1

[137] M. L. Miller, K. Reygers, S. J. Sanders, and P. Steinberg, "Glauber modeling in high energy nuclear collisions," *Ann. Rev. Nucl. Part. Sci.*, vol. 57, pp. 205–243, 2007. 4.3

[138] B.Kardan, "Centrality determination at 1.23 AGeV Gold-Gold collisions aand readout-electronics for the HADES electromagnetic calorimeter," Master's thesis, Goethe-Universitaet Frankfurt, 2015. 4.3

[139] S. Harabasz, *Reconstruction of virtual photons from Au+Au collisions at 1.23 GeV/u*. PhD thesis, Jagiellonian University Krakow and Technische Universität Darmstadt, 2017. To be published. 5, 8.1.3, 8.6, 8.4

[140] A. Brenschede, "Pattern recognition for the HADES RICH detector," *Czechoslovak Journal of Physics*, vol. 45, no. 7-8, pp. 645–650, 1995. 5.3

[141] "Garfield 7.02. simulation of gaseous detectors; http://www.cern.ch/garfield; online userroot guide," 2000. 6.2

[142] H. A. Bethe and J. Ashkin, "Passage of radiation through matter," *Experimental Nuclear Physics*, vol. 1, 1953. 6.1.4.2

[143] A. Hoecker and others", "TMVA - Toolkit for Multivariate Data Analysis," *ArXiv Physics e-prints*, Mar. 2007. 7.3.1

[144] Ihler, Alexander, "Neural Network, https://www.youtube.com/watch?v=bH6VnezBZfI," 2016. 7.3

[145] M. Gazdzicki and M. Gorenstein, "Charm estimate from the dilepton spectra in nuclear collisions," *J. Phys.*, vol. G27, pp. L41–L46, 2001. 8.1.2

[146] A. Adare *et al.*, "Detailed measurement of the e^+e^- pair continuum in $p+p$ and $\mathrm{Au}+\mathrm{Au}$ collisions at $\sqrt{s_{NN}} = 200$ GeV and implications for direct photon production," *Phys. Rev. C*, vol. 81, p. 034911, Mar 2010. 8.2

[147] M. J. Clerk, "On the Dynamical Theory of Gases," *JPhil. Trans. R. Soc. Lond.*., vol. 167, pp. 49–88, 1867. 10.5

[148] "Collective flow measurements with HADES in Au+Au collisions at 1.23A GeV, https://indico.cern.ch/event/433345/contributions/2358279/attachments/1408651/2153611/QM17_02_2017_kardan.pdf," 2017. 10.11, 10.5

[149] M. PLanck, "The theory of heat radiation," 1914. 10.5

[150] "Dilepton production at SIS energies with the GiBUU transport model, https://indico.gsi.de/getFile.py/access?contribId=9&sessionId=6&resId=0&materialId=slides&confId=14931," 2012. 10.16

[151] "S. Lebedev, HADES Collaboration Meeting XXXII, https://indico.gsi.de/getFile.py/access?contribId=17&sessionId=5&resId=0&materialId=slides&confId=5175." 11.3

[152] O. Svoboda *et al.*, "Electromagnetic calorimeter for the HADES@FAIR experiment," *JINST*, vol. 9, p. C05002, 2014. 11.3

[153] "A.Zinchenko, HADES Collaboration Meeting XXXIII, https://indico.gsi.de/getFile.py/access?contribId=25&sessionId=5&resId=0&materialId=slides&confId=4673." 11.3

[154] "M. Wiebusch, HADES Collaboration Meeting XXXIII , https://indico.gsi.de/getFile.py/access?contribId=3&sessionId=0&resId=0&materialId=slides&confId=4673." 11.3

Rechtliches

Die vorliegende Druckfassung enthält kleinere, inhaltlich nicht relevante Änderungen gegenüber der dem Promotionsbüro vorgelegten Version.

Danksagung

Hiermit möchte ich allen Danken, die zu dem Gelingen meiner Arbeit beigetragen haben und diese Tätigkeit für mich zu eine lehrreichen und tollen Zeit gemacht haben. Daher möchte ich zunächst meinem Doktorvater Joachim Stroth danken, der mir schon seit meiner Bachelorarbeit die Mitarbeit an diesem spannenden Projekt ermöglichte. Dabei hat er mich stets mit seinem breiten Wissen unterstützt und ich konnte mir auch immer etwas von seiner strukturierten Herangehensweise bei der Lösung von Problemen abschauen. Ein besonderes Dankeschön gilt auch Tetyana Galatyuk, die mich schon seit dem Beginn meiner Bachelorarbeit betreut hat, und dabei keine Mühen gescheut hat um mir geduldig nahezu alles über Dileptonen und vieles mehr zu erklären. Bengt Friman möchte ich danken, dass er in meinem PhD Komitee dabei geholfen hat, dass auch die theoretischen Aspekte in meiner Arbeit nicht zu kurz kommen. Des Weiteren danke ich Stephan Endres und Florian Seck für die Bereitstellung theoretischer Modelrechnungen und Elena Bratkovskaya für das Bereitstellen des HSD Models zum Durchführen Modellrechnungen.

Georgy Kornakov und Malgorzata Gumberidze möchte ich für die zahlreichen Ratschläge bezüglich meiner Analyse und Arbeit danken. Zudem möchte ich Wolfgang König danken, der durch seine lange Erfahrung immer einen guten Tipp parat hatte. Auch Manuel Lorenz möchte ich für die Ratschläge und vielen beantworteten Fragen danken. Des Weiteren möchte ich auch Jochen Markert danken, den man immer mit Fragen bezüglich Software löchern kann. Auch bei plötzlich auftauchenden Fehlern, obwohl nichts am Code geändert wurde, hat er eine Lösung parat. Christian Müntz danke ich für die vielen Fragen aus einem anderen Blickwinkel und hilfreichen Antworten auf all meine Fragen zu Detektoren.

Danken möchte ich Lea Wunderlich, Annette Zimbelius und im besonderen Marianne Frey für die Hilfe bei organisatorischen Tätigkeiten mit der sie mir viel Arbeit abgenommen und Probleme schnell gelöst haben.

Des Weiteren, danke ich allen HADESianern aus Frankfurt, Darmstadt und der GSI Gruppe für die Unterstützung und Anregungen zur Analyse. Ich möchte auch allen Mitgliedern der HADES Kollaboration danken. Nur durch die Beiträge aller zur Hardware und Software des HADES Experiments konnten die aufgenommenen Daten eine solch hohe Qualität erreichen. Auch viele Fragen und Diskussionen haben dazu beigetragen mir immer neue Anregungen für die Analyse gegeben.

Besonderer Dank gilt auch meinen Mitstreitern, im besonderen Claudia Behnke, Heidi Schuldes, Timo Scheib, Adrian Rost und Behruz Kardan, die mich bei HADES schon lange begleitet haben und auch gerne für eine Ablenkung abseits der Physik zu begeistern waren. Zudem möchte ich auch meinem langjährigen Büronachbarn Szymon Harabasz für die zahlreichen Beiträge zur Dileptonenanlyse, von denen ich sehr profitiert habe, danken. Auch der Frankfurter ALICE-Gruppe möchte ich, für die unterhaltsame Zeit auf Tagungen und auf dem Fußballplatz danken.

Für die Ablenkung von der Physik und die vielen lustigen Abende, Tage und Trips möchte ich der "JBG" danken. Zudem hoffe ich, dass ich die aufkommenden, wenn auch teilweise etwas komischen, physikalischen Fragen zufriedenstellend beantworten konnte. Auch Svenja möchte ich, für die schöne gemeinsame Zeit bei der sie mich ganz schnell auf andere Gedanken bringt, bedanken. Auch für die Rücksicht in stressigen Phasen bin ich dir sehr dankbar. Meinen Eltern und Großeltern möchte ich für die volle Unterstützung während meiner Schul- und Studienzeit bedanken. Ihr habt mich durch Eure Unterstützung motiviert und meine Arbeit in stressigen Zeiten erleichtert.